https://ntrs.nasa.gov/search.jsp?R=19660026818 2020-03-16T20:30:26+00:00Z

TECH LIBRARY KAFB, NM
0099516

NASA CONTRACTOR REPORT

NASA CR-537

NASA CR-537

ANALYSIS OF PRESSURE AND HEAT TRANSFER TESTS ON SURFACE ROUGHNESS ELEMENTS WITH LAMINAR AND TURBULENT BOUNDARY LAYERS

by C. L. Jaeck

Prepared by
THE BOEING COMPANY
Seattle, Wash.
for Langley Research Center

NATIONAL AERONAUTICS AND SPACE ADMINISTRATION • WASHINGTON, D. C. • AUGUST 196

TECH LIBRARY KAFB, NM
0099516

NASA CR-537

ANALYSIS OF PRESSURE AND HEAT TRANSFER TESTS ON SURFACE ROUGHNESS ELEMENTS WITH LAMINAR AND TURBULENT BOUNDARY LAYERS

By C. L. Jaeck

Distribution of this report is provided in the interest of information exchange. Responsibility for the contents resides in the author or organization that prepared it.

Prepared under Contract No. NAS 1-4301 by
THE BOEING COMPANY
Seattle, Wash.

for Langley Research Center

NATIONAL AERONAUTICS AND SPACE ADMINISTRATION

For sale by the Clearinghouse for Federal Scientific and Technical Information
Springfield, Virginia 22151 – Price $4.00

PREFACE

This is one of three final reports on a program to complete the analysis of existing aerothermodynamic test data obtained during the X-20 program. The work has been accomplished by The Boeing Company under Contract NAS 1-4301 with NASA Langley Research Center, Hampton, Virginia. A. L. Nagel was the program manager, H. L. Giles was the principal investigator, and M. H. Bertram was the NASA contract monitor. Final reports have been prepared for each of three tasks:

Task I - Analysis of Hypersonic Pressure and Heat Transfer Tests on Delta Wings with Laminar and Turbulent Boundary Layers.

Task II - Analysis of Hypersonic Pressure and Heat Transfer Tests on a Flat Plate with a Flap and a Delta Wing with a Body, Elevons, Fins, and Rudders.

Task III - Analysis of Pressure and Heat Transfer Tests on Surface Roughness Elements with Laminar and Turbulent Boundary Layers.

Results of Task III are presented in this report.

CONTENTS

ANALYSIS OF PRESSURE AND HEAT TRANSFER TESTS ON SURFACE ROUGHNESS ELEMENTS WITH LAMINAR AND TURBULENT BOUNDARY LAYERS

By C. L. Jaeck

SUMMARY

An analysis is presented of data obtained during the X-20 program in which the effect of surface roughness on heat transfer and pressure was measured. Experimental data for both laminar and turbulent flow and at Mach numbers from 6.9 through 15 are presented for three basic types of surface distortions: (1) surface waves, (2) grooves or cavities, and (3) aft facing steps. Configurations tested included convex waves on sharp and blunt leading edge flat plates, concave waves on a sharp leading edge flat plate, a V-groove and an aft facing step on a swept-hemicylinder leading edge, a V-groove and a T-groove on hemisphere cylinder, circumferential grooves on a delta wing leading edge, and transverse and swept grooves on a wind tunnel wall.

Data are compared with theory and previously published empirical approaches. In the case of surface waves, laminar heat transfer data are compared with a shallow wave theory presented in an appendix of this report. Surface wave heat transfer data are presented for various geometry and flow conditions up to Mach 15 in air. Geometric variables studied were wave sweep angle, wave height and width, and the spacing between multiple waves.

Turbulent flow over waves was also studied. The laminar shallow wave theory was empirically extended to turbulent flow using both X-20 and NASA data. The turbulent "theory" adequately predicts the increase of the heating rate on the first wave, but underpredicts the maximum heating rate to the second wave.

The maximum increase in laminar heating rate for grooves and cavities was correlated using a Nusselt number based on cavity width in the direction of flow. The data correlated in this manner show that the heating increases as width to depth ratio is decreased. Data are also presented for an aft facing step on a hemicylinder leading edge. A semi-empirical method was developed to predict the maximum heating at reattachment downstream of the step. This method is based on empirical correlations of the step base pressure and maximum reattachment pressures.

INTRODUCTION

Heat transfer prediction methods generally assume that the body surface is smooth. However, manufacturing requirements, load deformations, and thermal expansion effects can be expected to cause surface roughness to exist on full scale vehicles. For this reason the X-20 aerothermodynamic program included a series of tests to determine the effect of typical surface distortions on aerothermodynamic heating and pressure. Seven series of tests were conducted in NASA, Air Force, and private facilities. Roughness elements included waves, grooves, and steps mounted on flat plate, cylinder and delta wing models.

The analysis of these data was not completed at the time the X-20 program was terminated; indeed, some of the tests were still in progress. Since the models tested were basic shapes rather than specific X-20 configurations, and provide research results not otherwise available, NASA has financed the continued analysis and publication of the data that had been obtained.

During and after the X-20 program, work of other investigators was appearing in the literature. Bertram and Wiggs, reference (1), presented heat transfer data for unswept steep waves in laminar flow; reference (2) presented experimental results for unswept waves in turbulent flow. A theoretical calculation of boundary layer over a small wave, using finite difference methods was published by Flugge-Lotz and Baxter (ref. 3). Various other authors (for example, references 4 through 13) have presented experimental results for grooves, cavities, and steps.

The present report provides information on several geometries not previously tested, including swept waves, swept grooves, and grooves and steps in the presence of pressure gradients. A wave analysis, similar to that of reference 3, but more detailed, and including real gas effects, is presented in an appendix of this report. The analysis is verified and extended with the aid of the experimental data.

Two other reports in this series, references (14) and (15), present the results of delta wing studies and flow separation studies that were conducted as a part of the X-20 program.

SYMBOLS

c	specific heat of model skin
c_p	specific heat at constant pressure
C_f	skin friction coefficient, $\tau / [1/2(\rho u^2)]$
C_p	pressure coefficient
D	diameter
h	aerodynamic heat transfer coefficient; $\dot{q}/(T_{aw} - T_w)$
H	total enthalpy; groove depth; step height; $\dot{q} / (i_{aw} - i_w)$
i	static enthalpy
k	thermal conductivity
L	length
M	Mach number
N_{Re}	Reynolds number based on boundary layer edge conditions at x, $(\rho_e u_e x)/\mu_e$
$N_{Re,L}$	free stream Reynolds number based on a model reference length (L), $(\rho_\infty u_\infty L)/\mu_\infty$
N_{St}	Stanton number, $h/(\rho_\infty U_\infty C_p)$
P	pressure
P_o	nozzle supply pressure
P_o'	total pressure behind a normal shock
Pr	Prandtl number
q	aerodynamic heating rate
r	streamline divergence due to body geometry
R	roughness height; gas constant
S	surface distance
t	time

T	temperature
u	velocity parallel to surface
v	velocity normal to surface
W	wave or groove width in direction of flow, $W = W'/\cos\lambda$
W'	wave or groove width measured normal to the wave or groove
x	distance measured parallel to surface
y	distance measured normal to surface
z	compressibility factor; distance measured parallel to surface
α	angle of attack
γ	specific heat ratio
δ	boundary layer thickness
δ^*	boundary layer displacement thickness
$\Delta\nu$	flow expansion angle (see figures 54, 55, 56)
θ	angle from geometric stagnation line or point around body; boundary layer momentum thickness
λ	wave or groove sweep angle
Λ	sweep angle, measured from a line normal to the flow
μ	dynamic viscosity
ρ	density
τ	shear stress; model skin thickness
ψ	angle of yaw

Subscripts:

aw	adiabatic wall
e	boundary layer edge; condition downstream aft facing step expansion
eff	effective

min	minimum
max	maximum
o	stagnation; tunnel total condition
r	reference
RT	turbulent reference condition on a 60° swept leading edge
s	top of aft facing step
SL	stagnation line
sm	smooth
w	fluid property at the wall
∞	undisturbed free stream conditions

APPARATUS AND TESTS

Test Facilities

The X-20 surface roughness program consisted of seven tests. Five tests were conducted in three conventional wind tunnels, and two tests in the Cornell Aeronautical Laboratories (CAL) shock tunnel. All tests were conducted in air.

The three conventional wind tunnels utilized were:

1. Boeing Hypersonic Wind Tunnel (BHWT)

2. Arnold Engineering Development Center Wind Tunnel C (AEDC-C)

3. Jet Propulsion Laboratory 21-inch Hypersonic Wind Tunnel (JPL)

These four facilities will be discussed briefly, starting with conventional wind tunnels.

Boeing Hypersonic Wind Tunnel. - The Boeing Hypersonic 12-inch Wind Tunnel is a blowdown type providing steady flow for periods up to two minutes, depending upon flow conditions. Stagnation pressure and temperature maximums utilized were 1100 psia and 1500°R, respectively. A 12" x 12" Mach 7 contoured two-dimensional nozzle and quick start equipment were added to this wind tunnel for the surface roughness test. The surface roughness panels were mounted in the tunnel test section wall. Transient model temperature measurements for heat transfer data were recorded on multi-channel oscillographs. Pressure data were punched directly into IBM cards from a scanning-valve transducer system.

Arnold Engineering Development Center Tunnel C. - The Mach 10 Tunnel C at Arnold Engineering Development Center is of the continuous flow, closed-test-section type. Stagnation pressures and temperatures utilized were 340 and 1640 psia, 1720 and 1880°R, respectively. The corresponding free stream Reynolds numbers were 5×10^5 and 2×10^6 per foot. Sting mounted models were protected from the flow by a cooling chamber below the tunnel test section. To expose the model, cooling chamber doors were retracted and the model raised into the tunnel. The movement of the model from tunnel wall to tunnel centerline, was accomplished in approximately .5 seconds. Model temperature data were recorded on magnetic tape from the output of a digital voltmeter which scanned each thermocouple 20 times per second. Pressure data were similarly recorded on magnetic tape from a scanning-valve transducer system. Reference 16 may be consulted for further facility information.

Jet Propulsion Laboratory Hypersonic Tunnel. - The 21-inch Jet Propulsion Laboratory Wind Tunnel provided continuous flow at Mach 8.04 and a free stream Reynolds number of .76 x 10^6 per foot. Total pressure was 250 psia at a total temperature of 1660°R. This tunnel utilized a removable cooling shroud to protect the sting mounted model from the flow. Shroud removal took approximately 0.25 second. Temperature and pressure data were recorded on magnetic tape directly from digital readout systems. Each thermocouple was read 20 times per second.

Cornell Aeronautical Laboratory Shock Tunnel. - The Cornell Aeronautical Laboratory Shock Tunnel tests were conducted in a 48-inch contoured nozzle having a Mach number of 15, and a 24-inch contoured nozzle having a nominal Mach number of 6. The total pressure in these tests were up to 700 psia and the total temperature was up to 5,950°R. Further facility details may be obtained from reference 17.

A brief description of each test and its associated models appears below. Nominal wind tunnel flow conditions are summarized in Table I while details of model geometry are shown in figure 1.

In the remainder of this report the tests will be referred to by their respective Boeing Model numbers, such as AD465M-1.

Models and Tests

AD465M-1[a] - The AD465M-1 model shown in figure 1(a) is a 73° sharp prow delta wing with circumferential leading edge grooves. The test program was conducted in the Jet Propulsion Laboratories 21" Hypersonic Tunnel at a Mach number of 8 and freestream Reynolds number of 4.7 x 10^4 based on leading edge diameter. For some tests the leading edge grooves were filled with cement to obtain smooth body data.

AD633M-1[b] and Rerun[c] - AD633M-1 model shown in figure 1(b) is a flat plate with roughness inserts that was tested at Arnold Center Tunnel C at a Mach number of 10. The roughness inserts are shown in figure 1(c) and included an unswept sine wave, unswept circular arc waves of two different heights, and a circular arc wave swept 70° to the flow. The model was equipped

---

Data reports are identified by alphabetical superscripts and may be obtained on loan from The Boeing Company, Seattle, Washington.

[a] Data Report JPL 21-83 Heat Transfer and Pressure Test on a Slotted Leading Edge Wing Model, Boeing Document D2-80491, June 27, 1962.

[b] Data Report AEDC-C, AD633M-1, Boeing Document D2-80767, June 1963.

[c] Data Report AEDC AD633M-1 Rerun, Boeing Document D2-80767-1, September 1963.

with separate heat transfer and pressure inserts and both sharp and blunt leading edges. The sharp leading edge configuration was tested at -5°, 0°, and 10° angles of attack at free stream Reynolds numbers (based on the sharp leading edge model length) of 1.16×10^6 and 4.66×10^6. This configuration was tested at the high Reynolds number both with and without boundary layer trip wires. The blunt configuration was tested only at the high Reynolds number and without trip wires. Both configurations were tested with end plates in order to avoid three-dimensional flow effects. Many data runs in the original AD633M-1 tests were spoiled when sticking of the injection system caused excessively long model injection times. Some of these tests were repeated in the AD633M-1[c] rerun series. Only the sharp leading edge configuration was retested and only at angles of attack of 0°, 5° and 10°.

AD633M-2[d] - The AD633M-1 sharp leading edge model was retested in AEDC Tunnel C with different roughness inserts and designated as AD633M-2. The roughness elements are shown in figure 1(d) and include four waves, one of which was swept 70° to the flow; an inverted circular arc wave and a groove. Test conditions were the same as for the AD633M-1 rerun.

AD642M-1[e] - AD642M-1 included a series of basic shapes which were tested in the Cornell Aeronautical Laboratory Hypersonic Shock Tunnel. These shapes included a sharp nosed hemicylindrical leading edge tested at sweep angles of 55°, 60°, 65°, and a hemisphere cylinder tested at angles of attack of 0°, 10°, 20°, and 50°. Sketches of the two models are shown in figures 1(e) and 1(f). Heat transfer and pressure measurements were obtained in laminar flow at a Mach number of 15 and in turbulent flow at a Mach number of 6 over a wide range of Reynolds numbers. A sharp flat plate was also tested and reported under Task II of the present contract.

AD647M-1[f] - AD647M-1 was to have been a series of tests of roughness elements mounted in the wall of a 12" x 12" Mach 7 contoured nozzle for the Boeing Hypersonic Tunnel. The two-dimensional nozzle was specially constructed to simulate flight values of roughness height relative to the turbulent boundary layer thickness with very large roughness elements that would allow dense instrumentation. At the time of X-20 program termination, only one run on each of three elements had been completed. Sketches of the nozzle and roughness panels are presented in figures 1(g) and 1(h.)

---

[d] Data Report AEDC-C, AD633M-2, Boeing Document D2-80912, dated June 1963.

[e] Turbulent Reference, Roughness Leakage, and Deflected Surface Heat Transfer and Pressure Tests for The Boeing Company Conducted on the CAL 48" Hypersonic Shock Tunnel, Boeing Document D2-80910, dated January 3, 1963.

[f] Boeing Hypersonic Wind Tunnel No. 062 Heat Transfer and Pressure Tests on AD647M-1, a Surface Roughness Model in a Two-Dimensional Test Section, Boeing Document D2-81248, dated March 1964.

AD713M-1[g] - The AD713M-1 sharp flat plate model, presented in figure 1(i), was tested in the CAL 48" shock tunnel at a Mach number of 15. The model was tested without side plates during the entire test series. Pressure and laminar heat transfer distributions were obtained on a 70° swept wave and 70° swept groove inserts. Data obtained at two Reynolds numbers and at angles of attack of 0°, 5°, 10°, 15°.

EXPERIMENTAL TECHNIQUE AND DATA REDUCTION

Pressure Data

Conventional Wind Tunnels. - Conventional wind tunnel pressure measuring techniques were used in tests AD465M-1, AD647M-1, and AD633M-1. Piezoelectric pressure transducers were employed throughout. Model pressure readings were scanned prior to recording to ensure stable conditions. Data were read simultaneously with the tunnel total pressure and temperature.

Where pressure and heat transfer models were combined, the pressure taps and thermocouple instrumentation were installed on opposite sides of the model to avoid heat sink effects.

Heat Transfer Data

Conventional Wind Tunnels. - Heat transfer data from all conventional wind tunnel tests were obtained by the well-known thin skin calorimeter technique. This method consists of measuring the rate of temperature increase of the thin metal skin of the model exposed to aerodynamic heating. A local heat balance on the thin skin relates the heating rate to the skin temperature as follows:

$$q = \rho c \tau_{eff} \frac{\partial T_w}{\partial t} - k \tau \left[\frac{\partial^2 T_w}{\partial x^2} + \frac{\partial^2 T_w}{\partial z^2} \right] \qquad (1)$$

where ρ, c, and k are density, specific heats and thermal conductivity of the model skin. The term $\rho c \tau_{eff} \partial T_w/\partial t$ represents the net rate at which heat is being added to the skin; the term $k \tau (\partial^2 T_w/\partial x^2 + \partial^2 T_w/\partial z^2)$ represents only that rate of heat addition by conduction along the model skin.

---

[g] Hypersonic Shock Tunnel Test of Two Roughened Flat Plates for The Boeing Company, Boeing Document D2-80955, dated July 1963.

Prior to each run the models were isolated from the wind tunnel flow and cooled in order to maximize the aerodynamic heating rate and to minimize conduction effects due to initial skin temperature gradients. Models were then exposed to the flow by model injection (AEDC-C) or shroud removal (JPL) as quickly as possible. The time required for shroud removal and model injection was approximately .25 and .5 seconds respectively.

The wall temperature, T_w, was measured with No. 30 gage (.010 inch diameter) chromel-alumel thermocouples spotwelded to the inside surface of the model skin. The skin was made sufficiently thin so that temperature differences between the internal and external surfaces of the skin were negligible. Nominal skin thickness for each calorimeter model are shown on figure 1.

The local aerodynamic heat transfer rate was calculated using the relation:

$$\dot{q}_m = \rho c \tau \frac{\partial T_w}{\partial t} = h_m (T_{aw} - T_w) \qquad (2)$$

where,

ρ = skin density
c = skin specific heat
τ = skin thickness
T_{aw} = the adiabatic wall (local recovery) temperature
T_w = the wall temperature

The adiabatic wall temperature was calculated from the following equation:

$$\frac{T_{aw}}{T_o} = r + (1-r) \frac{1 + \frac{\gamma-1}{2} M_\infty^2 \sin^2 \alpha_{local}}{1 + \frac{\gamma-1}{2} M_\infty^2} \qquad (3)$$

where α_{local} is the angle between the free stream velocity vector and the local tangent plane. The recovery factor, r, was taken as 0.85 for laminar flow and 0.90 for turbulent flow. Although equation (3) is not exact except at the wing leading edge, the error will be small because of the small value of (1-r).

The symbol τ in equation (2) is the local ratio of the skin volume to the heated surface - actually [d (skin volume)/d (skin external surface area)]- which for a flat surface is just the measured skin thickness. On models with curved skins the [d (skin volume)/d (skin external surface area)] is no longer the measured skin thickness, τ, but an effective thickness, τ_{eff}, which is a function of τ. A correction was applied to the measured heat transfer coefficient to account for the change of skin volume per unit

surface area on curved surfaces.

$$h_{corr} = \frac{\tau_{eff}}{\tau} h_m = \frac{\rho c \tau_{eff}}{T_{aw} - T_w} \frac{d T_w}{d t} \quad (2a)$$

For cylindrical surfaces, the measured heat transfer coefficient may be corrected approximately by:

$$\frac{\tau_{eff}}{\tau} = 1 - \frac{\tau}{2R} \quad (2b)$$

where R is the radius of curvature. The maximum volume correction used in this report occurs on the AD465M-1 leading edge. For this position

$$\tau_{eff} = .94 \tau \quad (2c)$$

The model skin properties were determined from published data. The values used are as follows:

Nickel:

$\rho = 554$ ($Lb_m/ft.^3$)

$c = .05378 + .12529 \times 10^{-3} T_w - .50699 \times 10^{-7} T_w^2$ ($Btu/lb_m-°R$)

Stainless Steel

$\rho = 492.5$ ($Lb_m/ft.^3$)

$c = 9.27286 \times 10^{-2} + 4.23286 \times 10^{-5} T_w - 6.57143 \times 10^{-9} T_w^2$ ($Btu/lb_m-°R$)

Thermocouple measurements were recorded in digital form at the rate of twenty times per second for each thermocouple for 5 to 10 seconds depending upon the severity of the heating rates. The temperature-time derivative (dT_w/dt) were evaluated at the midpoint of 11 or 21 point second degree least squares curve (one second duration) fitted to the digital data. A separate curve fit was made for each time at which heating data were desired. Usually heat transfer coefficients were calculated at ten different times during the test run in order to determine conduction effects.

All calorimeter model heat transfer data were corrected for lateral conduction by the Thomas-Fitzsimmons method, which was developed in the course of the X-20 program. This method which is described in detail in reference 15 , used the time variation of the measured temperature rise rate to evaluate conduction errors. In essence the method consists of

extrapolating the curve of heat transfer coefficient versus time (or temperature) back to an effective start of the test run. For data reduction purposes, the test run was assumed to start at the time the model entered the inviscid core of the tunnel flow. A sample raw data trace from a AD633 model is shown in figure 2. In this case the time of test initiation was taken to be at point A. An illustration of the temperature extrapolation process is shown in figure 3.

Shock Tunnel. - Tests AD642M-1 and AD713M-1 (CAL Shock tunnel) utilized thin film heat transfer gages to measure heating rates. The thin gages have the necessary rapid response time for use in shock tunnels. Thin film gages consist of a platinum film vacuum deposited over a pyrex glass substrate. The surface temperature history of the glass defines the aerodynamic heating rate by use of the solutions of the heat conduction equation for a semi-infinite slab (references 18 and 19). Because of the short test times, lateral conduction of the type experienced in thin skin calorimeter models is insignificant.

DATA APPRAISAL

Wind tunnel testing for surface roughness effects on aerodynamic heating is unusually difficult. The requirement to scale the size of the roughness element to the boundary layer thickness limits model size and multiplies errors due to conduction. Large variations in the local heating rate occur that not only increase conduction effects but also make it very difficult to ensure that instruments are placed at peak heating locations. Accordingly, the first phase of this study was an appraisal of the quality of the existing data with particular attention to the effects of conduction, boundary layer trips, and tunnel flow irregularities.

Pressure Data

Conventional Wind Tunnel Pressure Data. - No unusual difficulties arose in the measurement of pressure data in conventional wind tunnels except in test AD465M-1. These pressure data exhibited a significant variation with time. Since there were few pressure gages located along the slotted leading edge, pressure data have been omitted from this report. Pressure data from other conventional wind tunnel tests exhibited good repeatability.

Heat Transfer Data

Heat transfer data are subject to numerous and often large sources of error, which may be either systematic or random. Systematic errors may arise from conduction, model thermal distortion, or gage temperature effects. Random errors may arise from lack of complete control of test conditions, measurement errors, and human error.

In the present study, careful consideration was given to sources of error and steps were taken to prevent, minimize or correct for them wherever

possible. Due to the large quantity of data in the present report, individual attention could not be given to all apparent data discrepancies. Data obviously erroneous were omitted whenever noticed. In turbulent flow, data from several different, but similar, models and tests are presented. Agreement between such data is, at times, only fair and is attributed to transitional flow. The major problems encountered and the corrective action taken are described below.

Conduction Effects. - For the thin skin calorimeter heat transfer models, the major systematic error was lateral conduction in the model skin. To estimate the degree to which the present data are affected by conduction errors, a sample of data uncorrected for conduction and corrected by the method of reference (15) has been compared in figure 4. All of the AD633 model heat transfer data originally documented prior to the contract were either uncorrected or corrected using a correction given by

$$q = \rho c \tau_{eff} \frac{\partial T_w}{\partial t} - \tau k \frac{\partial^2 T_w}{\partial x^2} \qquad (1a)$$

It is assumed in equation (1a) that only temperature gradients in the streamwise direction are important for two dimensional, thin skin models. The spatial derivative $\partial^2 T_w / \partial x^2$ was approximated by a three-point, parabolic curve fit. The AD633 data, even when corrected in this manner, were not considered satisfactory, inasmuch as the corrected data exhibited irregular variations of the heat transfer coefficient with time. The data were therefore reduced from the original time-temperature data and corrected by the method of reference (15). As shown in figure 4, even on the relatively large models of the present test, conduction effects at the peak heating locations were an appreciable percent of the observed roughness effect. In view of the large model sizes employed, the correction methods that were used, and the self-consistency of the data, it is felt that the AD633 data are among the most reliable surface roughness data in existence.

Other Systematic Errors. - Other systematic errors in heating data have been considered. The heat sink effect of No. 30 gage thermocouple wire has been estimated to contribute less than 1 percent error. Errors due to radiation are similarly considered negligible. Model skin thickness was carefully controlled in manufacture and locally measured to 0.0005 inch, or approximately 1 percent. The specific heat of the skin perhaps accounts for the second largest systematic error, but is felt to be known to about 3 percent.

Boundary Layer Tripping Devices. - Boundary layer wire devices were used to obtain turbulent flow on the AD633 flat plate models. The wire spanned the plate at a distance of 12 inches from the leading edge. The wire diameter was .035 inches, about 1/2 the laminar boundary layer displacement thickness. The trip wire did not always cause transition, and its effectiveness could only be judged by observing trends downstream of the trip. Comparisons of

measured and theoretical heating rates are not definitive, since the effect of the trip on the external flow and the effective origin of turbulent boundary layer is not known. In view of the general lack of data on roughness effects in turbulent flow, the tripped boundary layer data are included in this report. In all cases the upstream data are presented so that the reader can judge the validity of the conclusion drawn. A sample of the AD633 tripped data are presented in figure 5 and compared with both laminar and turbulent predictions by the $\rho_r \mu_r$ method (reference 15). Both predictions are based on distance from the leading edge.

Flow Irregularities. - The only flow irregularity known to be present in AEDC-C tunnel data is an axial Mach number gradient of approximately 0.01 per foot. This effect is considered to be negligible.

CAL Gage Calibration. - The CAL heat transfer data are obtained with a gage that consists of a thin film of platinum fused to a glass substrate. The platinum film is used as a resistence thermometer to measure the increase in substrate surface temperature during the test. The heating rate can be determined from the temperature increase if the density, specific heat, and thermal conductivity of the substrate are known. The quantity actually required is the square root of their product (ρck) which is determined from a calibration procedure in which a step pulse electric current is passed through the platinum film. The small amount of resistance heating causes a slight temperature increase and allows $\sqrt{\rho ck}$ to be determined at the initial gage temperature. The variation of $\sqrt{\rho ck}$ with temperature is obtained by preheating the gage in an electric oven and repeating the electric pulse heating calibration.

Some time after the AD642 tests were completed, CAL made new measurements of $\sqrt{\rho ck}$ that lead to a considerably different variation with temperature than previously indicated. It was not feasible to rereduce the data at the time this report was written. It was determined, however, that the laminar data shown would be lowered by 0 to 6 percent on the basis of the new calibration. The highest heating rate data (obtained on the leading edge model in turbulent flow) would be reduced by up to about 30 percent.

After examining the effects of the "new" calibration would have on the data, particularly such trends as heating rate versus time during the test run, the authors feel that some uncertainty in calibration remains. A test will be made in 1966 as a part of an Air Force research contract that is expected to provide additional information.

The data are presented as originally reduced. The AD642M-1 heat data analyzed in this report are used in the form of ratios, that is, the measured roughness heat rate are compared to the measured smooth body heating rate. Thus the effect of gage calibration errors should be minimized.

RESULTS AND DISCUSSION

Protruding Surface Waves

Pressure data.- Pressures were measured on protruding surface waves on both blunt and sharp leading edge flat plates. The sharp plate was tested at each of two Reynolds numbers. Pressure measurements from wave inserts on both flat plate configurations are presented in figures 6 through 13. Data both on the waves and forward of the waves are presented.

The pressure data forward of the waves on the smooth portion of the sharp flat plate are compared with both oblique shock theory and an unpublished viscous interaction method of Bertram (ref. 20). The low Reynolds number sharp plate data, presented in figures 6, 7, and 8, are shown to be 15 to 20 percent higher than wedge theory. Correction for viscous effects are seen to improve the agreement. There is however an uncertainty in the pressure comparisons since the temperature of the pressure models was not measured. Therefore, the viscous interaction effect on pressure was computed for both the adiabatic conditions and the nominal model temperature (520°R). The pressure data tend to agree more closely with the interaction calculation based on adiabatic wall temperature, as is shown in figures 6 through 11. At high angles of attack the viscous interaction of Bertram method (ref. 20) is in good agreement with the data; however at low angles this method under predicts the data. The data at $\alpha = 0°$ presented in figures 6 and 7 show some variation between repeat tests on each of the two wave inserts.

Inspection of the smooth sharp flat plate pressure data at the high Reynolds number, figures 9 through 11, show a reduced effect of viscous interaction. The viscous interaction method of Bertram is in excellent agreement with the data, assuming the model is at the adiabatic wall temperature.

Smooth blunt plate pressure data are shown in figures 12 and 13 to be in excellent agreement with the method Bertram and Bardell (ref. 21).

Thus far only the smooth body pressure data have been examined and analyzed. The smooth body pressures were shown to be influenced by the boundary layer. The pressure distribution over the wave is also strongly influenced by the boundary layer, which has a smoothing effect on the pressure distributions. According to local flow wedge (oblique shock) theory for the conditions of figure 6, the peak pressure ratio at 10° angle of attack would be 95, or more than 8 times higher than the observed value. Pressure data on the swept wave, figure 8, show a similar effect, as may be seen from the wedge-expansion theory curve also shown.

The existence of the smoothing effect of the boundary layer is further confirmed by the observation that the high Reynolds number data, figure 9 through 11, consistently show larger pressure perturbations for each wave

shape than do the low Reynolds number data, figures 6 through 8. Consistent with this trend is the increase of the pressure perturbations with angle of attack which reduces the boundary layer thickness. The edge Mach number is also reduced, but linear theory calculations indicate that the effect of Mach number differences is small.

Similar comparisons of pressure data from waves on a blunted plate, figures 12 and 13 cannot be made since data are available at only one free-stream Reynolds number. However, the high Reynolds number data from the blunt leading edge model show smaller pressure effects than do the low Reynolds number data from the sharp leading plate. Calculation show both the local Mach number and Reynolds number are lower on the blunted plate and this result is therefore consistent with the previously noted trends.

Comparisons are presented in figures 14 through 15 of the maximum pressure measured on the first wave with that predicted by the shallow wave theory of Appendix A. The comparisons are presented as a function of angle of attack, due to the dependence of maximum wave pressure on both the local Mach number and the boundary layer displacement thickness. Since the model temperature is not known, the theory was evaluated for both the model initial temperature and for adiabatic wall temperature. The displacement thickness was calculated with the curves of Appendix B.

The measured pressure increase is within the spread of the theory for the three unswept waves. Considering that the inviscid theory predicts values 5 to 10 or more times higher than the observed effect, the agreement with the shallow wave theory is considered excellent.

For the swept wave, and for the blunt leading edge plate data the prediction is much less successful, although again the comparison with the inviscid prediction shows that the viscous theory is correct in predicting that the actual pressure perturbation is a small fraction of that predicted by inviscid theory.

Wave pressure data from the sharp leading edge plate at a length Reynolds number of 4.66×10^6 are not compared to the laminar theory because the heat transfer data of figure 5 indicate that the boundary layer was transitional ($\alpha = 0°, 5°$) or turbulent ($\alpha = 10°$). Since a theory does not exist for turbulent flow, the shallow wave theory must be extended empirically. The data are presented in figure 16 compared with the laminar shallow wave theory and an empirical modification for turbulent flow. The turbulent prediction is based on a fit to the heat transfer data, as described under "Heat transfer data - turbulent flow." The two methods are compared with data in figure 16. The turbulent displacement thickness used in the theoretical predictions shown in figure 16 are calculated with the curves of Appendix B and based on the distance from the leading edge. The agreement obtained is only fair. As with the laminar data, agreement is poorest for the swept wave.

Heat transfer data - laminar flow.- Laminar heat transfer data for three types of protruding waves on sharp and blunt leading edge flat plates have been analyzed. The three wave configurations are: circular arc protruding waves, convexo-concave sine wave, and 70° swept circular arc waves. Heat transfer distributions on unswept circular arc waves are presented in figures 17 through 19. Heat transfer data for a series of six successive waves are presented in figure 17. These data show little reduction in the peak wave heating on the downstream waves relative to the smooth body values. The boundary layer remains laminar, even after flowing over the six waves as indicated by the agreement of the smooth body data aft of the waves with laminar flat plate theory.

Since the peak heating relative to the smooth body value did not change significantly over the multiple surface distortions, only the data from the initial waves were conduction corrected and analyzed for the remaining tests. The data for the smooth sharp flat plate, figures 17 and 18 show good agreement with the flat plate $\rho_r \mu_r$ theory (ref. 15). The theory predictions are based on nominal measured pressures forward of the first wave, but neglecting variation of pressure with distance.

Maximum wave heating rates as predicted by the shallow wave theory of Appendix A are shown in figures 18 for comparison with the experimental results and the empirical equation of Bertram and Wiggs (ref. 1). The effect of pressure gradients has been neglected in all calculations of the smooth body displacement thickness. The data agree well with the shallow wave theory, but are below the predictions of reference 1. Both methods indicate the wave heating rate ($\dot{q}_{max}/\dot{q}_{sm}$) should decrease slightly over the multiple wave due to an increase in smooth body displacement thickness. The data show little reduction of the maximum wave heating rate ratio ($\dot{q}_{max}/\dot{q}_{sm}$). The data previously shown indicate that boundary separation has occurred over the waves. The shallow wave theory however assumes attached flow. Analysis of flow over a deflected flap model (ref. 14) with separation indicated that the peak or reattachment heating rate is less than or equal to that predicted by attached flow theory, from which it appears that attached flow theory should also predict the maximum heating rate due to the wave. A further example of the attached flow theory applied to a flow separation case is presented in this report in the section on aft facing steps.

Data for the same wave shape tested on a blunted plate are presented in figure 19. The first wave peak heating data show fair agreement with the shallow wave theory and reference 1 with the latter giving slightly better agreement. Both of these predictions are based on flow conditions obtained from the measured pressures and normal shock entropy.

Heating rates at 10 degrees angle of attack, figures 19 and 20, show a rising trend with distance. This trend is believed to indicate boundary layer transition. Transition appears to have begun slightly before or over the first wave and appears fully turbulent aft of the waves.

To verify that boundary layer transition has occurred the data are compared with the laminar-turbulent $\rho_r \mu_r$ theory. Turbulent theory lines are shown in figure 20, for four virtual flow origins. Their agreement with the data indicates that the boundary layer is fully turbulent aft of the waves.

A summary of laminar heat transfer data from waves on a sharp flat plate is presented in figures 21 and 22 and shows good agreement with the predictions of the shallow wave theory. The maximum heating rate on the waves were nondimensionalized using the smooth body heating rate obtained from the gages forward of the wave with a $1/\sqrt{x}$ extrapolation. Only the gages unaffected by the waves were considered in this extrapolation. The extrapolation was compared with theory for several runs, found to agree well, and therefore used for the other comparisons.

The boundary layer displacement thicknesses were calculated using the curves presented in Appendix B, using nominal measured pressures and oblique shock theory.

The effect of distance between multiple waves is shown in figure 22. Tests were run on inserts containing similar waves but with different spacing to determine the effect on the maximum wave heating. Comparisons of the data from the three wave inserts show no conclusive results, however.

Heat transfer data from a second wave configuration, that of the convexo-concave sine wave are presented in figures 23 and 24. The data from sharp and blunt plates are compared with the shallow wave theory and the empirical relationship of reference 1. The shallow wave theory is in excellent agreement with the data, while reference 1 is higher than the data. However, both methods show good agreement with the blunt plate-wave data at $\alpha = 0°$ as is shown in figure 24. The $\alpha = 10°$ data show a rising trend over multiple waves and indicates boundary transition is occurring.

The heat transfer distributions for the third wave configuration, the swept wave, are presented in figures 25 and 26. The Mach 10 distribution, figure 25 resembles the previous unswept wave results, with the maximum being observed near the wave peak. In contrast to the previous Mach 10 data, the Mach 15 data presented in figure 26 show the points of maximum heating forward of the wave peaks. The observed difference between two sets of swept wave data may be the result of three dimensional flow effects since the CAL model was tested without side plates. The heating rate increase on the second wave is not significantly different from that observed on the first wave.

Figures 27, 28, and 29 present data and theory comparisons for the effect of sweep on maximum heating rate for three waves. The shallow wave theory was developed for two dimensional flow. A question therefore arises whether to evaluate the Mach number and W/R in the direction of flow or normal to the swept wave. Comparison of the two methods yielded approximately the same

numerical results. Figures 27 and 28 indicate that maximum heating rate on the swept wave is as high or higher than that observed on an unswept wave of the same geometry. The shallow wave predictions indicate a decrease in heating as a result of sweeping the wave, however the theory does not consider three dimensional effects.

The upper bound predicted by the shallow wave theory is shown in figure 29 to agree well with all the CAL data taken at a Mach number of 15, the data ranging from 10% below the theory to a maximum of 14% above the theory for the high Reynolds number at 15 degrees angle of attack. It should be noted that the shallow wave calculation for the heat transfer distribution over the wave does not lead to a single value of q/q_{sm} for each value of R/δ^*. A typical calculated distribution is plotted in figure 30 where it is seen that the theory predicts slightly higher values on the downstream side of the wave. These higher values, are due to the effects of pressure gradients, which are adverse on the forward face of the wave and favorable on the lee side. The theoretical trend is not confirmed by the test data, however, and the maximum experimental values invariably occur on the forward face of the wave. This slight difference in character could be due to the existence of secondary shocks or Mach waves in the tests, phenomena which are not described by the boundary layer equations.

Heat transfer data - turbulent flow.- A limited amount of turbulent heating data on surface waves was obtained during test AD633. As previously discussed under DATA APPRAISAL, tripping attempts are usually successful, and most of the data were transitional. The boundary layer is considered to be fully turbulent ahead of the first wave in only one run at $\alpha = 10°$ on the sharp leading edge model. In two additional runs the data ahead of the wave have reached turbulent levels, but still show a slight positive gradient indicating that transition is not complete. All three sets of data are presented in figure 31.

Heat transfer distributions for three wave models for tripped flow at 10 degrees angle of attack are presented in figure 31. The heat transfer is observed to increase aft of the trip wire and approaches the flat plate value for fully developed turbulent flow as given by the $\rho_r \mu_r$ theory (ref. 15), based on distance from the leading edge. The heat transfer coefficients on the .07" unswept wave are slightly higher on the second wave than on the first wave, which could indicate that fully developed turbulent flow was not attained. However, the flat distribution of heating ahead of the wave indicates that the flow is fully turbulent, so that the increase in heating on the second wave may indicate the effect of changing edge conditions or boundary layer characteristics. Unfortunately, no more definitive data were obtained in the present tests.

Additional turbulent wave data were obtained from test AD647M-1, which was a roughness panel in the tunnel wall. Unfortunately, this test was discontinued after only one data run due to the X-20 program termination. The single AD647M-1 heat transfer distribution for fully turbulent flow over a wave is presented in figure 31 (d). Data are presented only for the first wave, due to loss of the oscillograph traces for the second wave.

A summary of maximum turbulent heating rates to the waves is presented in figure 32. All the maximum heating rates except that for $M_\infty = 6.95$ were nondimensionalized using the $\rho_r \mu_r$ theory values. That datum which was taken from the AD647 test, was ratioed to the measured smooth body heating rate, since there was no reliable way to evaluate the correct effective origin of the turbulent boundary layer on the tunnel wall.

The displacement thicknesses for the AD633 runs were computed using the method presented in Appendix B. The displacement thickness for the AD647M-1 test was obtained from a probe survey of the boundary layer.

For turbulent flow over waves.- No analytic method is available for predicting heating effect of waves in a turbulent boundary layer. The laminar shallow wave method suggests a form of correlation in which the constants A, B, and C of equations (A7), (A8) and (A9) are evaluated empirically. The best overall agreement with the present data was obtained using:

$$A = 0$$
$$B = 2.5$$
$$C = 1$$

With these values the following implicit expression for the heating rate is obtained from equation (A12):

$$\frac{R}{\delta^*_{sm}} = \frac{\Delta q}{q}\left[\frac{1}{2.5 + \frac{\Delta q}{q}}\right]\frac{1}{1 - \frac{\sqrt{M_e{}^2 - 1}}{\gamma \pi M_e{}^2}\frac{\Delta q}{q}\frac{W}{R}} \tag{4}$$

This empirical method is based on only the first wave maximum heating points. The darkened symbols shown in figure 32 represent the maximum heating rate on the second wave. Equation (4) is compared with wave data from reference 2, in figure 33. Although the data reported in reference 2 are taken from three-dimensional "bumps" rather than waves, the data are also seen to agree reasonably well with equation 4, which it appears that three-dimensional effects are not large for sinusoidal waves in turbulent boundary layers.

Grooves and Inverted Waves

Pressure data.- Pressure distributions over an inverted circular arc wave and two swept grooves are presented in figure 34 through 36. The smooth plate pressure data forward of the grooves are compared with oblique shock theory and the viscous interaction method of Bertram (ref. 20). The oblique shock theory corrected for viscous effects is in good agreement with the data for $M_\infty = 10$, as shown in figures 34 and 35. The viscous interaction method (ref. 20) predicts a larger effect for the $M_\infty = 15$ data presented in figure 36. The wall temperature used in these calculations was 520°R.

In the case of the inverted wave the flow expands into the cavity and recompresses downstream of the cavity. As shown in figure 34 the peak pressure increase at reattachment does not change significantly with angle of attack. The peak pressure does however, change with cavity width, as is shown by the lower peaks aft of the second cavity.

The pressure distributions for the 70° swept groove, figure 35, show little or no effect of the grooves. The higher Mach number data of figure 36 also show no effect. However, there is only one gage downstream of the groove, so that the absence of pressure effects is not well established in this case.

Heat transfer data - laminar flow.- Data from four groove or cavity configurations were analyzed during this study. Laminar heat transfer distributions are presented in figures 37 through 42 for the four groove types which are:

(a) Two unswept, concave circular arc or inverted waves in a sharp leading edge flat plate at $M_\infty = 10$, figure 37.

(b) A 70° swept curve bottom groove in a sharp leading edge flat plate at $M_\infty = 10$, figure 38.

(c) A 70° swept rectangular cross sectional groove in a sharp leading edge flat plate at $M_\infty = 15$, figure 39.

(d) A circumferential rectangular groove on the cylindrical leading edge of 73° sharp prow delta wing, at $M_\infty = 8$, figures 40, 41 and 42.

Inspection of the data for the four configurations reveals much the same heating distributions for all models. The heat transfer distributions are characterized by a sharp decrease over the groove, followed by a rise above smooth body values downstream of the groove. In all cases the point of maximum heating occurs at the downstream groove edge or outside of the groove. This is apparently due to boundary layer separation beginning at the groove followed by reattachment downstream of the groove. Bertram and Wiggs (ref. 1) previously observed such an effect in oil flow patterns on a sine wave cavity.

The heating distributions for circumferential leading edge grooves, are presented in figures 40 through 42. In order to more easily examine the maximum heating rate, the data are plotted against distance from the nearest upstream groove. Data from several stations were found to agree well when plotted in this manner.

Zero angle of attack, zero yaw stagnation line data are shown in figure 40 (a). As shown in figure 40 (a), heating rates downstream of the groove are approximately 35 percent above the smooth cylinder theory, and remains above the theory for about 10 groove-widths.

An attempt was made to obtain smooth body heat transfer coefficients by retesting the model with the leading edge grooves filled with cement. These data are also shown in figure 40 (b). The filled groove data show effects that are similar to, but smaller than those exhibited by the open groove data, which may be the result of some small remaining surface distortions. The effect could also be due to differences in surface temperature caused by differences in thermal properties of the cement and the base metal.

Data from the same model at 10 degrees angle of attack, or 10 degrees angle of yaw (figure 41) show effects similar to those of figure 40, with slightly larger percentage increases. The largest percentage increases, however (as compared to the theoretical smooth cylinder theory), are observed at locations away from the stagnation line. Those data, shown in figure 42, are in some cases as much as 90 percent above the smooth cylinder theory. However, part of the increase may be due to the effect of the wing, since the filled groove data also fall well above the cylinder theory. Therefore, a line was faired through the filled groove data, ignoring data in the proximity of the groove. When compared to this faired line, the increase due to the groove is still over 50 percent, however.

Since an analytic solution for flow over grooves does not exist, empirical correlations were attempted. The best correlation was obtained using a Nusselt number based on groove width ($h_{sm}W/k_w$) and the groove width to depth ratio. The Nusselt number so evaluated represents a ratio of groove width to a boundary layer or film thickness. The groove width (w) is taken at the model surface in the direction of flow, and the depth (H) is the maximum value.

The proposed correlation is presented in figure 43, using the observed maximum heating rates for several types of grooves. Some additional data from references 1 and 4 are also presented. The smooth body heating rate for the reference 4 data was calculated from $\rho_r \mu_r$ theory.

The data are seen to increase with the Nusselt number $h_{sm}W/k_w$, and to decrease with W/H. It is of interest to note that the data from circumferential grooves located on a delta wing leading edge are also correlated. (The non stagnation line data are ratioed to the filled groove data rather than to the cylinder theory.) The agreement of the leading edge data with the general correlation suggests that crossflow pressure gradients have no large effect on groove heating.

Heat transfer data - turbulent flow.- Two turbulent heating distributions for grooves are shown in figure 44. These data are from tests conducted in the Boeing Hypersonic Tunnel with roughness panels mounted in the tunnel wall. Placing the roughness panels in tunnel wall allowed detail instrumentation on large models in the presence of a turbulent boundary layer two inches deep.

The turbulent flow heating distributions are similar to the laminar distributions presented previously with the point of maximum heating occurring

downstream of the cavity. Comparison of the two curves indicates that for similar test conditions and W/H, rounding the downstream corner of the groove does not significantly reduce the peak heating.

V-Grooves

A hemisphere cylinder and a swept leading edge model provided with V-grooves were tested at the CAL shock tunnel. The V-grooves are located downstream of the lower surface shoulder of both models, and have a width to depth ratio of approximately 1.0.

Hemisphere cylinder model.- Laminar and turbulent heating distributions are presented in figure 45 and 46 for both the smooth and grooved surface of the hemisphere cylinder model. The smooth body data were obtained from gages on opposite side of the small model. The peak heating in all cases occurs downstream of the groove as with all previous groove data.

Maximum measured heating rates in the vicinity of the groove are presented in figure 47. Also shown in figure 47 is the faired curve for W/H = 1.66 from figure 43. The laminar data are not grossly inconsistent with the figure 43 curve, excepting the unexplained high data point at a Nusselt number of 1.6. The V-groove data show an increase of about 30 percent at the lowest Nusselt number tested, a characteristic also exhibited by the data of figure 43 for small values of W/H. Close agreement between the two sets of data is not to be expected, however. The V-groove data are subject to three-dimensional flow effects and streamwise pressure gradients not present in the data of figure 43.

The turbulent flow data show a consistent increase of about 25 percent, again excepting a single higher value. The smooth body data for the same run conditions show a local maximum in the heating rate approximately 2 inches from the hemisphere shoulder, from which it appears that the boundary layer may not be fully turbulent at the groove location.

Swept leading edge model.- The AD642 swept leading edge model, which was provided with a V-groove downstream of lower surface shoulder, was tested at sweep angles of 55°, 60°, 65°. Smooth body measurements were obtained from gages located on the upper surface. Spanwise laminar and turbulent distributions are presented in figure 48 and 49. The heating rates have been nondimensionalized with the $\rho_r \mu_r$ theoretical stagnation line heating rate, and are compared with the $\rho_r \mu_r$ theoretical heat transfer distributions. The laminar leading edge data are in good agreement with the theory. The turbulent data however fall somewhat below the theoretical distributions near the shoulder.

The laminar data from the grooved side of the model show little or no increase in heating except at a sweep angle of 55°. For this reason only the data at $\Lambda = 55°$ are shown in the correlation presented in figure 50. The

peak heating rates presented in figure 50 were normalized with the measured smooth body values and pres nted as a function of the width Nusselt number. There appears to be a slight increasing trend with Nusselt number, but much less than that shown in figure 43. As with the hemisphere model, the number of gages that could be installed on the model was limited, and the observed values may not be the actual maximums.

T-Groove on a Hemisphere Cylinder Model

The T-groove was provided to simulate a joint on a nose cap constructed of ceramic tiles. The groove shape, and location are shown in figure 1(e). Figure 51 presents laminar heat transfer data taken both within and outside of the T-groove, and are compared with the theoretical smooth body distributions. The theoretical distribution were obtained from the Nonsimilar Boundary Layer Computer Program, which is discussed in Appendix C of this report. The data have been normalized with the respect to the theoretical stagnation point heating rate. Some of the data near the stagnation point are higher than the predicted values, which is attributed to vorticity interaction effects.

Turbulent heat transfer distributions are presented in figure 52. The data have been normalized with the theoretical $\rho_r \mu_r$ turbulent heating rate on a 60° swept infinite cylinder. The turbulent data indicate the heat rate in the groove is nearly equal to the smooth body heating rates.

It was found that the laminar heat transfer data from gage 27, which is located at junction of the T, could be correlated as a function of Reynolds number based on local properties and slot width. This correlation, shown in figure 53, indicates the heating rate in the groove increases as the 1.8 power of the Reynolds number. As shown in figure 53, the laminar data are well predicted by:

$$\frac{q}{q_{sm}} = 5.71 \times 10^{-4} \left[\frac{\rho_e \, u_e \, W}{\mu_e} \right]^{1.8} \qquad (5)$$

Aft Facing Step

Pressure data.- Figure 54 shows aft facing step base pressure coefficient pressure data as a function of edge Mach number. Since the only aft step tested during the X-20 Program was that on the AD642M-1 swept leading edge, data of other investigations (such as [h] and [i] footnoted below) are used in the comparison. The pressure coefficient for the turbulent boundary layer

[h] Strack, S. L.: Heat transfer at Reattachment of a Turbulent Boundary Layer. D2-22430. Available on loan from The Boeing Company

[i] Strack, S. L. and Lorenz, G. C.: Heat transfer at Reattachment of a Turbulent Boundary Layer at M = 6. D2-23058. Available on loan from The Boeing Company.

data shows a general correlation with edge Mach number, decreasing approximately as the inverse-square of the Mach number. The few laminar data available exhibit a similar trend. The cylindrical leading edge data (AD642M-1) show slightly higher values than the other data for both laminar and turbulent boundary layers. Generally, however, the data show little effect of body geometry.

In order to determine boundary layer effects, the same data are plotted in figure 55. The ratio of step height to undisturbed boundary layer momentum thickness has been chosen as the scaling parameter. This selection was made for convenience; displacement thickness would be equally satisfactory. Figure 55 shows Mach number to be the primary variable. The effect of H/θ is confined to the region where H/θ is less than about 20. The faired lines of constant Mach number are seen to agree well with the limit established the theory of Korst (ref. 9) for large values of H/θ.

Figure 56 shows a correlation of the maximum pressure ratio near reattachment with the parameter $M_e \sin \Delta\nu$ for constant values of H/θ, where M_e is the Mach number of the inviscid flow after expansion over the step and $\Delta\nu$ is the Prandtl-Meyer expansion angle at separation corresponding to the measured base pressure. The AD642 data are from the farthest downstream gage which was always the highest value of the three gage measurements. The dashed lines in figure 56, indicate the apparent trends of the maximum pressure ratio for constant values of H/θ. The solid line in this figure represents the maximum pressure ratios which were calculated by Roshko and Thomke (ref. 8) using Korst results.

Heat transfer data - laminar flow.- Figure 57 shows heat transfer distributions for laminar boundary layer flow over the AD642M-1 model. These distributions were normalized with the measured stagnation line values and show a marked decrease in the heat transfer rate at separation with a gradual increase to the attached value. The reattachment points shown were predicted using measured base pressure and assuming a linear separating streamline and compression through a plane oblique shock. The predicted reattachment heating rates were obtained using equation (6) below.

$$\frac{h_{reattachment}}{h_{sm}} \doteq \frac{(P\,u_e)_{reattachment}}{(P\,u_e)_{sm}} \tag{6}$$

This approximate relation is based on the equation:

$$h = \frac{\text{constant}}{Pr^{2/3}} \frac{\rho^* \mu^{*1/n} u_e}{\left[\int_0^x \rho^* \mu^* u_e \, dx\right]^{1/(n+1)}} \tag{7}$$

which is a slight generalization of an equation by Lees (ref. 22). In equation (7) n is one for laminar flow and 4 for turbulent flow. The star (*) denotes evaluation at the reference temperature condition defined as

$$T^* = .5\ T_w + .28\ T_e + .22\ T_{aw} \tag{8}$$

To evaluate the effect of a sudden compression on heat transfer coefficent as given by equation (8) we write

$$\frac{h_+}{h_-} = \frac{(\rho^* \mu^{*1/n} u_e)_+}{(\rho^* \mu^{*1/n} u_e)_-} \left[\frac{\int_0^{x_-} \rho^* \mu^* u_e\ dx}{\int_0^{x_+} \rho^* \mu^* u_e\ dx} \right]^{1/n+1} \tag{9}$$

where subscripts + and - indicate evaluation just downstream and just upstream of the compression respectively. If the compression occurs over a small distance the two integrals must be equal, since

$$\int_0^{x_+} \rho^* \mu^* u_e\ dx = \int_0^{x_-} \rho^* \mu^* u_e\ dx + (x_+ - x_-)\ \rho^* \mu^* u_e + \ldots \tag{10}$$

and for small values of $(x_+ - x_-)$

$$\int_0^{x_+} \rho^* \mu^* u_e\ dx \doteq \int_0^{x_-} \rho^* \mu^* u_e\ dx \tag{11}$$

Therefore equation (9) reduces to:

$$\frac{h_+}{h_-} \doteq \frac{(\rho^* \mu^{*1/n} u_e)_+}{(\rho^* \mu^{*1/n} u_e)_-} \tag{12}$$

Since the change in T* are small and changes in T* and μ^* tend to compensate equation (12) reduces to

$$\frac{h_+}{h_-} \doteq \frac{(P\ u_e)_+}{(P\ u_e)_-} \tag{6}$$

Since no assumption has been made regarding boundary layer state, equation (6) applies to either laminar or turbulent flow. Equation (6) would also be applicable in the presence of flow separation provided no

appreciable increase in the integral of equation (9) occurred over the separated region. Since the integral represents the effect of wall shear on the boundary layer growth, it seems reasonable that small shear forces in the separated region are also negligible. In the case of separation the subscripts + and - would refer to conditions just ahead of separation and just downstream of reattachment respectively.

The aft facing step heat transfer predictions presented in this report are obtained from equation (6). Since the velocity change is small, a prediction based on the pressure ratio alone would give nearly the same result as equation (6).

The point of peak heating and pressure are assumed to occur at the reattachment point. In the physical case the point of reattachment is forward of the point of peak pressure (ref. 8 and 10).

The AD642M-1 laminar heat transfer data were compared with that of Rom and Seginer (ref. 7). Rom and Seginer indicated an increase in heating aft of the step of seven times smooth body values. These data are believed to be high because of incorrect smooth values due to boundary layer transition. Data from a gage aft of the reattachment point show a trend with Reynolds number to the .8 power, which indicates transition occurred between the step and the reattachment point.

Heat transfer data - turbulent flow.- Figures 58 and 59 shows AD642M-1 heat transfer distributions across the step for various edge conditions. These distributions show that the heat transfer rates decrease to a very low value in the separated region with rather abrupt increase across the reattachment zone with a maximum occurring just downstream of reattachment. After reaching a maximum, there is a tendency for the heat transfer rates to decrease slightly. The maximum heat transfer rates in these distributions appear to be less than have previously been observed for reattaching flows (ref. 5, 6 and 12). The point of peak heating, however, may have been missed due to insufficient instrumentation.

The heat transfer rates shown are referenced to the heat transfer upstream from the step edge and not the heat transfer rate at the step edge. A comparison of the theoretical heating rates, based on $\rho_r \mu_r$ theory (ref. 15) are presented in figure 60. The data shown in this figure indicate that stagnation line heating rates agree with the theory upstream of the step. However, just ahead (.12" from step) of the step edge the measured heating rate departs from the theoretical values. The erratic behavior of the heating rates in this area might be suspected to be the result of pressure disturbances being transmitted upstream from the separated zone through the subsonic portion of the boundary layer or flow acceleration. The limited amount of pressure data available did not show a variation other than data scatter. Additional experimental investigation would be advisable to determine whether a critical condition exists in this area.

The peak heating rates aft of the step are presented in figure 61 as a function of base pressure and H/θ. The curves shown represent the heat

transfer coefficient ratios calculated using equation (6) and the pressure correlations in figures 55 and 56. Although there is considerable data scatter, equation (6) appears to predict the general level of the data.

CONCLUDING REMARKS

An analysis of experimental data was performed to determine the effect of surface waves, grooves and aft facing steps on heat transfer and pressure. The data show that large increases in local heating rates can result from small irregularities. In contrast to most aerodynamic heating effects, the effect of surface roughness on the heating rate was found to be much greater than the accompanying effect on the local pressure. Comparison of the wave pressure data with the calculated inviscid value indicates the presence of the boundary layer has a significant smoothing effect on the pressure distribution.

For the conditions of the test, the increase in heating due to a wave has been shown to be primarily dependent on roughness height and Mach number. The effect of wave shape and sweep on heating are secondary of importance. Sweepin a wave generally resulted in a little or no reduction of peak heating rate as compared with a wave of similar cross section. Data from one swept wave was shown to be higher than the unswept values.

Theoretical considerations suggest the trends observed are not general. For waves that are small compared to the boundary layer thickness, theory indicates the heating effect is primarily due to the protrusion of the waves into the hot boundary layer. In this case the external flow is relatively unaffected and the heating increase depends primarily on the wave height to boundary layer thickness ratio. If the wave is large compared to the boundary layer thickness, however, the effect on the external flow will be much more important. For very large waves the discussion of reference 14 suggests that the heating trends may be expected to be qualitatively similar to the pressure distribution and thus would be affected by wave sweep and wave shape.

An analytic solution for laminar attached flow over two-dimensional shallow waves has been shown to be in good agreement with experimental results. The attached flow theory was indicated to represent the maximum increase in heating even for the separated case and compared well with data where separation had occurred ahead of the waves.

Analytical predictions for the swept wave were not as good. The theory predicted a decrease in heating rate due to sweeping a wave, while a limited amount of data indicated the peak heating rate on the swept wave to be equal to or greater than on the same unswept wave of similar geometry. The theory however does not consider three dimensional effects, and this may account for some of the observed difference between the theory and data.

Maximum heating rate increase due to a groove or cavity occurs downstream of the groove. The maximum heating rate data from grooves of many different geometric shapes and test conditions correlate well with the use of a Nusselt number based on groove width and a ratio of groove width to depth. Data from V-grooves on a hemisphere cylinder and swept hemicylinder-flat plate models fall below the proposed correlation. The models, however did not contain sufficient instrumentation downstream of the groove to measure peak heating rate. The cavity data correlated in this manner indicated the heating rate increase to be independent of the local Mach number which was also observed by Bertram and Wiggs (ref. 1). Pressure gradient effects on maximum groove heating were observed to be small as shown by comparison of data from a grooved delta wing leading edge model with that from a flat plate.

A semi-empirical method to predict aft facing step reattachment heating based on step base pressure and a maximum reattachment pressure correlation was in agreement with the data. The base pressure data approach the values predicted by the thin boundary layer theory of Korst (ref. 9).

The overall pressure change (reattachment to value at top of step) was shown to be small. Since heat transfer is related to pressure, the small observed changes in peak heating at reattachment are therefore consistent with the pressure. Comparison of data from a step on a swept leading edge with results from flat plates show little effect of pressure gradient on peak heating.

Heat transfer data from a gage located just upstream of the step indicated heating substantially above that predicted by swept cylinder theory. The pressure data from the same location did not show an effect other than data scatter. Further experimental investigation may be required to determine if a heating problem exists at the upstream edge of the step.

APPENDIX A

SHALLOW WAVE THEORY FOR LAMINAR FLOW

By R. T. Savage and A. L. Nagel*

Shallow surface waves can originate because of thermal buckling or can be intentionally introduced during fabrication to stiffen surface panels. Because of the relatively smooth contours presented by this type of surface, the local boundary layer flow is more amenable to analysis than that over other types of surface irregularities. The analysis presented in this section is limited to attached flow over two-dimensional waves with a height to width ratio sufficiently small so that the usual boundary layer concepts are valid. For sinusoidal waves this condition is satisfied if:

$$R/W \leq .1$$

$$\left[R/W\right]\left[\delta/W\right] \leq .005$$

where δ is the boundary layer thickness.

These criteria were obtained from an order of magnitude analysis of the terms usually neglected in the boundary layer solutions. Application of the theory beyond these limits require experimental verification before the results can be accepted with confidence.

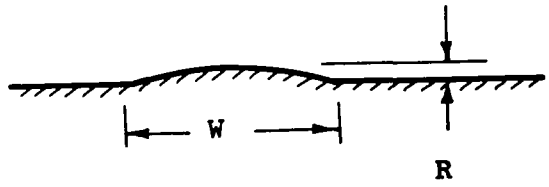

The variation in distance of a streamline outside of the boundary layer is given by the displacement thickness. The displacement thickness for a smooth plate is given by:

$$\delta^*_{sm} = Y_{ref} - \int_0^{Y_{ref}} \frac{(\rho\ u)}{(\rho_e\ u_e)_{sm}}\ dy \qquad \text{(A1)}$$

*The Shallow Wave Analysis was developed by R. T. Savage and A. L. Nagel during the X-20 development period. This analysis was further extended during Contract NAS 8-11321.

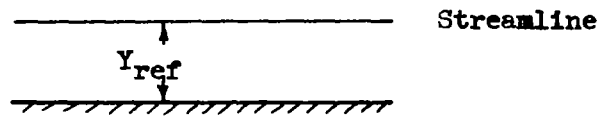

where Y_{ref} is equal to or greater than the boundary layer thickness.

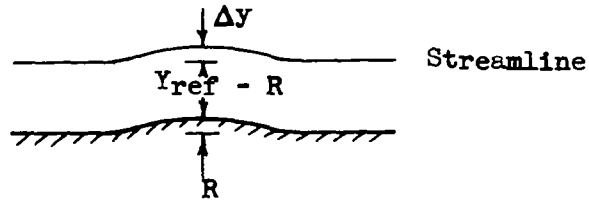

The displacement thickness over the wave is given by:

$$\delta^*_{min} = Y_{ref} + \Delta y - R - \int_o^{Y_{ref}+\Delta y-R} \frac{\rho\ u}{(\rho_e\ u_e)}\ dy \qquad (A2)$$

where Δy is the streamline displacement due to the wave. In order to satisfy conservation of mass

$$\int_o^{Y_{ref}+\Delta y-R} \rho\ u\ dy = \int_o^{Y_{ref}} (\rho\ u)_{sm}\ dy \qquad (A3)$$

Substituting (A1) and (A2) into (A3) and rearranging gives

$$R/\delta^*_{sm} = \left[1 - \frac{(\rho_e\ u_e)_{sm}}{(\rho_e\ u_e)}\right]\left[\frac{Y_{ref}}{\delta^*_{sm}} - 1\right] + 1 - \frac{\delta^*_{min}}{\delta^*_{sm}} + \left(\frac{\Delta y}{\delta^*_{sm}}\right) \qquad (A4)$$

If it is assumed that the pressure distribution can be computed from small perturbation theory, the maximum change in pressure over a sinusoidal surface is, for supersonic flow,

$$\frac{P_{max} - P_{sm}}{P_{sm}} = \frac{\gamma \pi M_e^2}{\left[M_e^2 - 1\right]^{1/2}} \frac{\Delta y}{W} \tag{A5}$$

Hence,

$$\frac{\Delta y}{\delta^*_{sm}} = \frac{\Delta P}{P} \frac{\left[M_e^2 - 1\right]^{1/2}}{M_e^2} \frac{W}{R} \left(R/\delta^*_{sm}\right) \tag{A5a}$$

Substituting (A5a) into (A4) gives

$$R/\delta^*_{sm} = \left\{ \left[1 - \frac{(\rho_e u_e)_{sm}}{\rho_e u_e} \right] \left[\frac{Y_{ref}}{\delta^*_{sm}} - 1 \right] + 1 - \delta^*_{min}/\delta^*_{sm} \right\} + \frac{\Delta P}{P} \frac{\left[M_e^2 - 1\right]^{1/2}}{\gamma \pi M_e^2} \frac{W}{R} R/\delta^*_{sm} \tag{A5b}$$

Equation (A5b) is rearranged to give

$$R/\delta^*_{sm} = \left\{ \left[1 - \frac{(\rho_e u_e)_{sm}}{\rho_e u_e} \right] \left[\frac{Y_{ref}}{\delta^*_{sm}} - 1 \right] + 1 - \frac{\delta^*_{min}}{\delta^*_{sm}} \right\} \Bigg/ \left[1 - \frac{1}{\gamma \pi} \frac{\left[M_e^2 - 1\right]^{1/2}}{M_e^2} (\Delta P/P)\, W/R \right] \tag{A6}$$

Defining the following:

$$A = \left[\frac{Y_{ref}}{\delta^*_{sm}} - 1 \right] \left[1 - \frac{(\rho_e u_e)_{sm}}{\rho_e u_e} \right] \Bigg/ \frac{\Delta P}{P} \tag{A7}$$

$$B = \frac{q_{max} - q_{sm}}{q_{sm}} \Bigg/ \frac{\delta^*_{sm} - \delta^*_{min}}{\delta^*_{min}} = \frac{\Delta q/q}{\Delta\delta^*/\delta^*_{min}} \tag{A8}$$

$$C = \frac{P_{max} - P_{sm}}{P_{sm}} \Bigg/ \frac{q_{max} - q_{sm}}{q_{sm}} = \frac{\Delta P/P}{\Delta q/q} \tag{A9}$$

$$D = \frac{1}{\gamma\, \pi} \frac{\left[M_e^2 - 1\right]^{1/2}}{M_e^2} \frac{W}{R} \tag{A10}$$

also,

$$1 - \frac{\delta^*_{min}}{\delta^*_{sm}} = \frac{\delta^*_{sm}/\delta^*_{min} - 1}{\delta^*_{sm}/\delta^*_{min} - 1 + 1} = \frac{\delta^*_{sm} - \delta^*_{min}}{\delta^*_{min}} \Bigg/ \left[\frac{\delta^*_{sm} - \delta^*_{min}}{\delta^*_{min}} + 1\right]$$

$$= \frac{1}{B}\frac{\Delta q}{q} \Bigg/ \left(\frac{1}{B}\frac{\Delta q}{q} + 1\right) = \frac{\Delta q}{q} \Bigg/ \left(\frac{\Delta q}{q} + B\right) \tag{A8a}$$

equation (A6) can be transformed into

$$R/\delta^*_{sm} = \left[A\,\frac{\Delta P}{P} + \frac{\Delta q}{q} \Bigg/ \left(\frac{\Delta q}{q} + B\right)\right] \Bigg/ \left[1 - D\,\frac{\Delta P}{P}\right] \tag{A11}$$

we can replace $\frac{\Delta P}{P}$ with $\frac{\Delta q}{q}$ using (A9).

Now,

$$R/\delta^*_{sm} = \left[AC\ \frac{\Delta q}{q} + \frac{\Delta q}{q} \Big/ \left(\frac{\Delta q}{q} + B\right)\right] \Big/ \left(1 - DC\ \frac{\Delta q}{q}\right) \tag{A12}$$

or

$$\left(1 - DC\ \frac{\Delta q}{q}\right) R/\delta^*_{sm} = AC\ \frac{\Delta q}{q} + \frac{\Delta q}{q} \Big/ \left(\frac{\Delta q}{q} + B\right) \tag{A13}$$

This can be expanded to

$$- (R/\delta^*_{sm})\ \frac{\Delta q}{q} - (R/\delta^*_{sm})\ B + CD\ (R/\delta^*_{sm}) \left(\frac{\Delta q}{q}\right)^2 + BCD\ (R/\delta^*_{sm})\ \frac{\Delta q}{q}$$

$$+ AC \left(\frac{\Delta q}{q}\right)^2 + ABC\ \frac{\Delta q}{q} + \frac{\Delta q}{q} = 0 \tag{A14}$$

Collecting common powers of $\frac{\Delta q}{q}$

$$\left[AC + CD\ (R/\delta^*_{sm})\right] \left(\frac{\Delta q}{q}\right)^2 + \left[1 + ABC + (BCD - 1)\ R/\delta^*_{sm}\right] \frac{\Delta q}{q}$$

$$- B\ (R/\delta^*_{sm}) = 0 \tag{A15}$$

or

$$\left(\frac{\Delta q}{q}\right)^2 + \frac{\left[1 + ABC + (BCD - 1)\ R/\delta^*_{sm}\right]}{AC + CD\ (R/\delta^*_{sm})} \frac{\Delta q}{q} - \frac{B\ (R/\delta^*_{sm})}{AC + CD\ (R/\delta^*_{sm})} = 0 \tag{A16}$$

Then $\frac{\Delta q}{q}$ can be obtained using the quadratic equation as given by

$$\frac{q_{max} - q_{sm}}{q_{sm}} = \frac{1}{2} \left\{- K_1 + \left[K_1^2 + 4 K_2\right]^{1/2}\right\} \tag{A17}$$

where

$$K_1 = \left[1 + ABC + (R/\delta^*_{sm})\ (BCD - 1)\right] \Big/ (AC + CD\ R/\delta^*_{sm}) \tag{A18}$$

$$K_2 = (R/\delta^*_{sm})\ B \Big/ (AC + CD\ R/\delta^*_{sm}) \qquad (A19)$$

Correlations of parameters B and C have been obtained for laminar flows using the Nonsimilar Boundary Layer Program (Appendix C). The effects of sinusoidal pressure perturbations on peak heating rates are shown in figures 62 and 63. Results shown in figure 62 indicate that the peak heating rate is nearly proportional to the pressure rise except when boundary layer separation is approached. This linearity is used in establishing the correlation shown in figure 63. Results indicate that the increase in heating is independent of Mach number, but is somewhat dependent on wall cooling. It is seen that $C \approx 1/(.78 + .84\ H_w/H_o)$ except for very highly cooled surfaces. This expression is recommended for all surface cooling ratios, since any inaccuracies should lead to increased estimates of heating rate.

A similar approach is used to determine the effects of sinusoidal pressure perturbations on displacement thickness. Again, the displacement thickness parameter $(\delta^*_{sm}-\delta^*_{min})/\delta^*_{min}$ is nearly proportional to the pressure rise $\Delta P/P$. The value of $1/BC$ is seen to be roughly .4 except at for highly cooled surfaces. As with the heat transfer correlation, assuming a constant value of .4 will lead to conservative estimates of $(q_{max}-q_{sm})/q_{sm}$

It appears reasonable to assume that $Y_{ref} \sim \delta^*_{sm}$. For supersonic flow $\left[\rho_e u_e-(\rho_e u_e)_{sm}\right]/(\rho_e u_e)$ is roughly proportional to the pressure rise $\Delta P/P$.

Hence, the parameter AC should remain approximately constant. The value of AC has been selected as .3 based on analysis of experimental heating transfer data.

The increase in heating due to a wave in laminar flow was calculated using equation (A17). The results are presented in figures 64, 65, and 66, for R/δ^* and $\left[(M^2_e - 1)^{1/2}/M^2_e\right]$ (W/R).

CR-537

APPENDIX B

METHODS FOR COMPUTING BOUNDARY LAYER DISPLACEMENT THICKNESS

Laminar flow.- The δ^* presented herein were obtained from a computer program, which solves the laminar boundary layer equations for compressible flow of real gas. The equations were solved in the similarity form and are restricted to flat plate flow. The results are represented by the expression

$$\frac{\delta^*}{x}\sqrt{N_{Re}} = B\,M_e^2 + C\,\frac{T_w}{T_e} \qquad \text{(B1)}$$

The values for the coefficients B and C are presented in figures 67 and 68. The calculations for B and C coefficients were made for a constant pressure of .01 atmospheres. It was found that pressure has very little effect on $\delta^*\sqrt{N_{Re}}/x$ for edge temperatures less than about 6000°R. The Reynolds number is based on flow condition at the boundary layer edge.

The above calculations were made by W. K. H. Kressner of The Boeing Company.

Turbulent flow.- The turbulent δ^* used herein were obtained from the form factors of figure 69 and momentum thicknesses from the $\rho_r \mu_r$ method (reference 15). The turbulent form factors presented were obtained by R.T. Savage of The Boeing Company using the Crocco energy integral (Pr = 1) and the 1/7 power law. The results are supported by experimental data presented by Sivells and Payne (reference 23).

APPENDIX C

NONSIMILAR BOUNDARY LAYER PROGRAM*

The purpose of the Nonsimilar Boundary Layer Program is to integrate the laminar boundary partial differential equations using finite difference methods, but without the use of similarity assumptions.

Nearly all published exact laminar boundary layer solutions have been obtained using the concept of similarity. These solutions, which must be obtained numerically, require that the viscous flow partial differential equations be transformed to a set of ordinary, non-linear differential equations. In the transformed system the flow properties are expressed as functions of a single similarity variable, and are therefore independent of chordwise location. Unfortunately, the transformation is possible only for special flow conditions which are rarely realized on realistic configurations. The Boeing Nonsimilar Program was developed to avoid such limitations.

The Nonsimilar Program can calculate either stagnation or nonstagnation boundary layers with arbitrary pressure gradients, with or without mass injection. Three dimensional flow effects are calculated using the zero cross-flow approximation, which implies no rotation of the velocity vectors within the boundary layer. The program is also limited to attached flow. The program is capable of initiating its own boundary layer solutions, given only external flow properties, for either the stagnation point or sharp tip cones and plates.

The program described herein treats air in chemical equilibrium. The program can be applied to ideal gas and other fluids by changing the tabulated gas transport property tables.

Specific inputs required for the program are: pressure. wall enthalpy, a three dimensional flow parameter, r, and its derivative, $\frac{dr}{dx}$, streamwise velocity gradient and the normal velocity at the wall, as functions of streamwise distance (x). The user must also specify an initial and final value of x, x-increments, printout instructions, and a limit value η_{max} (described below).

---

* This computer program was developed by A. L. Nagel and R. T. Savage during the X-20 development program.

Basic equations.- The equations solved by this computer program are the standard boundary layer equations of state, continuity, x-momentum and energy. These equations are given below in the form used by the program for evaluation at a vertical position in the boundary layer y_i.

EQUATION OF STATE

$$\rho = \frac{P}{R\,(zT)} \tag{C1}$$

CONTINUITY

$$v = \frac{1}{\left[\frac{\partial u}{\partial y} - \frac{2u}{\Delta y}\right]} \left\{ u^2 \left[\frac{1}{r}\frac{dr}{dx} + \frac{1}{P}\frac{\partial P}{\partial x}\right] + \frac{1}{\rho}\left[\frac{\partial}{\partial y}\left(\mu \frac{\partial u}{\partial y}\right) - \frac{\partial P}{\partial x}\right] \right.$$

$$- \frac{u}{\rho\, zT} \frac{\partial (zT)}{\partial\left(H - \frac{u^2}{2}\right)} \left[\left[\frac{\partial}{\partial y}\left(\frac{\mu}{P_r}\frac{\partial H}{\partial y}\right) - u\frac{\partial}{\partial y}\left(\mu \frac{\partial u}{\partial y}\right) + u\frac{\partial P}{\partial x}\right.\right.$$

$$\left.\left. \left. + \frac{\partial}{\partial y}\left[\left(1 - \frac{1}{P_r}\right)\mu\, u \frac{\partial u}{\partial y}\right]\right] - u\left[\frac{2\, v_{i-1}}{\Delta y} + \left(\frac{\partial v}{\partial y}\right)_{i-1}\right] \right\} \tag{C2}$$

where subscript i - 1 refers to $y = y_i - \Delta y$.

X-MOMENTUM

$$\frac{\partial u}{\partial x} = \frac{1}{\rho u}\left[\frac{\partial}{\partial y}\left(\mu \frac{\partial u}{\partial y}\right) - \frac{\partial P}{\partial x}\right] - \frac{v}{u}\frac{\partial u}{\partial y} \tag{C3}$$

ENERGY

$$\frac{\partial H}{\partial x} = \frac{1}{\rho u}\left[\left[\frac{\partial}{\partial y}\left(\frac{\mu}{P_r}\frac{\partial H}{\partial y}\right) + \frac{\partial}{\partial y}\left[\left(1 - \frac{1}{P_r}\right)\mu\, u \frac{\partial u}{\partial y}\right]\right] - \frac{v}{u}\frac{\partial H}{\partial y}\right. \tag{C4}$$

Equation (C2) is obtained from the continuity equation by introducing equation (C3) and (C4) to eliminate $\partial u/\partial x$ and $\partial H/\partial x$. No atomic diffusion terms are required in equation (C4) as this mode of energy transport has been included in the Prandtl number. The numerical form of these equations as used by the program is obtained by replacing all y-derivatives with 3-point central differences.

Forward integration.- Since v is expressed as a function of input data, v can be determined explicitly at each point in the boundary layer at the initial or start position. With v defined and the initial u and H profiles, $\partial u/\partial x$ and $\partial H/\partial x$ can now be determined. With $\partial u/\partial x$ and $\partial H/\partial x$ determined, the profiles at the next station can be obtained by forward integration using equations (C5) and (C6)

$$u_{x+\Delta x} = u_x + \left.\frac{\partial u}{\partial x}\right]_x \Delta x \qquad (C5)$$

$$H_{x+\Delta x} = H_x + \left.\frac{\partial H}{\partial x}\right]_x \Delta x \qquad (C6)$$

This scheme of calculation is presented in the sketch below:

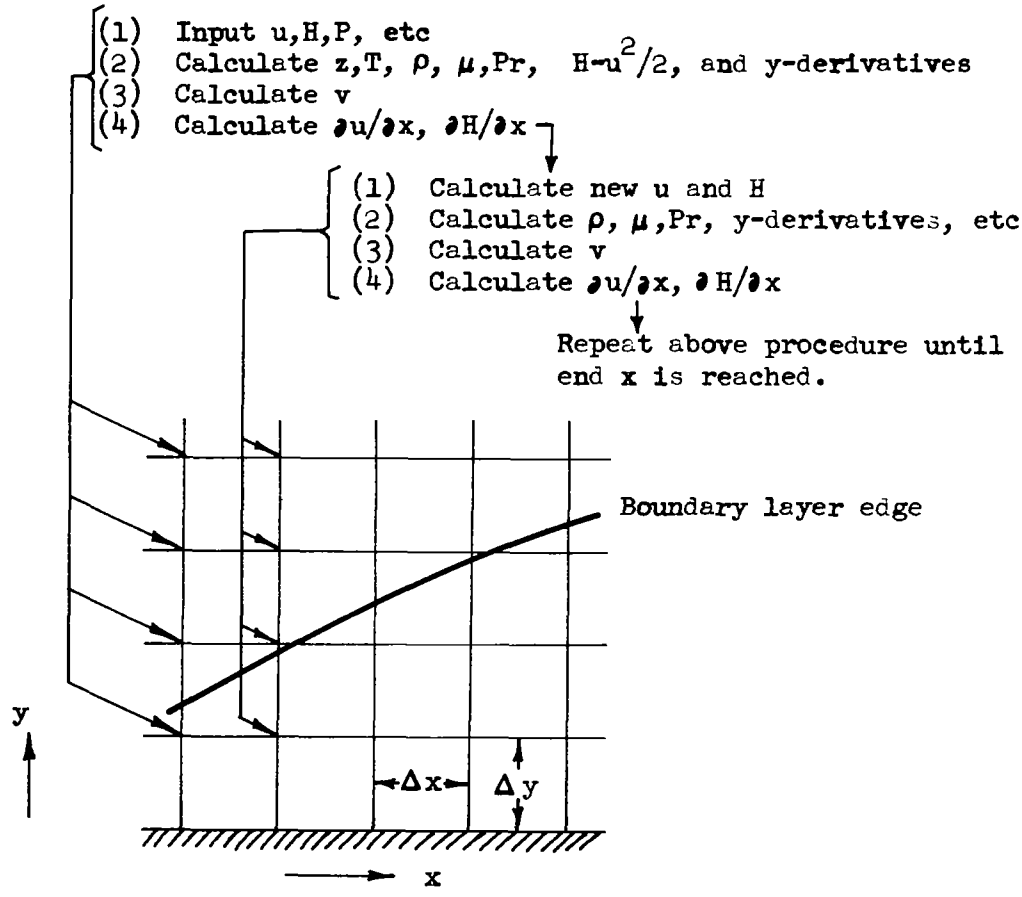

The sequence of calculations is as follows:

1) Calculate v, $\partial u/\partial x$ and $\partial H/\partial x$ for $y = i\Delta y$, $x = x_o$, beginning with $i = 1$ and continuing until i reaches a limit selected by the user as described below.

2) Calculate $u\ (x_o + \Delta x)$ and $H\ (x_o + \Delta x)$ using equations C5 and C6.

3) Repeat step 1 at $x = x_o + \Delta x$, repeating steps 1 and 2 until $x = x_{final}$, where x_{final} is a limit established by the user.

At each point in the boundary layer, a similarity parameter η is calculated using equation (C7)

$$\eta = \frac{\rho_e u_e r}{\left[\int_o^x \rho_e u_e \mu_e r^2 dx\right]} \int_o^\delta \frac{\rho}{\rho_e} dy \qquad (C7)$$

A value of η_{max} is an item of input used to limit the number of calculations in the y-direction, which are to be printed out.

Also calculated at each station (x) are the boundary layer displacement thickness, heating rate and shear at the wall, using equations (C8), (C9) and (C10).

$$\delta^* = \int_o^\delta \left[1 - \frac{\rho u}{\rho_e u_e}\right] dy \qquad (C8)$$

$$\dot{q}_w = -\frac{1}{778} \int_o^\delta \left[\rho u \frac{\partial H}{\partial x} + \rho v \frac{\partial H}{\partial y}\right] dy \qquad (C9)$$

$$\tau_w = \tau_e - \int_o^\delta \left[\rho u \frac{\partial u}{\partial x} + \rho v \frac{\partial u}{\partial y} + \frac{\partial P}{\partial x}\right] dy \qquad (C10)$$

The heating rate and shear at the wall are calculated using the energy and momentum integral equations rather than the definitions because much greater accuracy is obtained than by using numerical forms of

$$\tau_w = \mu \left(\frac{\partial u}{\partial y}\right)_w \tag{C11}$$

and

$$q_w = k \left(\frac{\partial T}{\partial y}\right)_w \tag{C12}$$

For problems without vorticity, $\tau_e = 0$. For cases with vorticity, $(\partial u/\partial y)_e$ is input as a function of x.

Stagnation point calculation.- The Nonsimilar Program has also been used to calculate stagnation point boundary layer characteristics by integrating with respect to a fictitious distance s, as follows:

$$H_i = H_i + \left.\frac{\partial H}{\partial x}\right|_i \Delta S \tag{C13}$$

$$u_i = \left[u_i + \left.\frac{\partial u}{\partial x}\right|_i \Delta S\right] \frac{x_o}{x_o + \Delta S} \tag{C14}$$

Where x_o = initial x location

ΔS = a fictitious increment of length

$\partial H/\partial x$ and $\partial u/\partial x$ are calculated exactly as before. In equation C13 x_o is a location arbitrarily near the stagnation point. Initial y-profiles of u and H must be provided at $x = x_o$; however, these may consist of values at only 3 points.

$$y = 0,\ y = \Delta y,\ y = 2\Delta y$$

The velocity and enthalpy profiles are corrected until the following convergence criteria is satisfied at each position in the boundary layer.

$$\left| \left(\frac{\partial u}{\partial x} \right)_i - \frac{u_i}{x} \right| < .1\, u_{LIST} \text{ for all i}$$

where u_{LIST} is a value from the input velocity profile.

The tolerance on the convergence criteria may seem unnecessarily large, however comparison of shear and heating rate results with other theories have been in excellent agreement.

Once the convergence criteria has been satisfied, the calculations proceed around the body as discussed in the previous section.

Gas properties.- The program treats air in chemical equilibrium. The program can be applied to air as an ideal gas and to other fluids by changing the tabulated gas transport property tables.

The transport properties for equilibrium air were based on a nine species model (N_2, O_2, NO, N, O, N+, O+, NO+ and e^-) and computed using the collision integral method of Chapman and Enskog (ref. 24). The transport properties are built into the program as tabular functions of enthalpy and pressure

$$T = f\left(P,\ H - \frac{u^2}{2}\right) \tag{C15}$$

$$z = f\left(P,\ H - \frac{u^2}{2}\right) \tag{C16}$$

$$\mu = f\left(P,\ H - \frac{u^2}{2}\right) \tag{C17}$$

$$\int Pr\, d\left(H - \frac{u^2}{2}\right) = f\left(P,\ H - \frac{u^2}{2}\right) \tag{C18}$$

The integral of the Prandtl number is used to eliminate errors introduced into the finite difference calculations by the oscillations in the Prandtl number, as sketched below:

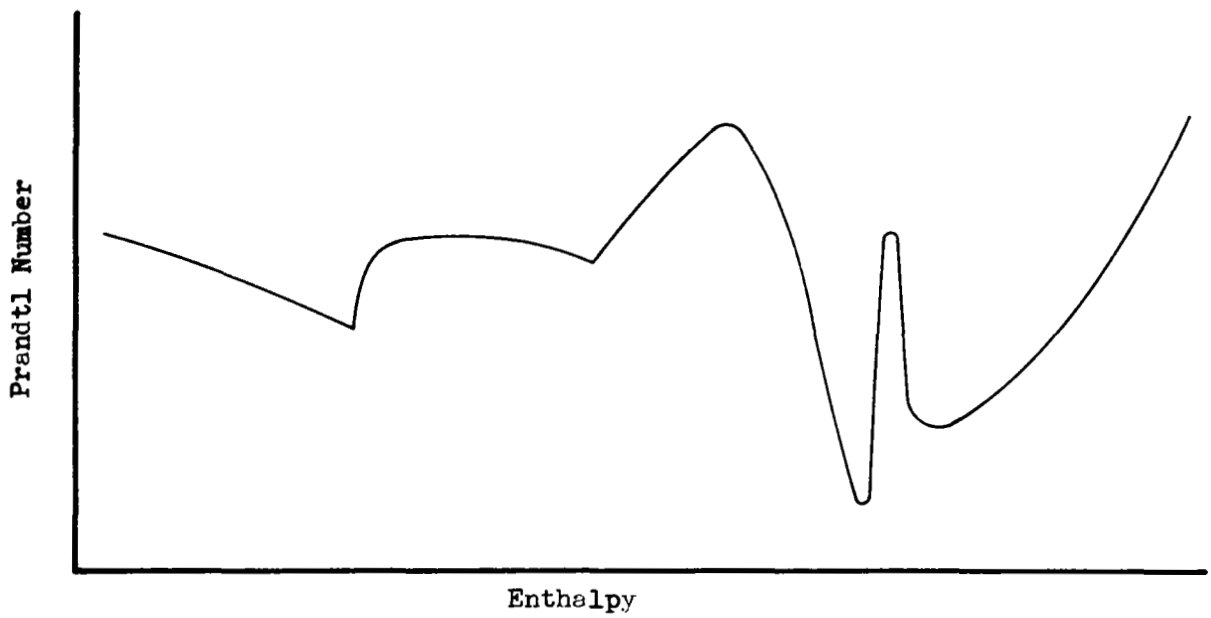

The oscillations cause a large Prandtl number gradient to exist between adjacent nodes at which claculations are made, leading to oscillations in the calculated heating distributions. Therefore an averaged Prandtl number is calculated over two nodes by:

$$Pr_i = \frac{\int \left[Pr\, d\left(H - \frac{u^2}{2}\right)\right]_{i+1} - \int \left[Pr\, d\left(H - \frac{u^2}{2}\right)\right]_{i-1}}{\left(H - \frac{u^2}{2}\right)_{i+1} - \left(H - \frac{u^2}{2}\right)_{i-1}} \tag{C19}$$

where i refers to evaluation at y_i

i + 1 refers to evaluation at $y_i + \Delta y$

i - 1 refers to evaluation at $y_i - \Delta y$

Numerical instability.- One of the major problems of the solution of partial differential equations by numerical methods is the stability of the numerical procedure. The finite difference solution is said to be numerically unstable if any small error introduced into the calculations increases as the computations progress.

A stability criteria was obtained by applying the small disturbance approach to the x-momentum equation. The resulting stability criteria is:

$$\Delta x \leq c \frac{\rho u}{\mu} \Delta y^2 \tag{C20}$$

where c is a constant on the order of 1. An analysis of the energy equation will yield similar results. This criteria is applicable at any point in the flow. The program uses the same Δx for all values of y and the minimum Δx is used to insure stability.

For incompressible flows, Δx is smallest at the first point ($y = \Delta y$) in the boundary layer. Therefore,

$$\Delta x_{STABLE} \leq \frac{\rho_{WALL} \Delta y^2}{\mu_{WALL}} u \Delta y \approx \frac{\rho_{WALL} u_e \Delta y^2}{\mu_{WALL} N} \tag{C21}$$

where N is the number of points in the boundary layer.

For the case of a highly cooled wall Δx_{STABLE} is generally smallest at the boundary layer edge. This leads to

$$\Delta x_{STABLE} \leq \frac{\rho_e u_e}{\mu_e} \Delta y^2 \tag{C22}$$

The maximum Δx_{STABLE} that the nonsimilar program will accept and still remain stable is the smallest of the two values from the above relations.

Sample solutions.- This program has been used with success on problems involving mass injection, mass removal (leakage), and shallow surface waves. A calculation of the incompressible flow flat plate boundary layer is compared with the classic solution in figure 70.

Test	Facility	Model description	M_∞	Freestream N_{Re}/ft	Nozzle supply pressure $P_o \sim$ Psia	Total enthalpy $H_o \sim ft^2/sec^2$	Shock mach number	Model total pressure $P_o \sim$ Psia	Nominal model T_w for heat transfer tests °R	α deg	Ψ deg
AD465M-1	JPL Hypersonic wind tunnel	73° sharp-prow delta wing	8.05	$.76 \times 10^6$	250	10.35×10^6	--	2.06	480	0	0
										10	0
										19.5	0
										12.5	5
										15.3	10
										0	5
										0	10
AD633M-1	AEDC tunnel "C"	Sharp and blunt flat plate	10.1	$.5 \times 10^6$	340	10.68×10^6	--	.965	520		
		with side plates	10.2	2.0×10^6	1640	11.85×10^6	--	4.48			
AD633M-1 Rerun and AD633M-2	AEDC tunnel "C"	Sharp flat plate	10.1	$.5 \times 10^6$	340	10.68×10^6	--	.965	520		
		with side plates	10.2	2.0×10^6	1640	11.85×10^6	--	4.48			
AD642M-1	CAL Shock tunnel	Hemisphere cylinder	6, 15	$.06\text{-}14 \times 10^6$	700 - 3300	$13\text{-}44 \times 10^6$	2.7-5.5	.26-90	520	0,10,20,50	0
		Swept leading edge model	6, 15	$.12\text{-}16 \times 10^6$	1200 - 3900	$13\text{-}44 \times 10^6$	2.8-5.5	.40-90		$\Lambda = 55°, 60°, 65°$	
AD647M-1	Boeing Hypersonic wind tunnel	Roughness panel mounted in tunnel wall	6.95	5.9×10^6	1100	9.12×10^6	--	174	530	0	0
AD713M-1	CAL Shock tunnel	Sharp flat plate	14.7	$.073 \times 10^6$	1000	30×10^6	4.45	.344	520	0	0
										5	
										10	
			15.2	$.260 \times 10^6$	3900	30.5×10^6	4.45	1.14	520	15	

Table 1.- Nominal test conditions.

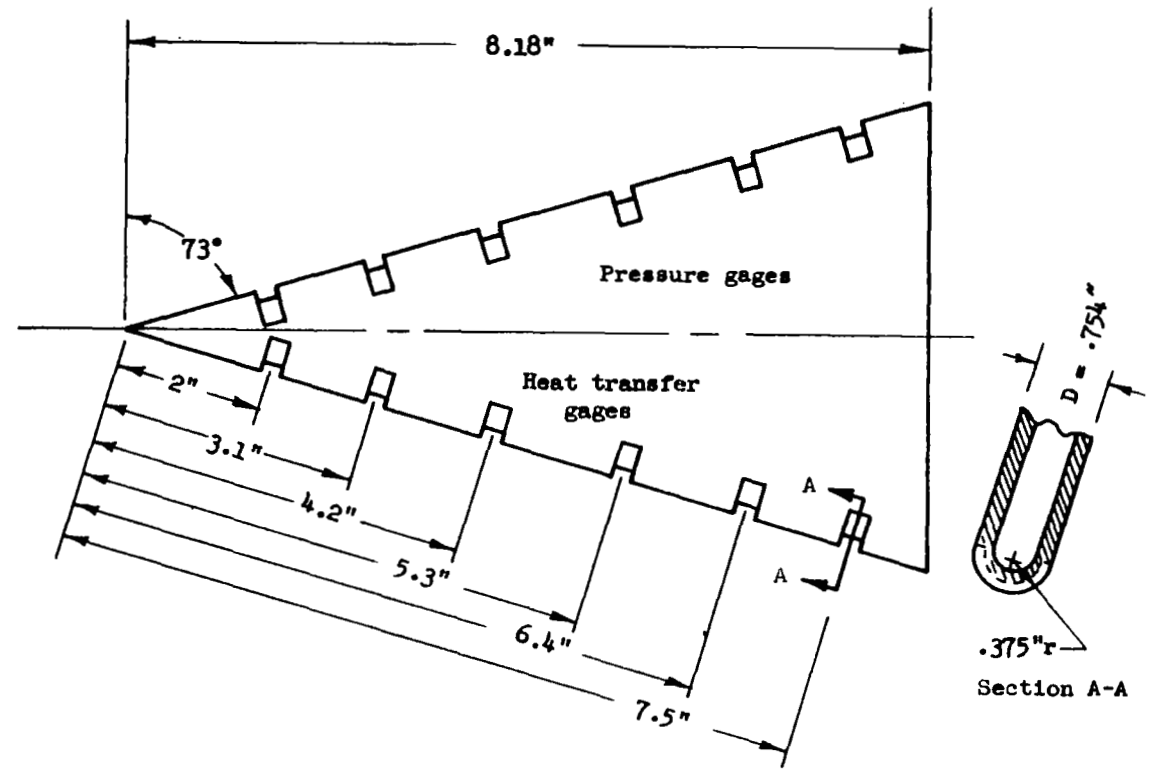

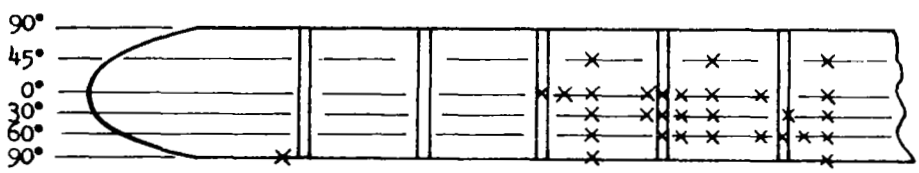

× Leading edge heat transfer gages.

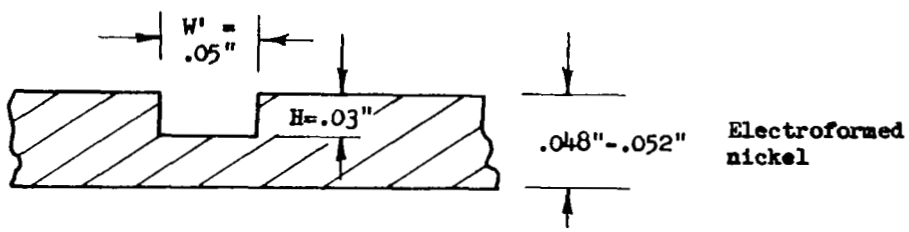

(a) AD465M-1 Delta wing model

Figure 1.- Model drawings

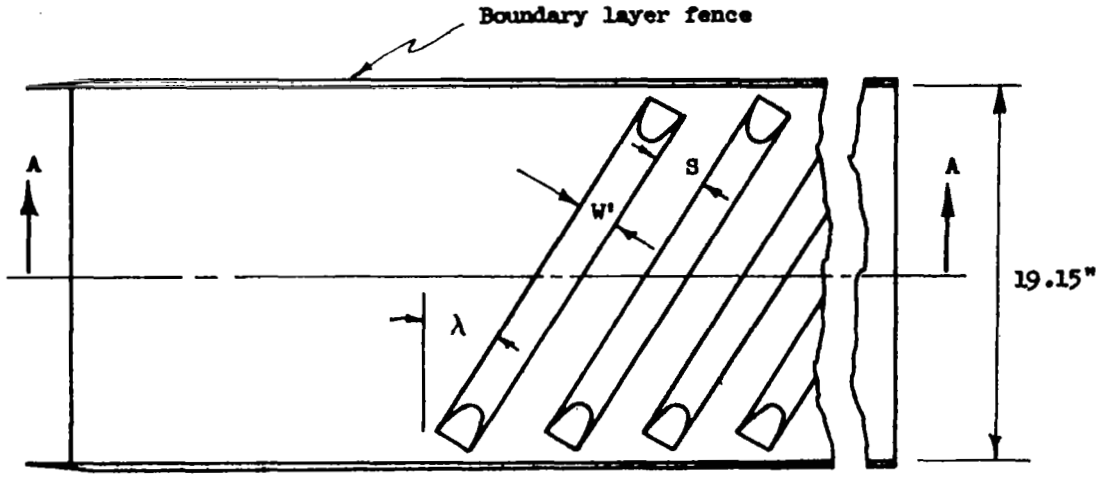

Note: Instruments located along centerline of plate for swept wave or groove inserts. For unswept roughness inserts gages located on centerline and 0.5 inches from centerline.

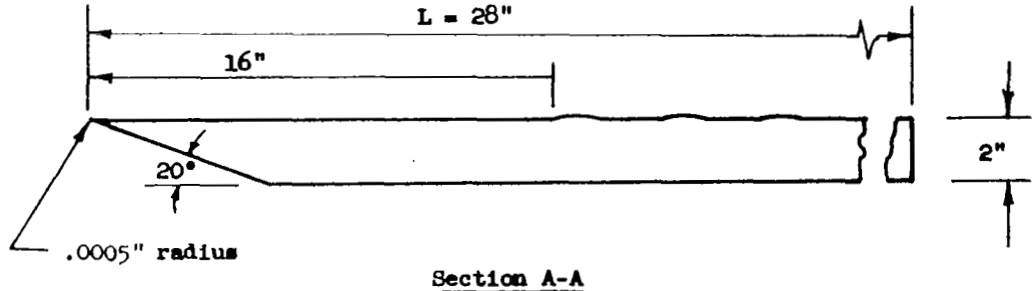

Section A-A

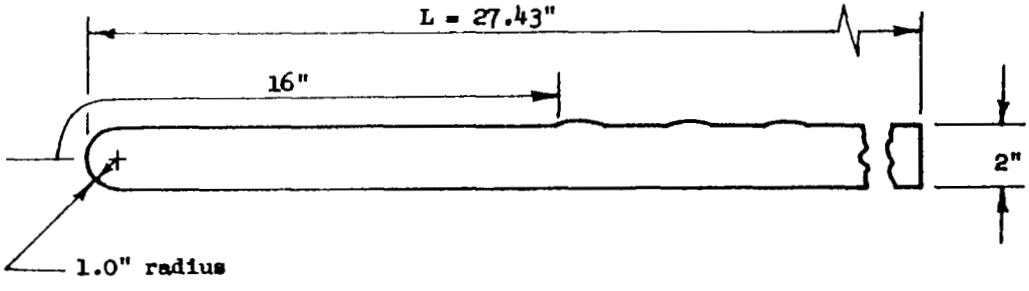

Section A-A

b) AD633 Flat plate models.

Figure 1.- Continued.

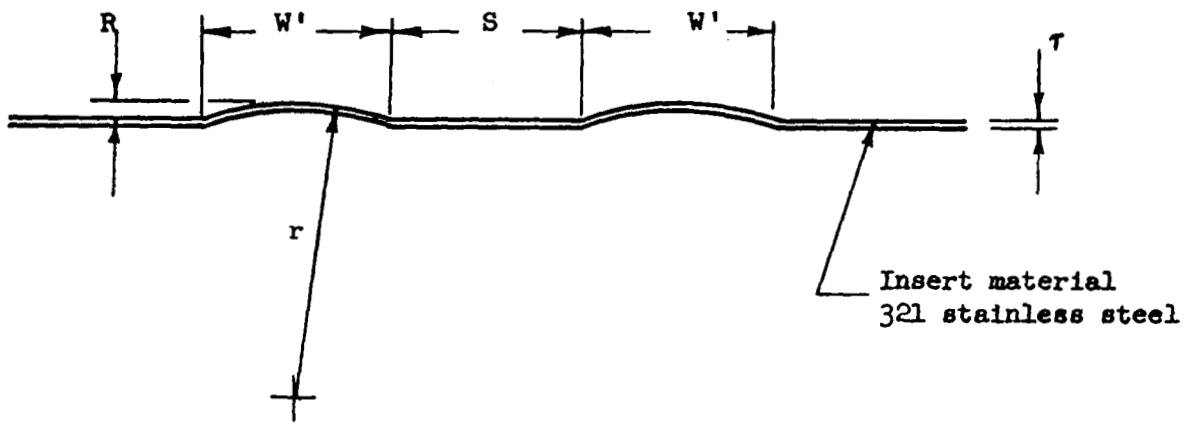

Insert	W'	R	S	λ	r	τ
I_1	.7"	.07"	.5"	0°	.91"	.0351"-.0365"
I_2	.7"	.07"	.5"	70°	.91"	.0351" - .0362"
I_4	← See Below →			0°	← →	.0316" - .0363"
I_4	.7"	.04"	.5"	0°	1.57"	.0363" - .0371"

I_3 Sine Wave

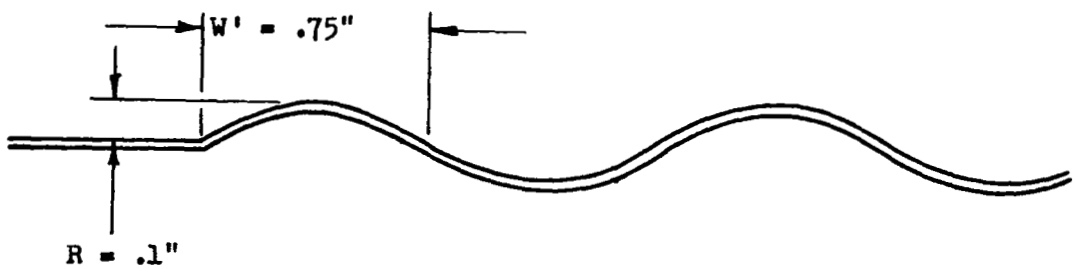

(c) AD633M-1 Re-run surface roughness inserts

Figure 1.- Continued

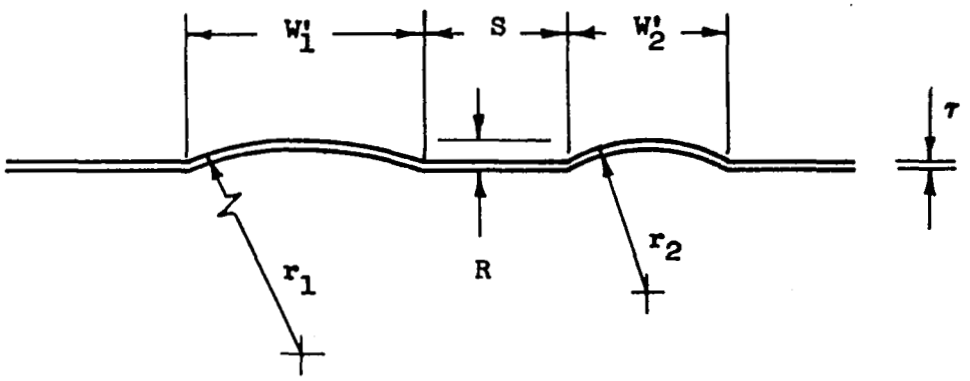

insert	W'_1	W'_2	R	S	λ	r_1	r_2	τ
I_5	1.1"	.8"	.07"	.5"	0°	2.04"	1.18"	.0297"-.0300"
I_6	1.1"	.8"	-.07"	.5"	0°	2.04"	1.18"	.0297"-.0299"
I_7	1.1"	.8"	.07"	.5"	70°	2.04"	1.18"	.0283"-.0295"
I_8	1.1"	1.1"	.07"	1.3"	0°	2.04"	2.04"	.0295"-.0298"
I_{10}	1.1"	1.1"	.07"	.375"	0°	2.04"	2.04"	.0297"-.0300"

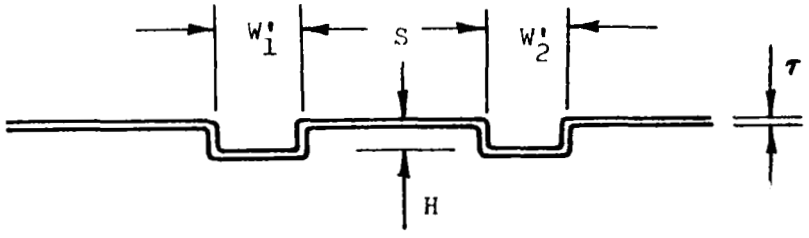

insert	W'_1	W'_2	H	S	Λ	τ
I_9	.25"	.25"	.1"	.5"	70°	.0251"-.0293"

(d) AD633M-2 Surface roughness inserts

Figure 1.- Continued

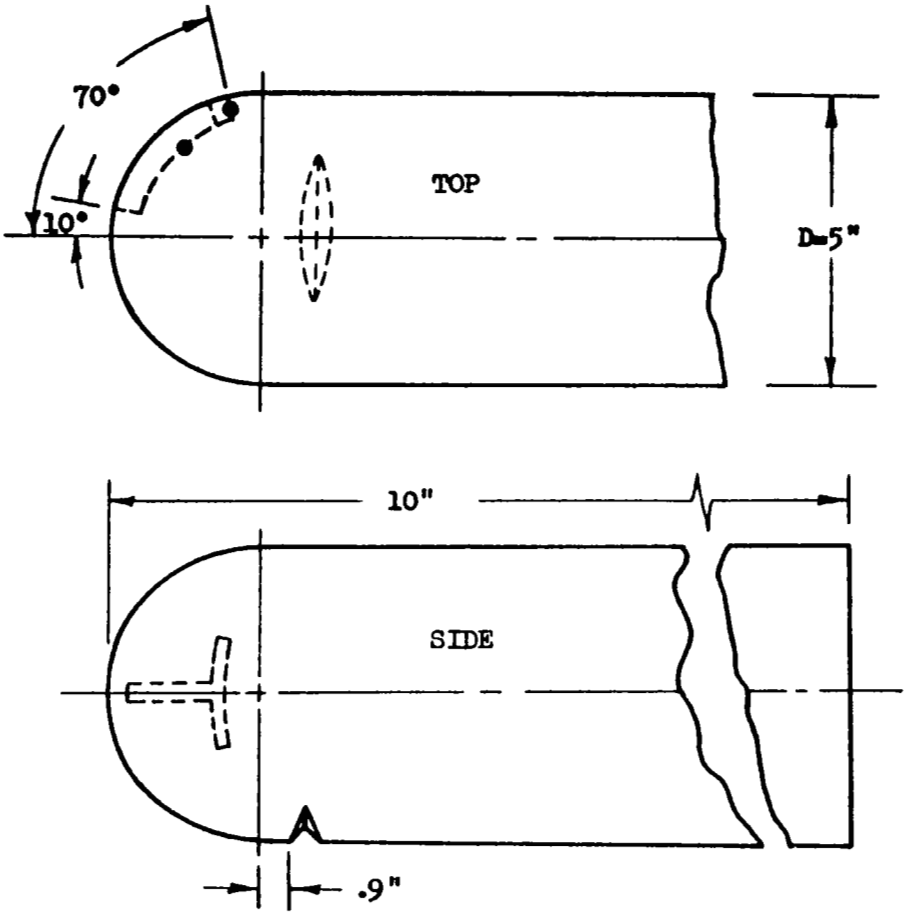

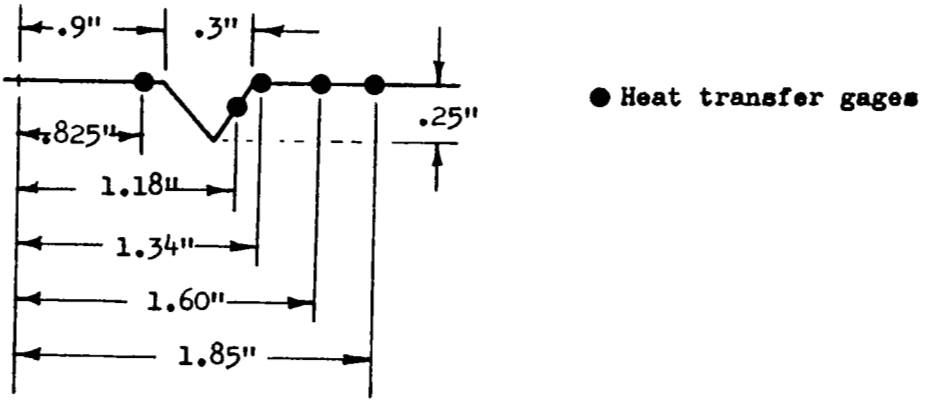

(e) AD642M-1 Hemisphere Cylinder Model

Figure 1.- Continued

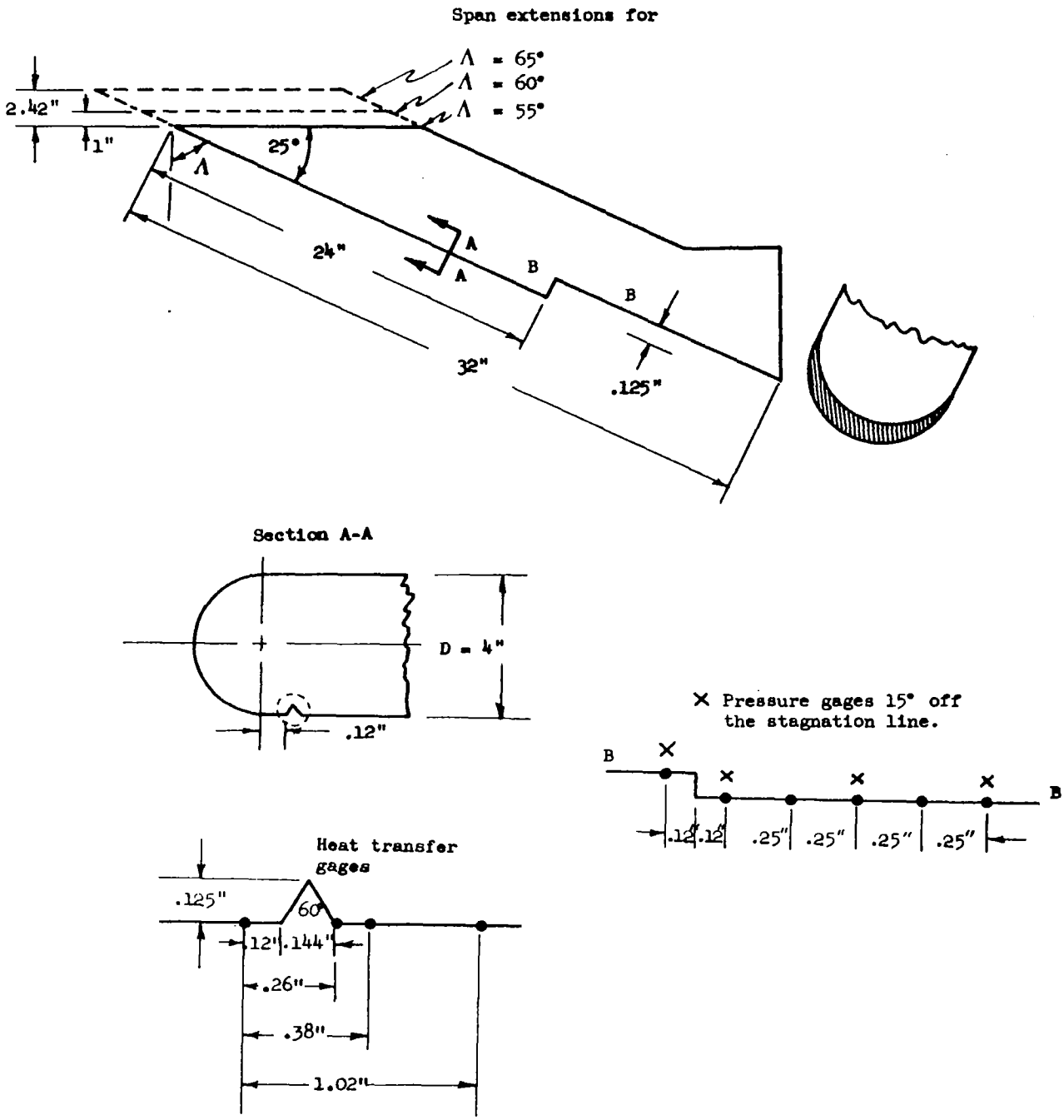

(f) AD642M-1 Swept hemicylinder leading edge model

Figure 1.- Continued

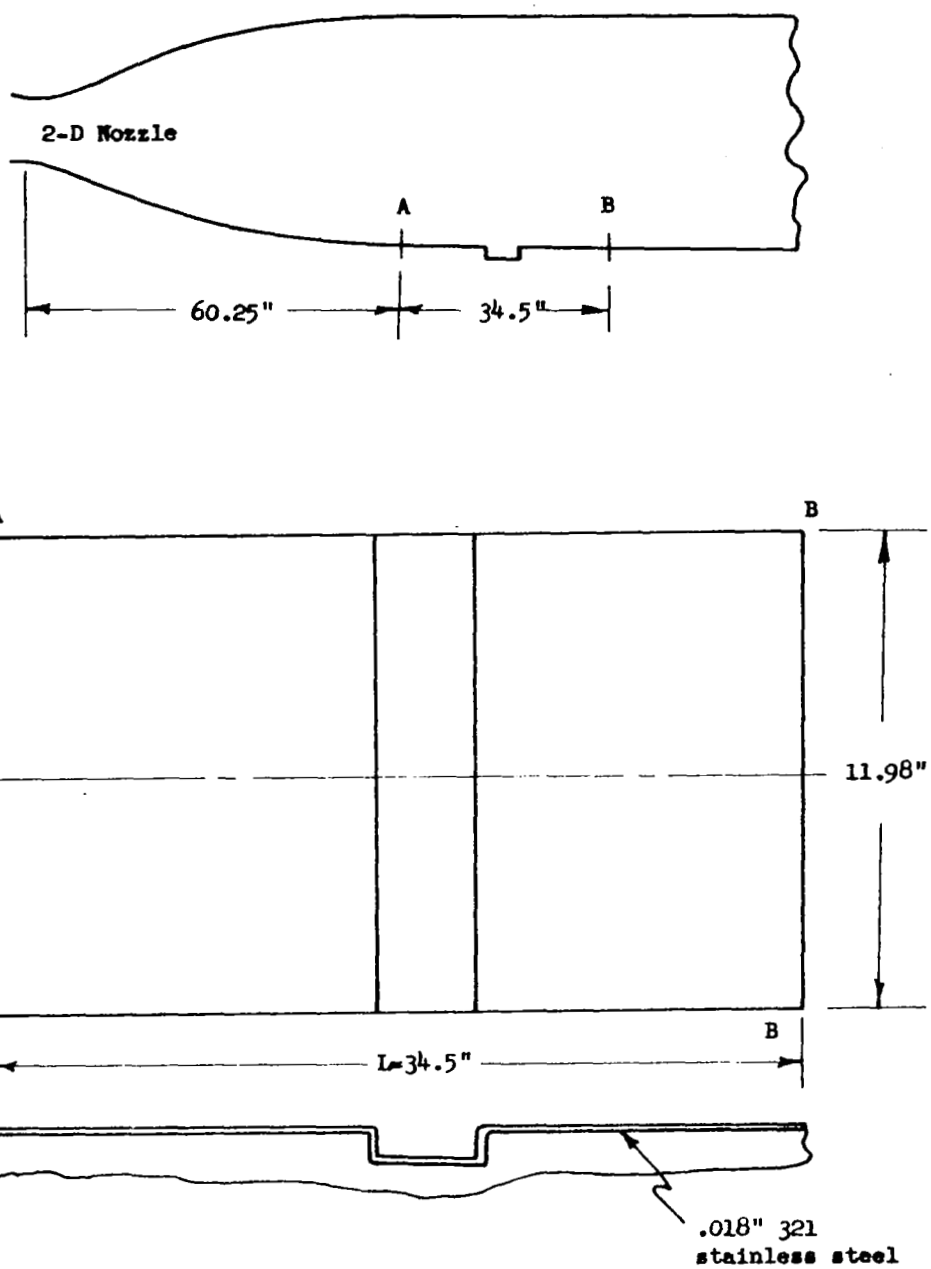

Note: Heat transfer gages located along centerline, pressure gages .75 inches off the centerline.

(g) AD647M-1 2-D Nozzle and roughness panel insert

Figure 1.- Continued

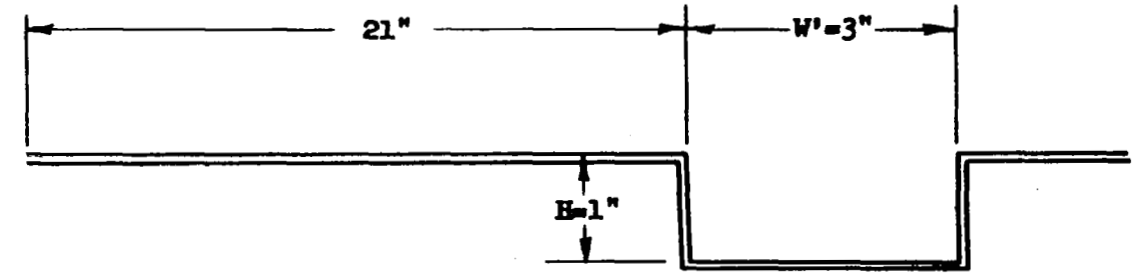

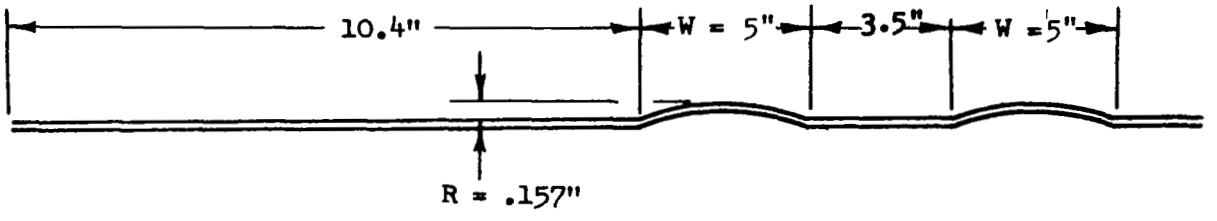

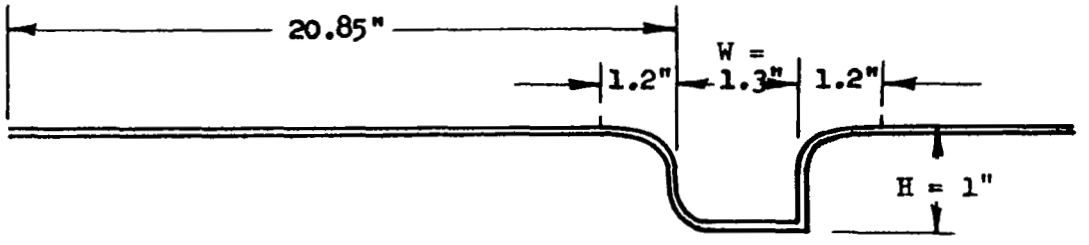

Note: All horizontal dimensions on panel centerline

(h) AD647M-1 Surface roughness panel inserts

Figure 1. - Continued

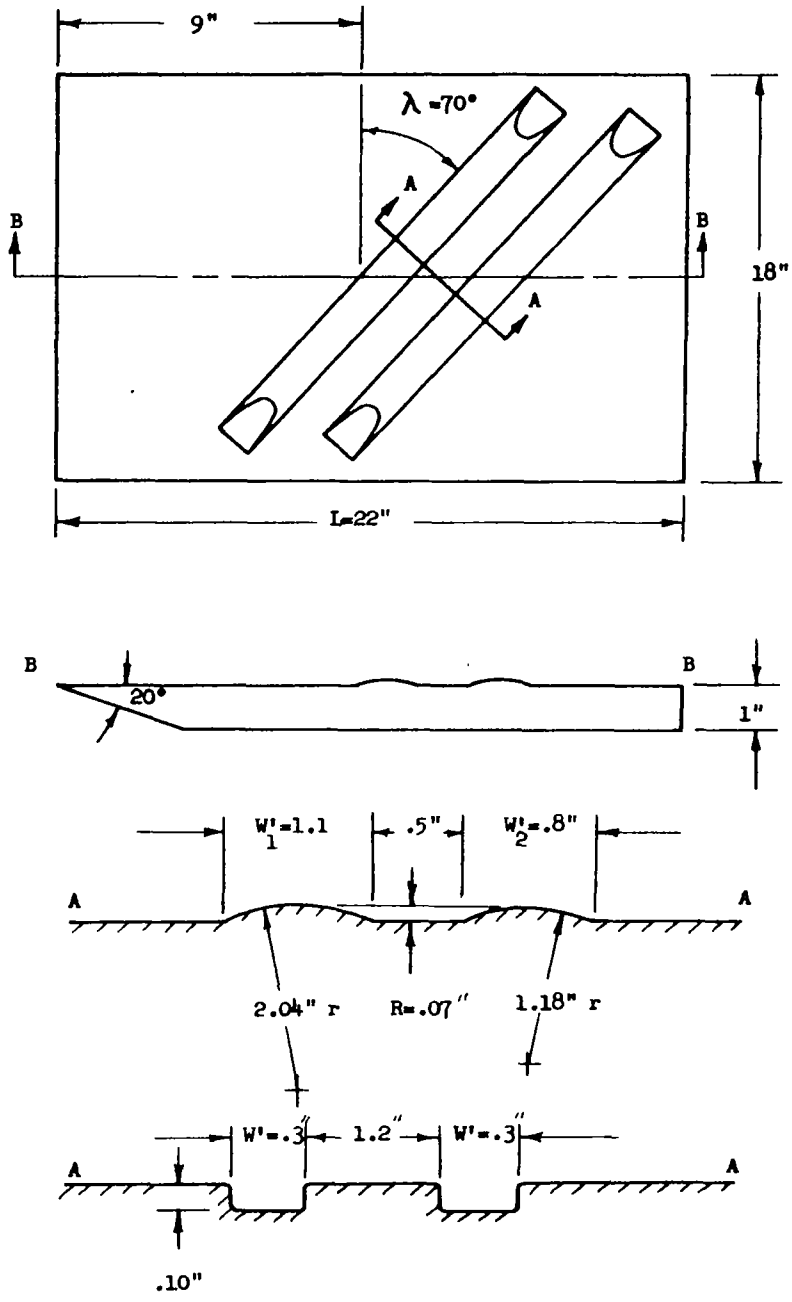

Note: Gages are located along centerline of model.

i) AD713 M-1 flat plate model and roughness inserts.

Figure 1.- Concluded.

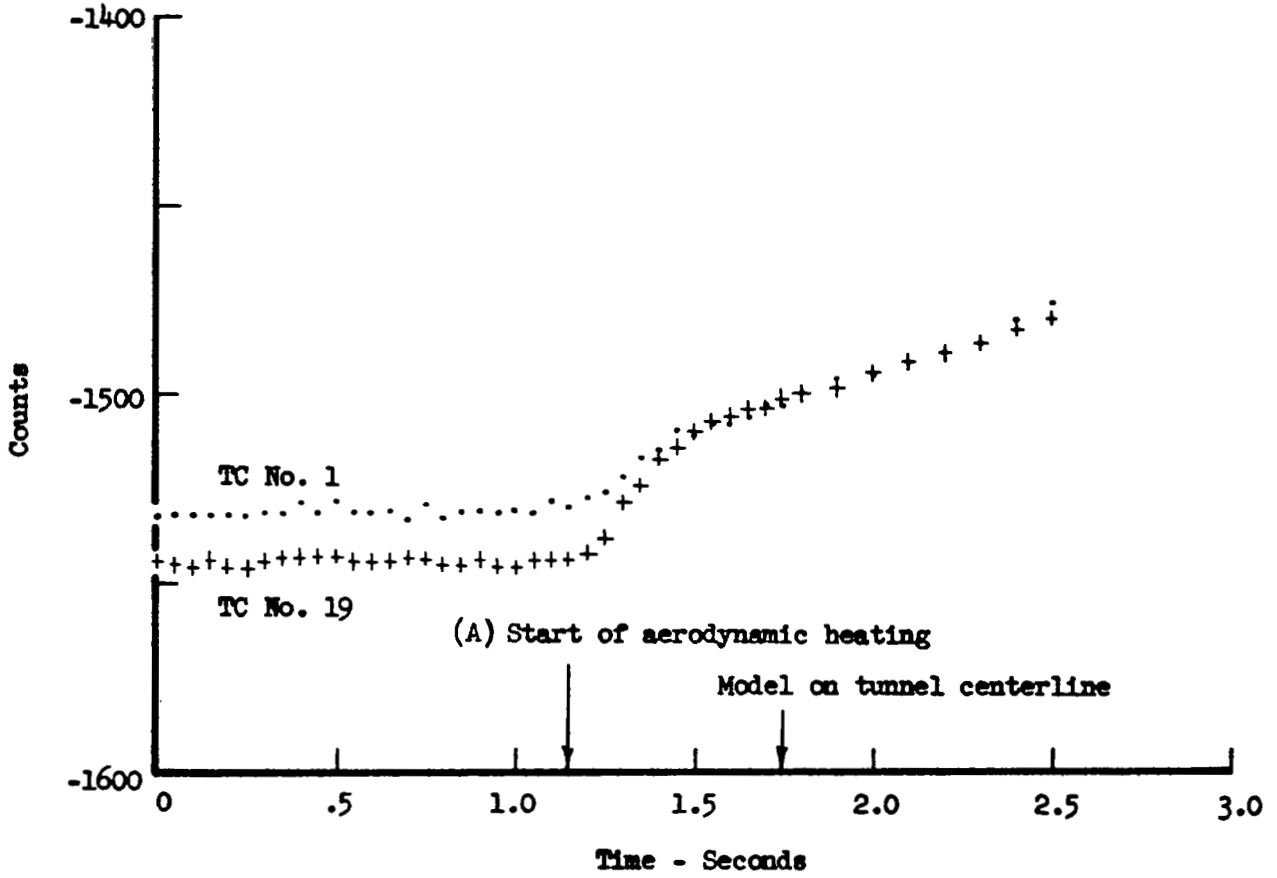

Figure 2.- Thermocouple trace

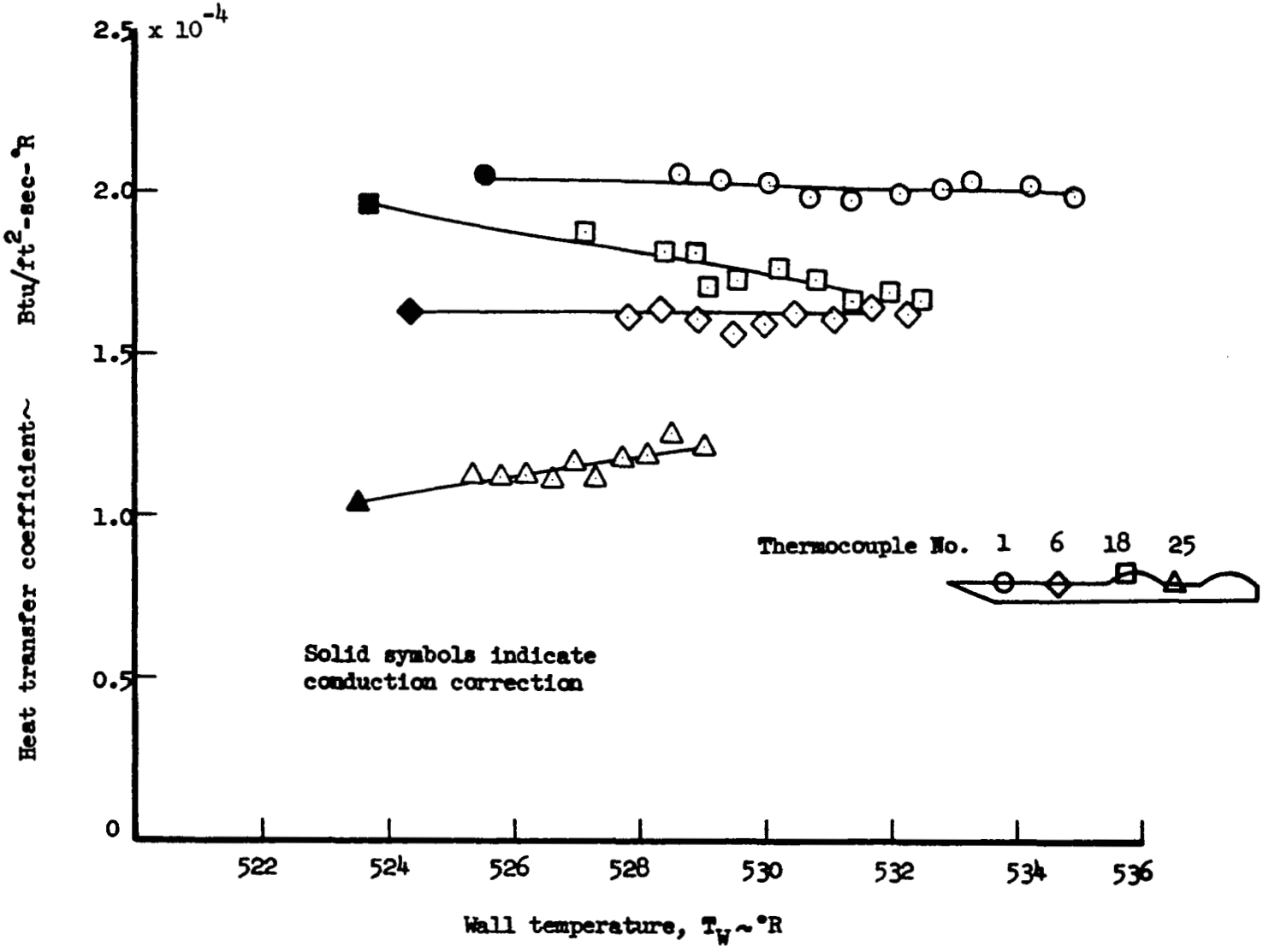

Figure 3.- AD633M-2 Conduction correction of heat transfer data based on Thomas-Fitzsimmons method.

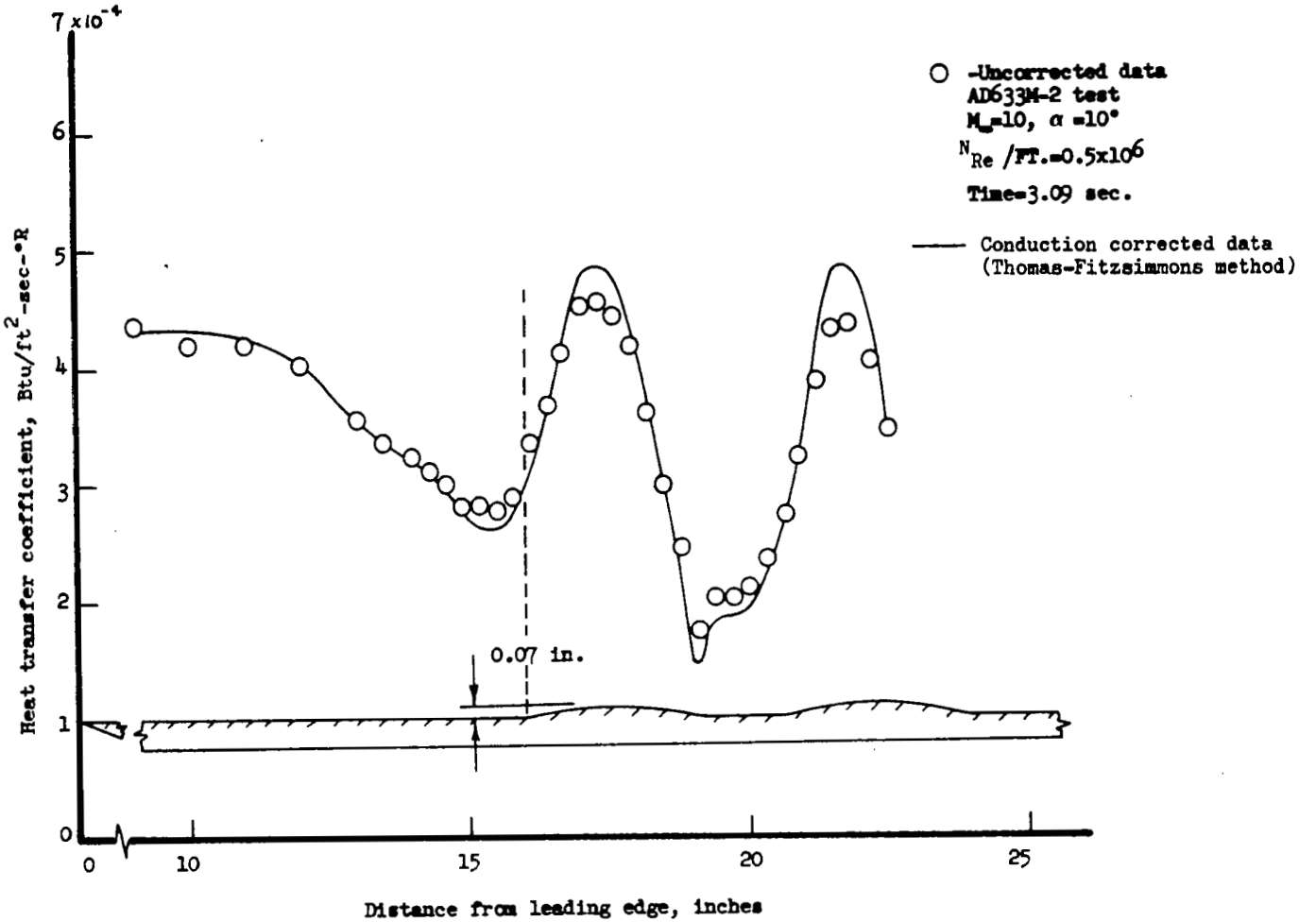

Figure 4.- Conduction error in surface roughness heat transfer data

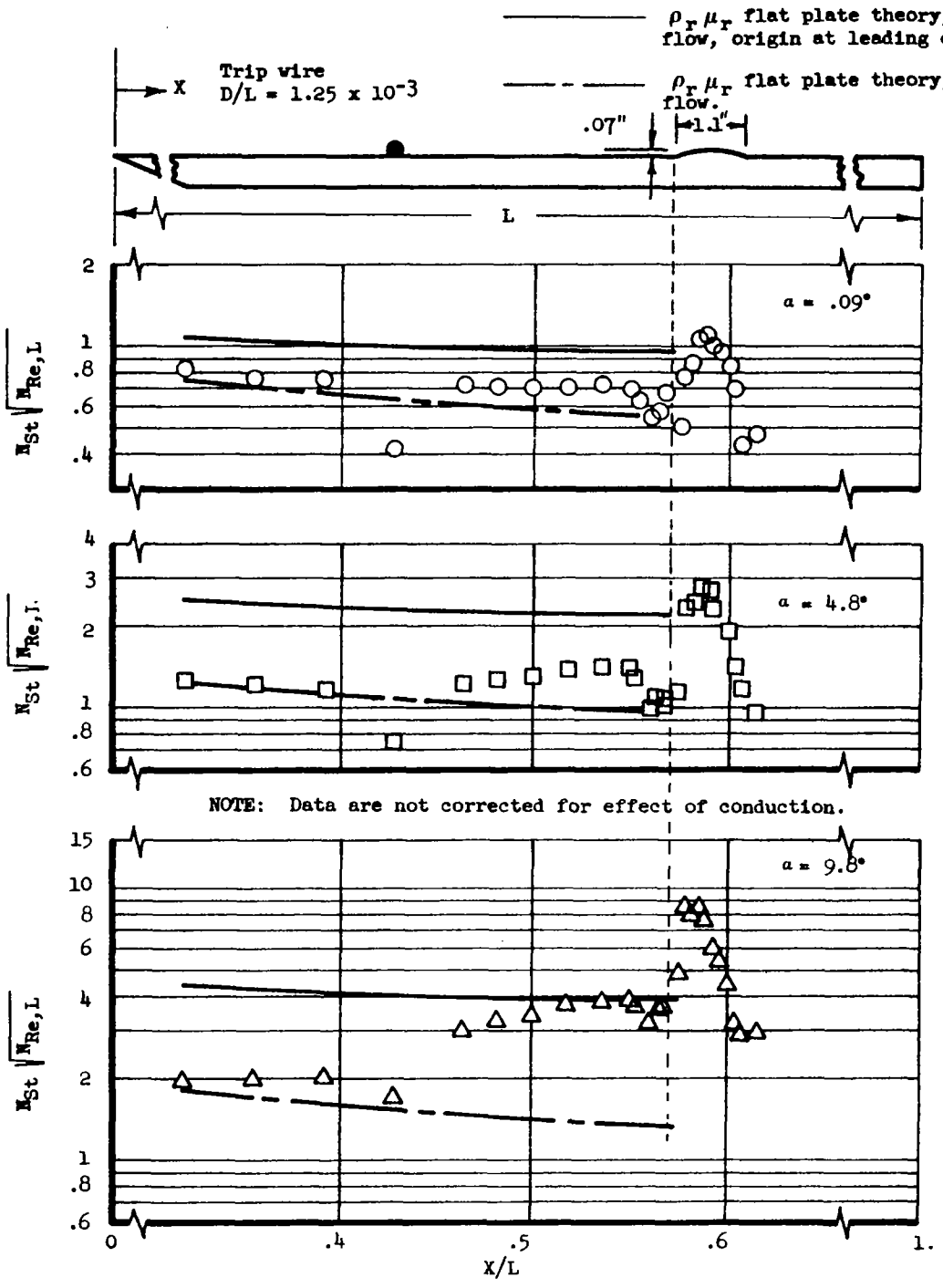

Figure 5.- Effect of trip wire on the wave heating distribution. M_∞ = 10.2 , P'_o = 4.48 psia; H_o = 11.85 x 10^6 ft^2/sec^2, $N_{Re,L}$ = 4.66 x 10^6

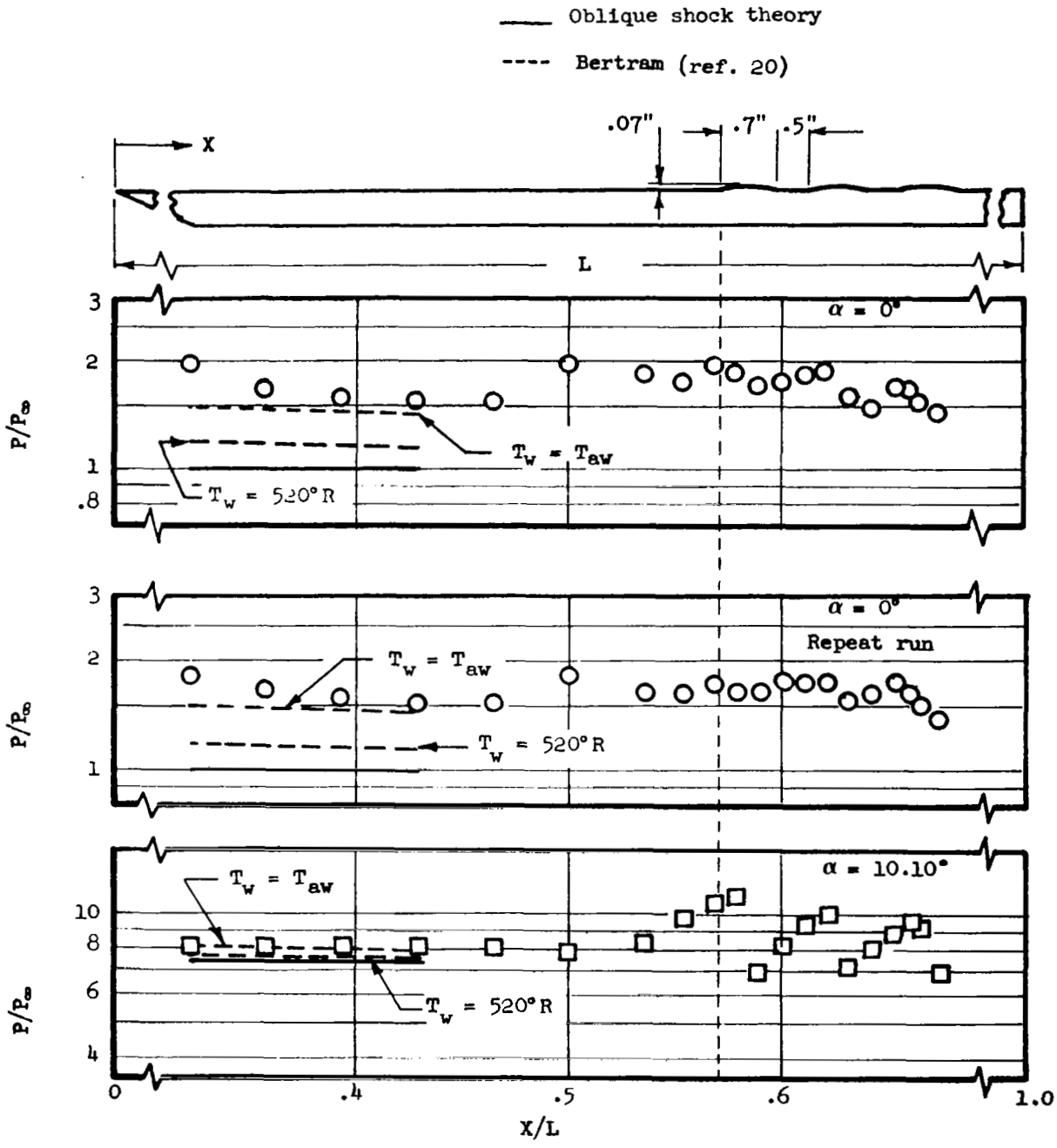

Figure 6.- Pressure distributions on an unswept circular arc wave on a sharp flat plate. M_∞ = 10.1; P'_o = .965 psia, H_o = 10.68 x 10^6 ft^2/sec^2; $N_{Re,L}$ = 1.16 x 10^6

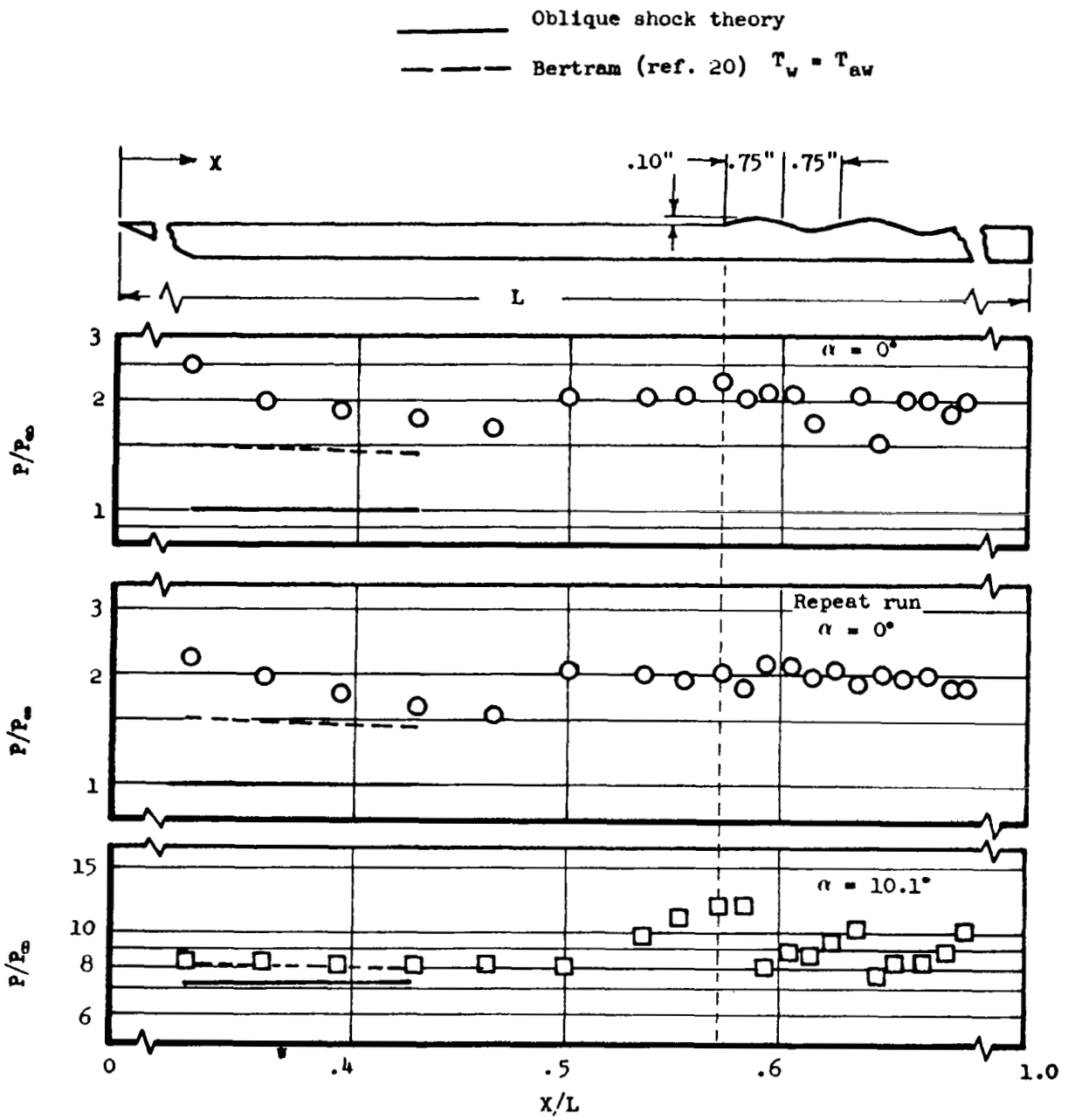

Figure 7.- Pressure distributions on an unswept sine wave on a sharp flat plate. M_∞ = 10.1; P'_o = .965 psia, H_o = 10.68 x 10^6 ft^2/sec^2; $N_{Re,L}$ = 1.16 x 10^6.

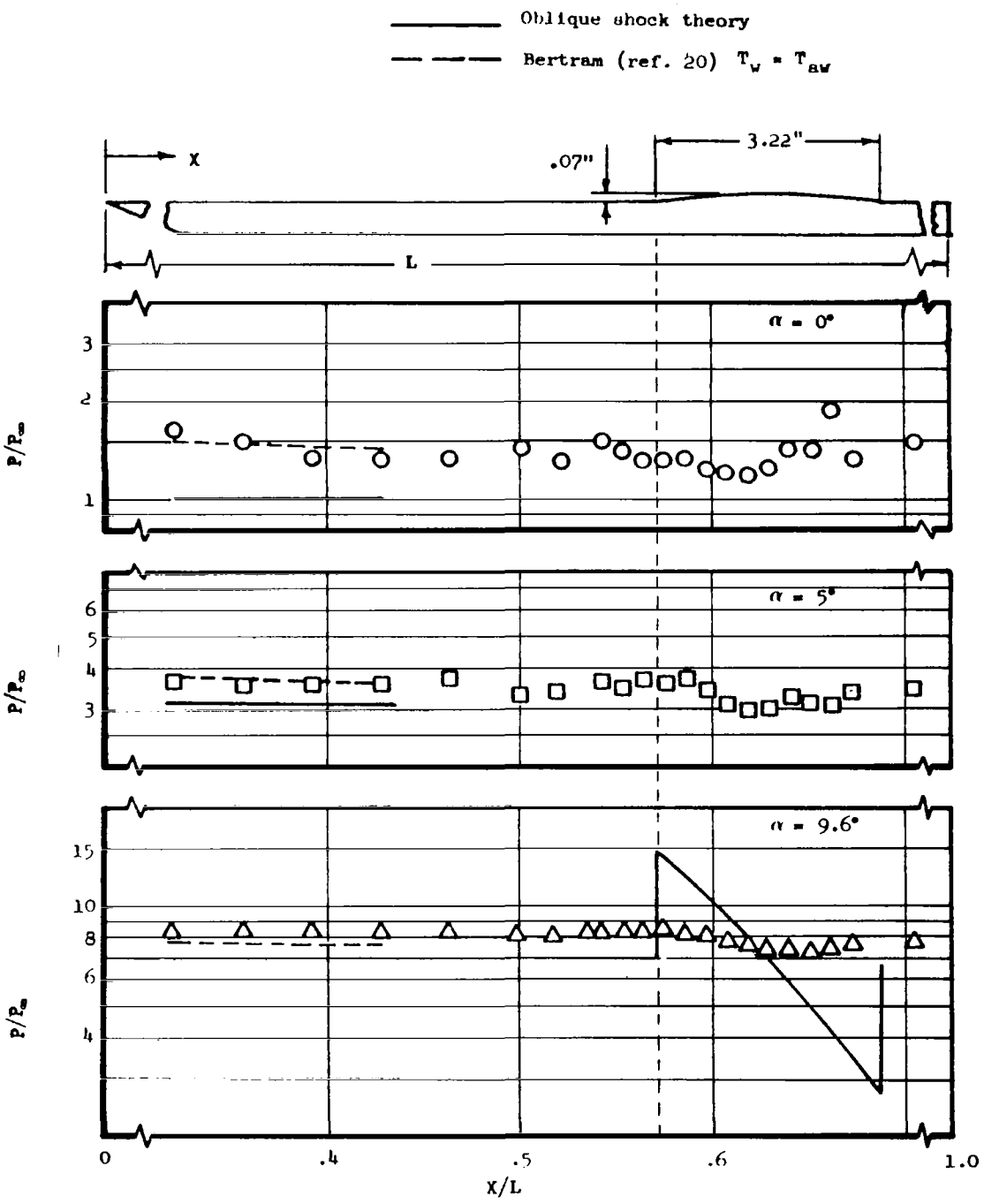

Figure 8.- Pressure distributions on a 70° swept circular arc wave on a sharp flat plate. $M_\infty = 10.1$; $P'_o = .965$ psia; $H_o = 10.68 \times 10^6$ ft^2/sec^2; $N_{Re,L} = 1.16 \times 10^6$.

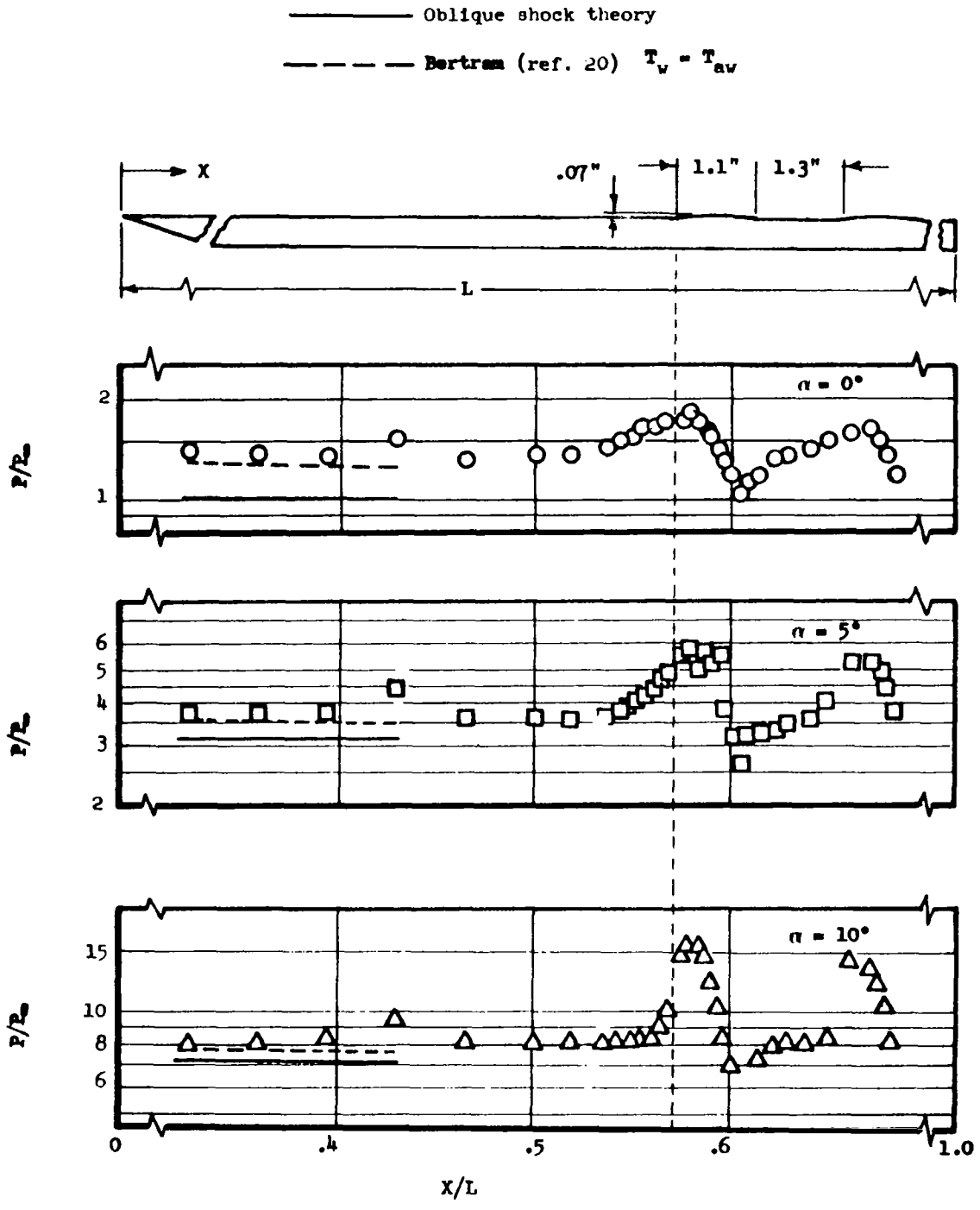

Figure 9.- Pressure distributions on an unswept circular arc wave on a sharp flat plate. $M_\infty = 10.2$; $P'_o = 4.48$ psia; $H_o = 11.85 \times 10^6$ ft^2/sec^2, $N_{Re,L} = 4.66 \times 10^6$.

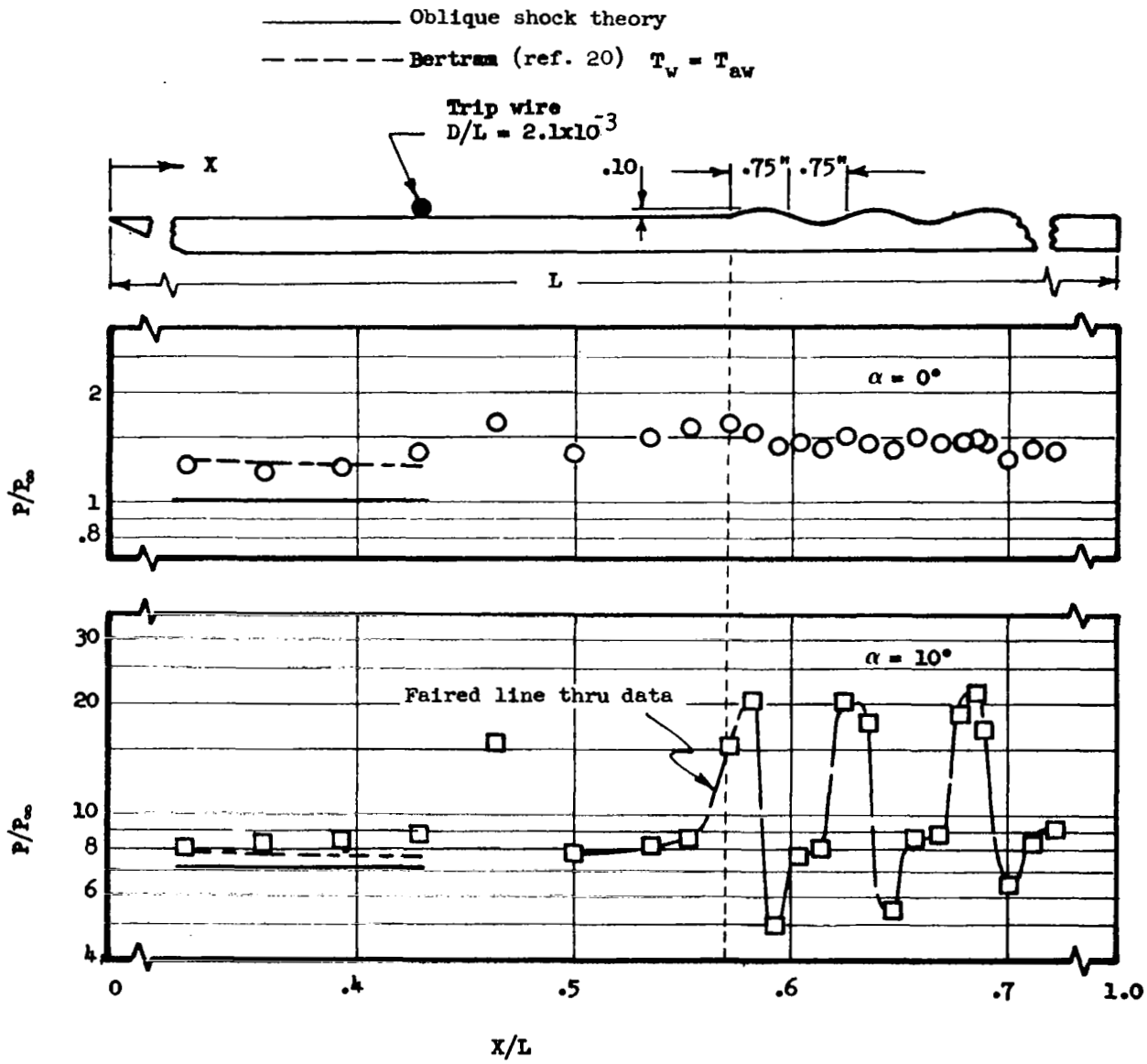

Figure 10.- Pressure distributions on an unswept sine wave on a sharp flat plate. M_∞ = 10.2; P'_o = 4.48 psia; H_o = 11.85 x 10^6 ft^2/sec^2/ $N_{Re,L}$ = 4.66 x 10^6.

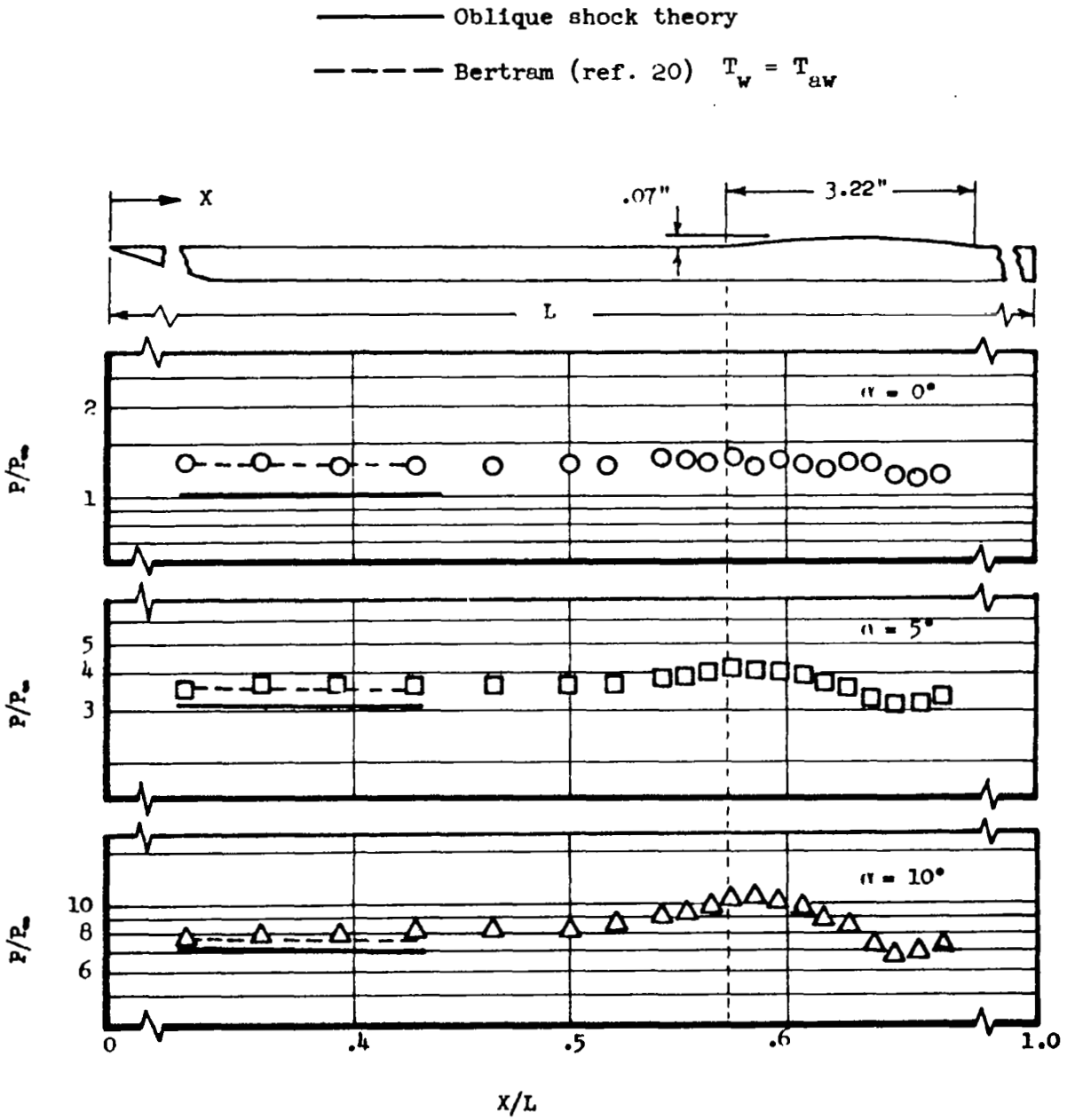

Figure 11.- Pressure distributions on a 70° swept circular arc wave on a sharp flat plate. $M_\infty = 10.2$; $P'_o = 4.48$ psia; $H_o = 11.85 \times 10^6$ ft^2/sec^2; $N_{Re,L} = 4.66 \times 10^6$.

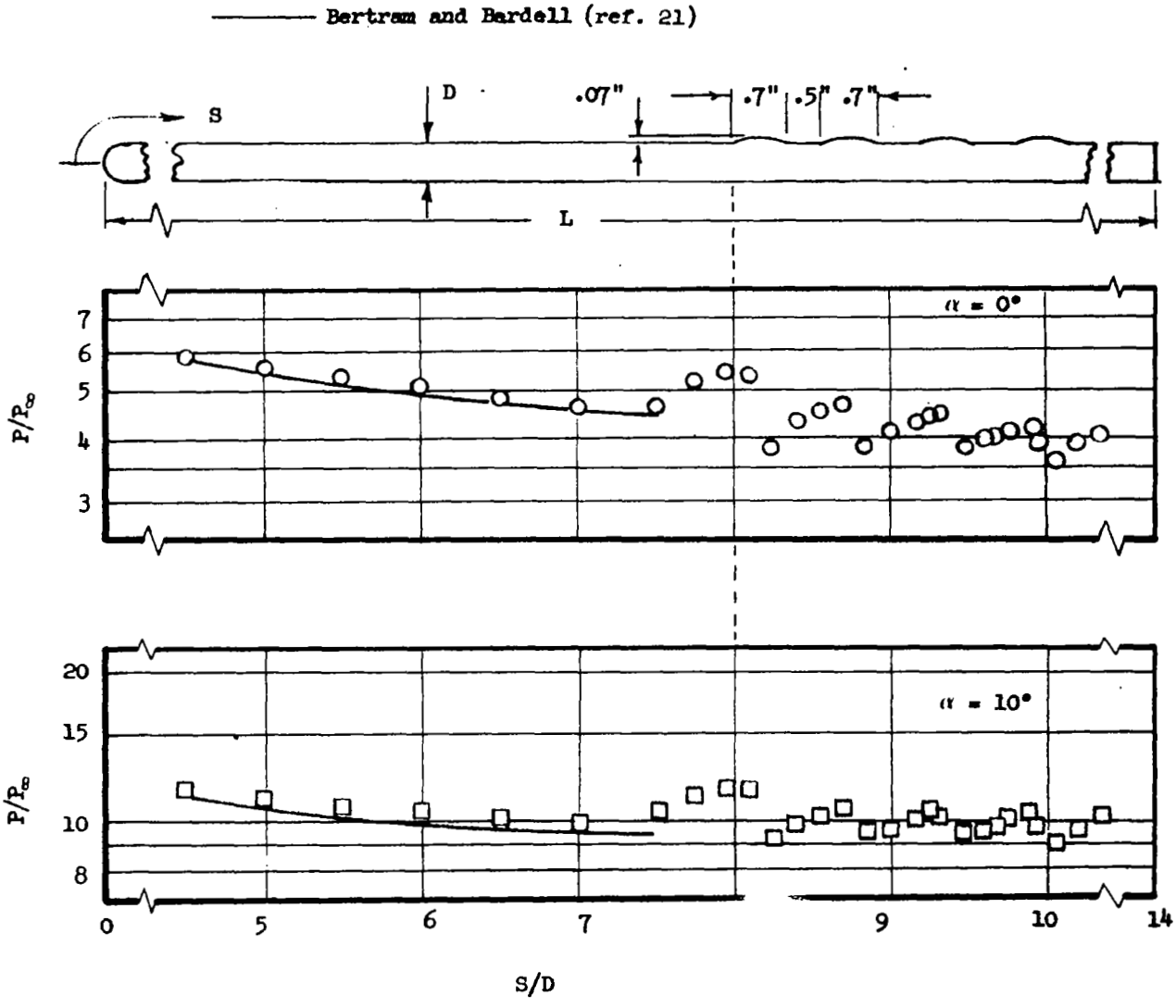

Figure 12- Pressure distributions on unswept circular arc wave on a blunt flat plate. $M_\infty = 10.2$; $P'_o = 4.48$ psia; $H_o = 11.85 \times 10^6$ ft^2/sec^2; $N_{Re,L} = 4.56 \times 10^6$

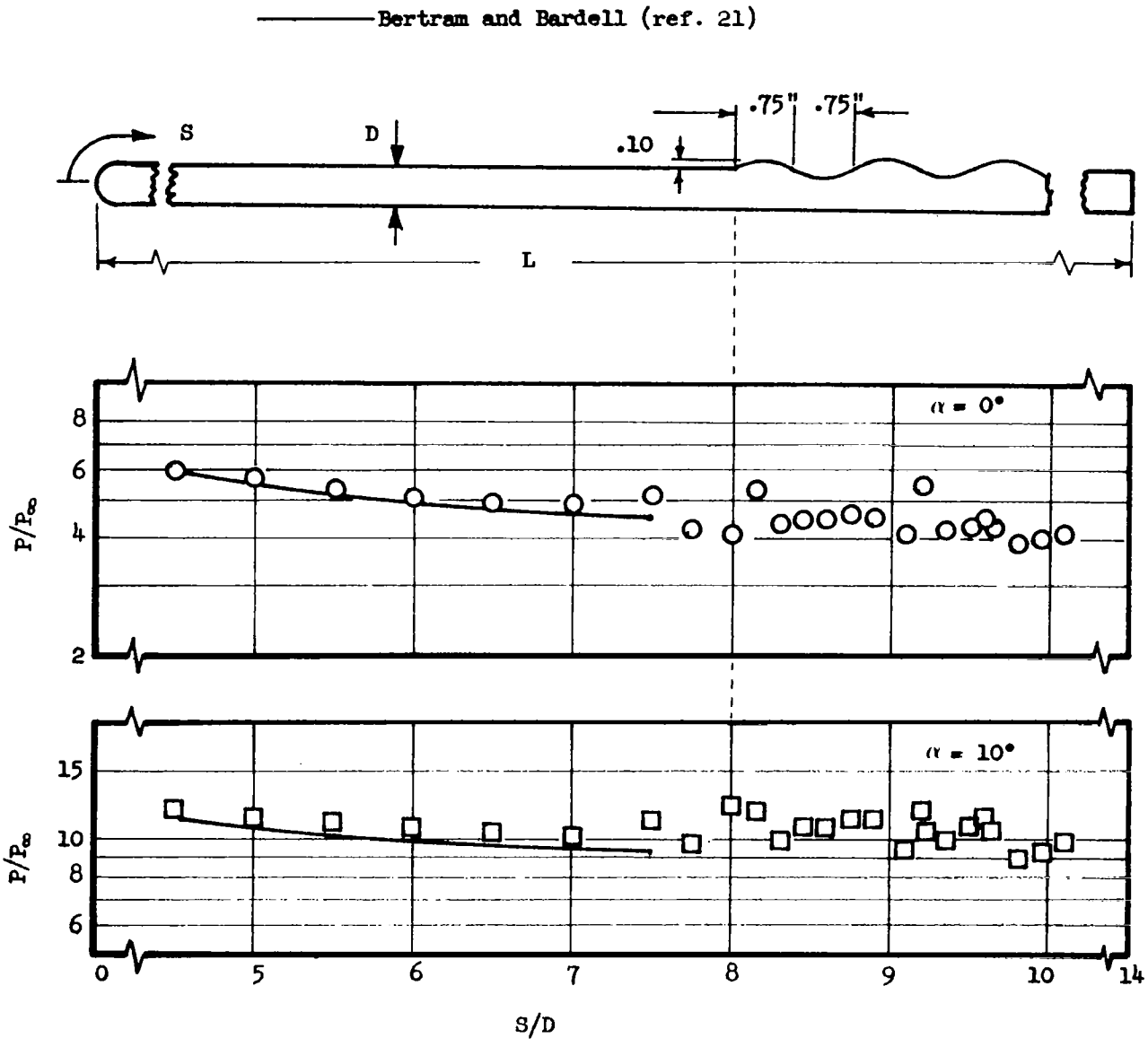

Figure 13.- Pressure distribution on an unswept sine wave on a blunt flat plate. M_∞ = 10.2; P'_o = 4.48 psia; H_o = 11.85 x 10^6 ft^2/sec^2; $N_{Re,L}$ = 4.56 x 10^6.

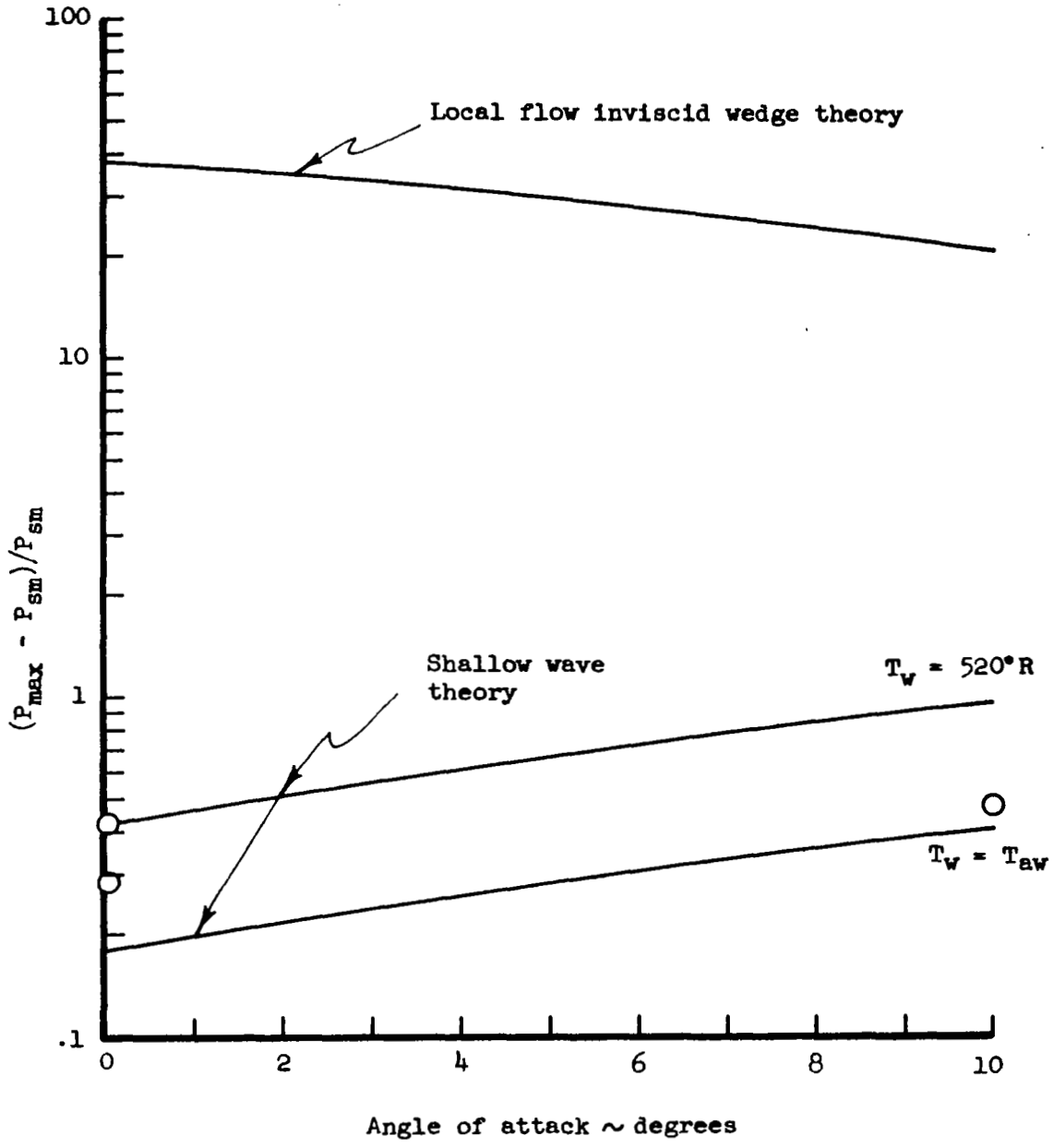

(a) Sine wave protuberance W/R = 7.5

Figure 14.- Maximum pressure data - theory comparison for waves on a sharp flat plate.-- Laminar flow, M_∞ = 10.1; P'_o = .965 psia; H_o = 10.68 x 10^6 ft^2/sec^2; $N_{Re,L}$ = 1.16 x 10^6.

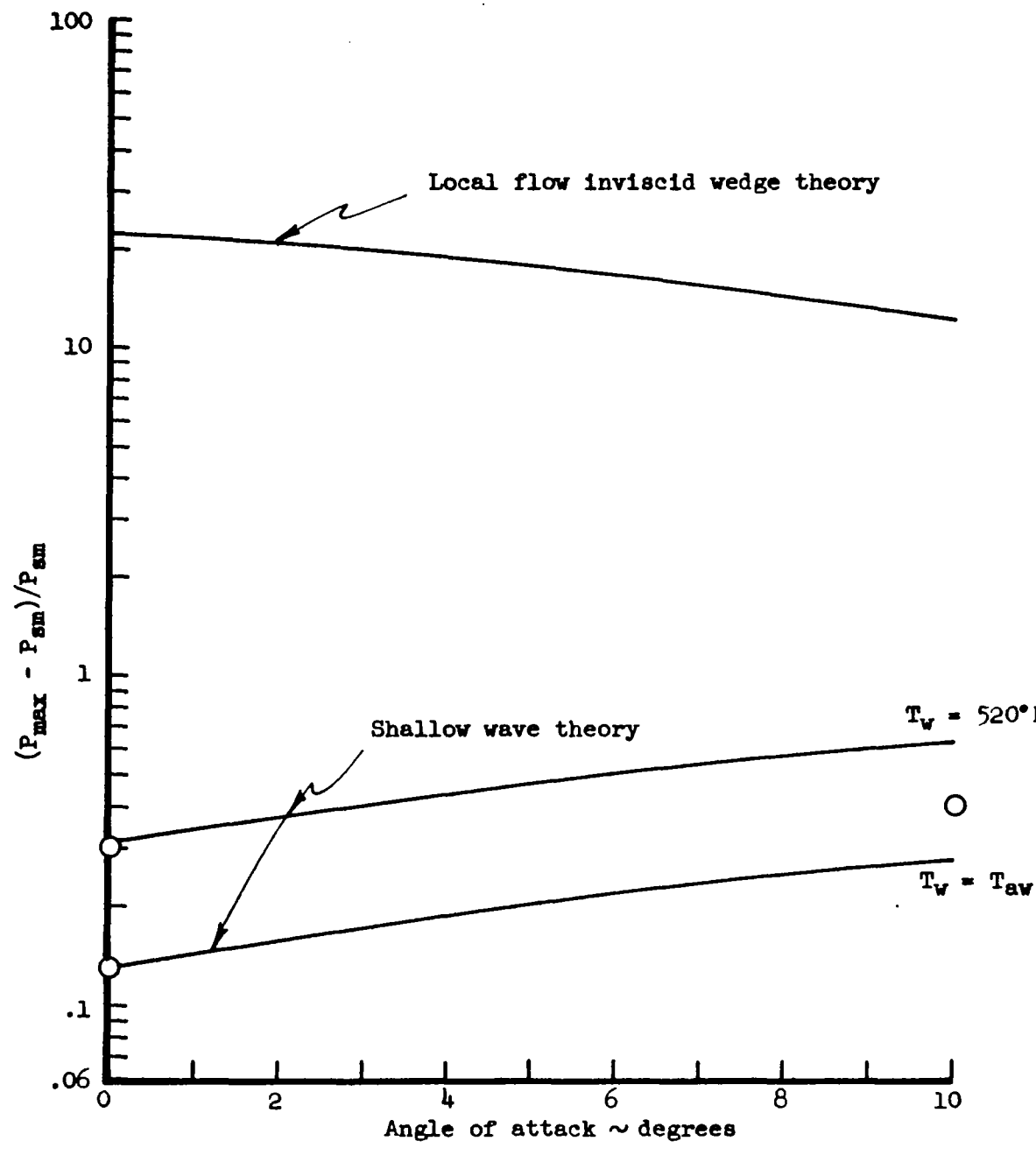

(b) Unswept circular arc wave W/R = 10

Figure 14.- Continued

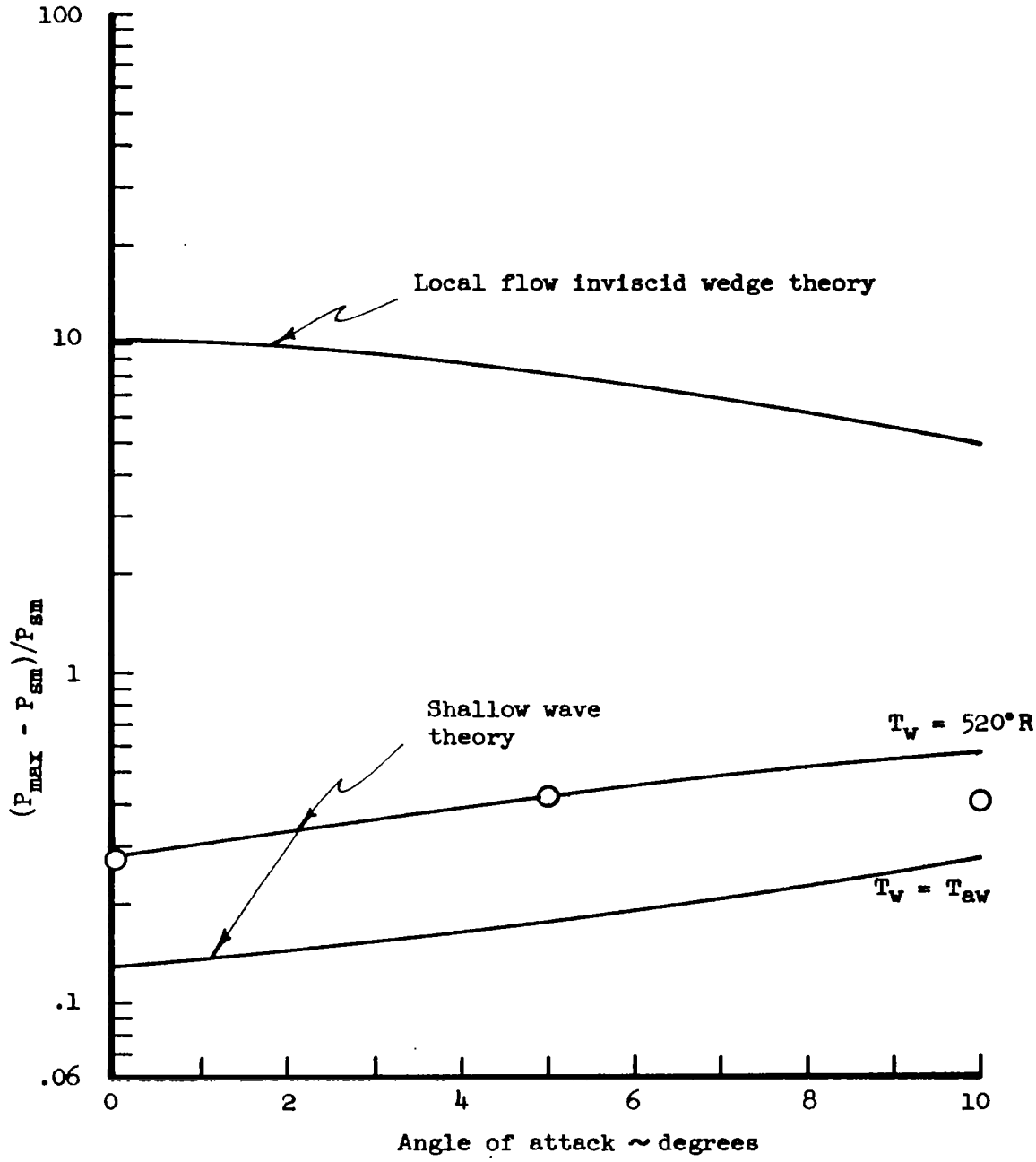

(c) Unswept circular arc wave W/R = 15.7

Figure 14.- Continued

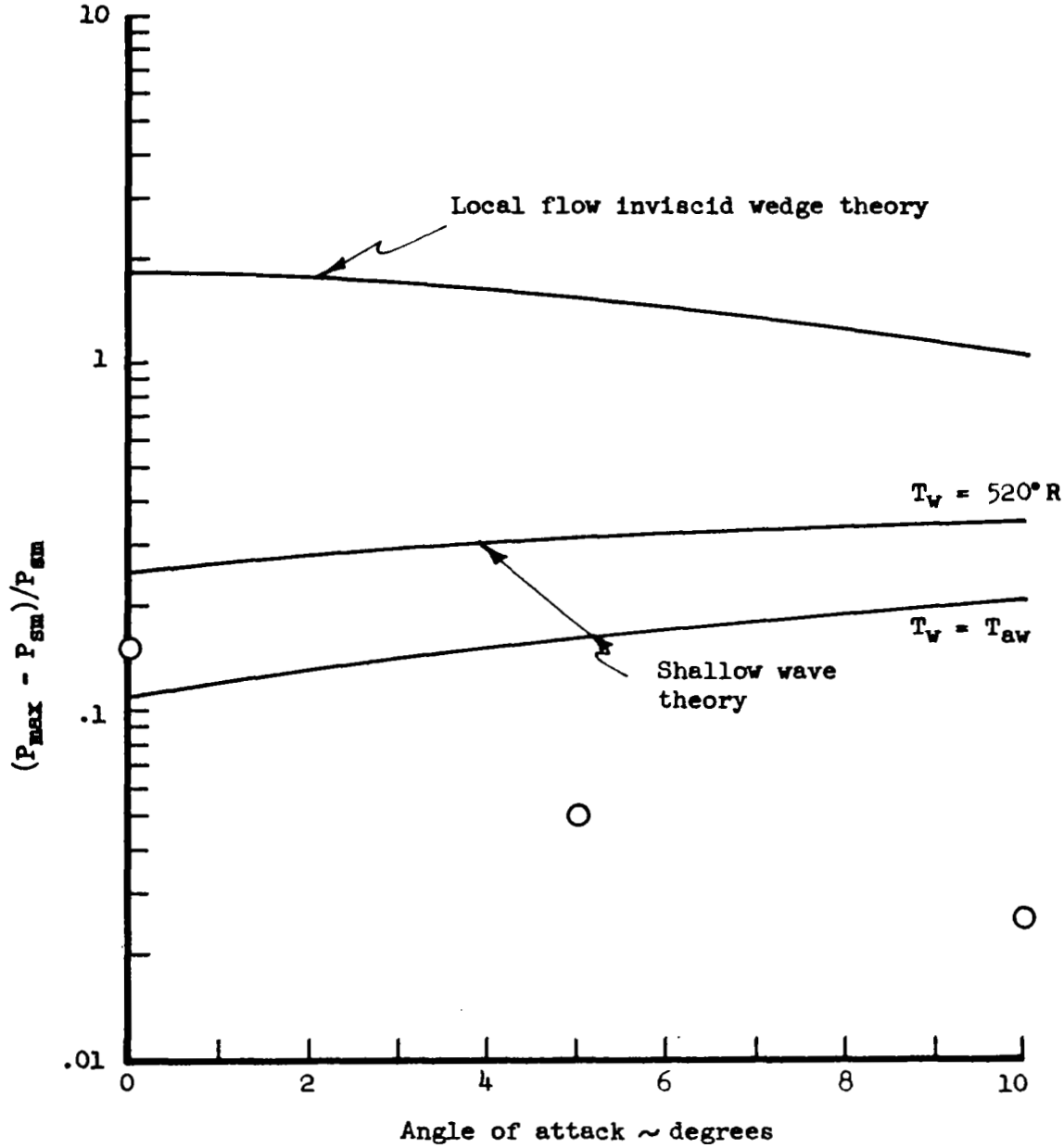

(d) 70° Swept circular arc wave W/R = 46

Figure 14.- Concluded.

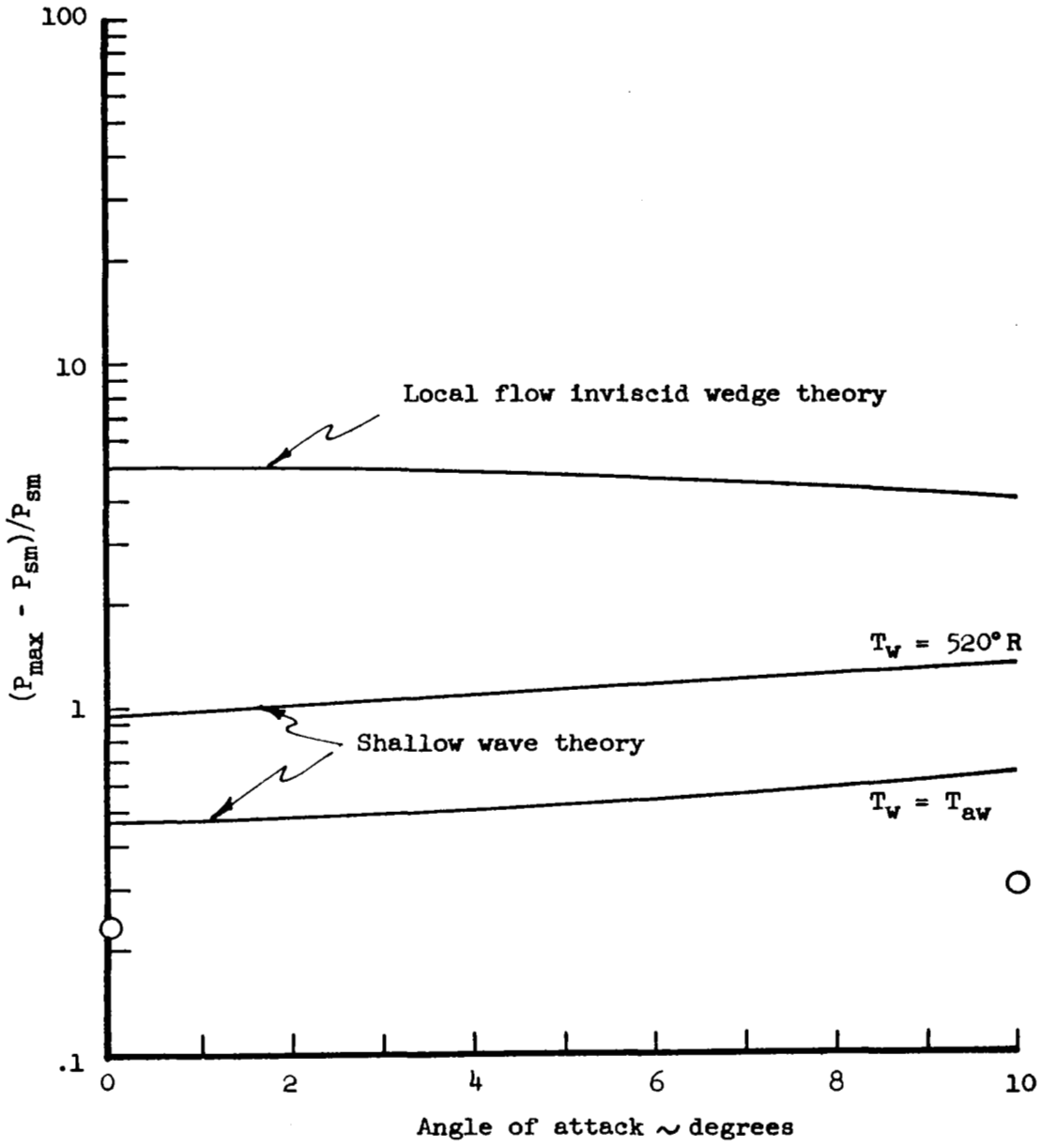

(a) Sine wave protuberance W/R = 7.5

Figure 15.- Maximum pressure data - theory comparison for waves on a blunt flat plate.-- Laminar flow; M_∞ = 10.2; P'_o = 4.48 psia; H_o = 11.85 x 10^6 ft^2/sec^2; $N_{Re,L}$ = 4.57 x 10^6.

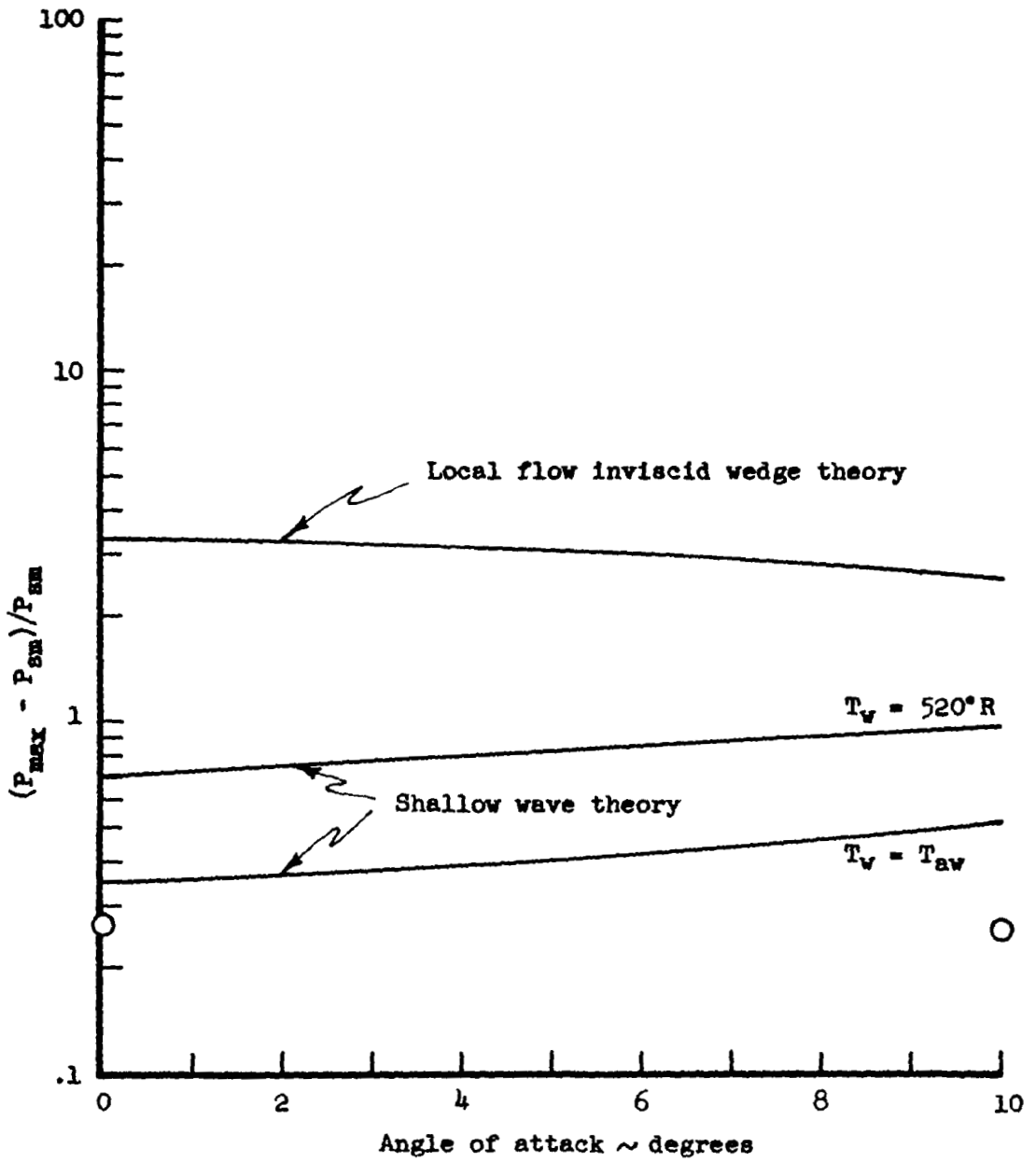

(b) Unswept circular arc wave W/R = 10

Figure 15.- Concluded.

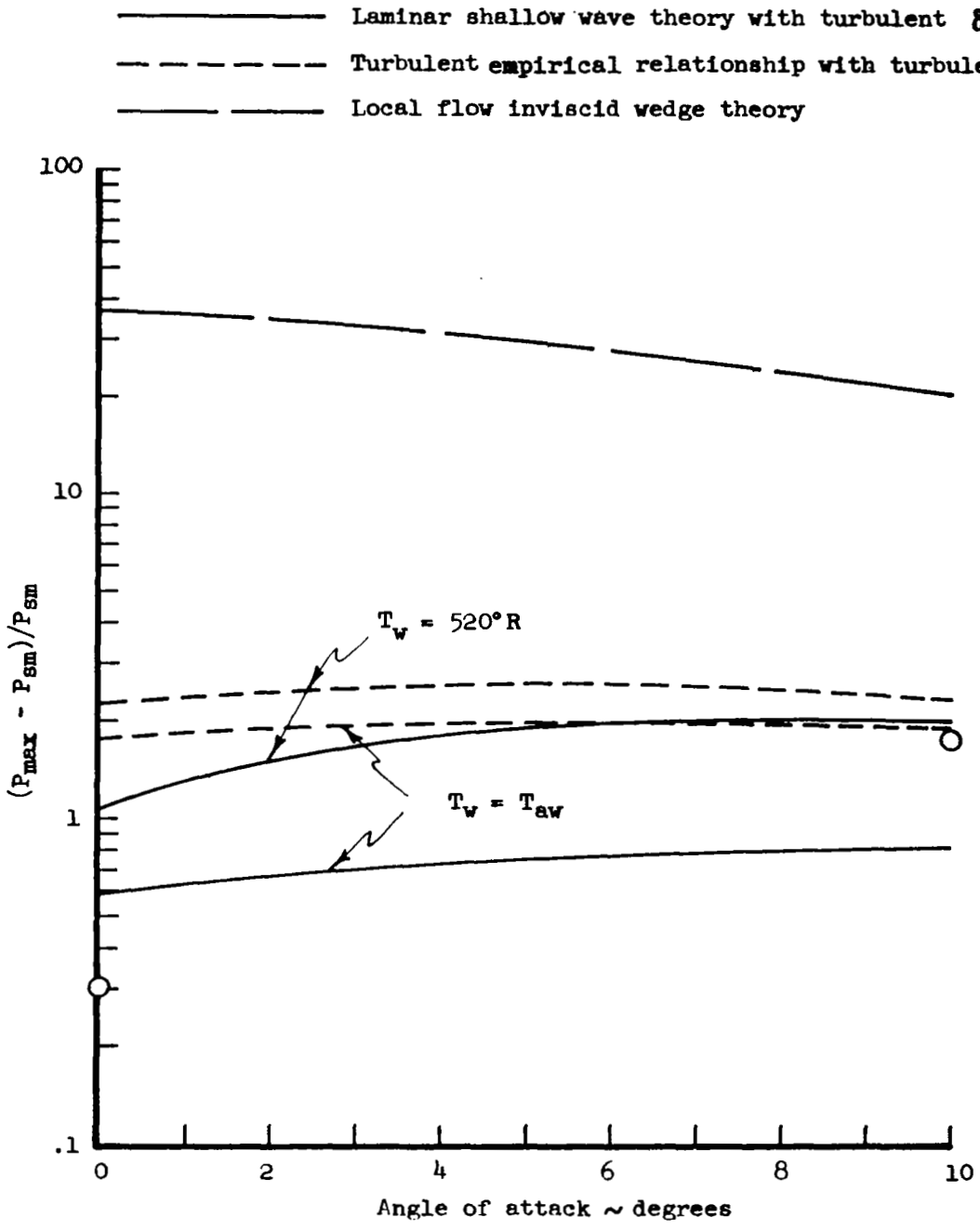

(a) Sine wave protuberance W/R = 7.5

Figure 16.- Maximum pressure data - theory comparison for waves on a sharp flat plate. M_∞ = 10.2; P'_o = 4.48 psia; H_o = 11.85 x 10^6 ft^2/sec^2; $N_{Re,L}$ = 4.66 x 10^6.

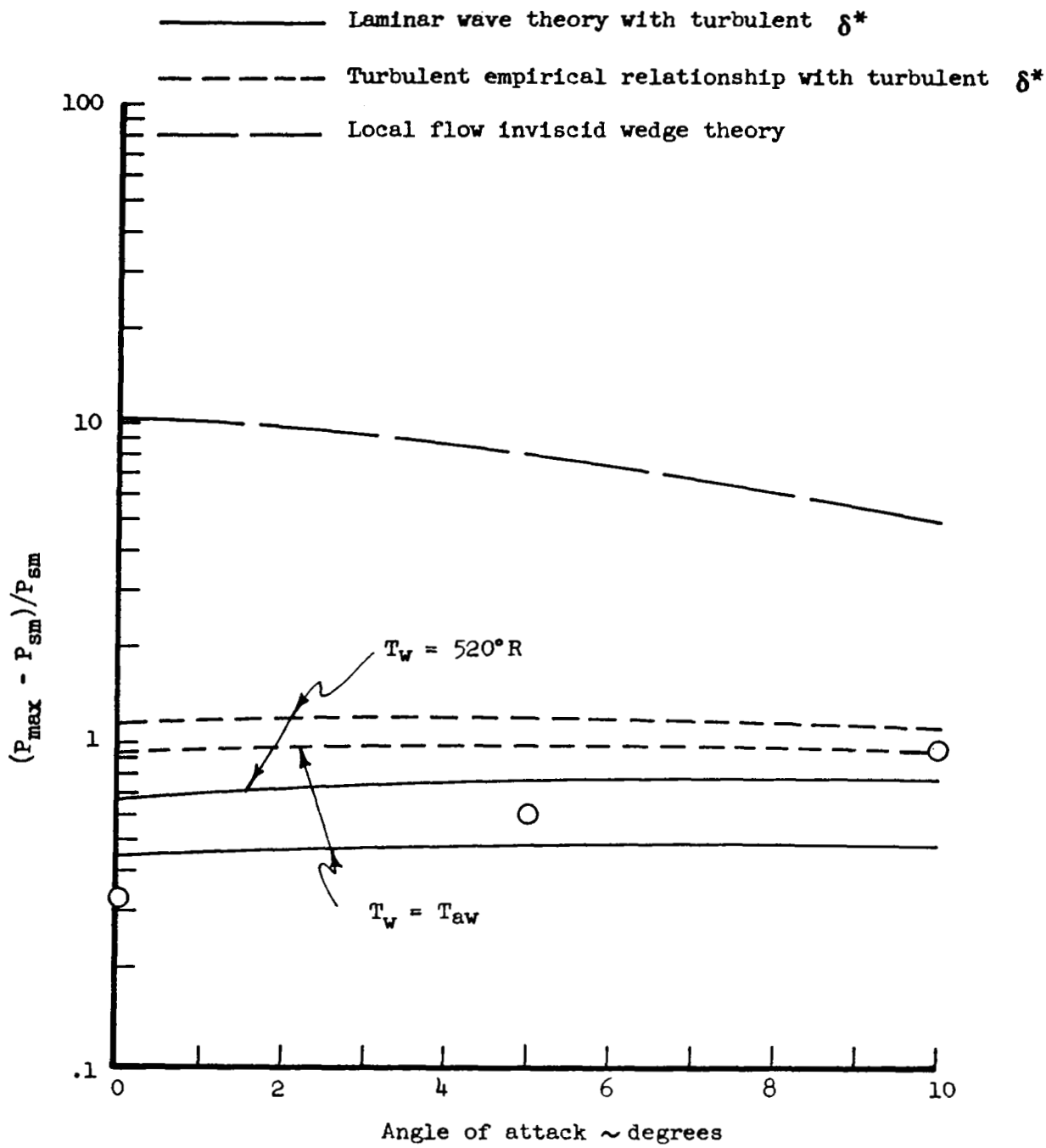

(b) Unswept circular arc wave W/R = 15.7

Figure 16.- Continued.

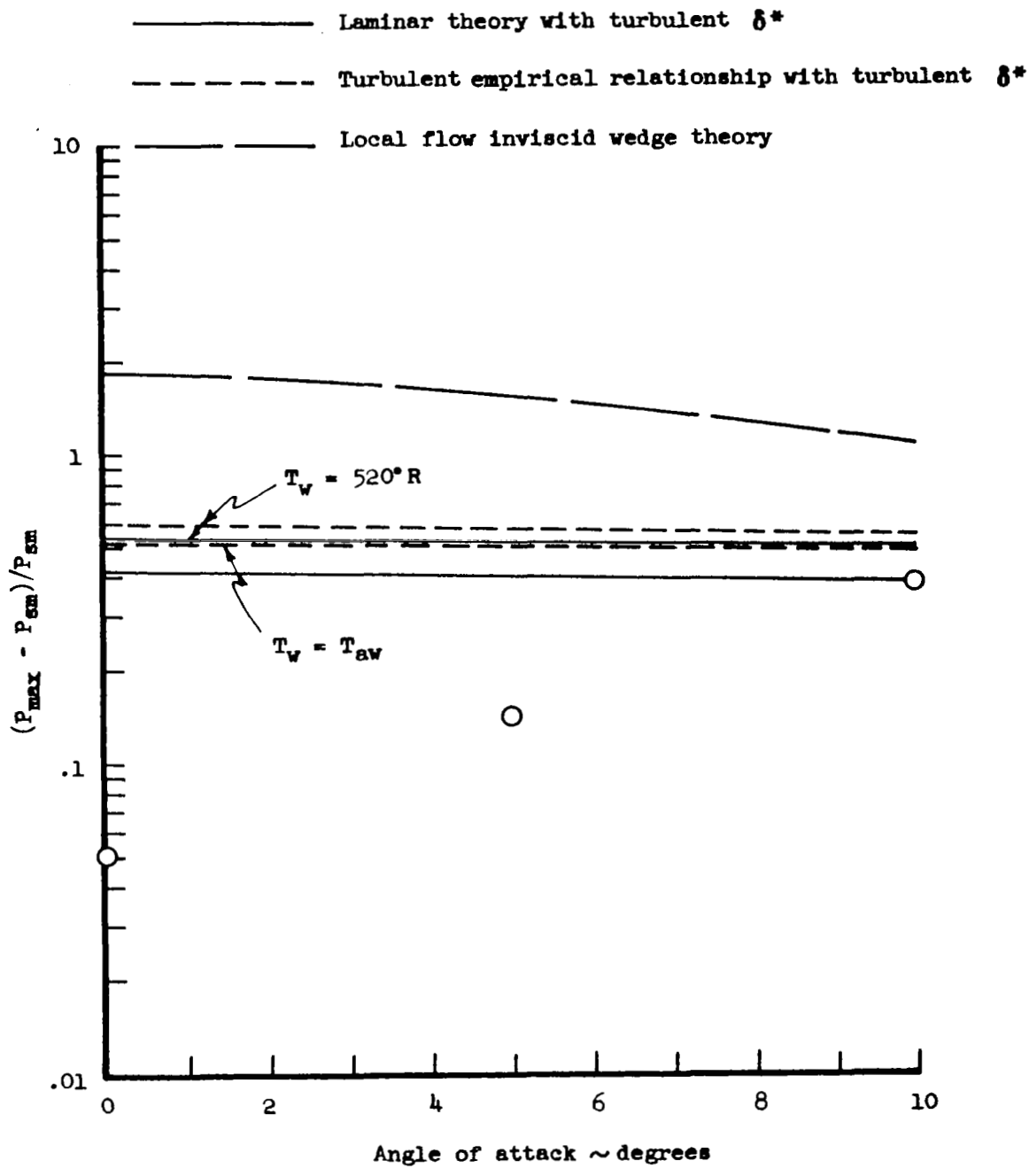

(c) 70° Swept curcular arc wave W/R = 46

Figure 16.- Concluded.

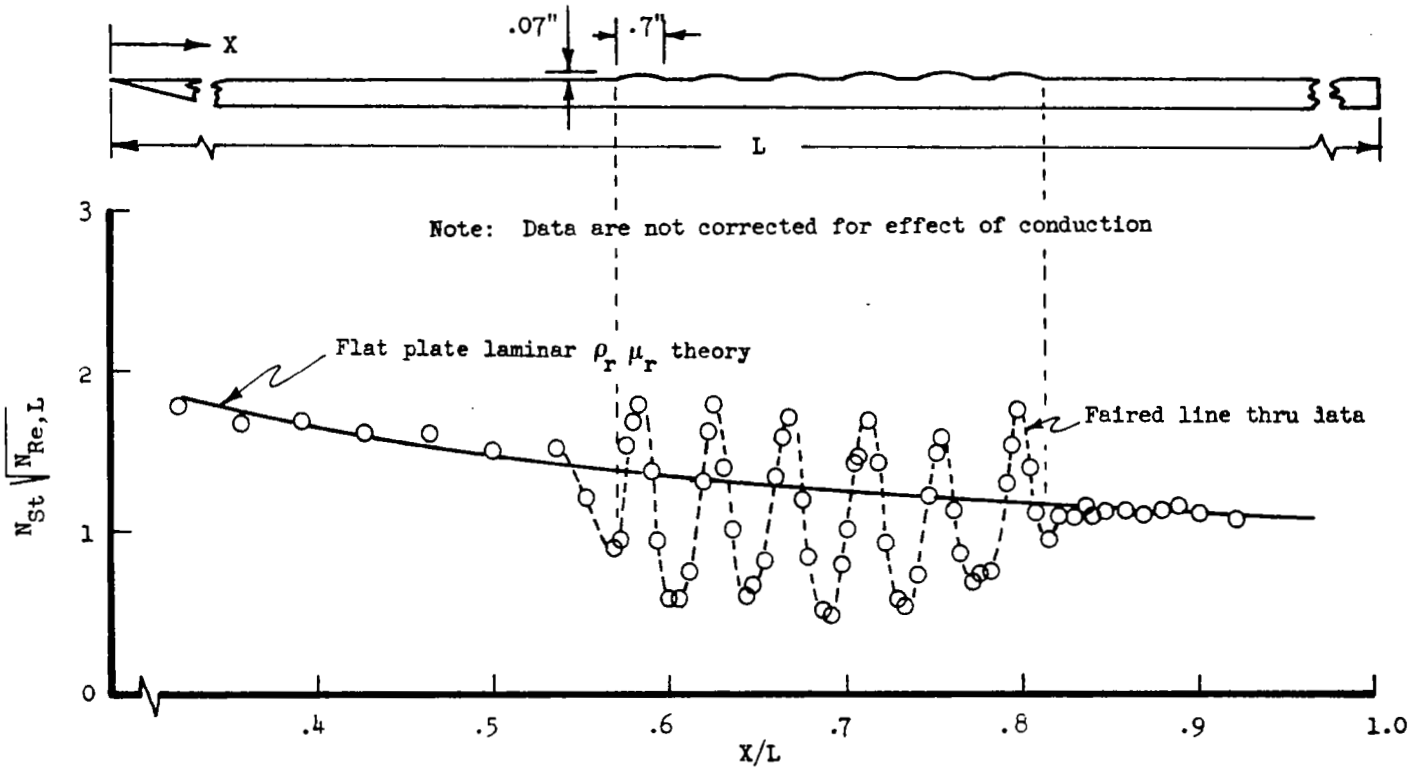

Figure 17.- Heat transfer distribution over multiple waves on a sharp flat plate. $\alpha = 10°$; $M_\infty = 10.1$; $P'_o = .965$ psia; $H_o = 10.68 \times 10^6$ ft^2/sec^2; $N_{Re,L} = 1.16 \times 10^6$

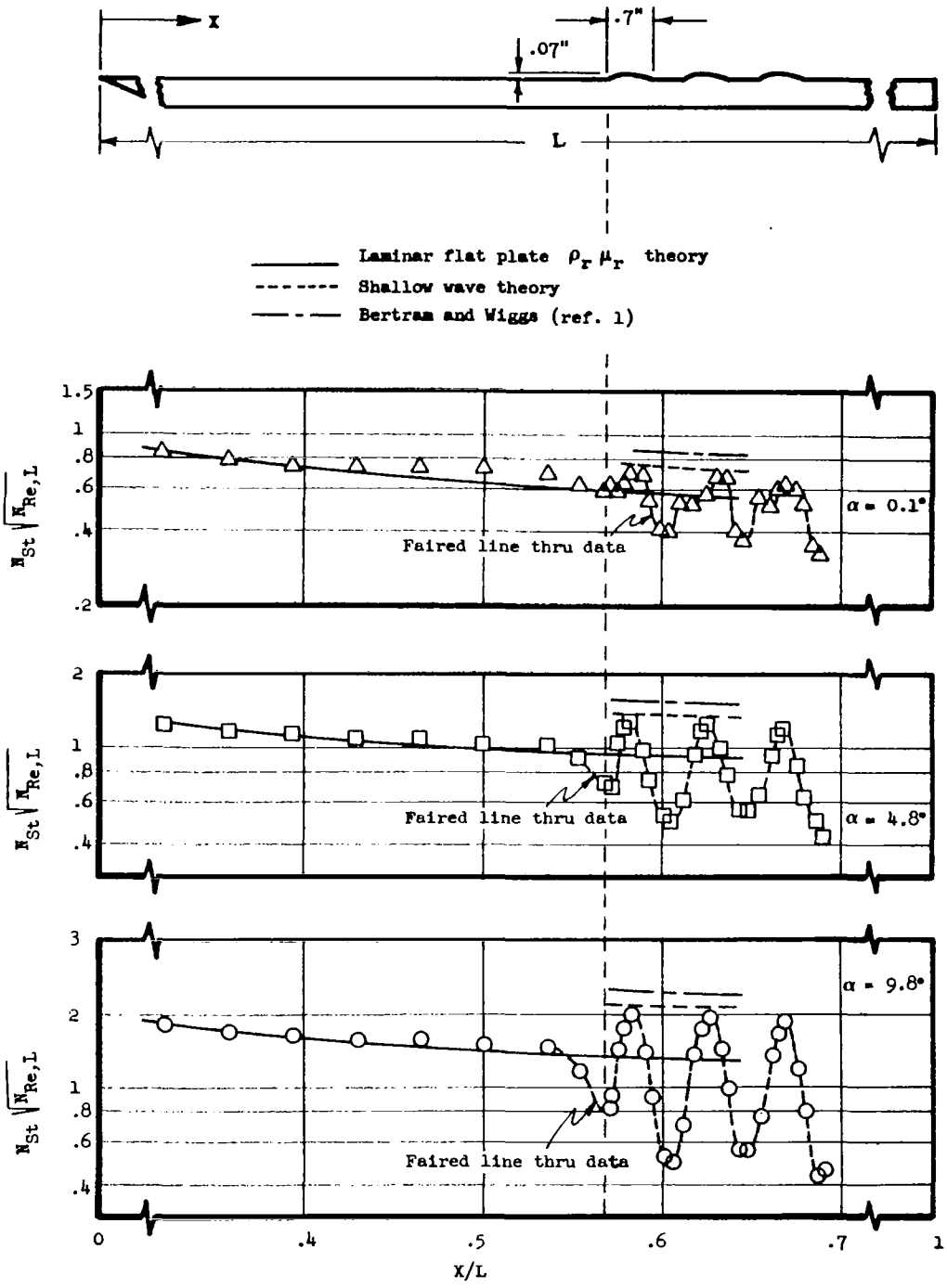

Figure 18.- Laminar heat transfer distributions on circular arc waves on a sharp flat plate. $M_\infty = 10.1$; $P'_o = .965$ psia; $H_o = 10.68 \times 10^6$ ft^2/sec^2; $N_{Re,L} = 1.16 \times 10^6$

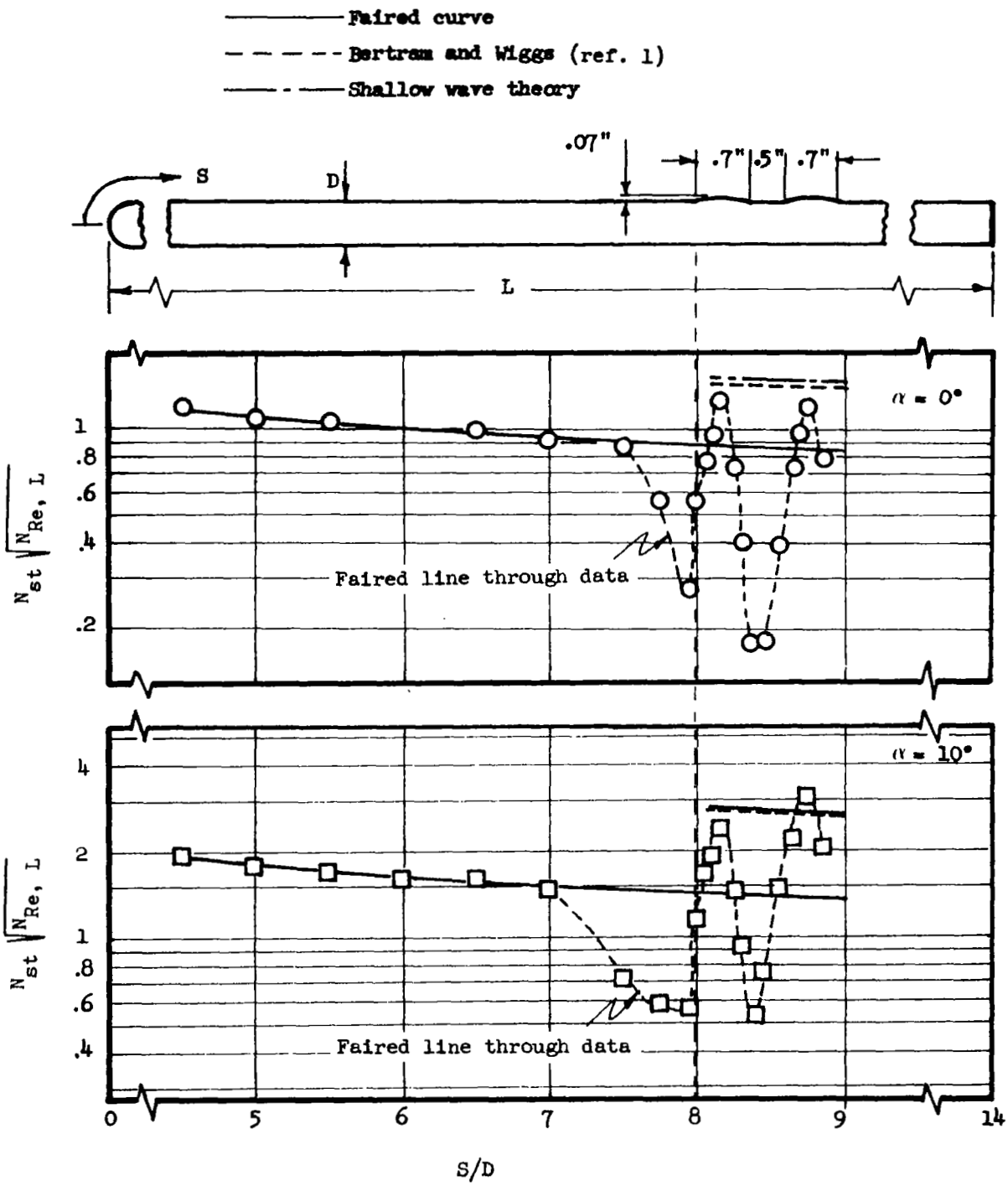

Figure 19.- Heat transfer distribution on unswept circular arc waves on a blunt flat plate. M_∞ = 10.2; P'_o = 4.48 psia; H_o = 11.85 x 10^6 ft^2/sec^2; $N_{Re,L}$ = 4.56 x 10^6.

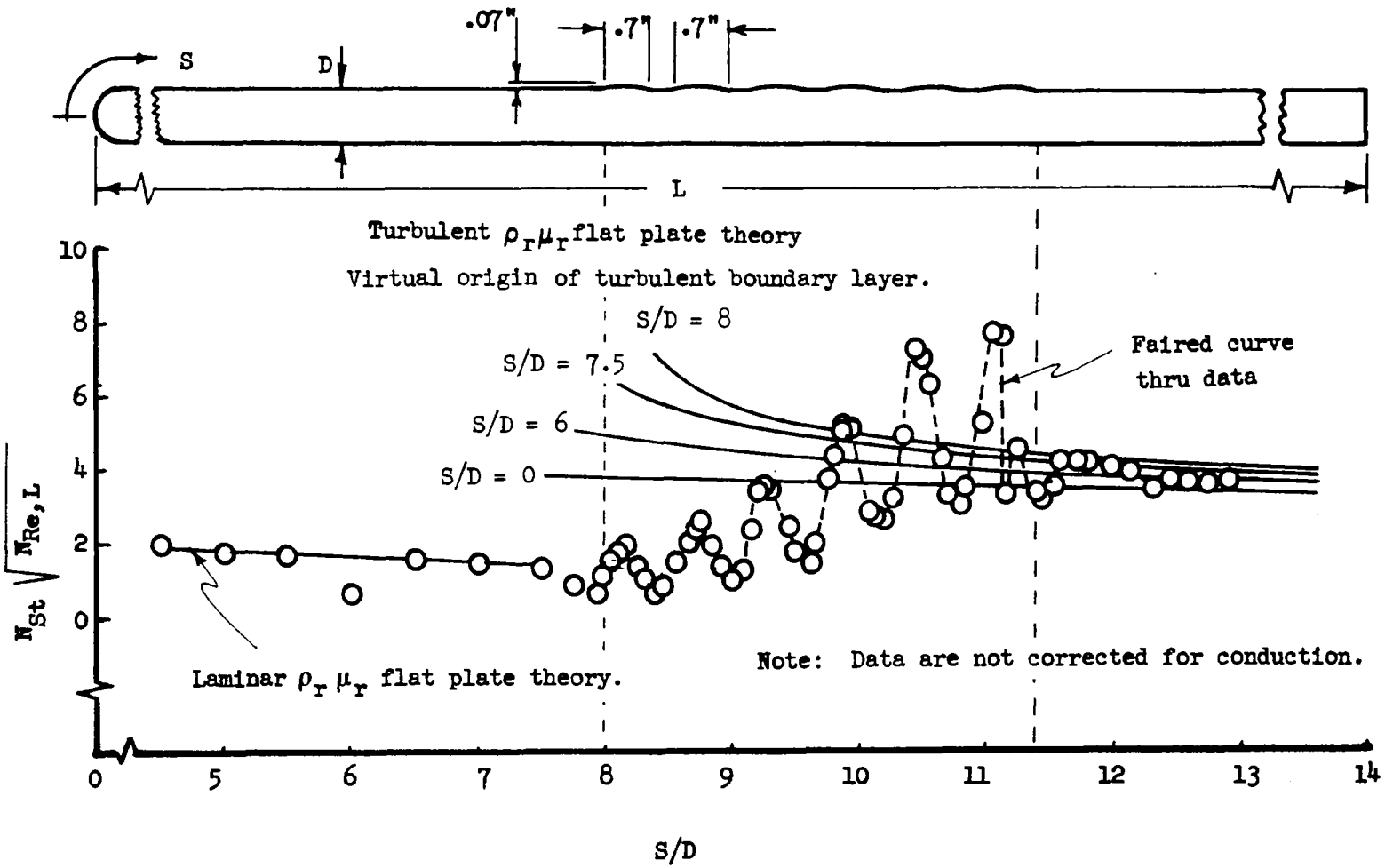

Figure 20.- Heat transfer distribution over multiple unswept circular arc waves on a blunt flat plate. $\alpha = 10°$; $M_\infty = 10.2$; $P'_o = 4.48$ psia; $H_o = 11.85 \times 10^6$; $N_{Re,L} = 4.56 \times 10^6$.

Theory		R	W	W/R
———	○	.07"	.7"	10
– – – – –	□	.07"	1.1"	15.7
——·——	△	.04"	.7"	17.5

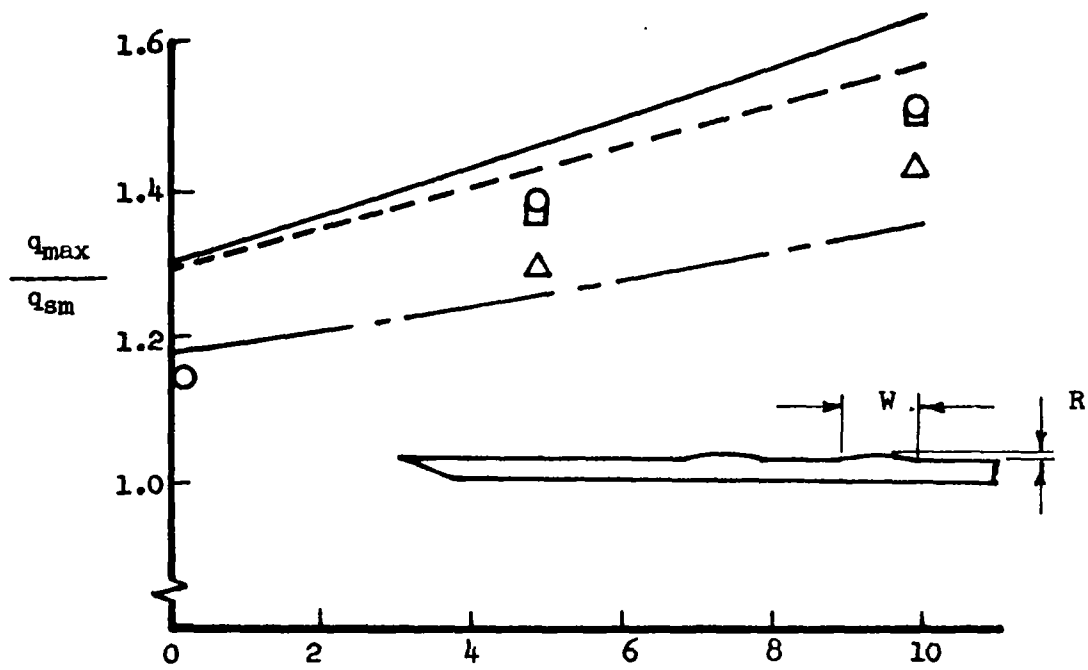

Figure 21.- Comparison of first wave data and shallow wave theory for effect of wave height to width ratio. M_∞ = 10.1; P'_o = .965 psia; H_o = 10.68 x 10^6 ft^2/sec^2; $N_{Re,L}$ = 1.16 x 10^6.

First Wave	Second Wave	R	W/R	S	Λ
○	●	.07"	15.7	.375"	0°
□	■	.07"	15.7	.50"	0°
△	▲	.07"	15.7	1.3"	0°

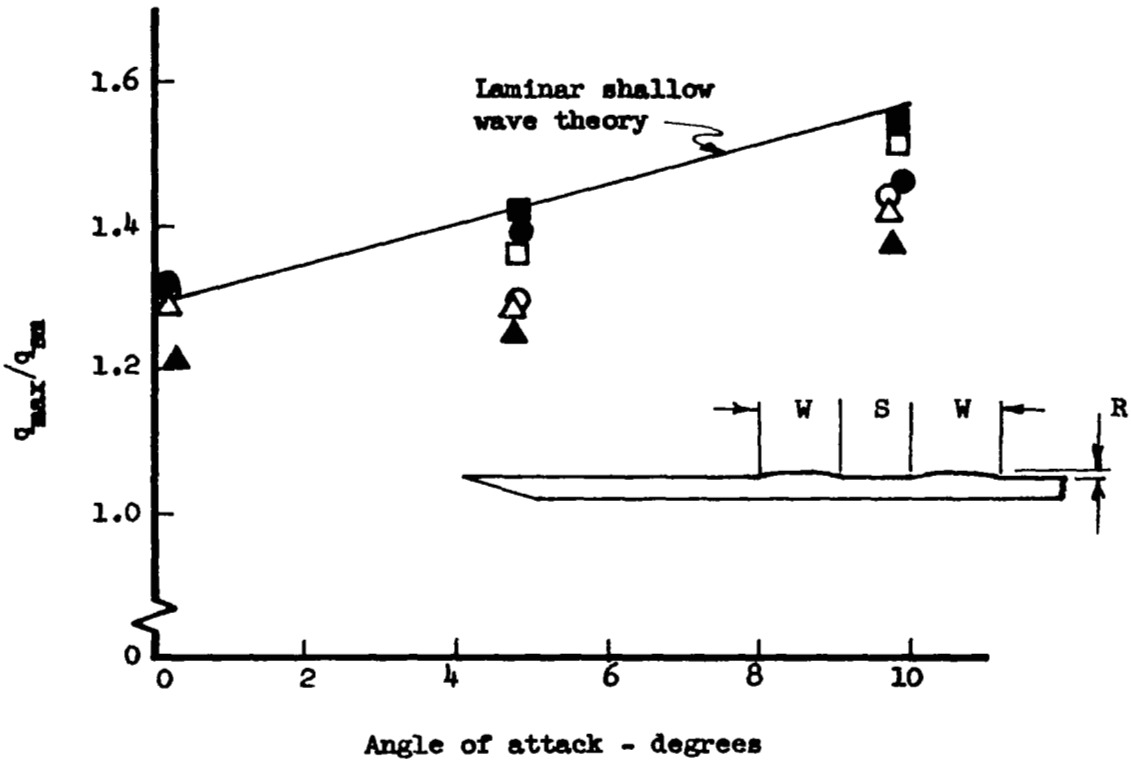

Figure 22.- The effect of wave spacing on maximum wave heating. $M_\infty = 10.1$; $P'_o = .965$ psia; $H_o = 10.68 \times 10^6$ ft^2/sec^2; $N_{Re,L} = 1.16 \times 10^6$.

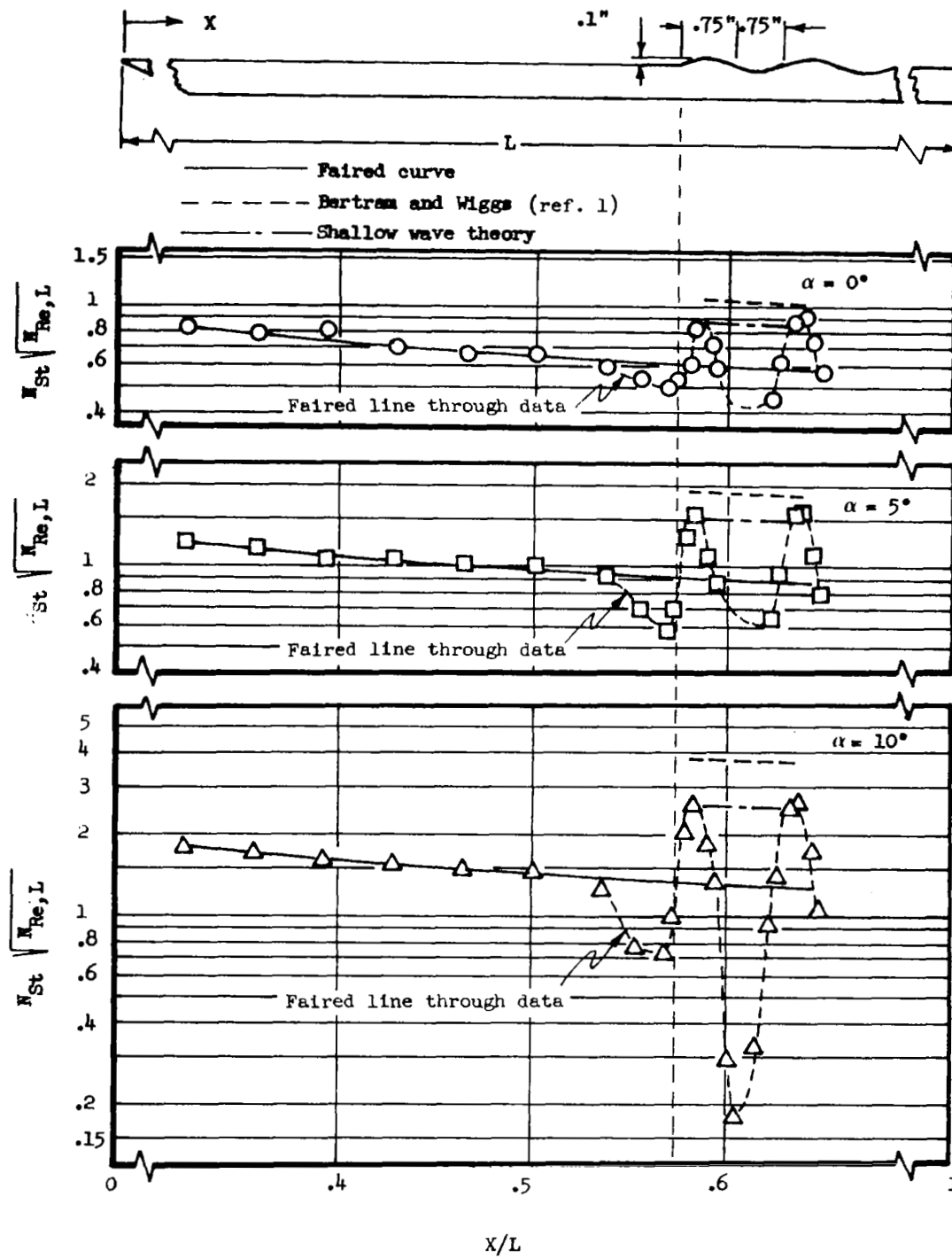

Figure 23.- Laminar heat transfer distribution on an unswept sine wave. M_∞ = 10.1; P'_o = .965 psia; H_o = 10.68 x 10^6 ft^2/sec^2; $N_{Re,L}$ = 1.16 x 10^6.

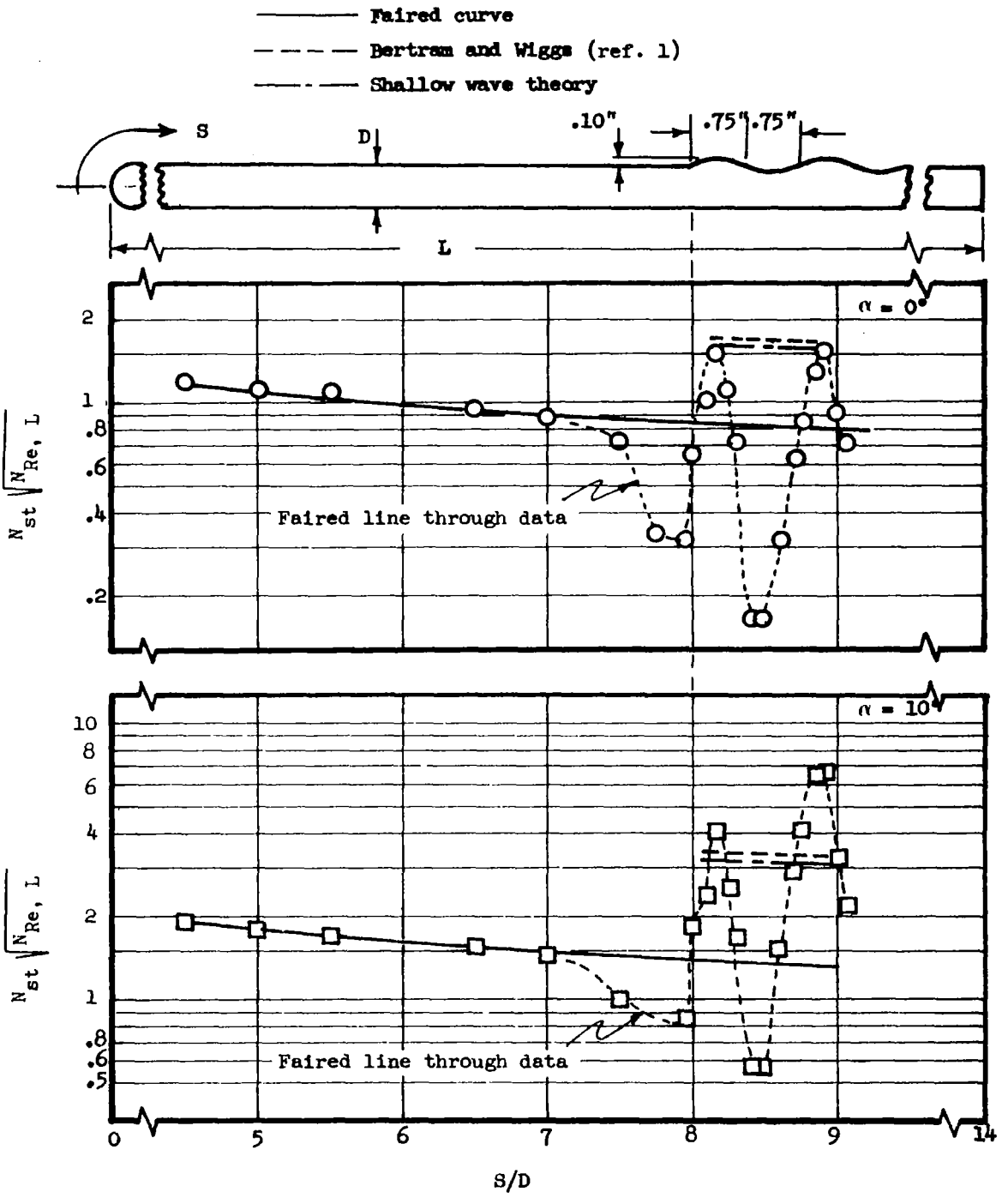

Figure 24.- Heat transfer distribution on an unswept sine wave on a blunt flat plate. M_∞ = 10.2; P'_o = 4.48 psia; H_o = 11.85 x 10^6 ft^2/sec^2; $N_{Re,L}$ = 4.56x10^6

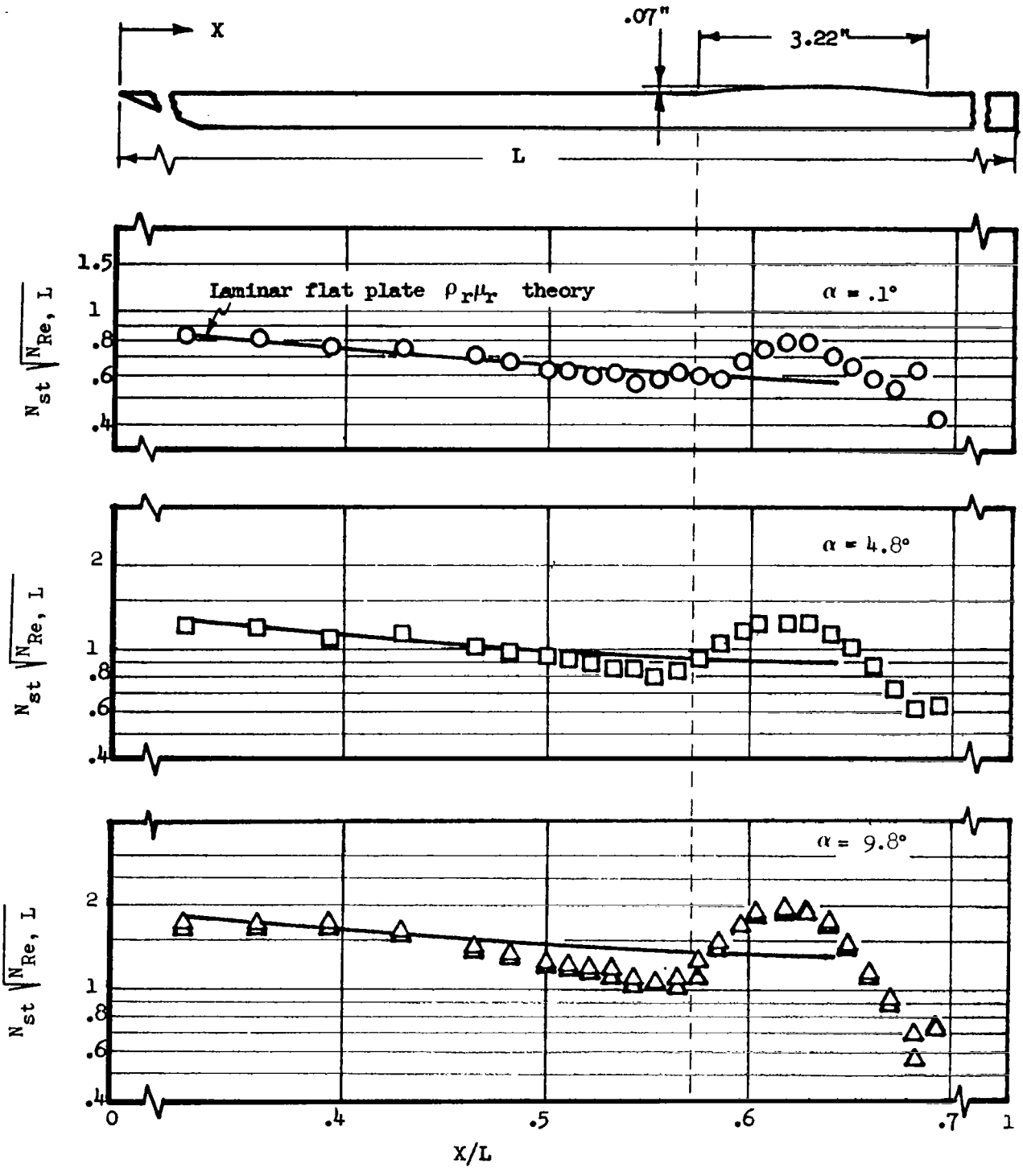

Figure 25.- Laminar heat transfer distributions on a 70° swept circular arc wave. M_∞ = 10.1; P'_o = .965 psia; H_o = 10.68 x 10^6 ft^2/sec^2; $N_{Re,L}$ = 1.16 x 10^6.

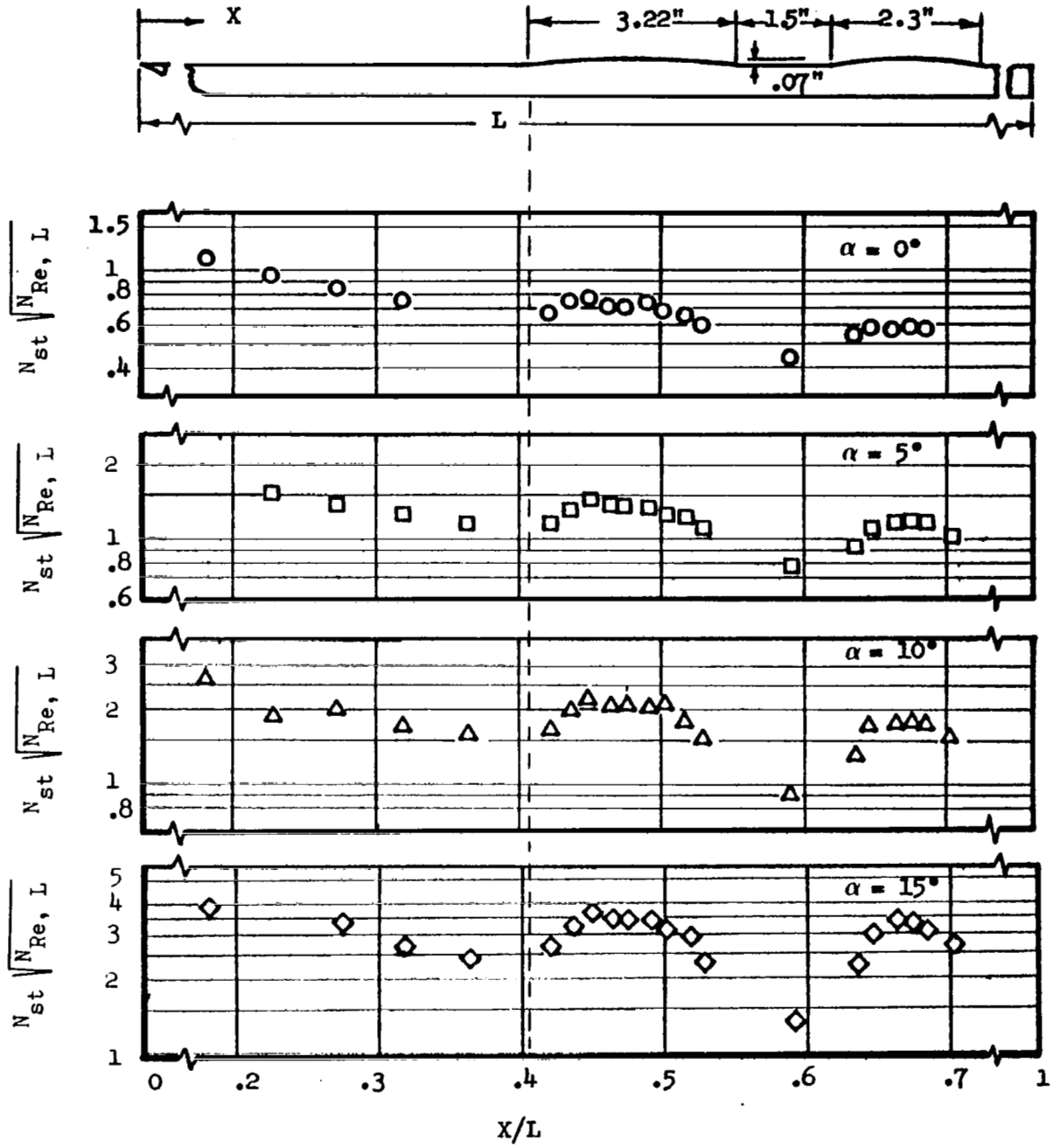

Figure 26.- Laminar heat transfer distributions over two 70° swept circular arc waves. M_∞ = 15.2; P'_o = 1.14 psia; H_o = 30.5 x 10^6 ft^2/sec^2; $N_{Re,L}$ = .48 x 10^6.

Theory		Λ	R	W	W/R
———	●	0°	.07"	1.1"	15.7
— — — —	○	70°	.07"	3.22"	46.0

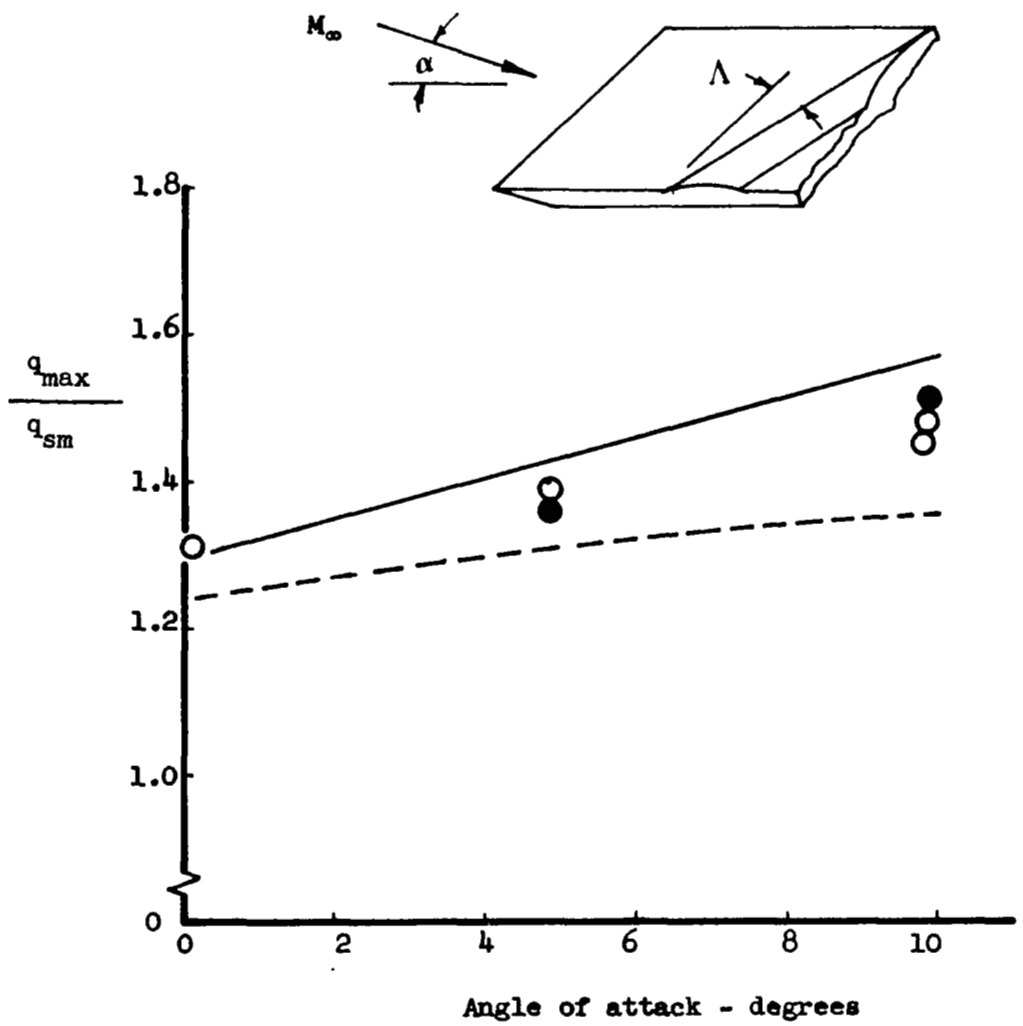

Figure 27.- Comparison of data and the shallow wave theory for the effect of sweep angle on maximum wave heating. M_∞ = 10.1; P'_o = .965 psia; H_o = 10.68 x 10^6 ft^2/sec^2; $N_{Re,L}$ = 1.16 x 10^6.

Theory		Λ	R	W	W/R
———	●	0°	.07"	.7"	10
— — — —	○	70°	.07"	2.05"	29.3

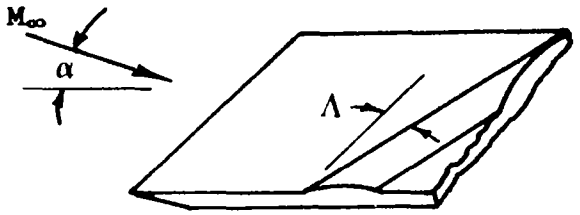

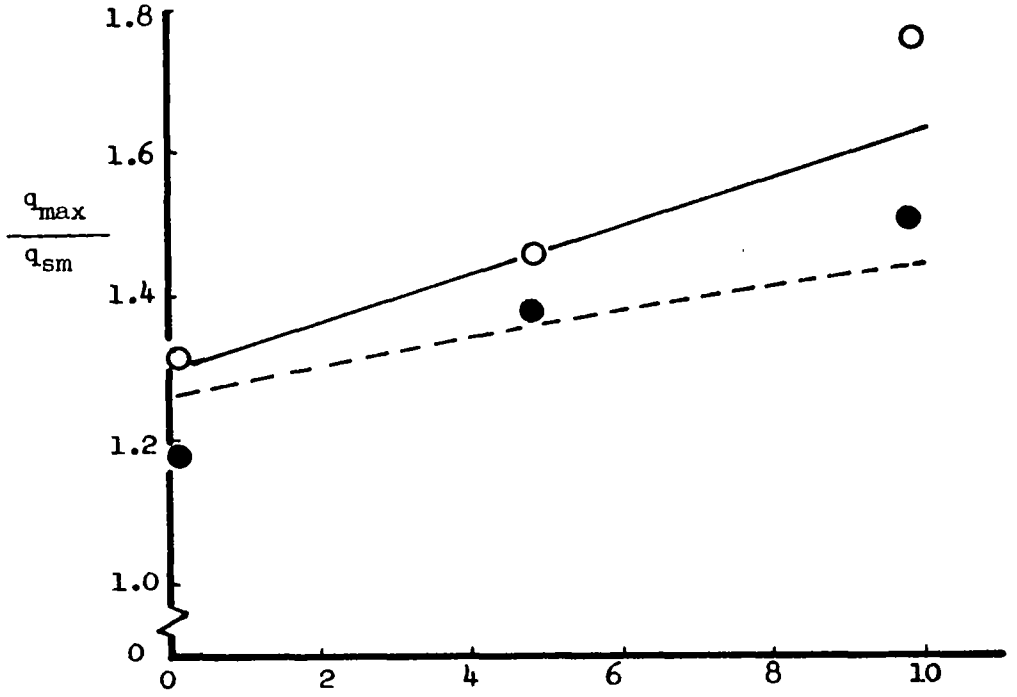

Figure 28.- Comparison of data and the shallow wave theory for the effect of sweep angle on maximum wave heating. M_∞ = 10.1; P'_o = .965 psia, H_o = 10.68 x 10^6 ft^2/sec^2; $N_{Re,L}$ = 1.16 x 10^6.

M_∞	14.7	15.2
Po, psia	1000	3900
P_o', Psia	.344	1.14
Ho, ft^2/sec^2	30×10^6	30.5×10^6
$N_{Re,L}$	$.137 \times 10^6$	$.48 \times 10^6$
α = 0°	○	○ ——— Shallow wave theory
5°	□	□
10°	△	△
15°	◇	◇ – – – – Shallow wave theory

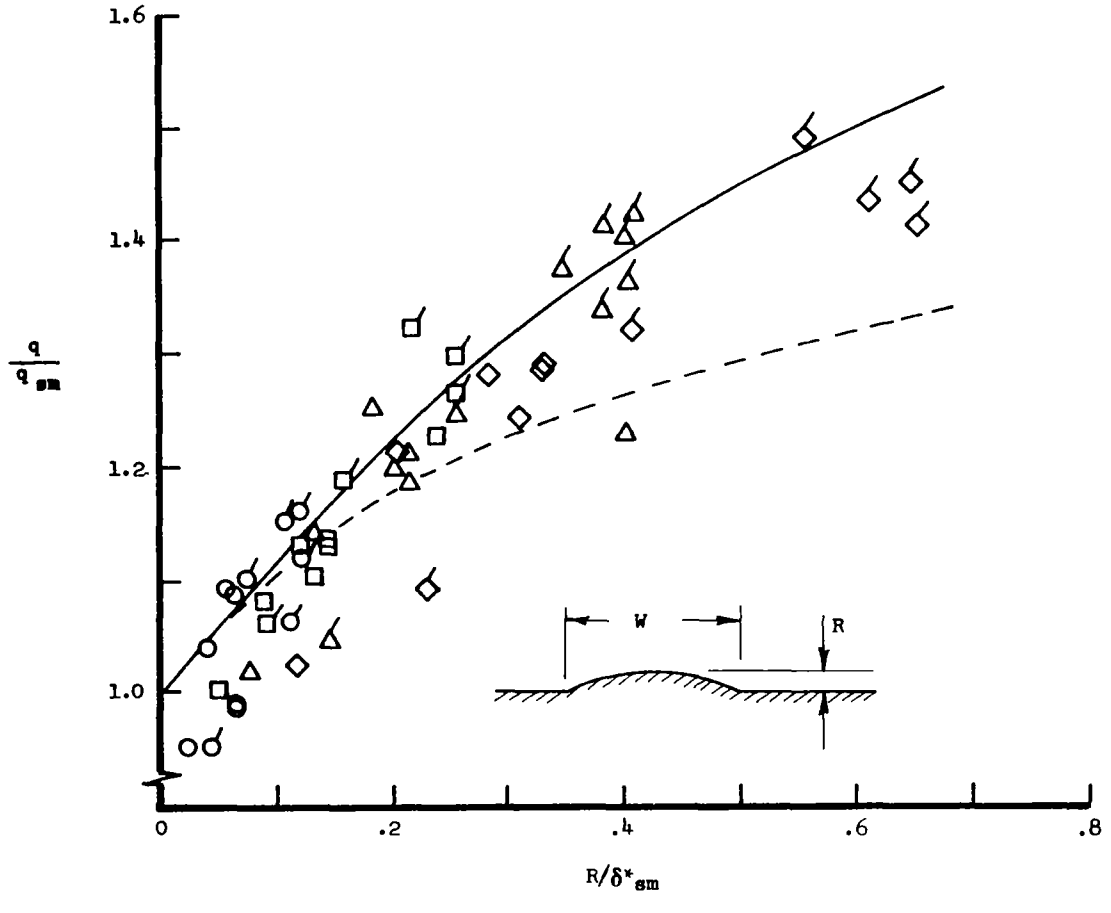

Figure 29.- Comparison of laminar heat transfer data and the shallow wave theory for a 70° swept circular arc wave. W/R = 46, R_{max} = .07 inches.

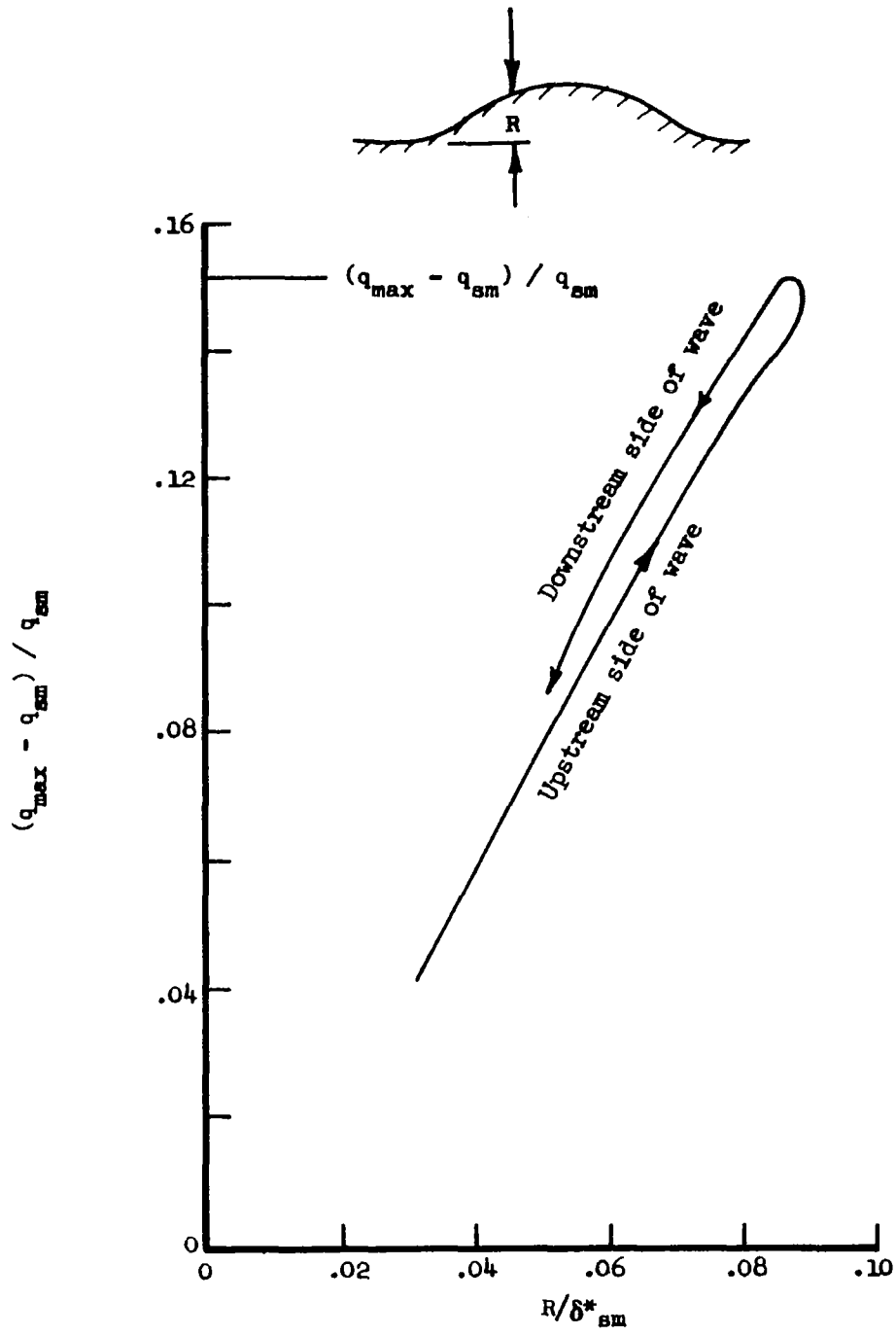

Figure 30.- Analytical laminar heat transfer distribution over a wave. M_e = 8.0, H_w/H_o = .5.

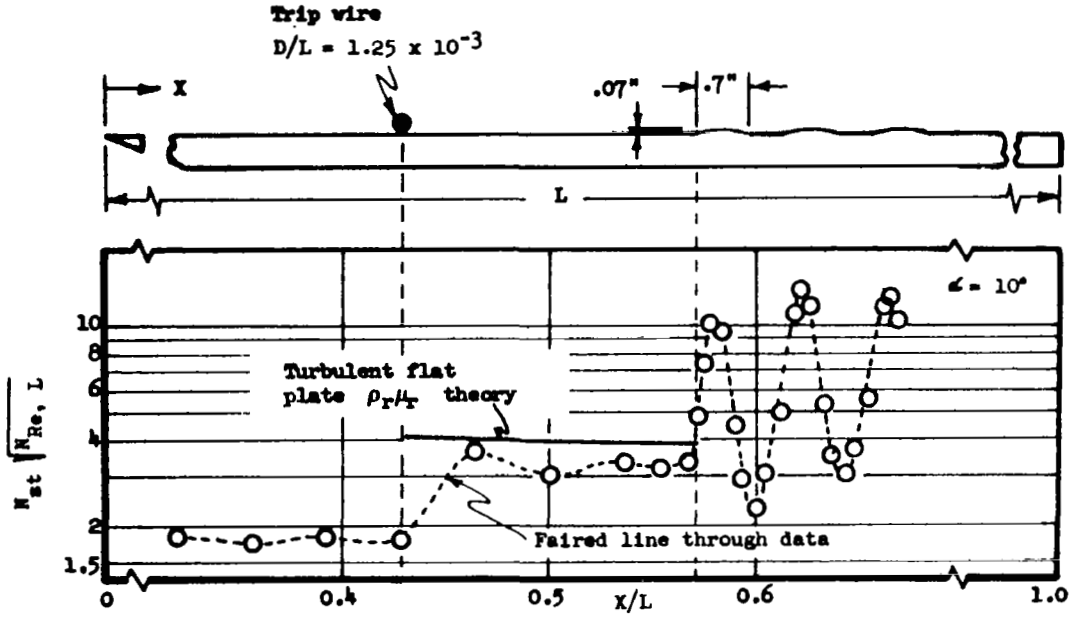

a) Unswept circular arc wave. $M_\infty = 10.2$; $N_{Re,L} = 4.66 \times 10^6$; $P_o' = 4.48$ psia; $H_o = 11.85 \times 10^6$ ft^2/sec^2

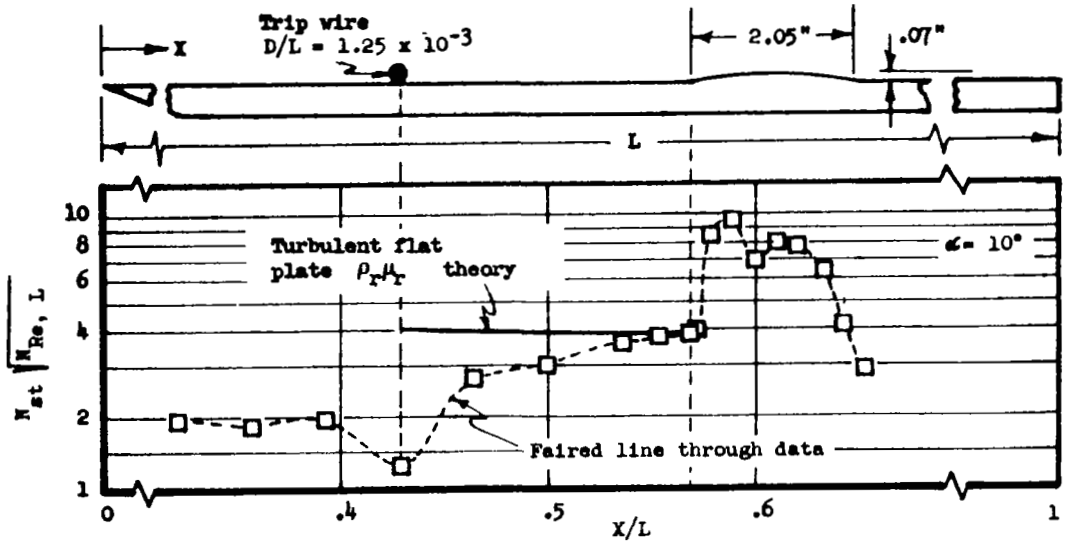

b) 70° swept circular arc wave. $M_\infty = 10.2$; $N_{Re,L} = 4.66 \times 10^6$; $P_o' = 4.48$ psia; $H_o = 11.85 \times 10^6$ ft^2/sec^2

Figure 31.- Turbulent heat transfer distribution on waves.

$M_\infty = 10.2$, $N_{Re,L} = 4.66 \times 10^6$

$P_o' = 4.48$ psia, $H_o = 11.85 \times 10^6$ ft^2/sec^2

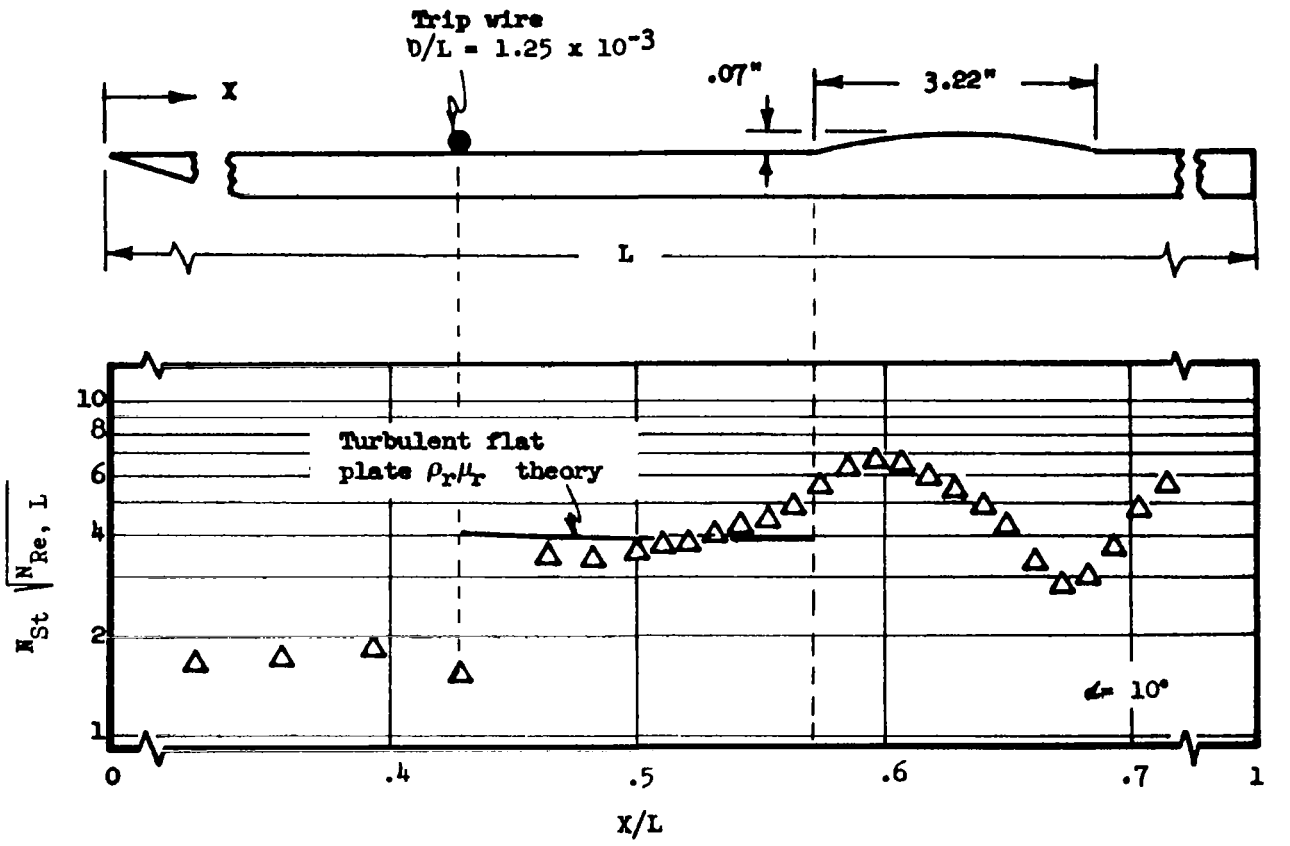

c) 70° swept circular arc wave

Figure 31.- Continued

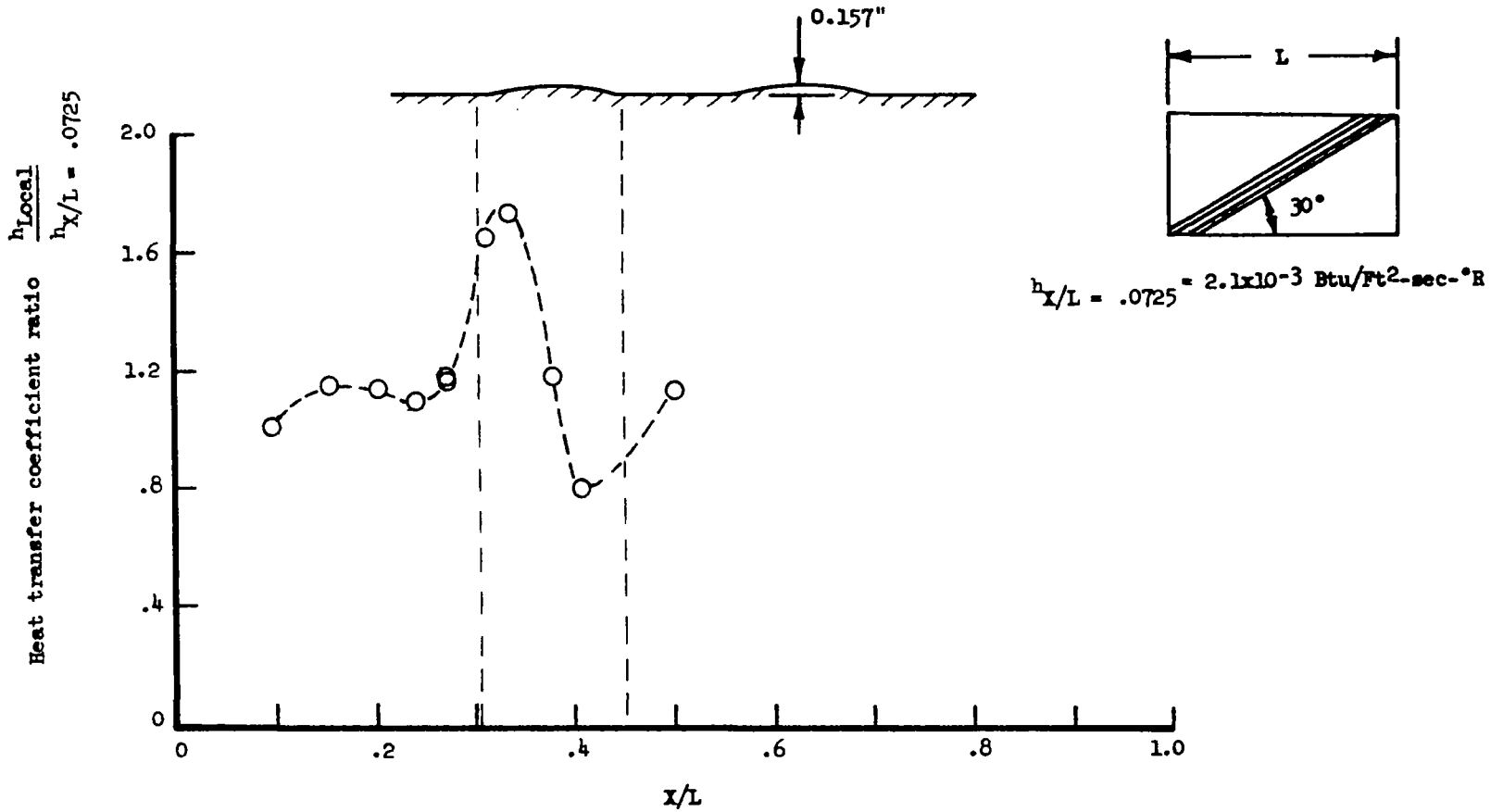

d) 60° swept wave mounted in the tunnel wall W/R = 31.8, M_∞ = 6.95, P_o = 1100 psia, $N_{Re,\delta} = .985 \times 10^6$

Figure 31.- Concluded.

First Wave	Second Wave	R	W/R	Λ	M_{∞}	P_o' Psia	H_o Ft^2/sec^2	$N_{Re,L}$
○		.07"	46	70°	10.2	4.48	11.85×10^6	4.66×10^6
□	■	.07"	15.7	0°				
△	▲	.10"	7.5	0°				
◇	◆	.04"	17.5	0°				
⌂	◗	.07"	10	0°				
⌂		.07"	29.3	70°				
◇		.157"	31.9	60°	6.95	174	9.12×10^6	17.3×10^6

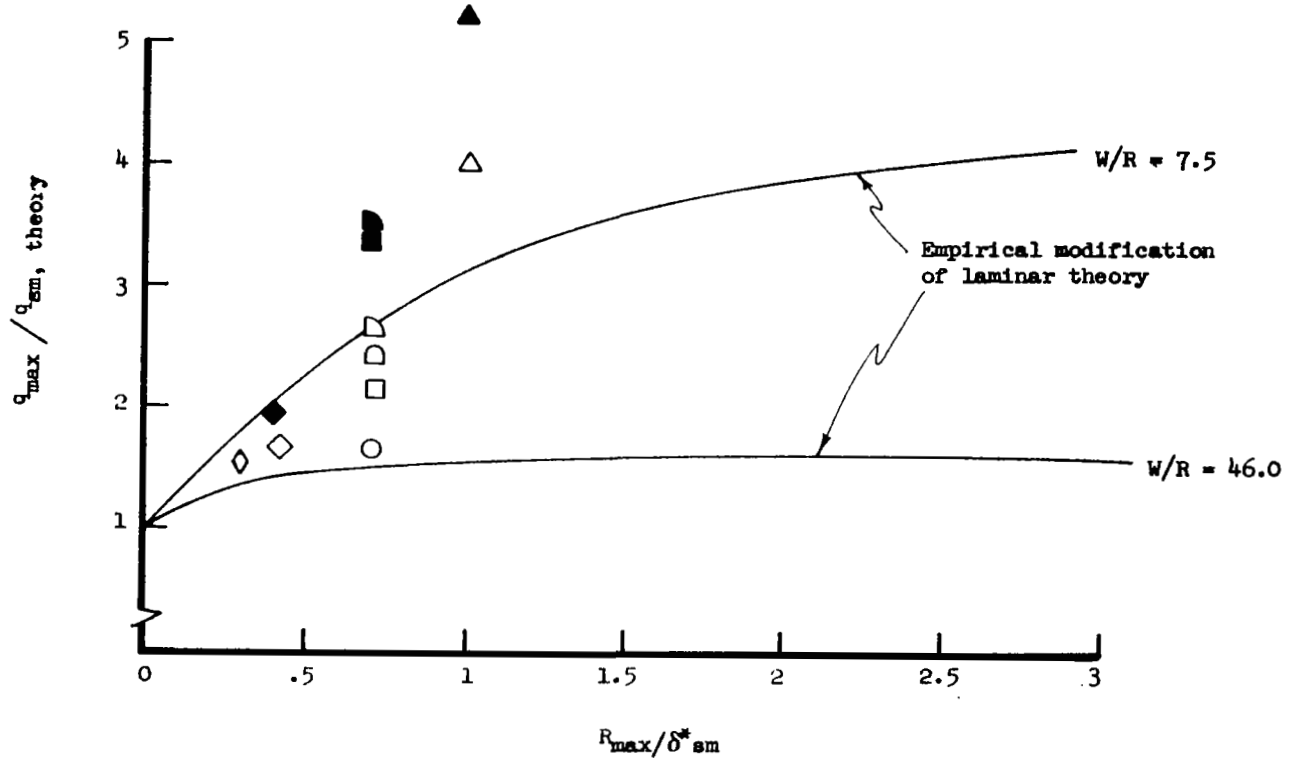

Figure 32.- Comparison of turbulent heating data from circular arc and sinusoidal surface waves.

	α	R	W	W/R
○	0°	.763"	7.00"	9.18
□	0°	.579"	6.25"	10.80
△	0°	.568"	6.25"	11.00
◇	0°	.490"	6.00"	12.25
⏢	0°	.258"	5.00"	19.40

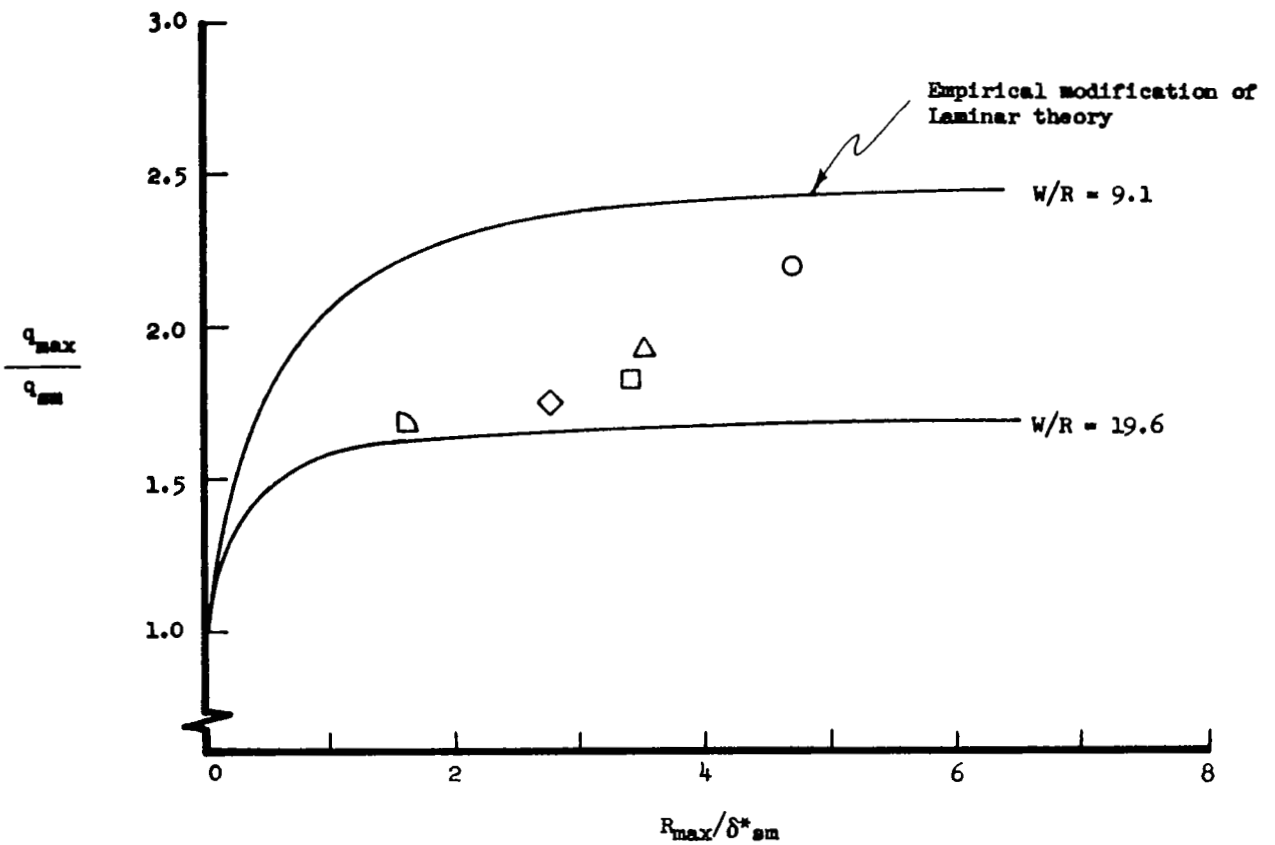

Figure 33.- Comparison of turbulent heating data from sinusoidal skin buckles (ref. 2) and the modified shallow wave theory. α = 0°; M_∞ = 3.0; P_o = 200 psia; T_o = 960°R; N_{Re}/Ft = 14×10^6.

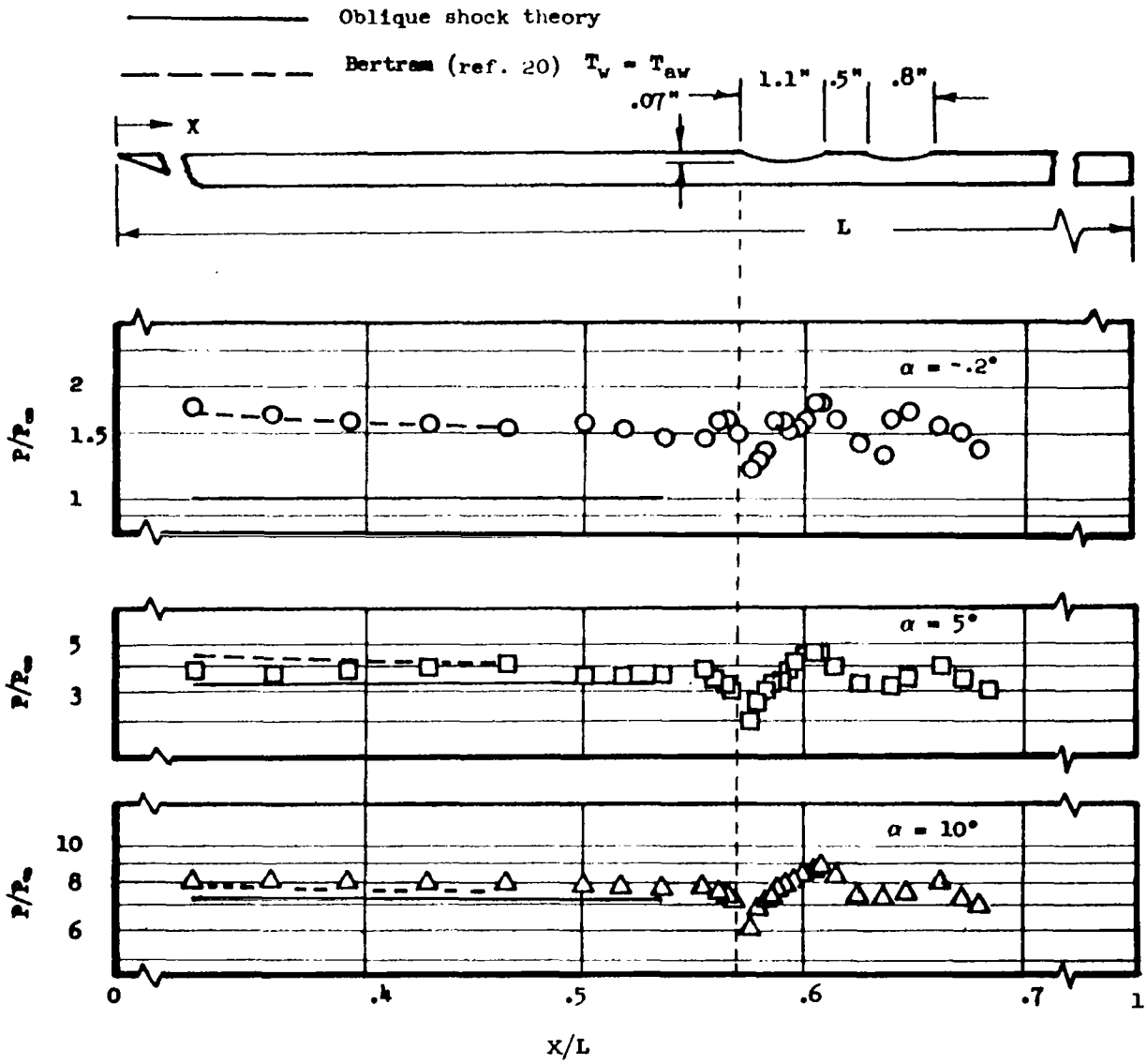

Figure 34.- Pressure distribution on two unswept inverted waves on a sharp flat plate. M_∞ = 10.1; P'_o = .965 psia; H_o = 10.68 x 10^6 ft^2/sec^2; $N_{Re,L}$ = 1.16 x 10^6.

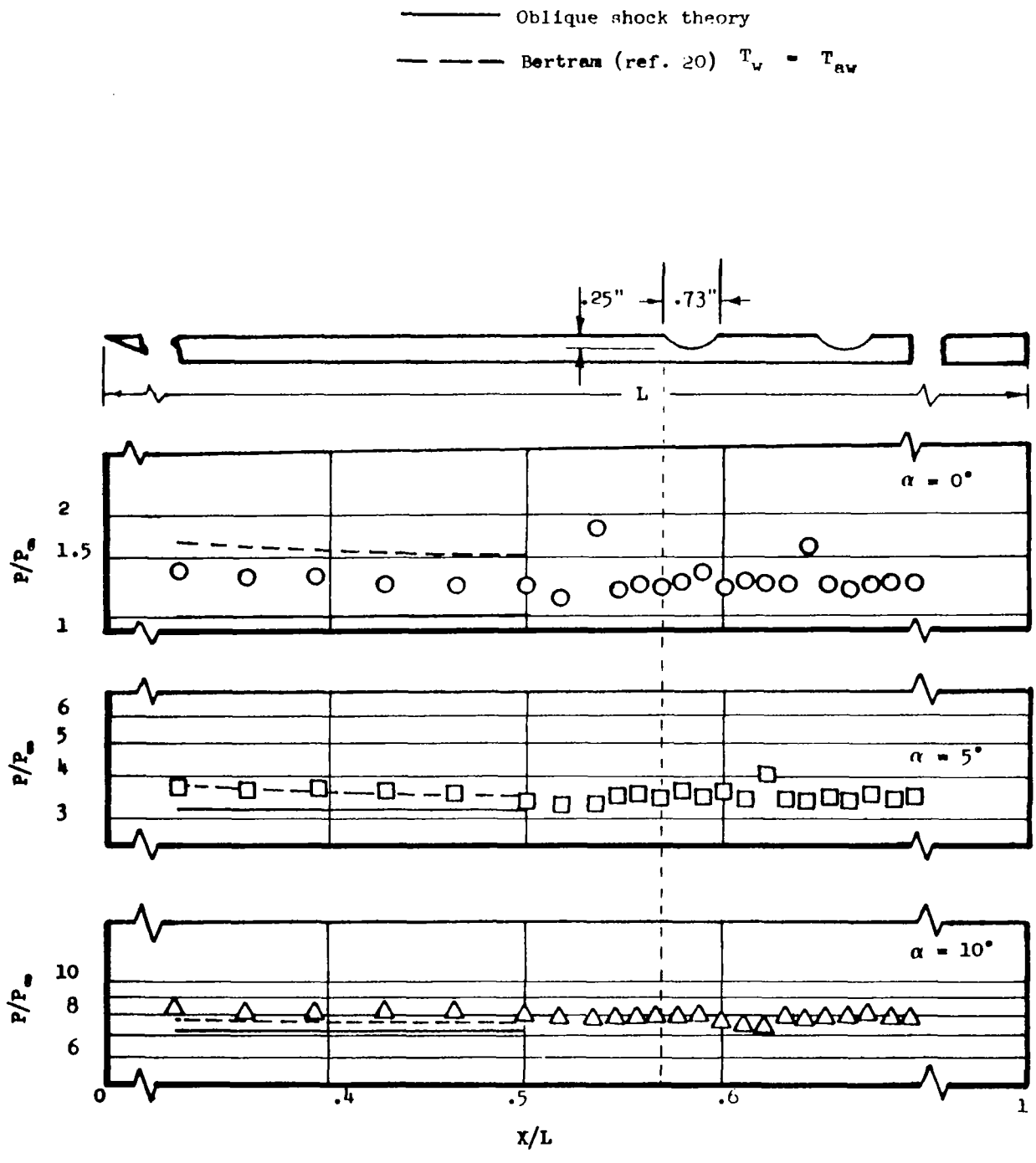

Figure 35.- Pressure distribution on a 70° swept groove. $M_\infty = 10.1$; $P'_o = .965$ psia; $H_o = 10.68 \times 10^6$ ft^2/sec^2; $N_{Re,L} = 1.16 \times 10^6$.

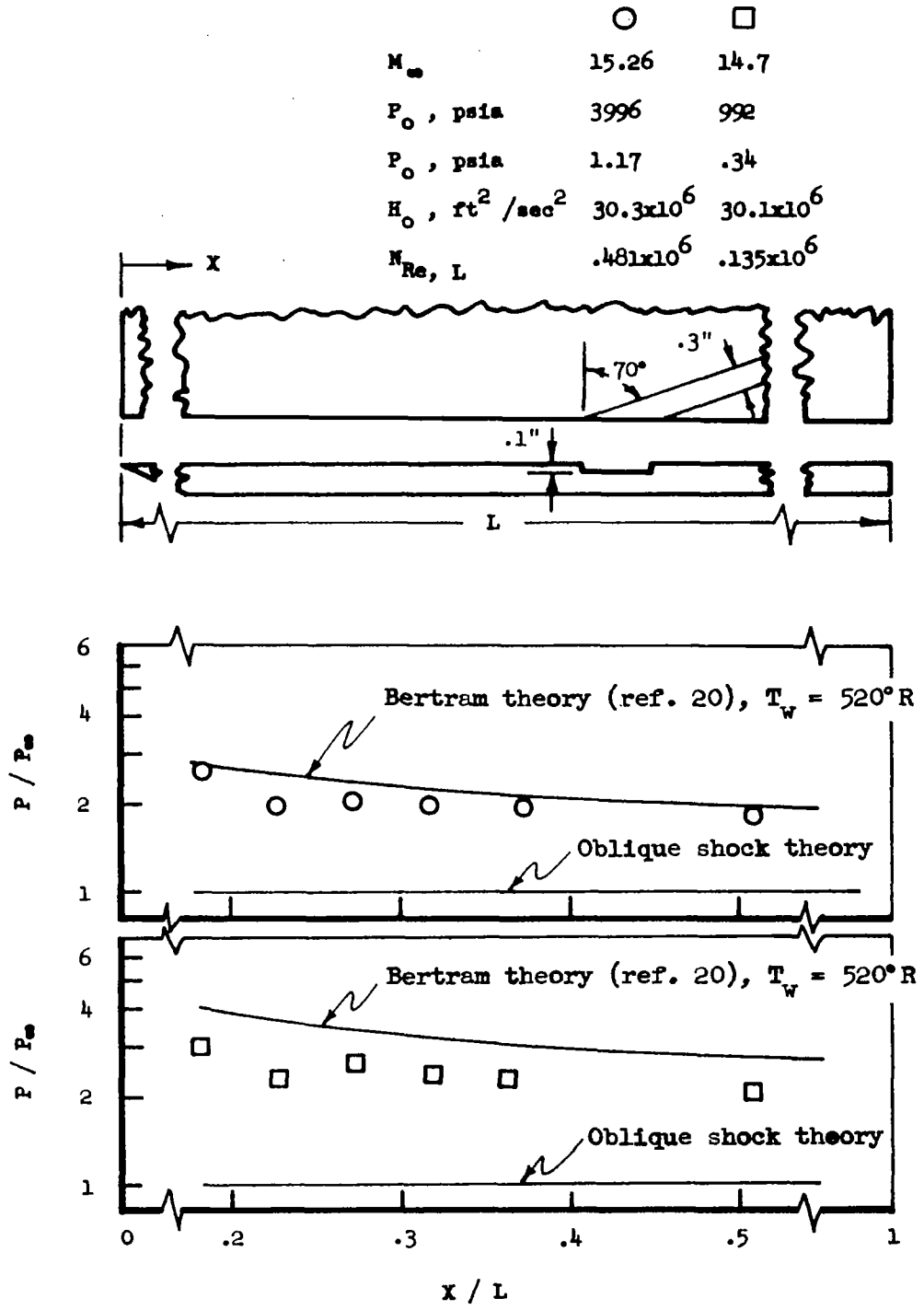

Figure 36.- Sharp flat plate pressure distribution. $\alpha = 0°$.

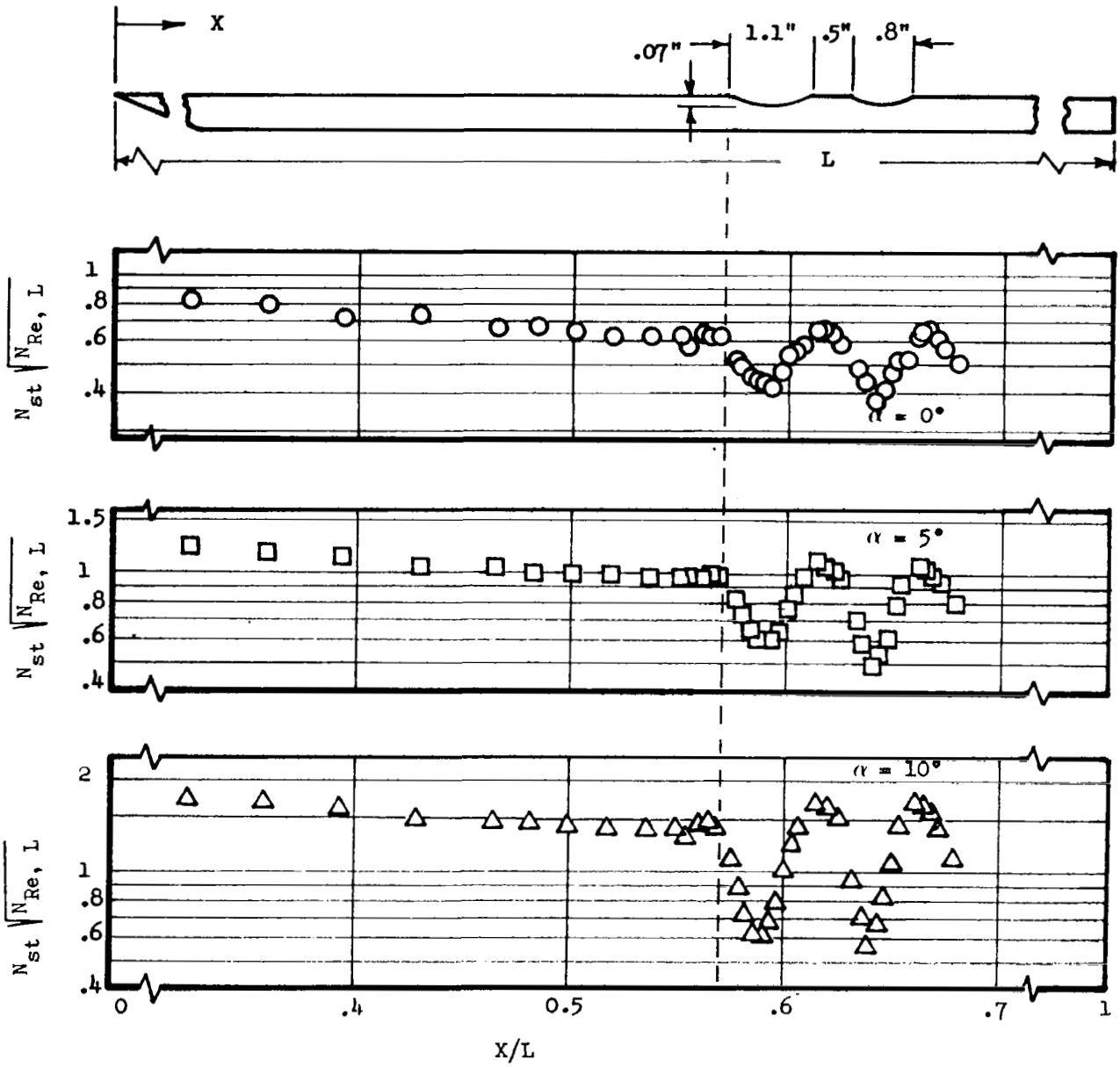

Figure 37.- Laminar heat transfer distributions on two unswept inverted waves on a sharp flat plate. $M_\infty = 10.1$; $P_o' = .965$ psia; $H_o = 10.68 \times 10^6$ ft^2/sec^2; $N_{Re,L} = 1.16 \times 10^6$

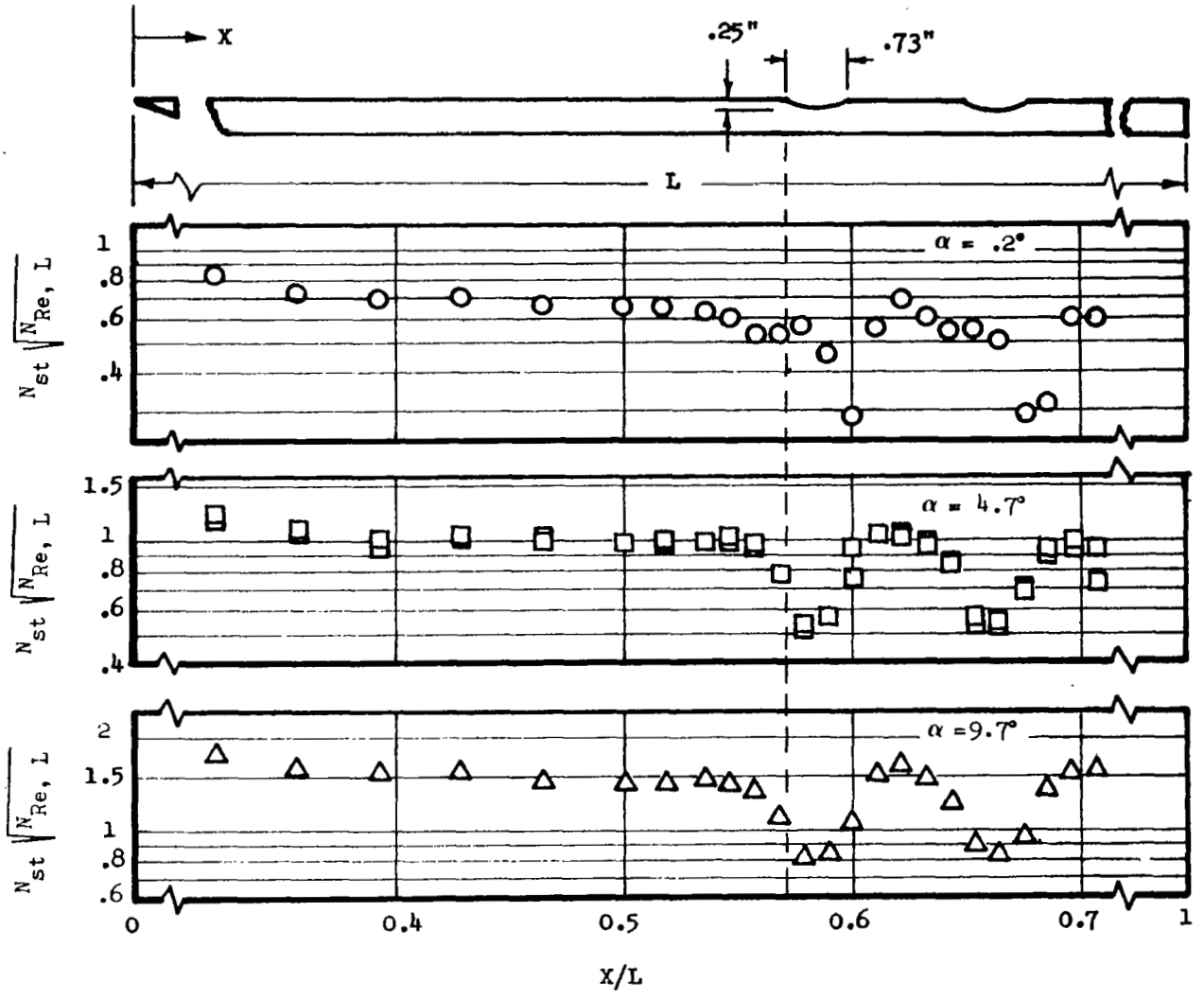

Figure 38.- Laminar heat transfer distribution on a 70° swept groove on a sharp flat plate. M_∞ = 10.1; P'_o = .965 psia; H_o = 10.68 x ft^2/sec^2; $N_{Re,L}$ = 1.16 x 10^6

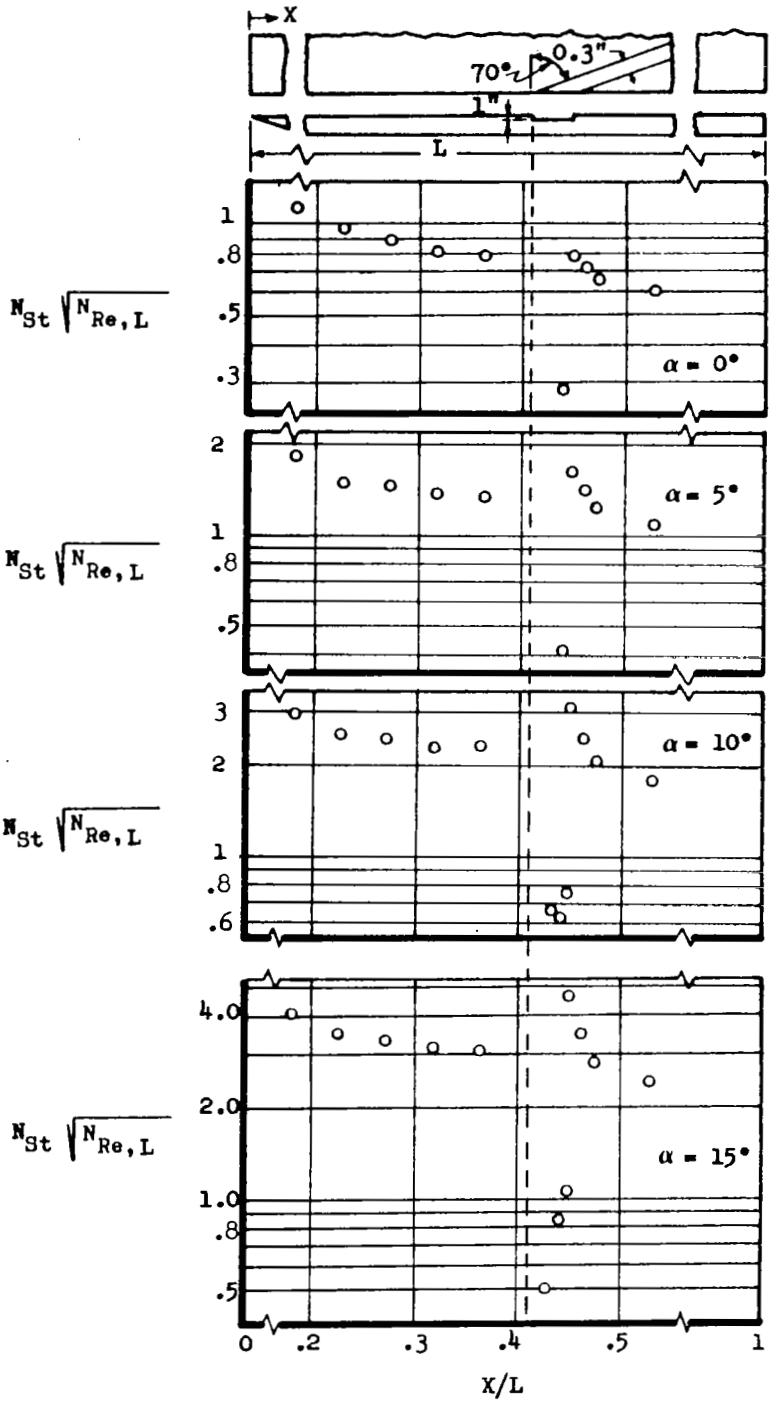

Figure 39.- Laminar heat transfer distribution on a 70° swept groove. $M_\infty = 15.2$; $p'_o = 1.14$ psia; $H_o = 30.5 \times 10^6$ ft^2/sec^2; $N_{Re,L} = 0.48 \times 10^6$

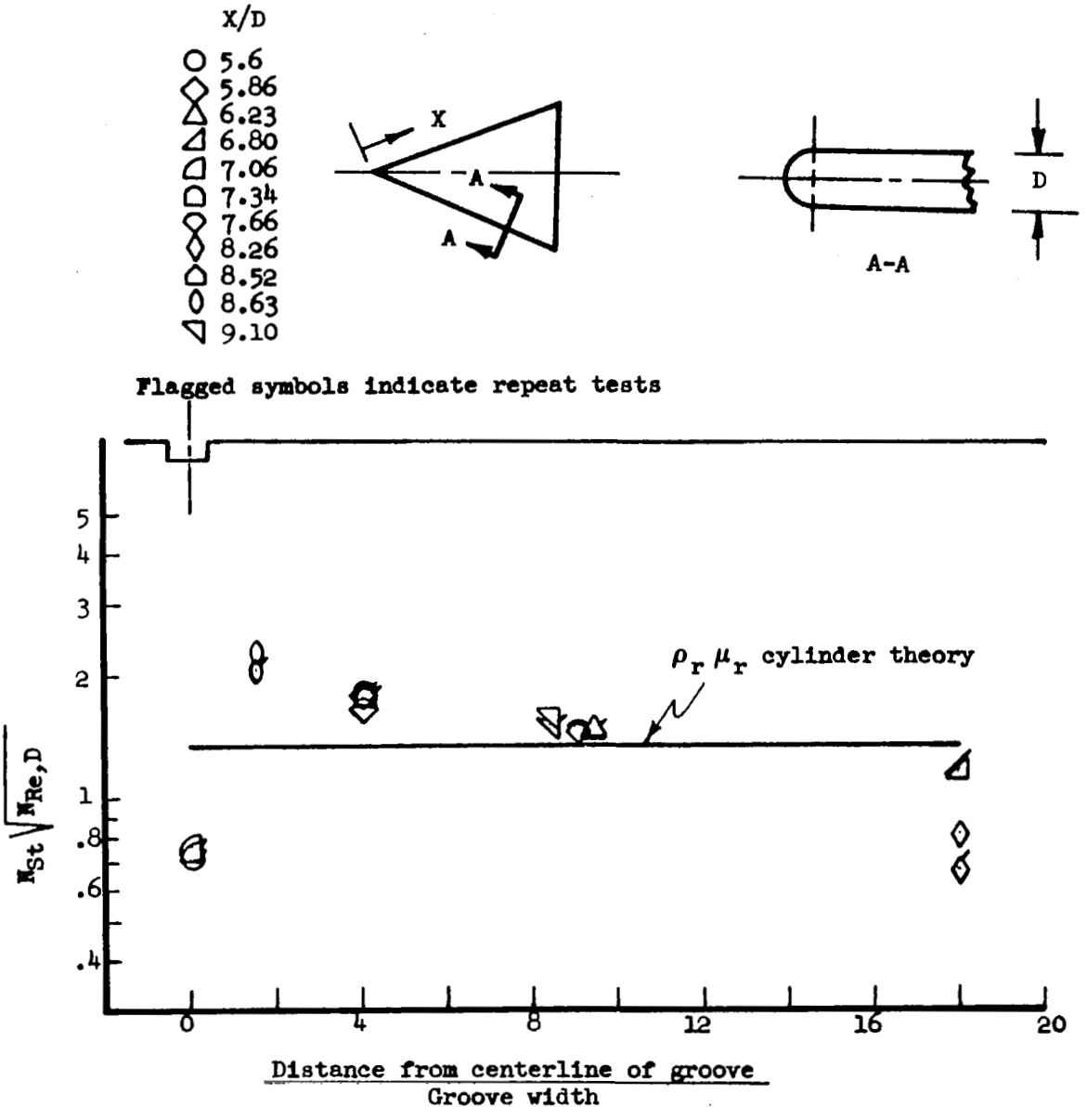

a) Groove open

Figure 40.- Laminar stagnation line heat transfer distribution on a circumferential grooved leading edge. $M_\infty = 8.05$; $P'_o = 2.06$ psia; $H_o = 10.35 \times 10^6$ ft^2/sec^2; $N_{Re,D} = 4.7 \times 10^6$; $\alpha = 0°$; $\psi = 0°$

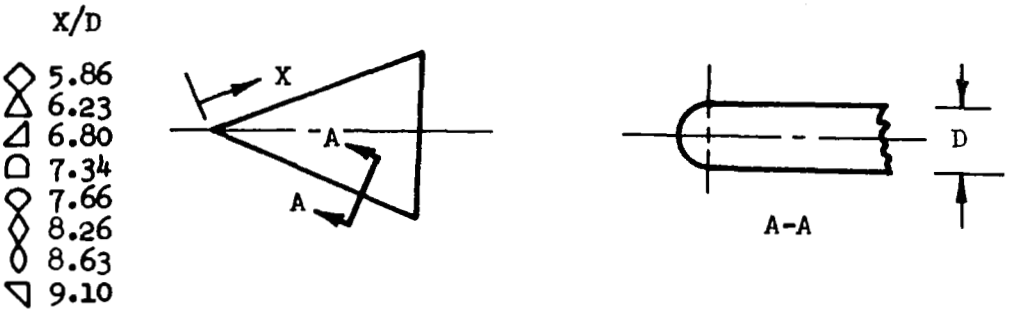

Flagged symbols indicate repeat tests

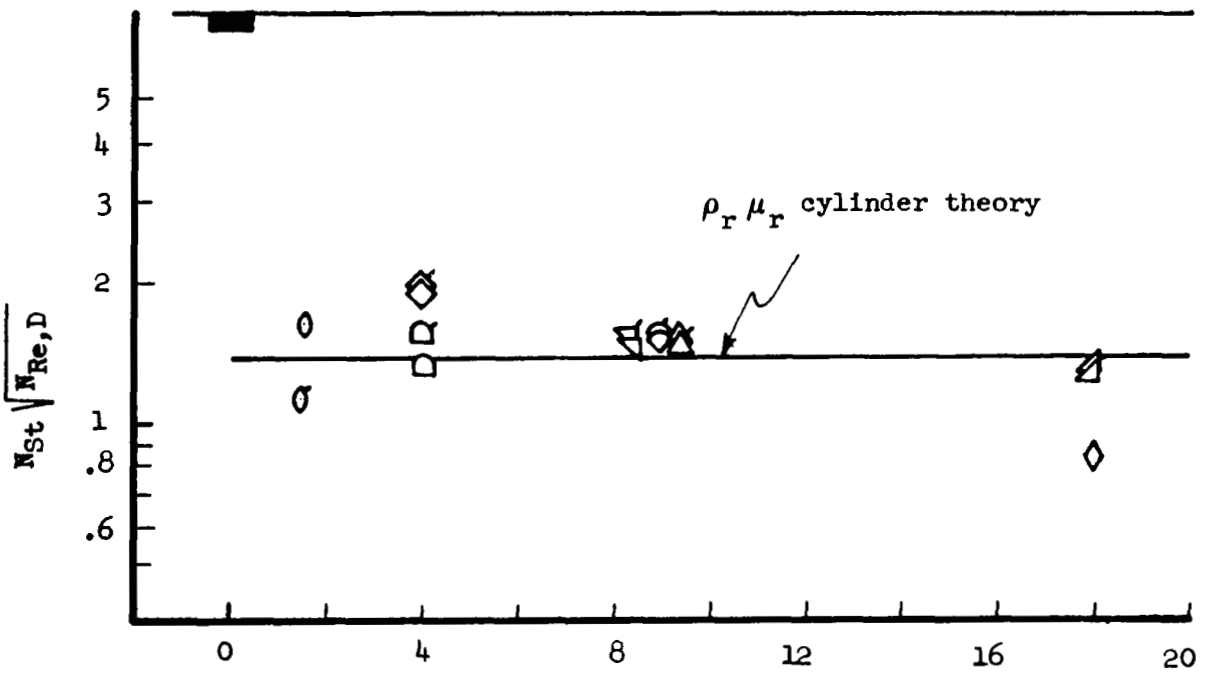

Distance from centerline of groove / Groove width

b) Groove filled with cement

Figure 40.- Concluded.

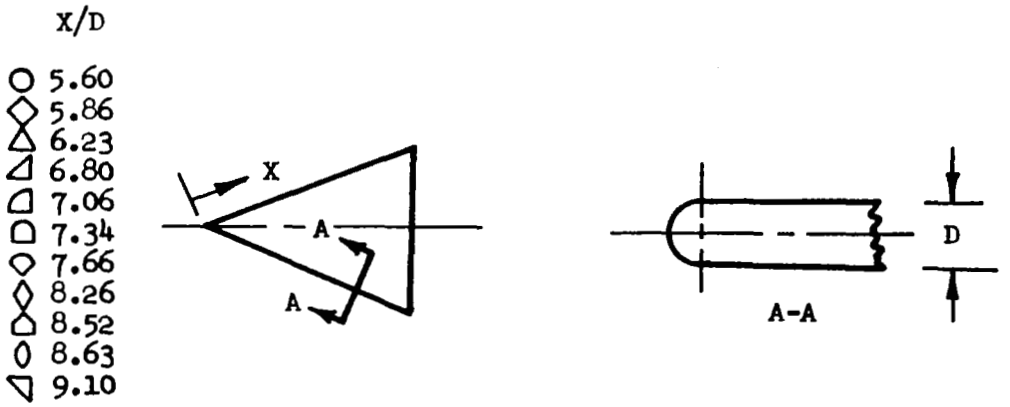

Flagged symbols indicate repeat tests

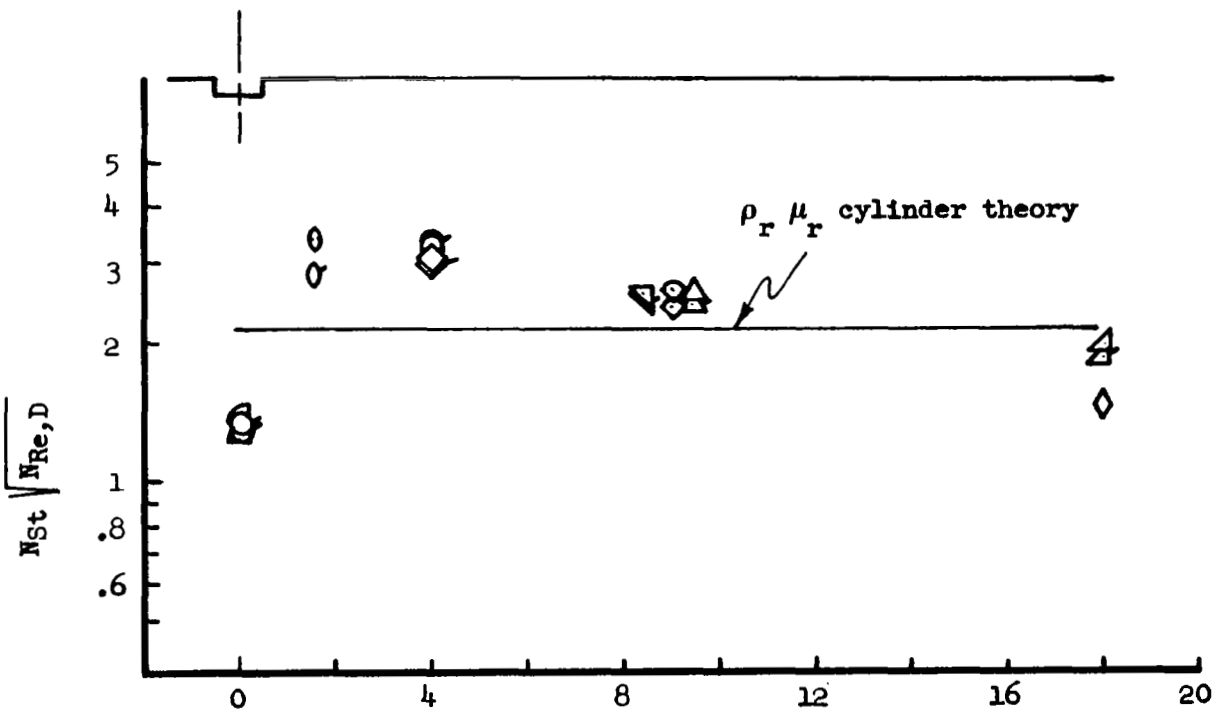

Distance from centerline of groove / Groove width

a) $\alpha = 0°$ $\psi = 10°$

Figure 41.- Laminar stagnation line heat transfer distribution on a circumferential grooved leading edge. $M_\infty = 8.05$; $P'_o = 2.06$ psia; $H_o = 10.35 \times 10^6$ ft^2/sec^2; $N_{Re,L} = 4.7 \times 10^6$.

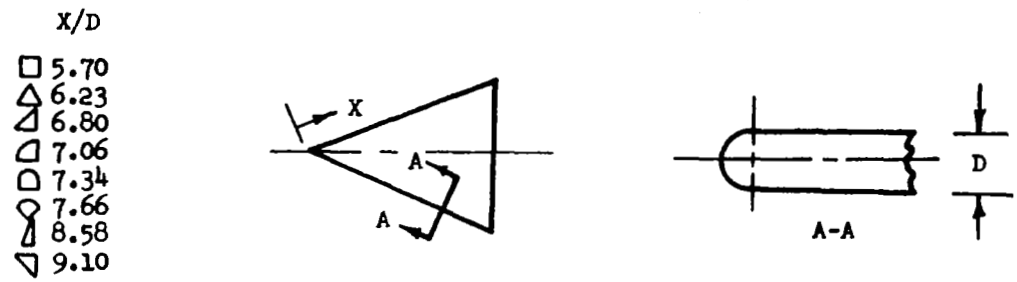

Flagged symbols indicate repeat tests

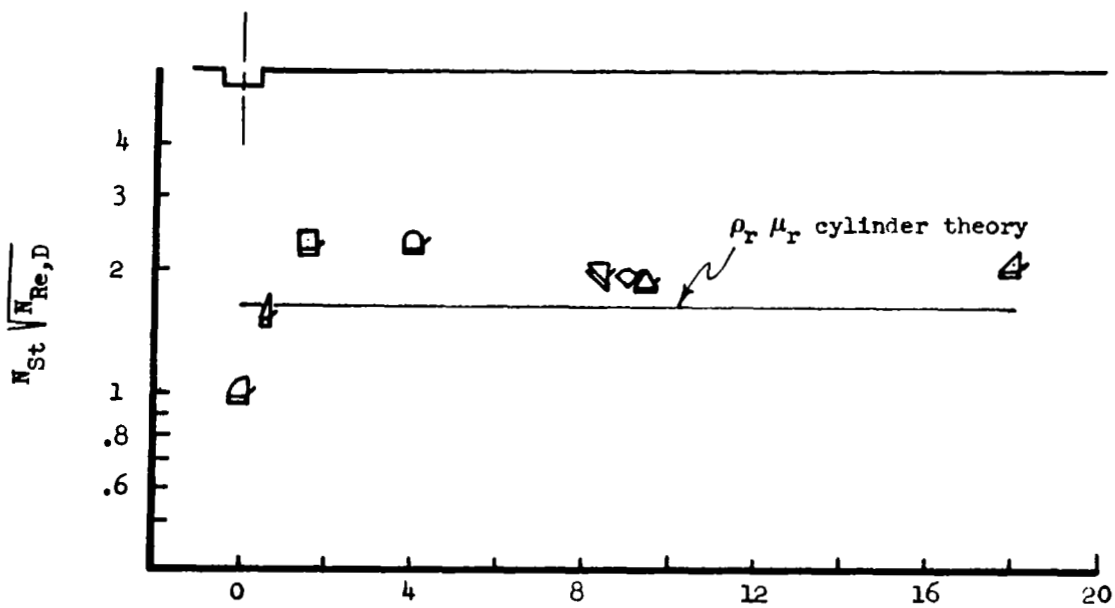

Distance from centerline of groove / Groove width

b) $\alpha = 10°$ $\psi = 0°$

Figure 41.- Concluded.

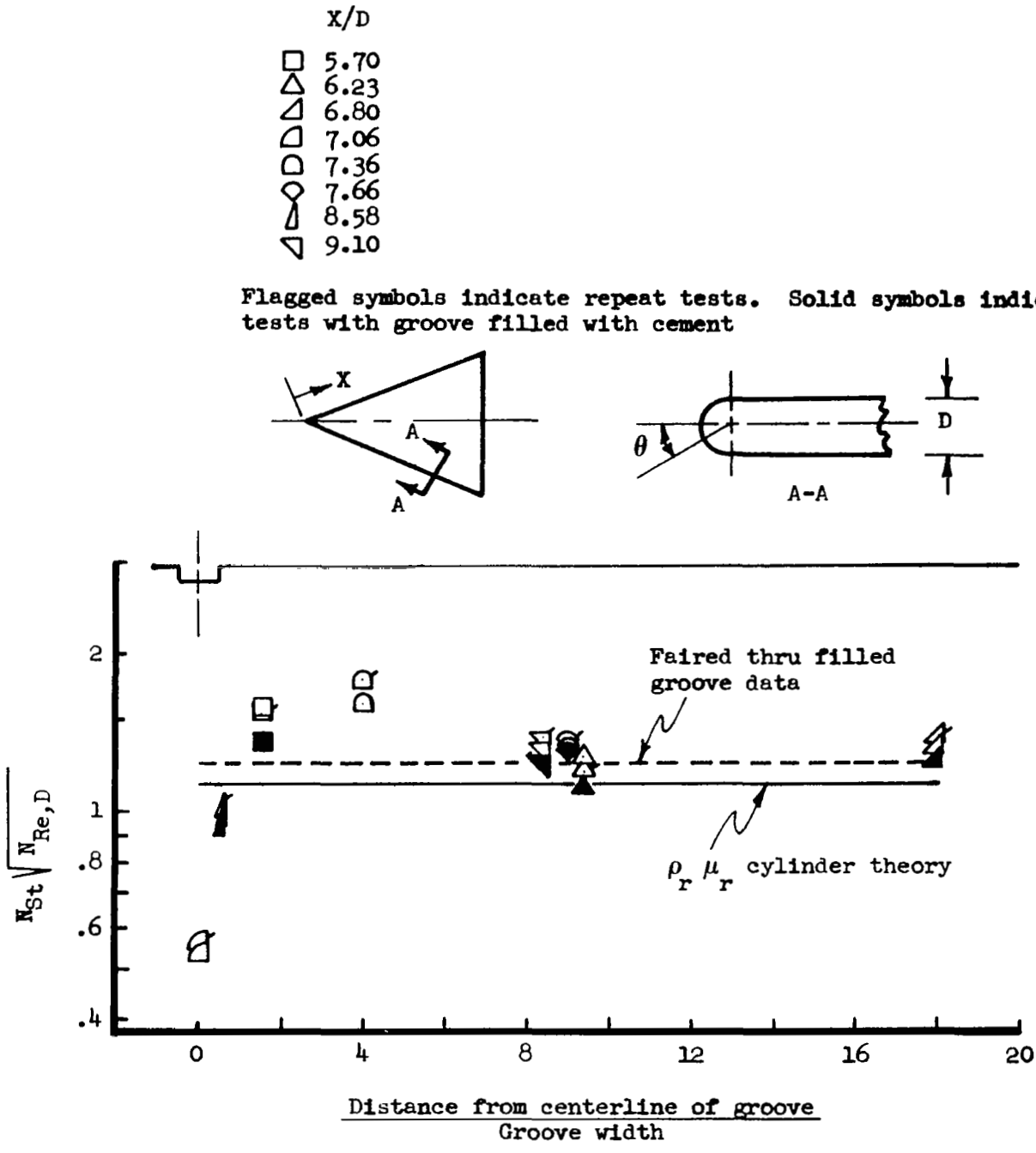

Flagged symbols indicate repeat tests. Solid symbols indicate tests with groove filled with cement

a) $\theta = 30°$

Figure 42.- Laminar heat transfer distribution on a circumferential grooved leading edge. $M_\infty = 8.05$; $P'_o = 2.06$ psia; $N_{Re,D} = 4.7 \times 10^4$, $\alpha = 0°$, $\psi = 0°$.

X/D

□ 5.70
△ 6.23
⌂ 7.06
⌂ 7.34
◇ 7.66
◇ 8.26
⌂ 8.52
▽ 8.80
◁ 9.10

Flagged symbols indicate repeat tests. Solid symbols indicate tests with groove filled with cement.

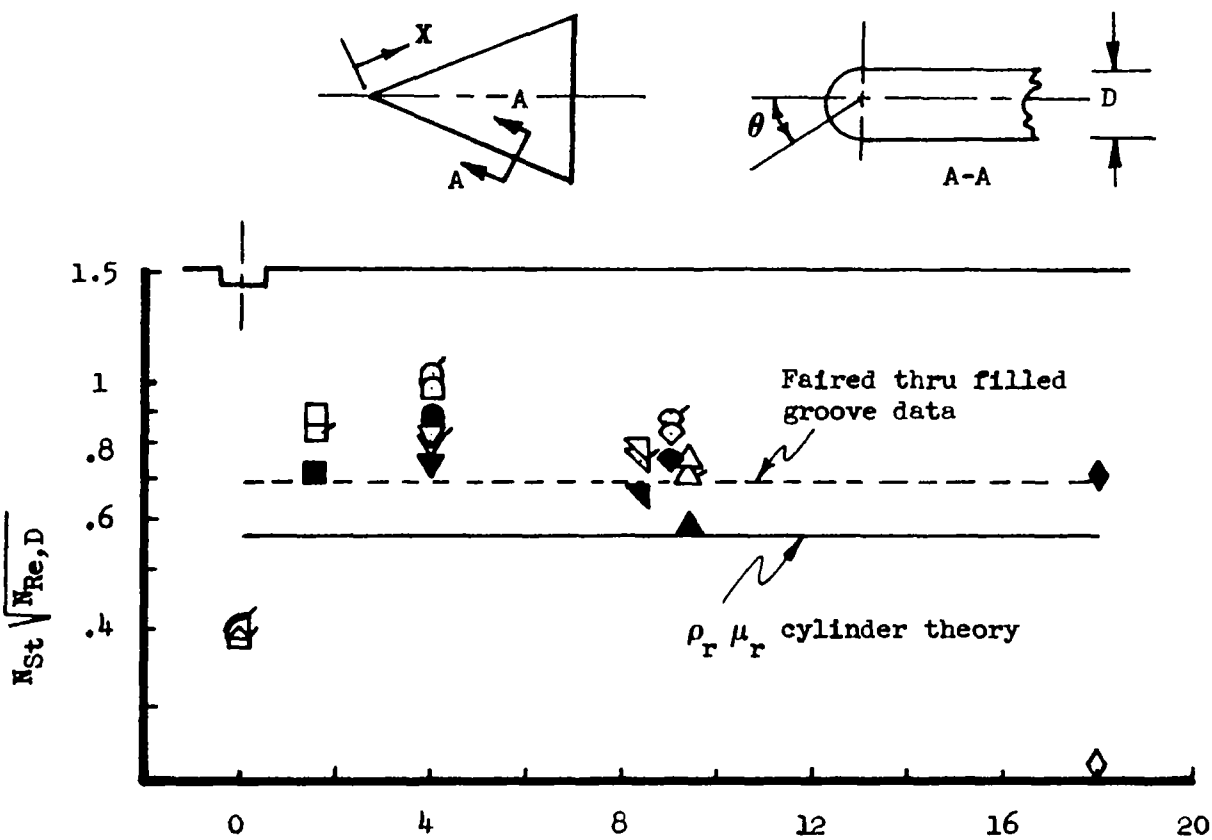

b) θ = 60°

Figure 42.- Concluded

	Test	Model	Groove Type	α	λ Sweep	W/H	M_∞
○	AD 7134-1	Flat plate		0,5,10,15°	70°	8.8	5.9-15.2
◌́	AD 7134-1	" "		0,5,10,15°	70°	8.8	5.9-15.2
□	AD 633	" "		0,5,10°	70°	2.9	6.7-10.1
△	Ref. 4	Cone		0°	0°	5.0	6.5
◇	AD 4654-1	Delta wing stagnation line		0-27°	0°	1.66	3.9-5.3
●	" "	Non stag. line		0-27°	0°	1.66	3.9-5.3
⊐	AD 633	Flat plate		0,5,10°	0°	15.7	6.7-10.1
◺	" "	" "		0,5,10°	0°	11.4	6.7-10.1
⊓	Ref. 1	" "		0°	0°	7.5	2.3-9.6
⊓	" 1	" "		-20°,0°,20°	0°	1.0	2.3-9.6

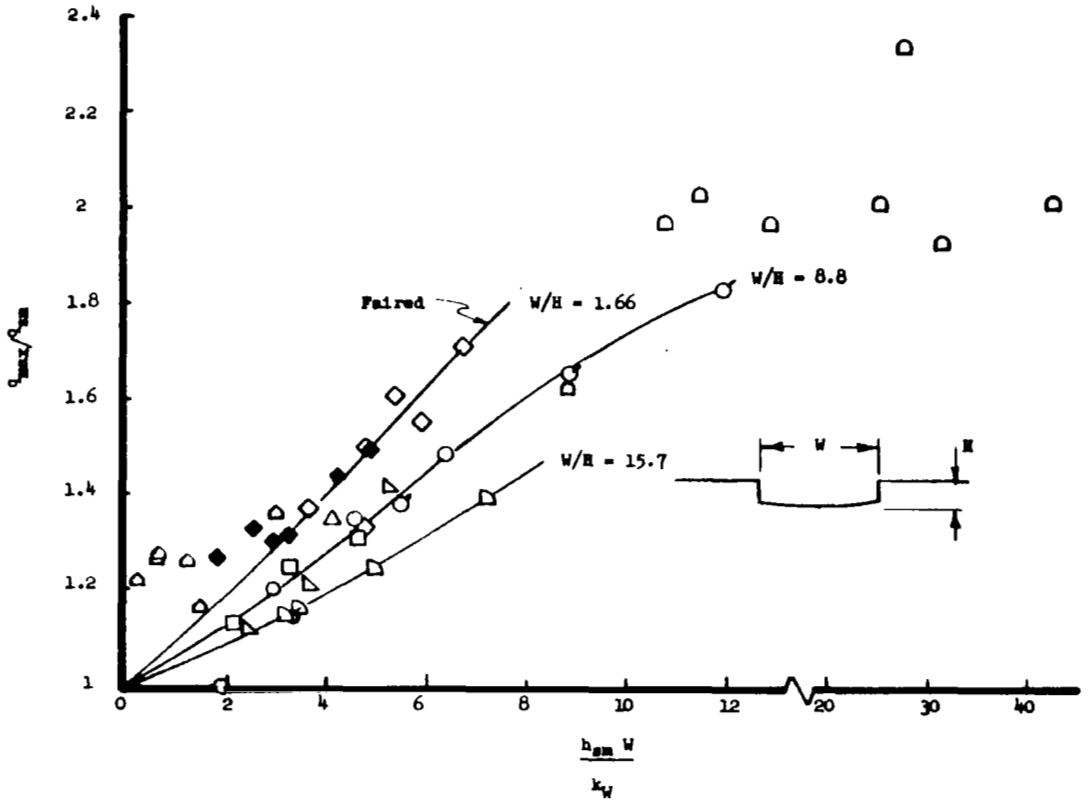

Figure 43.- Correlation of the maximum increase in laminar heating rates caused by grooves.

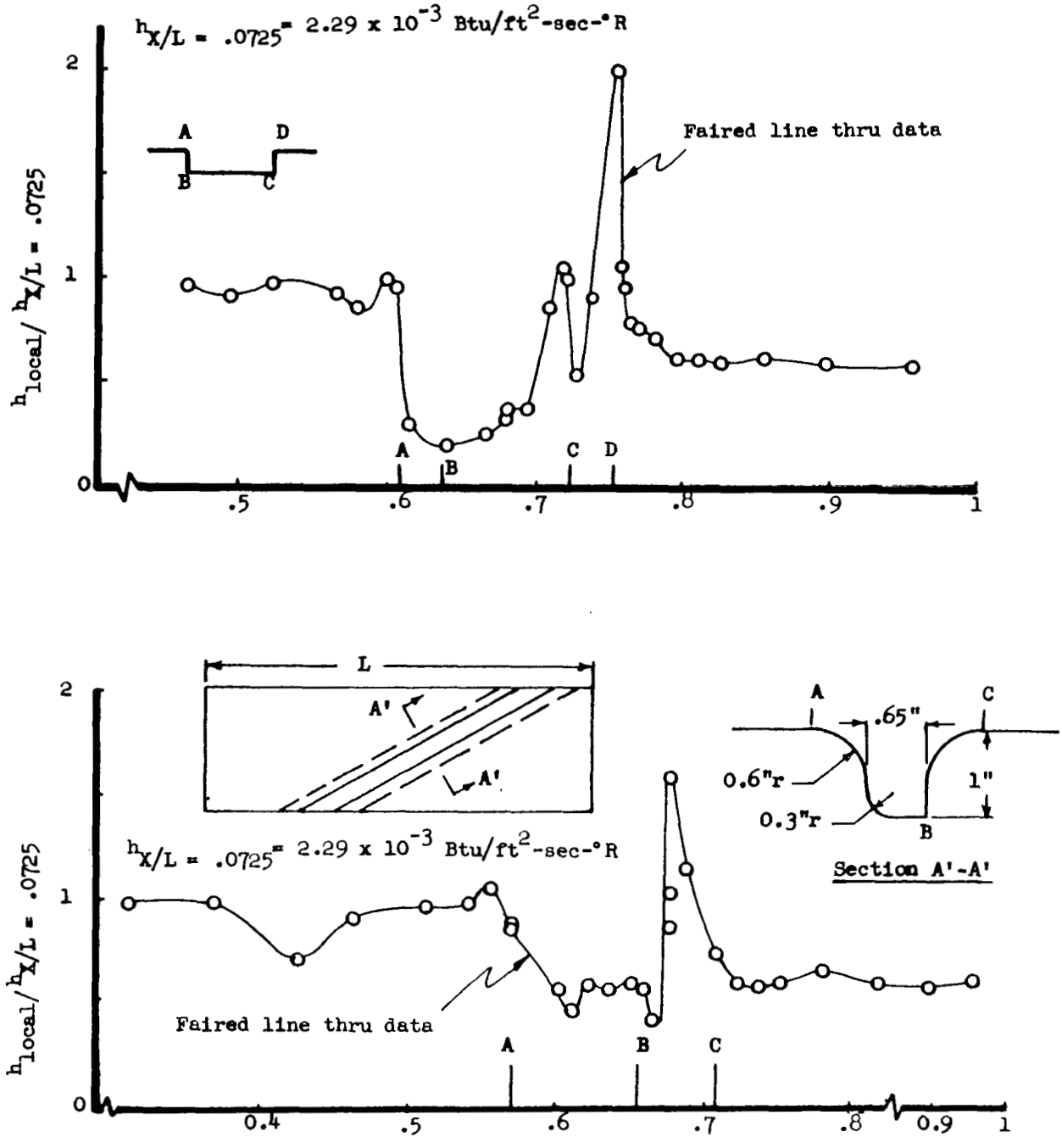

Figure 44.- Turbulent heat transfer distributions on two grooved panels mounted in tunnel wall. $M_\infty = 6.95$; $P_o' = 174$ psia; $H_o = 9.12 \times 10^6$ ft^2/sec^2; $N_{Re,\delta} = 9.85 \times 10^6$.

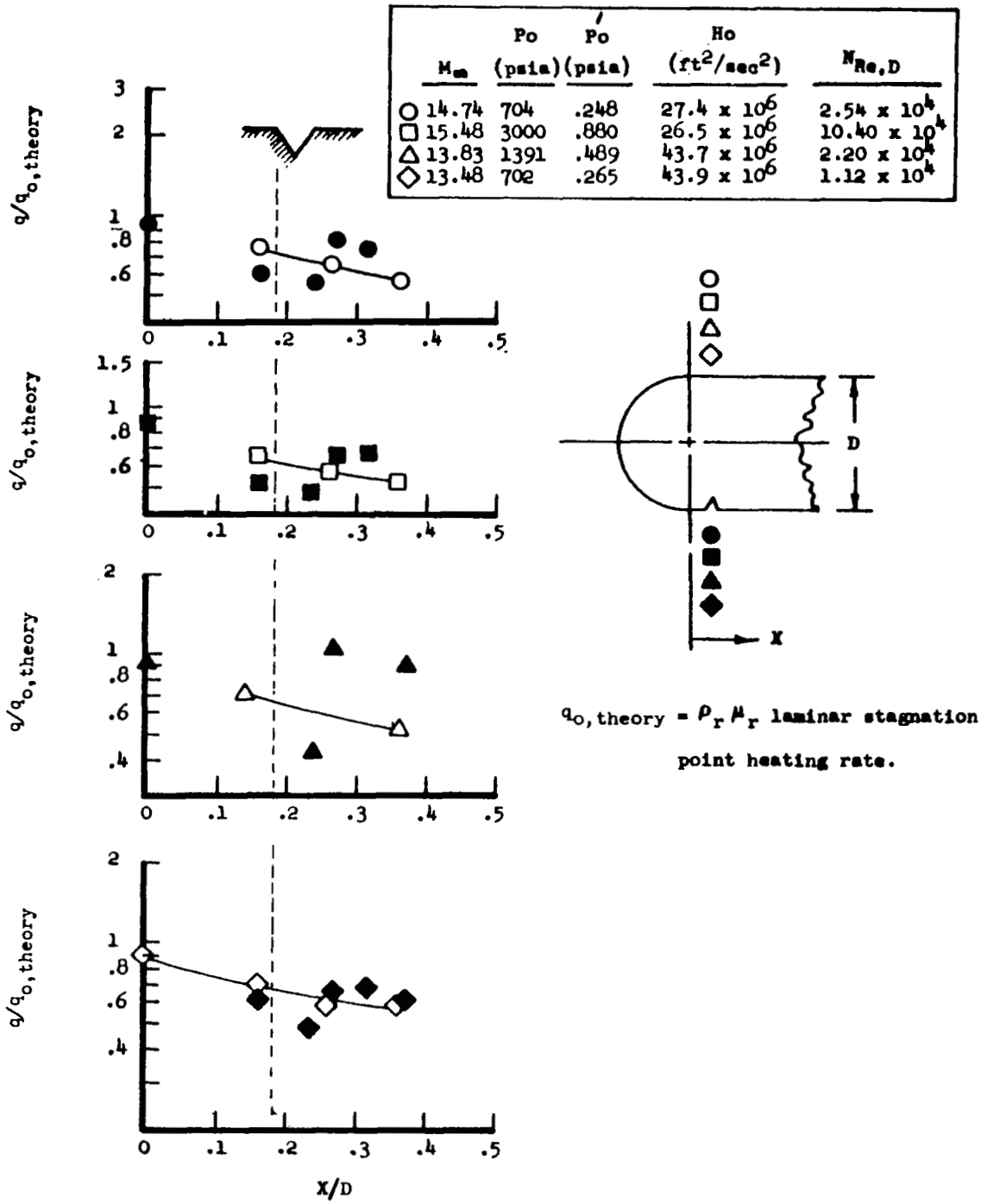

Figure 45.- Effect of a V-groove aft of the shoulder of a hemisphere-cylinder on laminar heating rates. $\alpha = 0°$

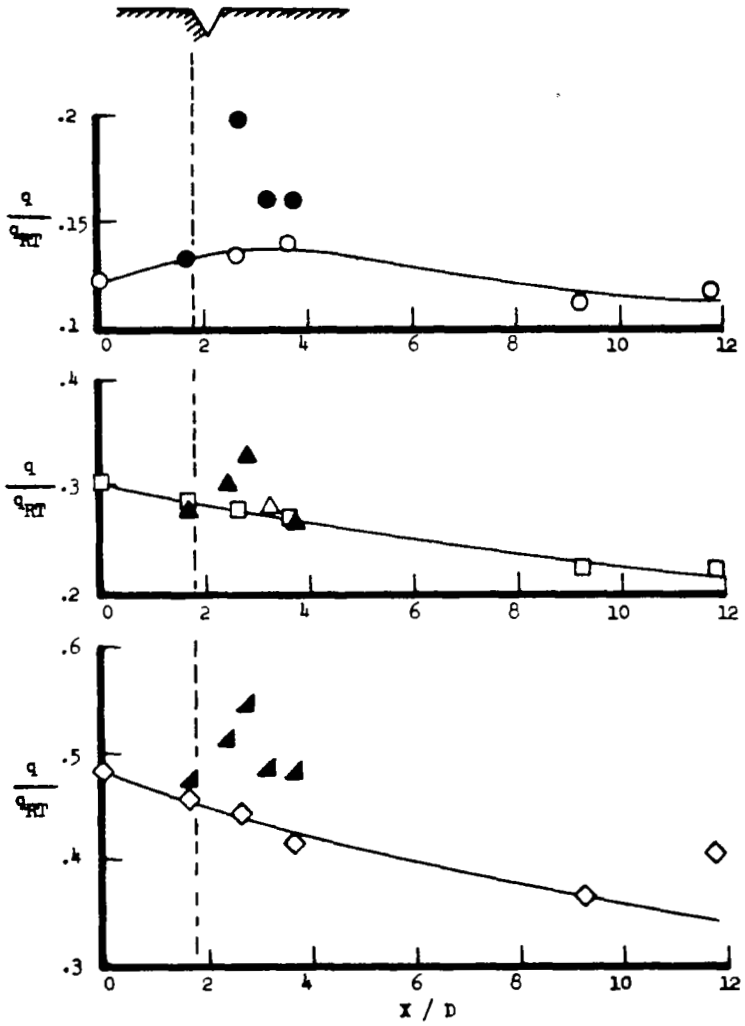

	α	M_∞	P_o psia	P_o' psia	H_o ft²/sec²	$R_{Re,D}$	Note
○ ●	0°	5.61	3810	77.9	44.8×10^6	$.92\times10^6$	
□	10°	6.38	3820	88.0	13.6×10^6	5.86×10^6	
▲	10°	6.38	3720	86.0	13.4×10^6	5.70×10^6	Model rolled 180°
◇	20°	6.38	3869	89.5	13.5×10^6	5.86×10^6	
◢	20°	6.38	3758	86.9	13.4×10^6	5.76×10^6	Model rolled 180°

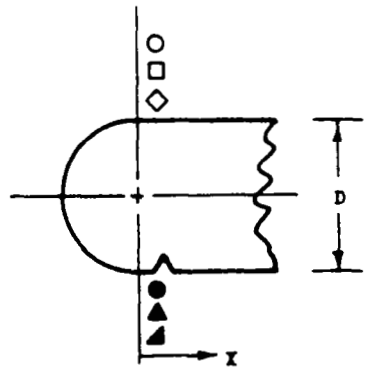

q_{RT} = Turbulent ρ_r μ_r reference heating rate on a 60° swept leading edge.

Figure 46.- Effect of V-groove aft of the shoulder of a hemisphere cylinder on turbulent heating rates.

	α (deg)	M_∞	P_o (psia)	P_o' (psia)	Ho (ft^2/sec^2)	$N_{Re,D}$
			Laminar flow			
○	0	13.5	702	.265	27.4×10^6	1.12×10^4
□	0	13.8	1391	.489	26.5×10^6	2.21×10^4
△	0	15.5	3000	.880	43.7×10^6	10.4×10^4
◇	0	14.7	704	.248	43.9×10^6	2.54×10^4
◺	20	14.8	675	.238	26.7×10^6	2.53×10^4
◺	50	15.1	1360	.435	26.6×10^6	4.84×10^4
			Turbulent flow			
●	0	6.4	3720	86.1	13.1×10^6	5.85×10^6
■	0	5.6	3810	77.9	44.8×10^6	0.92×10^6
▲	10	6.4	3820	88.0	13.6×10^6	5.66×10^6
◆	20	6.4	3870	89.5	13.5×10^6	5.84×10^6

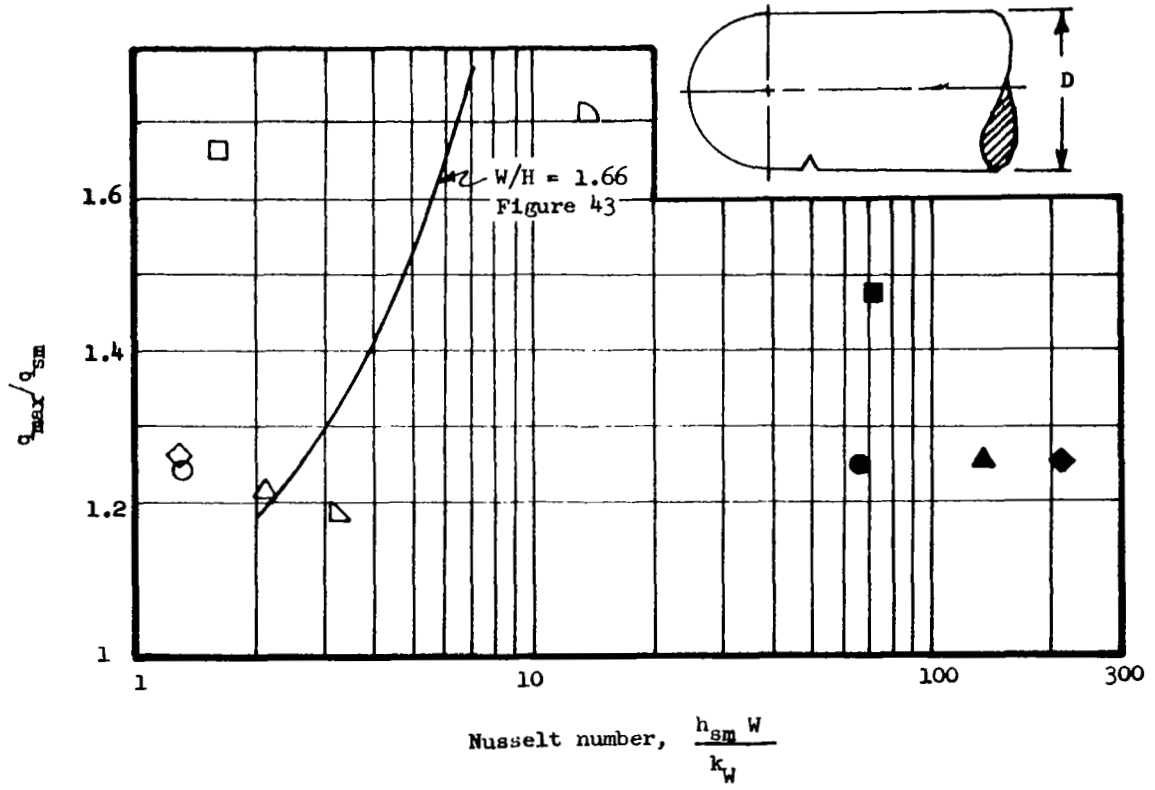

Figure 47.- Maximum increase due to a V-groove downstream of the shoulder of a hemisphere cylinder

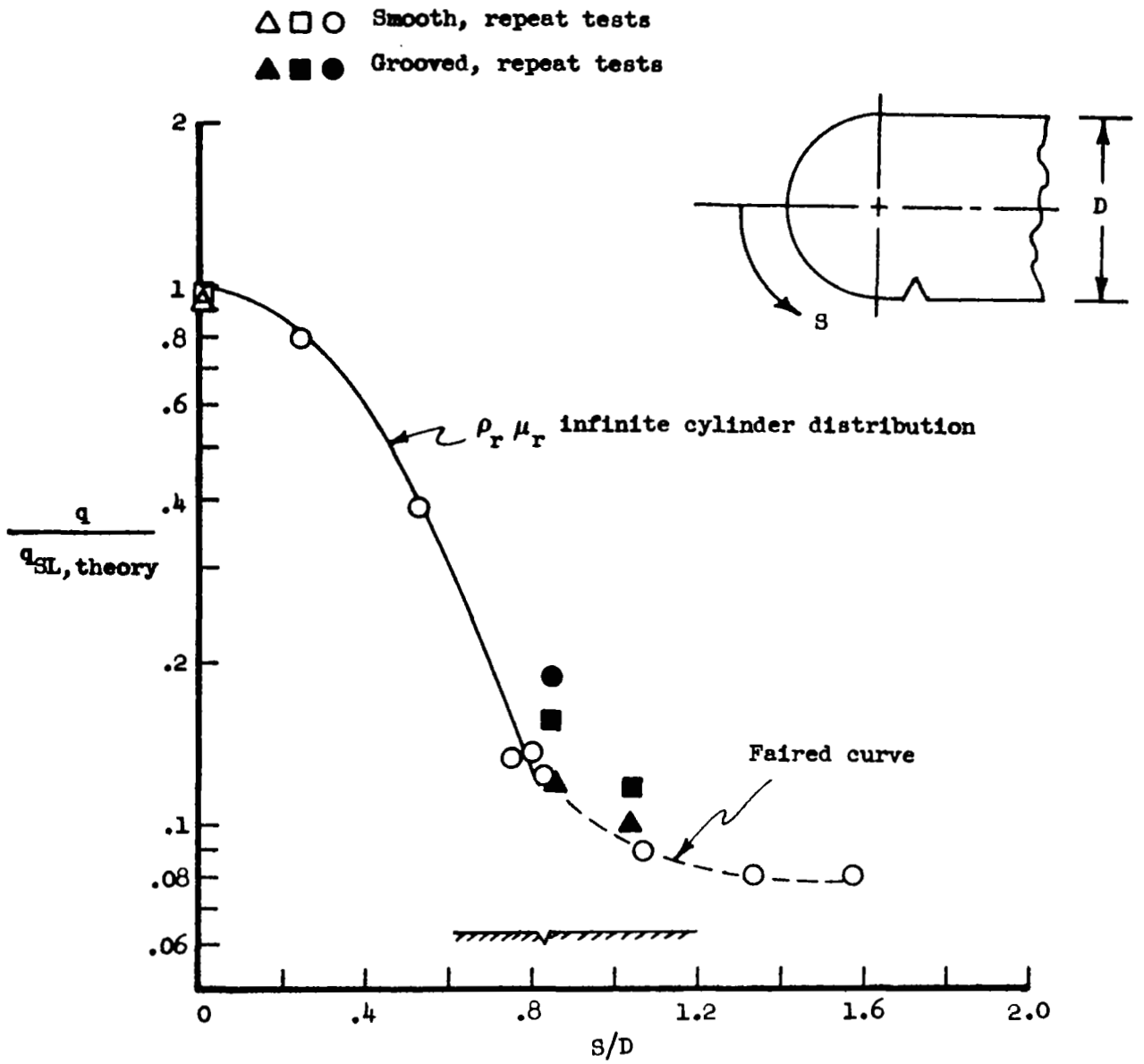

a) Λ = 55°; M_∞ = 15.18; P_o = 1410 psia; P_o' = .4487 psia; H_o = 26.1 x 10^6 ft^2/sec^2; $N_{Re,D}$ = 4.1 x 10^4

Figure 48.- Laminar heat transfer distribution due to a V-groove aft of the shoulder of a swept leading edge model. α = 0°.

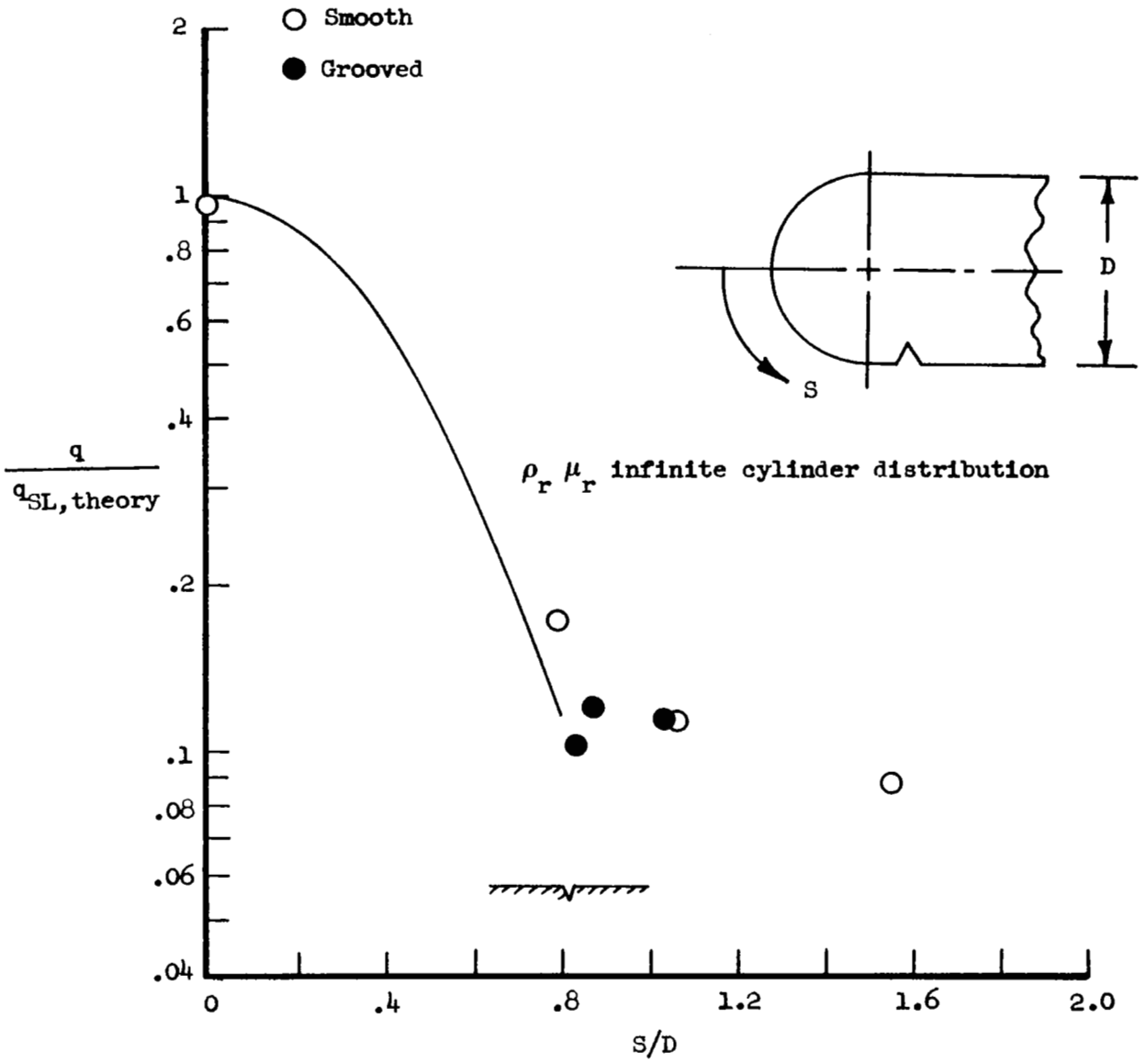

b) Λ = 60°; M_∞ = 15.13; P_o = 1262 psia; P_o' = .4053 psia; H_o = 26.2 ft^2/sec^2; $N_{Re,D}$ = 3.7 x 10^4

Figure 48.- Continued.

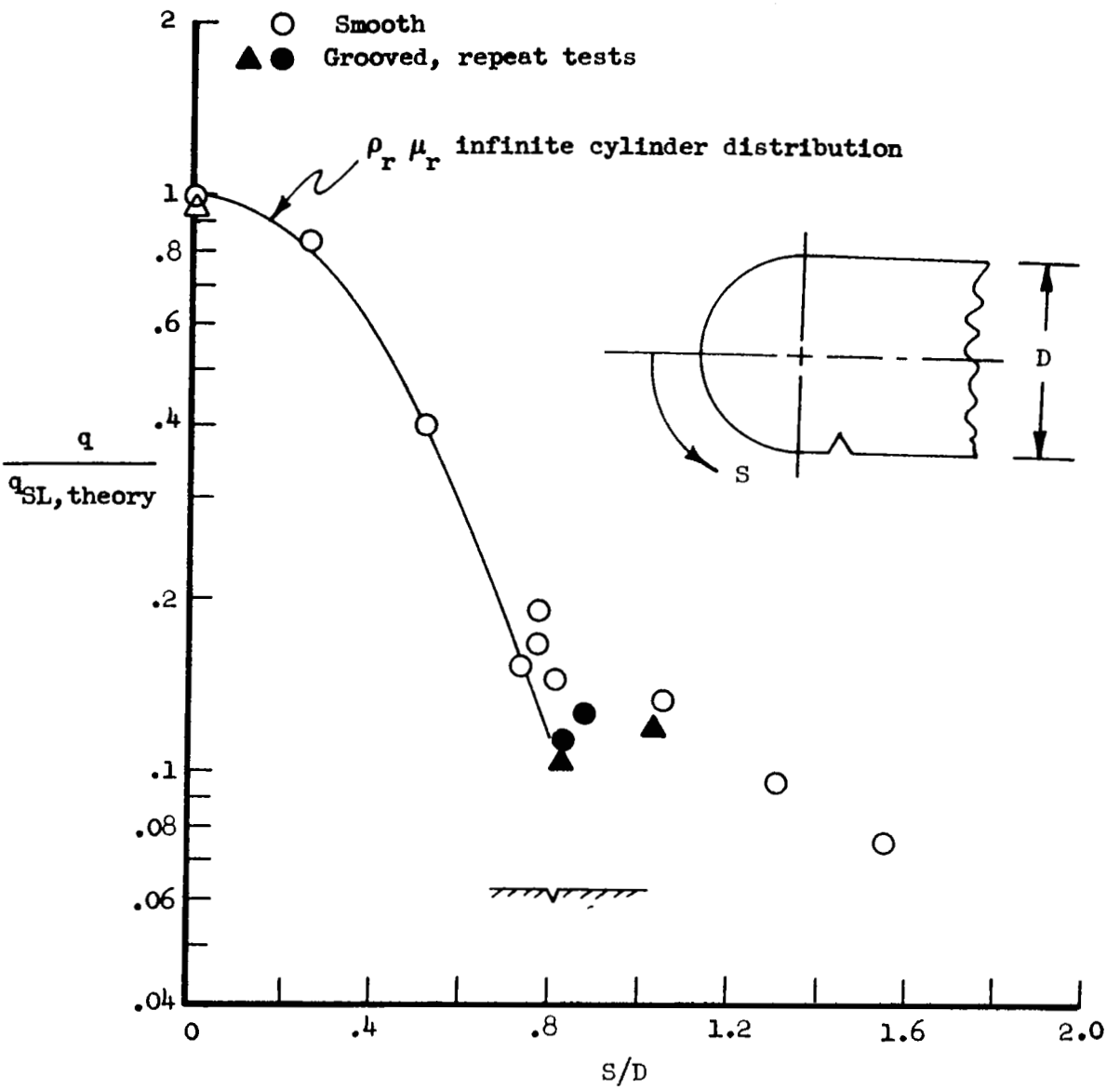

c) Λ = 65°; M_∞ = 15.18; P_o = 1390 psia; P_∞ = .441 psia; H_o = 26.2 ft^2/sec^2; $N_{Re,D}$ = 4.06×10^4

Figure 48.- Concluded.

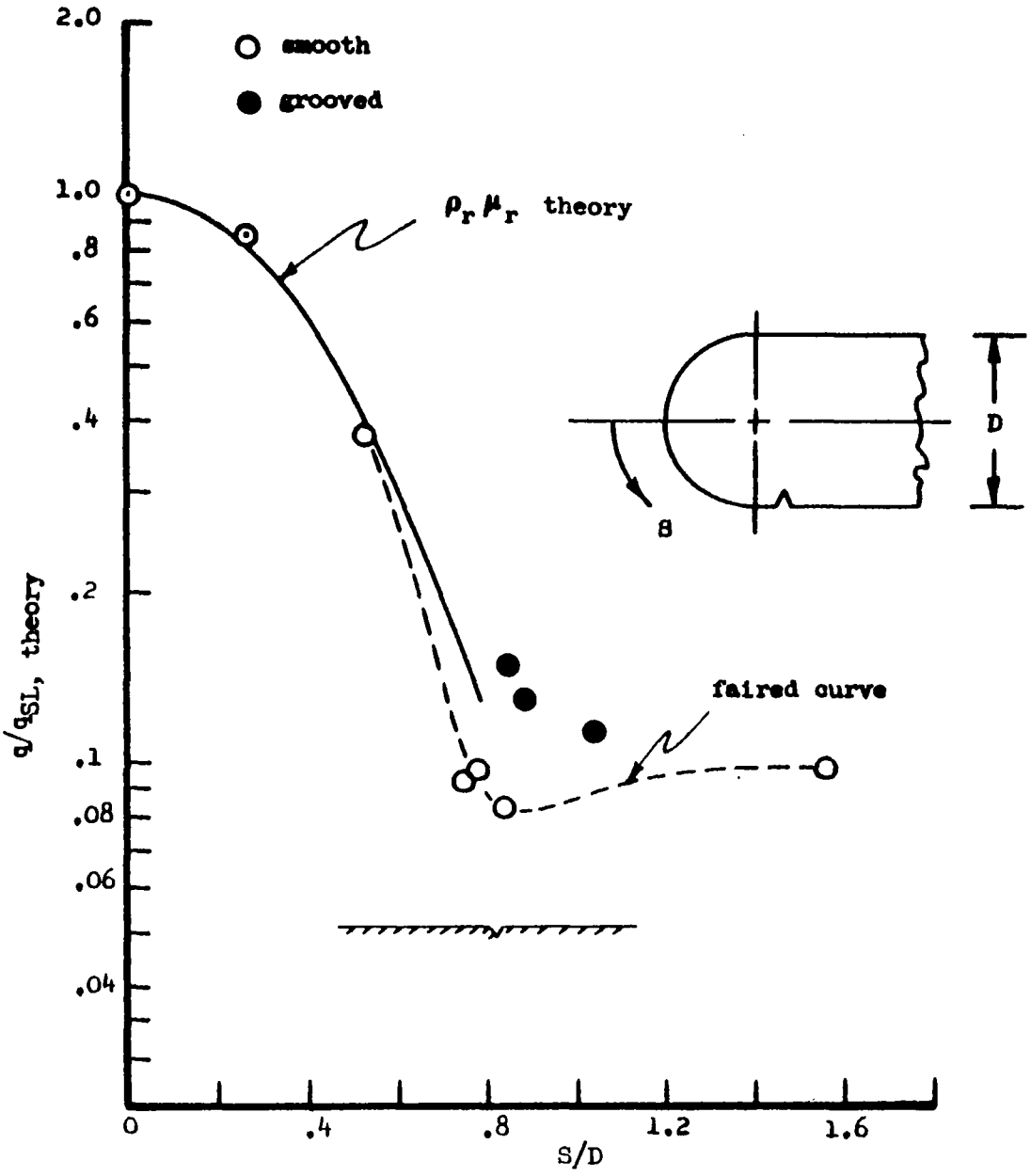

a) $\Lambda = 55°$; $M_\infty = 5.6$; $P_o = 3462$ psia; $P'_o = 70.7$ psia;
$H_o = 45.1 \times 10^6$ ft^2/sec^2; $N_{Re,D} = 6.66 \times 10^6$.

Figure 49.- Turbulent heat transfer distribution due to a V-groove aft of the shoulder of a swept leading edge model.

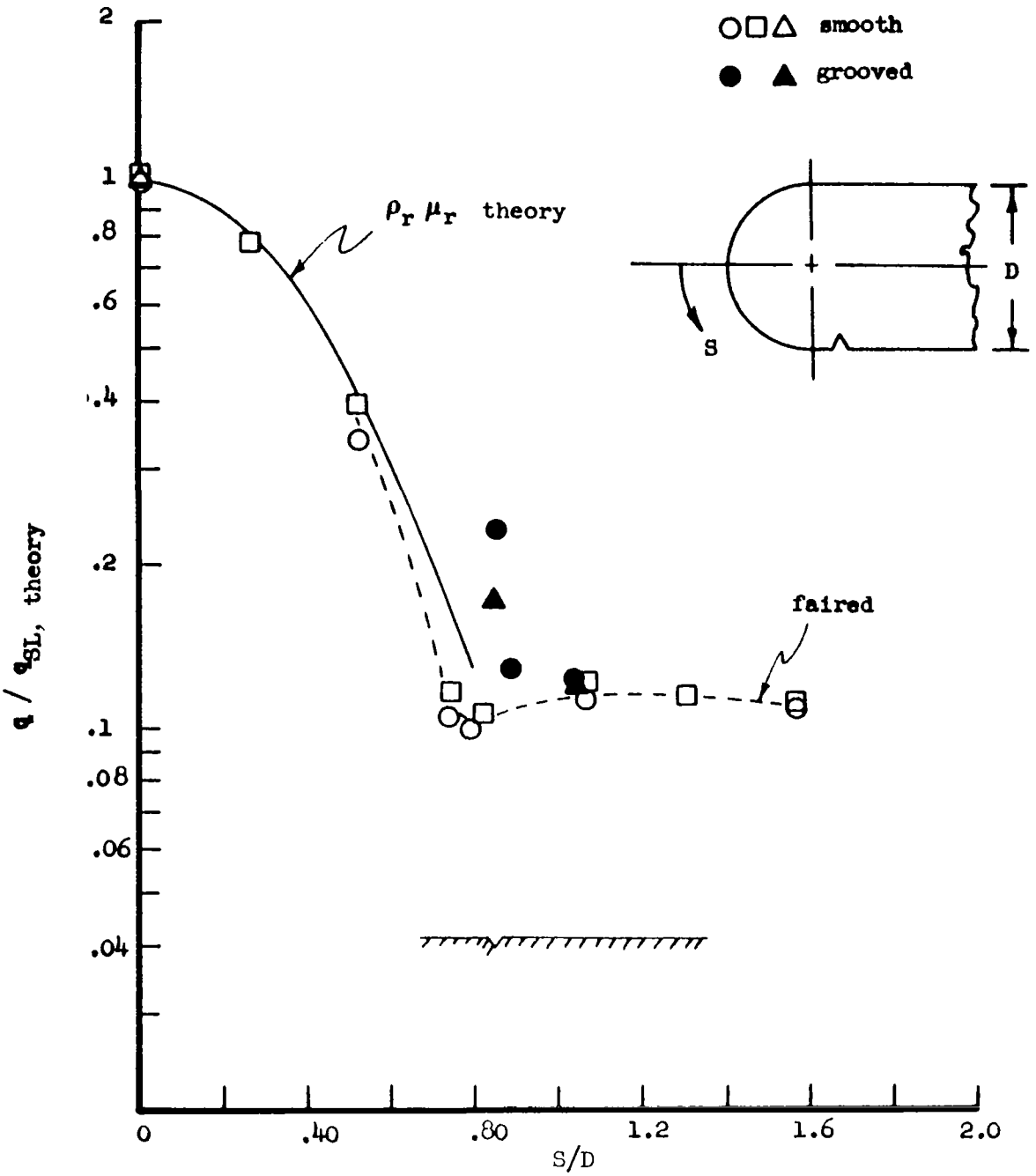

b) $\Lambda = 60°$; $M_\infty = 7.72$; $P'_o = 38.9$ psia, $H_o = 13.6 \times 10^6$ ft^2/sec^2; $N_{Re,D} = 2.77 \times 10^6$.

Figure 49.- Continued

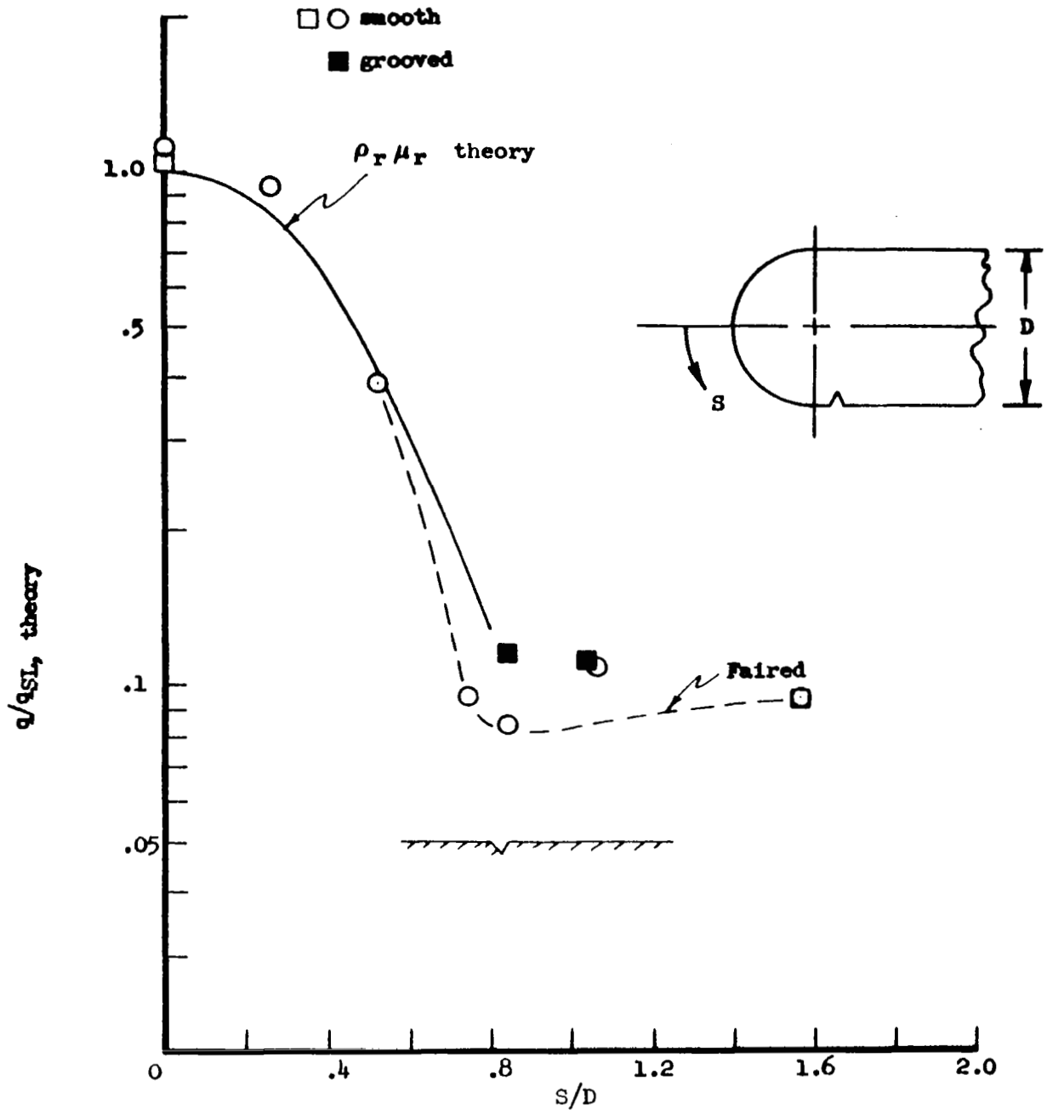

c) $\Lambda = 65°$; $M_\infty = 6.18$; $P_o = 3740$ psia; $P'_o = .85$ psia;
$H_o = 20.8 \times 10^6$ ft^2/sec^2; $N_{Re,D} = 2.38 \times 10^6$.

Figure 49.- Concluded

Λ Deg	M_∞	P_o Psia	P_o' Psia	H_o ft²/sec²	$N_{Re,D}$	W/H
			Laminar Flow			
● 55°	15.2	1380	.439	26.2 x 10^6	4.03x10^4	2.0
			Turbulent Flow			
○ 55°	7.72	3840	38.7	13.4 x 10^6	2.78x10^6	2.0
♂	6.30	3670	84.3	16.4 x 10^6	3.3x10^6	
♂	6.82	3640	33.5	44.2 x 10^6	4.05x10^5	
⊖	5.60	3460	70.7	45.1 x 10^6	6.66x10^5	
□ 60°	7.72	3870	38.6	13.5 x 10^6	2.76x10^6	2.3
□	6.18	3850	87.9	21.1 x 10^6	2.36x10^6	
△ 65°	6.38	3740	86.6	13.4 x 10^6	4.65x10^6	2.73
△	6.18	3731	84.9	20.8 x 10^6	2.38x10^6	
△	5.93	3580	78.8	30.6 x 10^6	1.27x10^6	

– – – – – Repeat tests

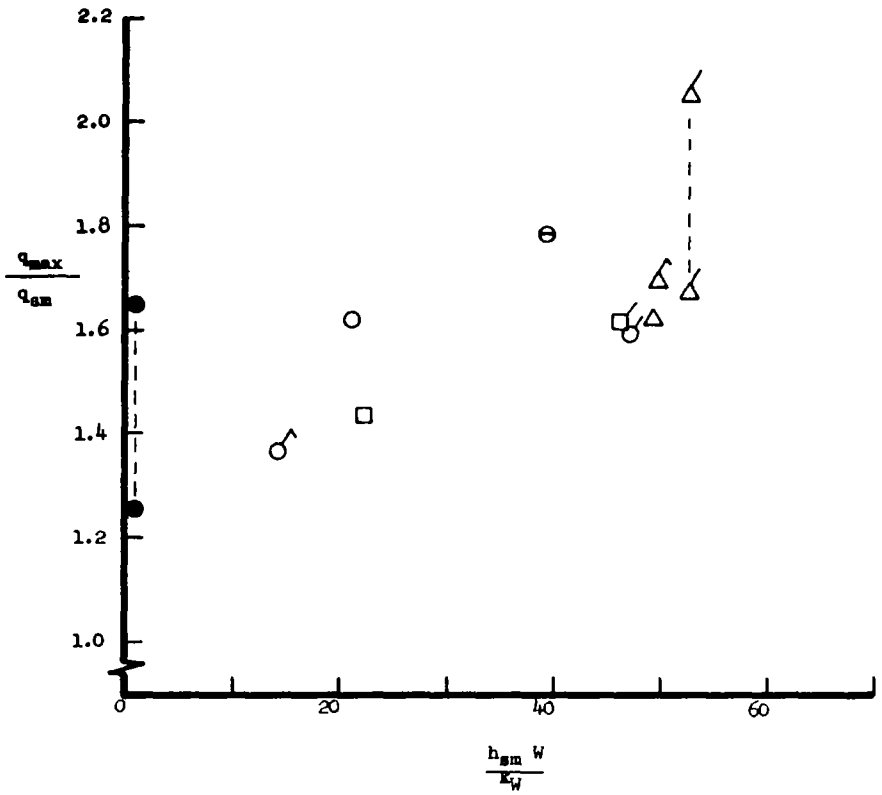

Figure 50.- Correlation of heating rate increase due to a V-groove located at the shoulder of a swept leading edge model. α = 0°.

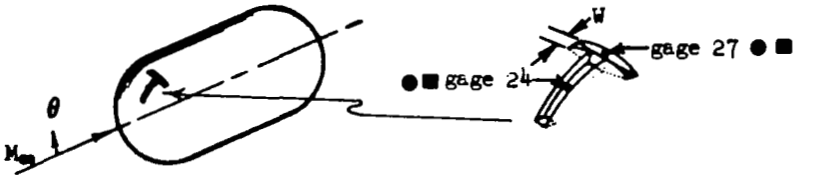

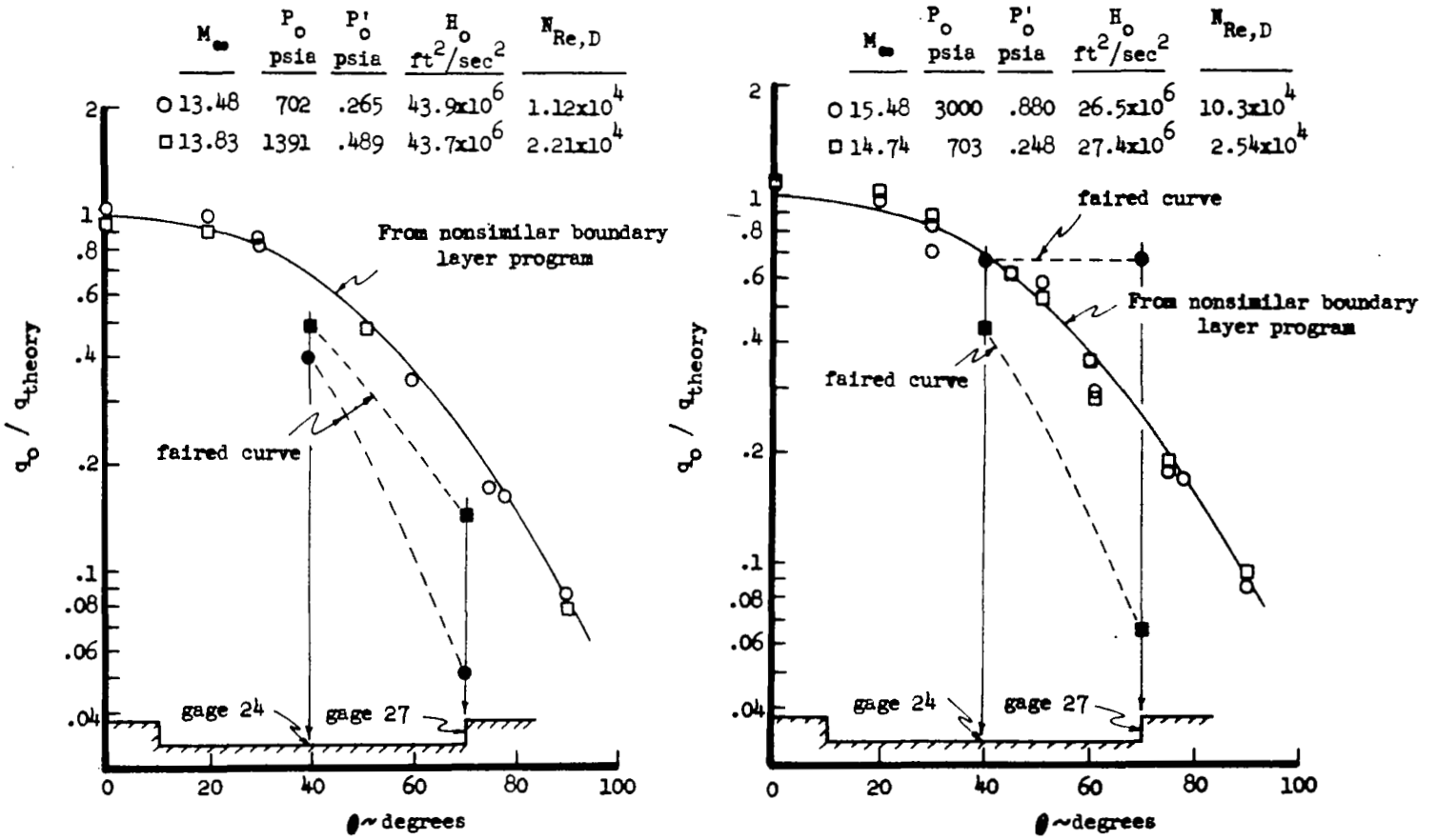

Figure 51.- T-groove laminar heat transfer distribution. $\alpha = 0°$

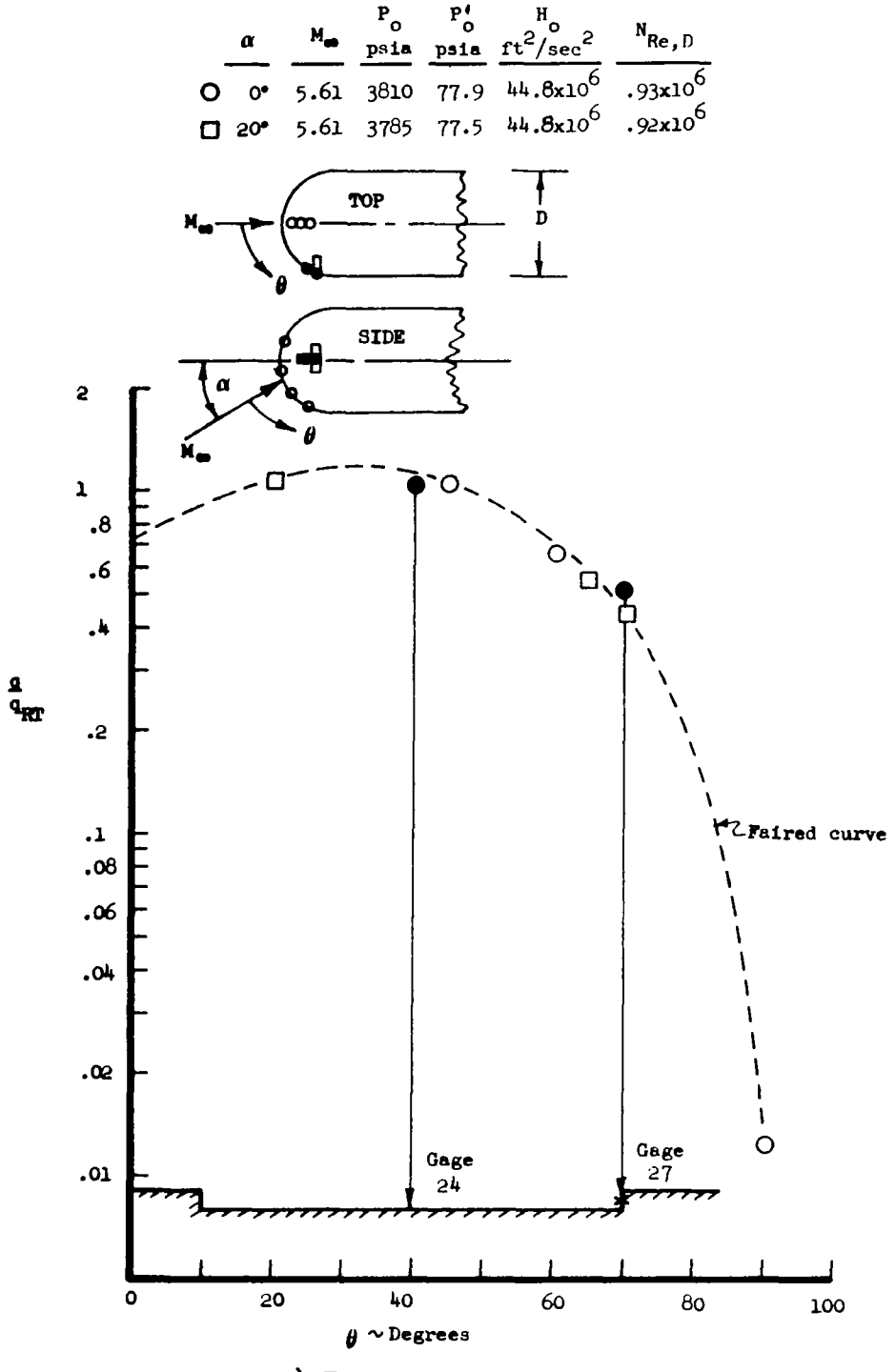

a) Turbulent flow

Figure 52.- T-groove heat transfer distributions.

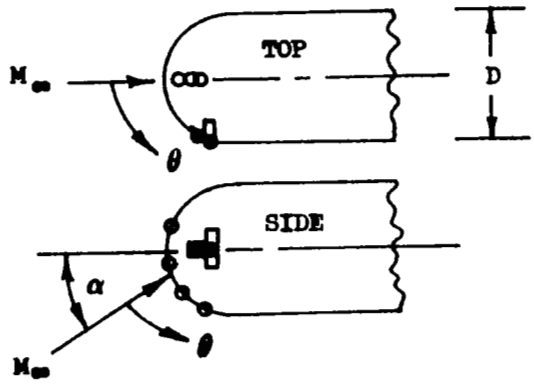

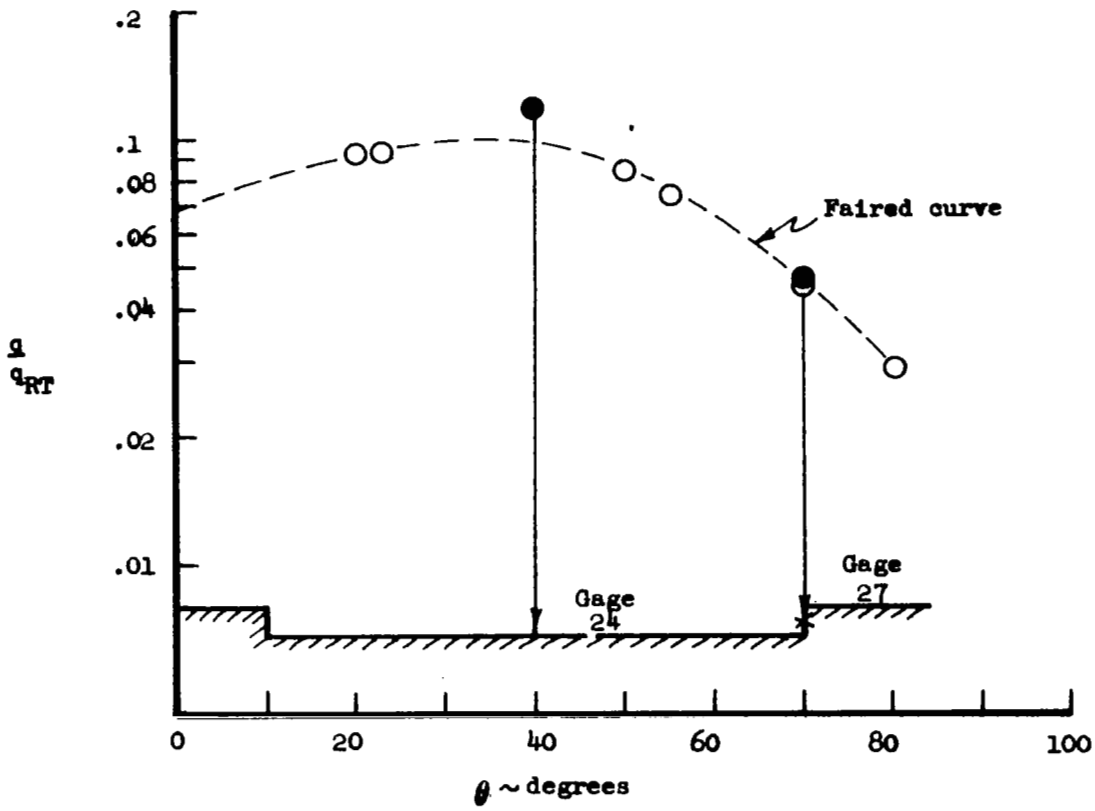

b) Turbulent flow. $\alpha = 20°$, $M_\infty = 5.95$; $P_o = 3645$ psia; $P_o' = 82.4$ psia; $H_o = 29.6 \times 10^6$ ft^2/sec^2/ $N_{Re,D} = 1.74 \times 10^6$.

Figure 52.- Concluded.

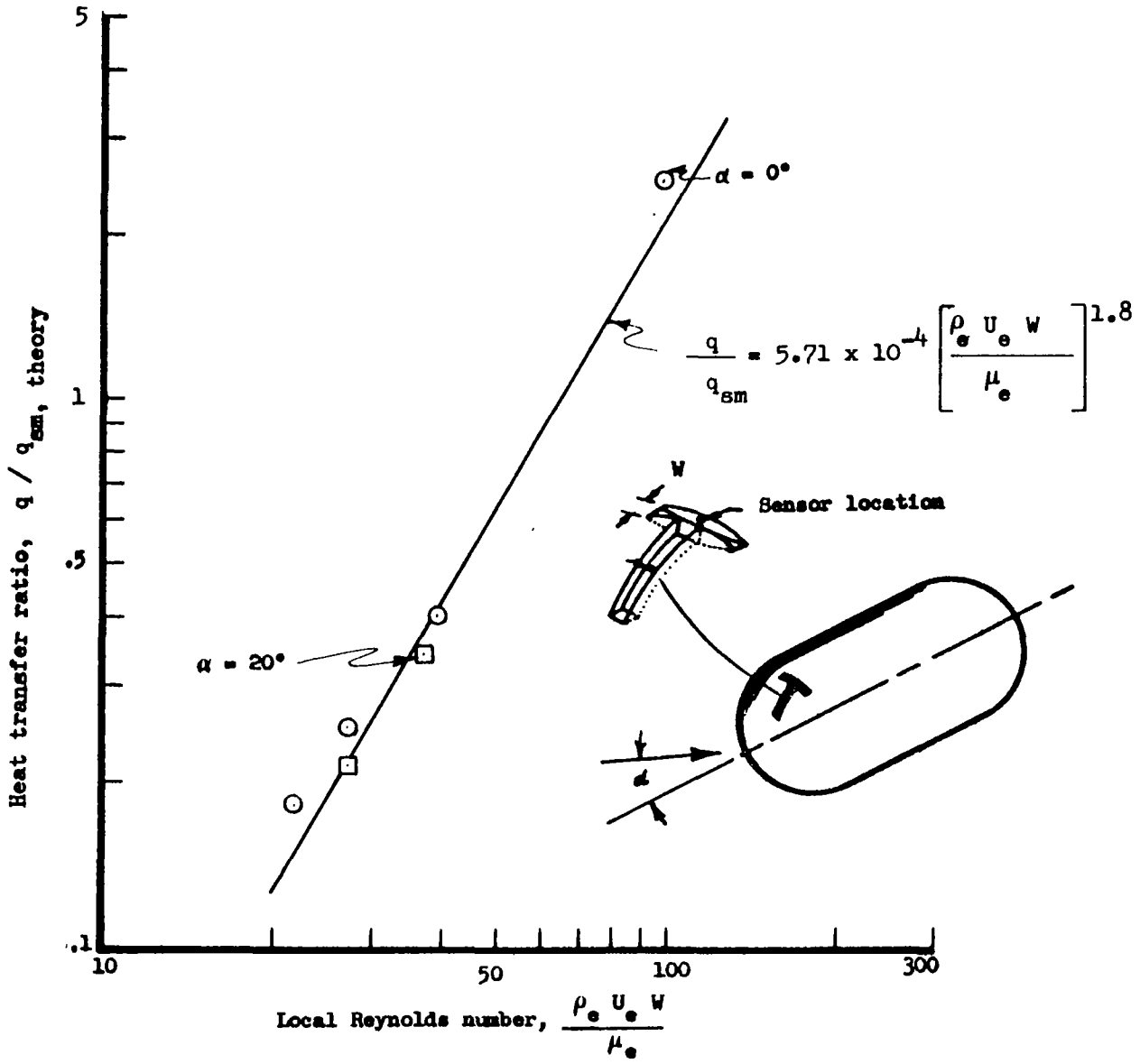

Figure 53.- Correlation of laminar heat transfer at the intersection of a "T" slot on a hemisphere nose. - M_∞ = 15, W = 0.032 inches.

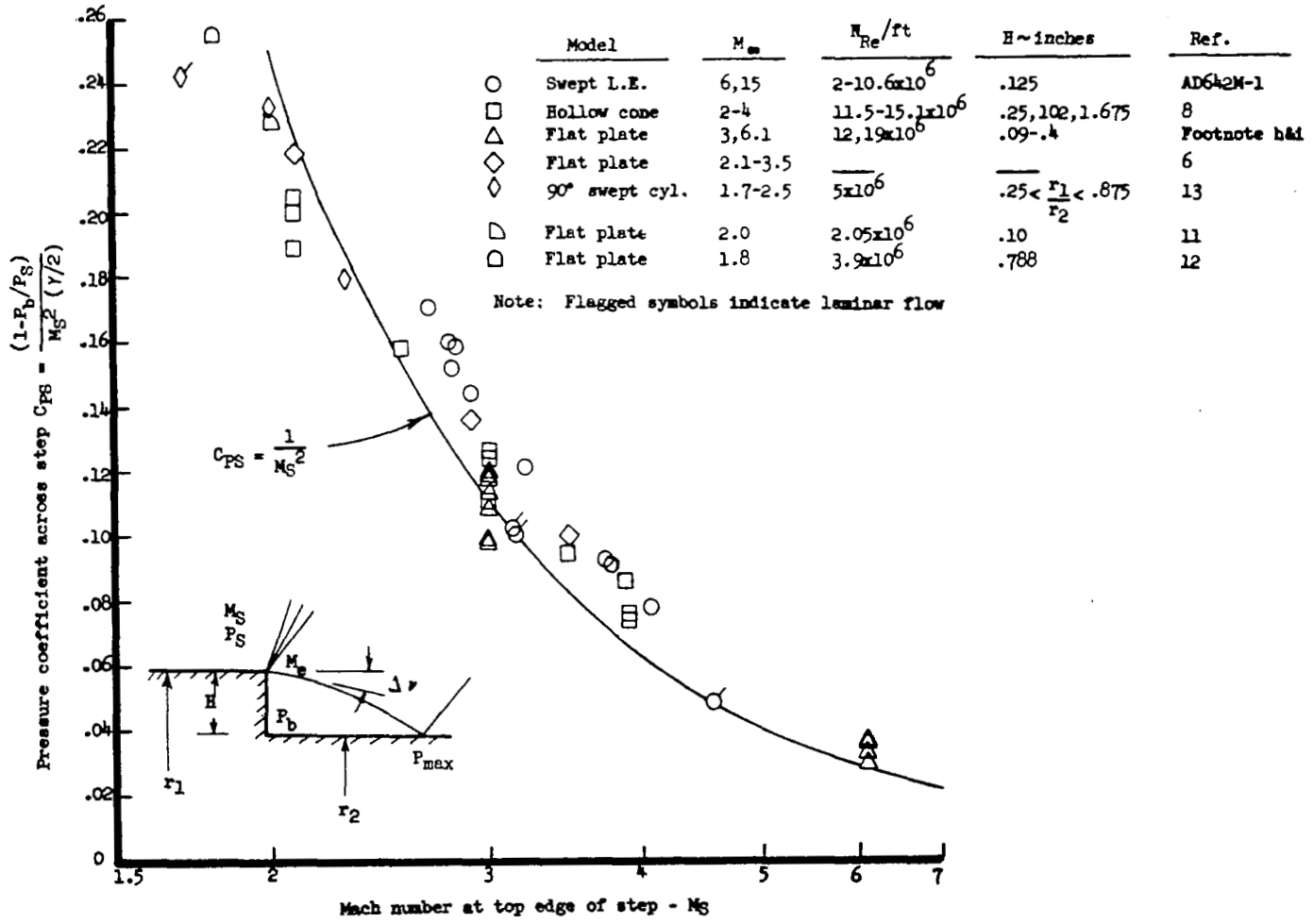

Figure 54.- Aft facing step base pressure coefficient correlation.

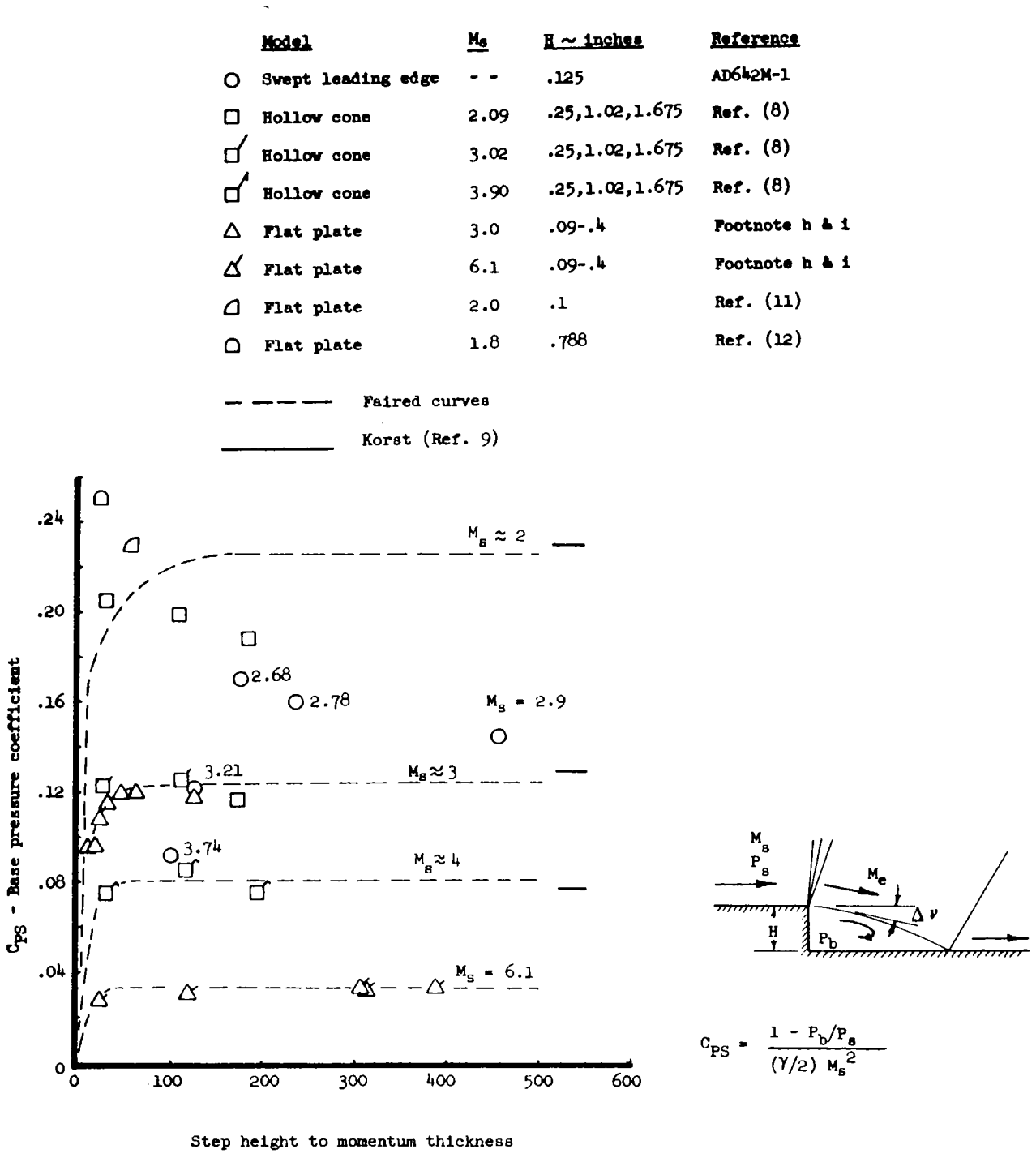

Figure 55.- Aft facing step base pressure correlation.

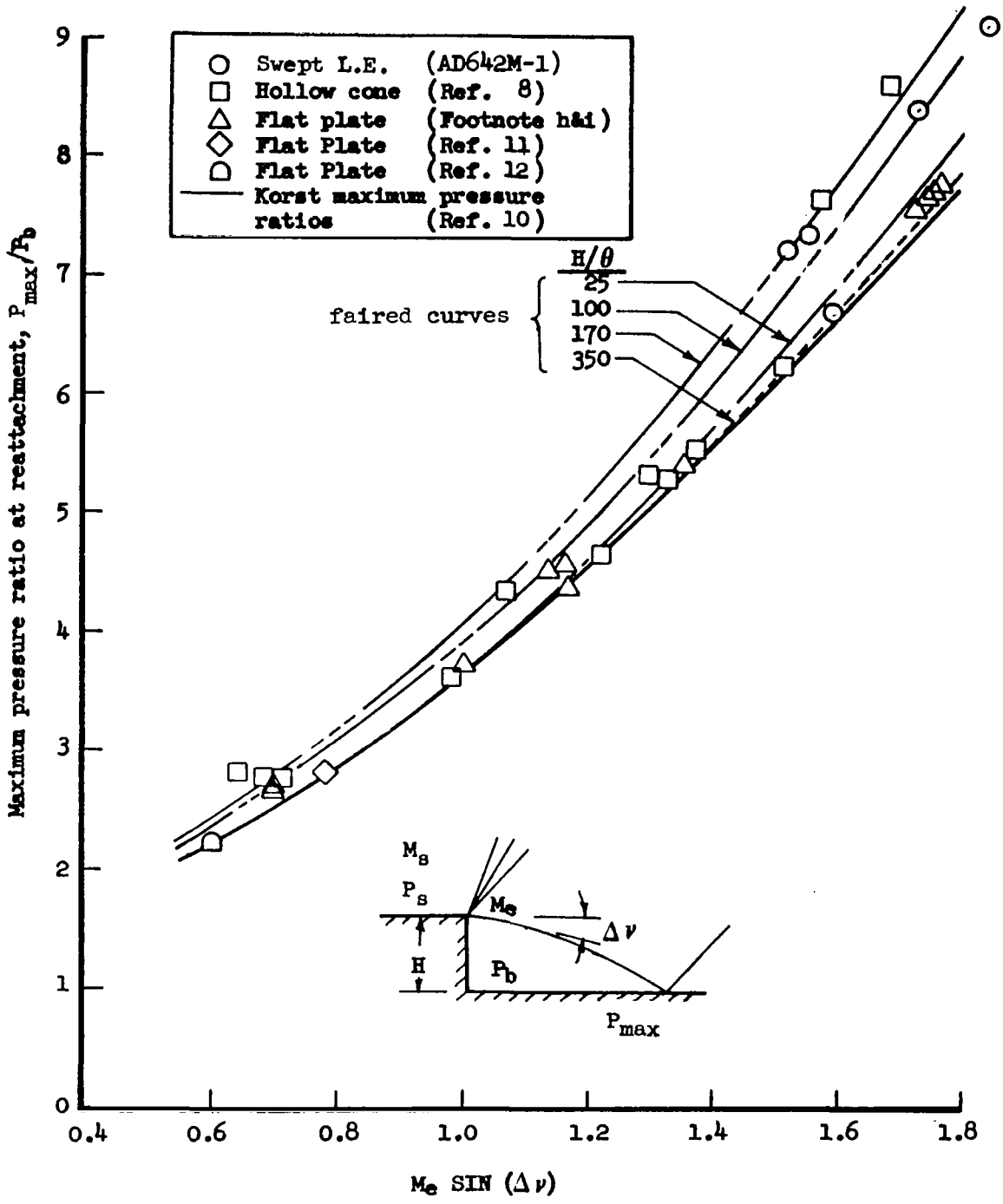

Figure 56.- Maximum pressure ratio at reattachment - aft-facing step, turbulent flow.

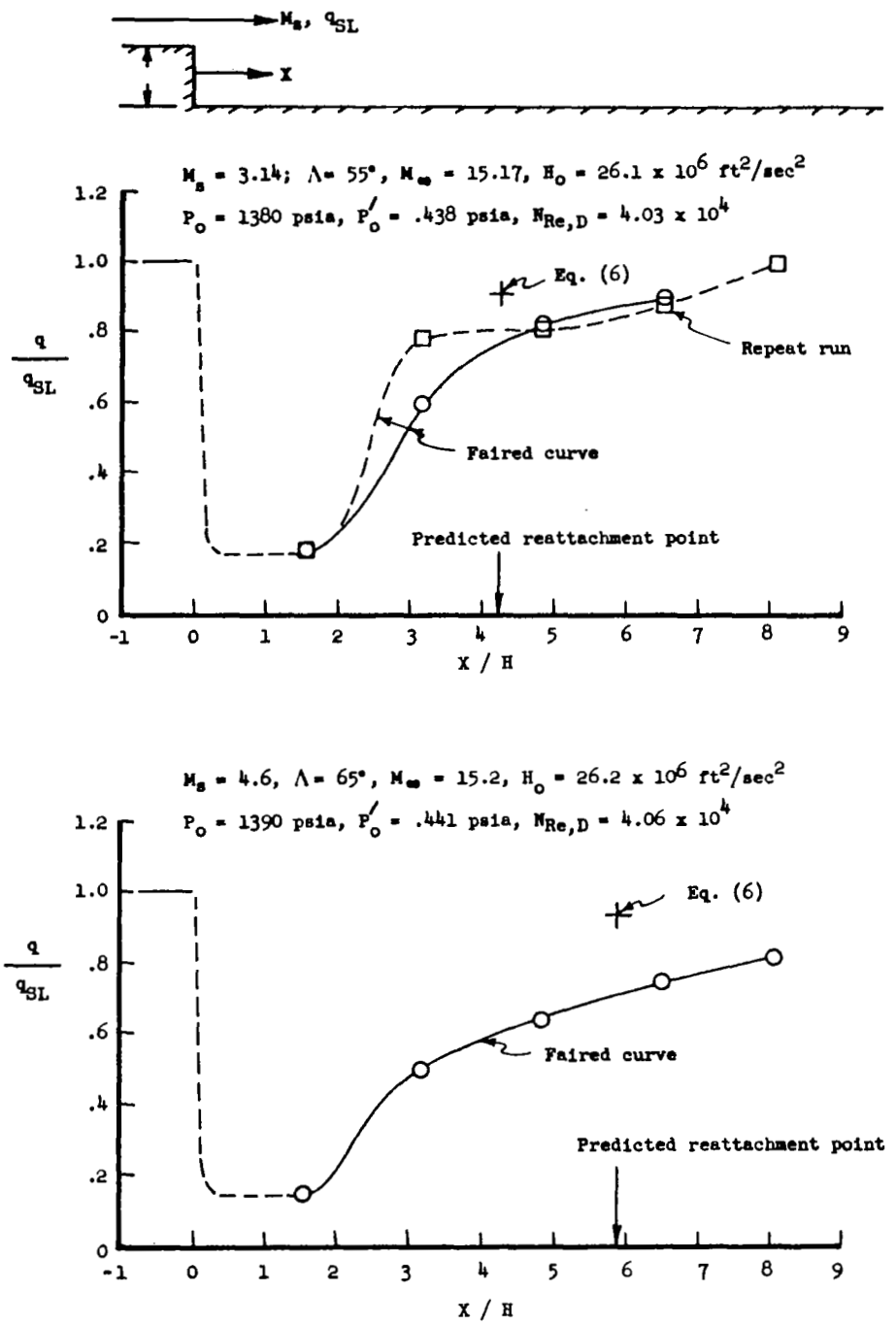

Figure 57.- Laminar heat transfer distribution for an aft-facing step on a swept leading edge

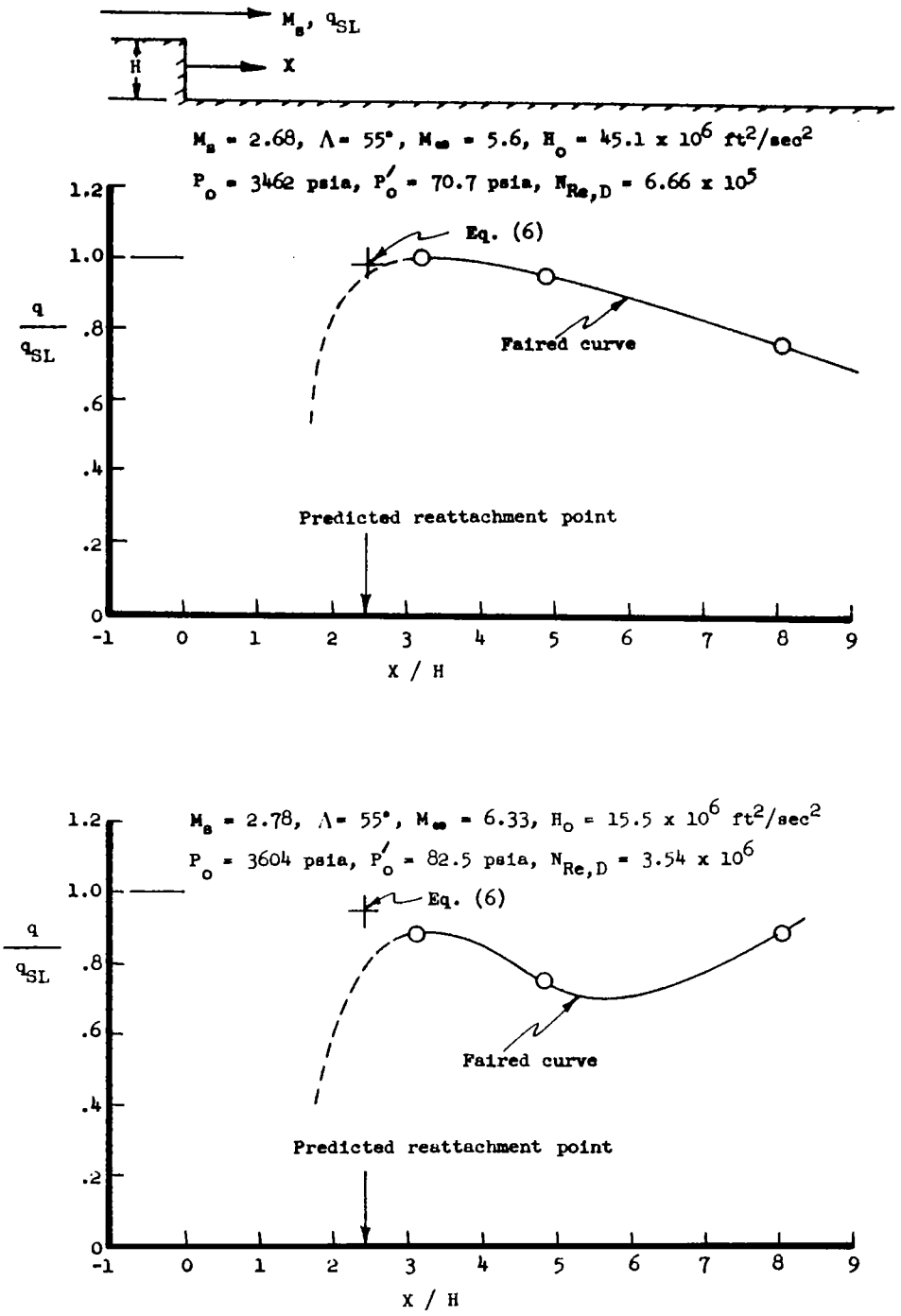

Figure 58.- Turbulent heat transfer distribution for an aft-facing step on a swept leading edge.

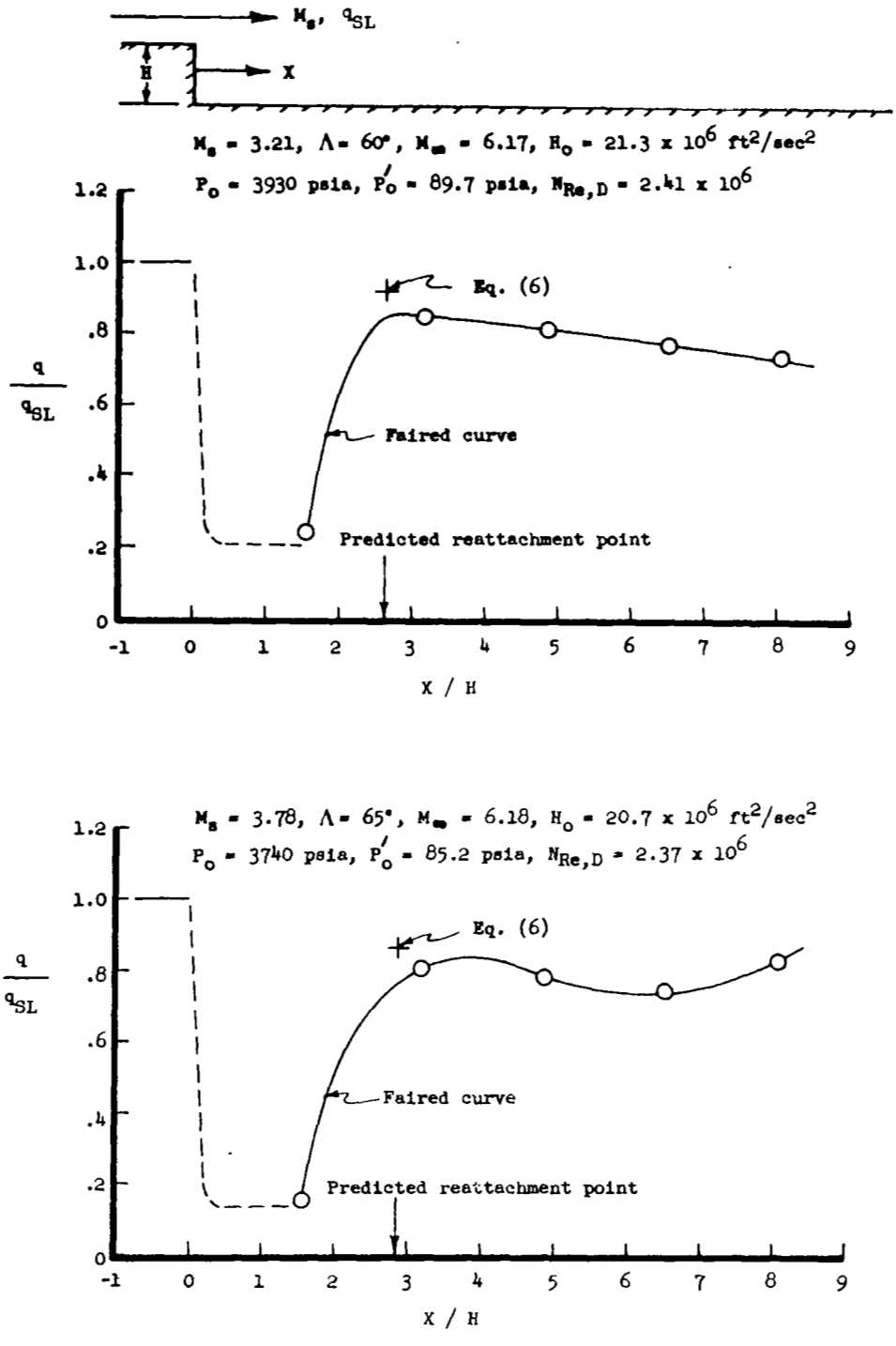

Figure 59.- Turbulent heat transfer distribution for an aft-facing step on a swept leading edge.

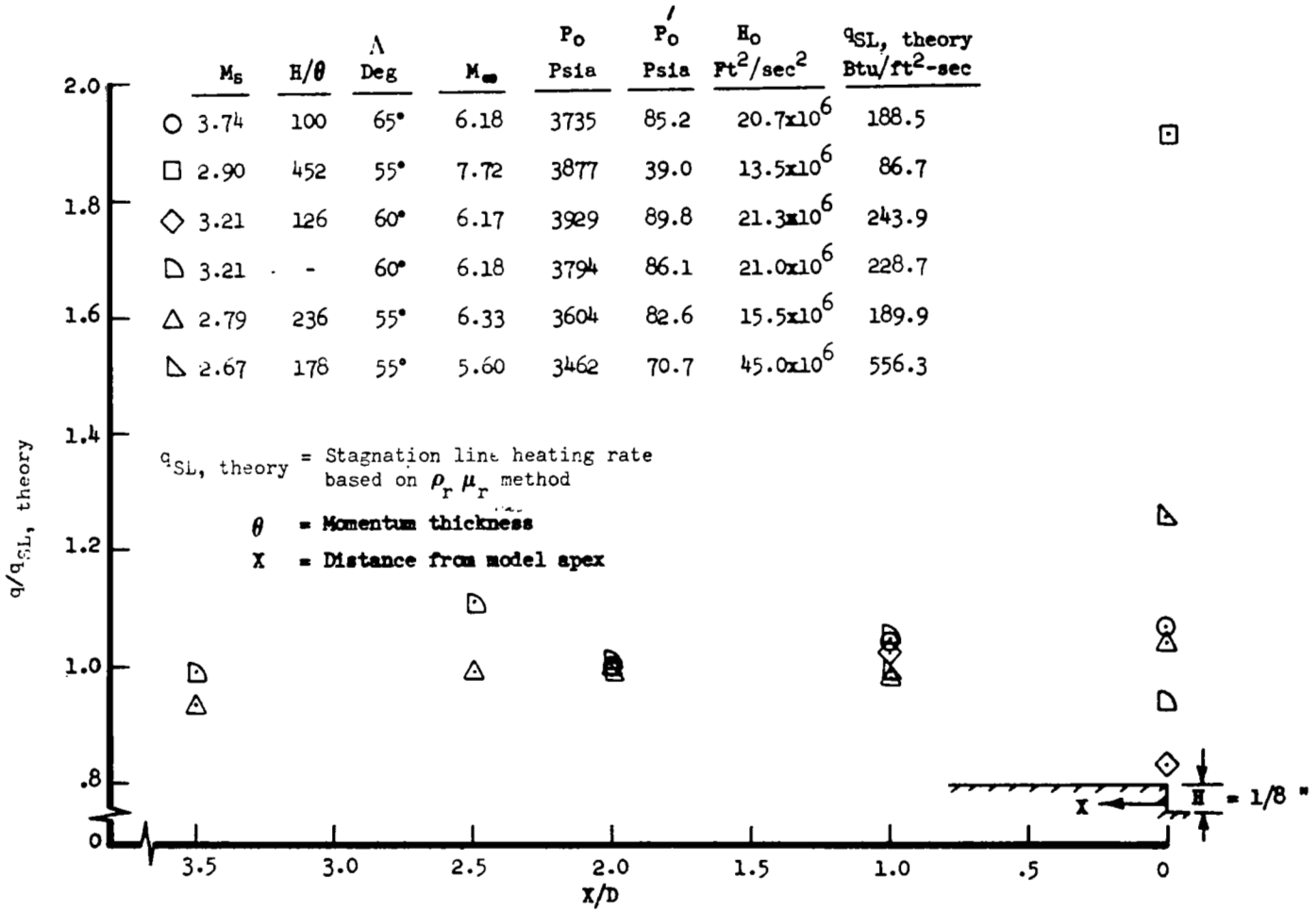

Figure 60.- AD642M-1 Swept leading edge stagnation line heat transfer data - turbulent flow.

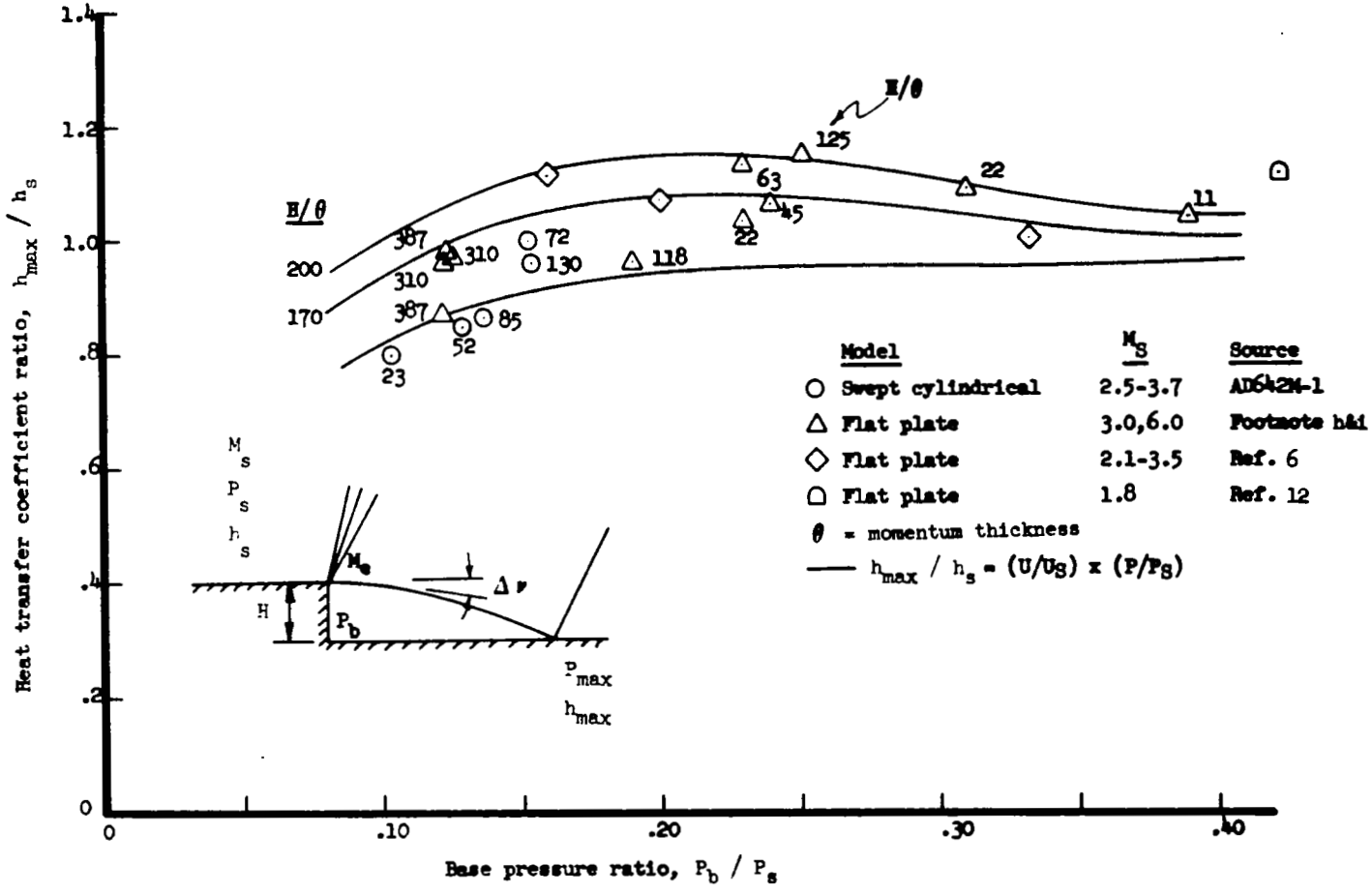

Figure 61.- Maximum aft-facing step reattachment heat transfer coefficients.

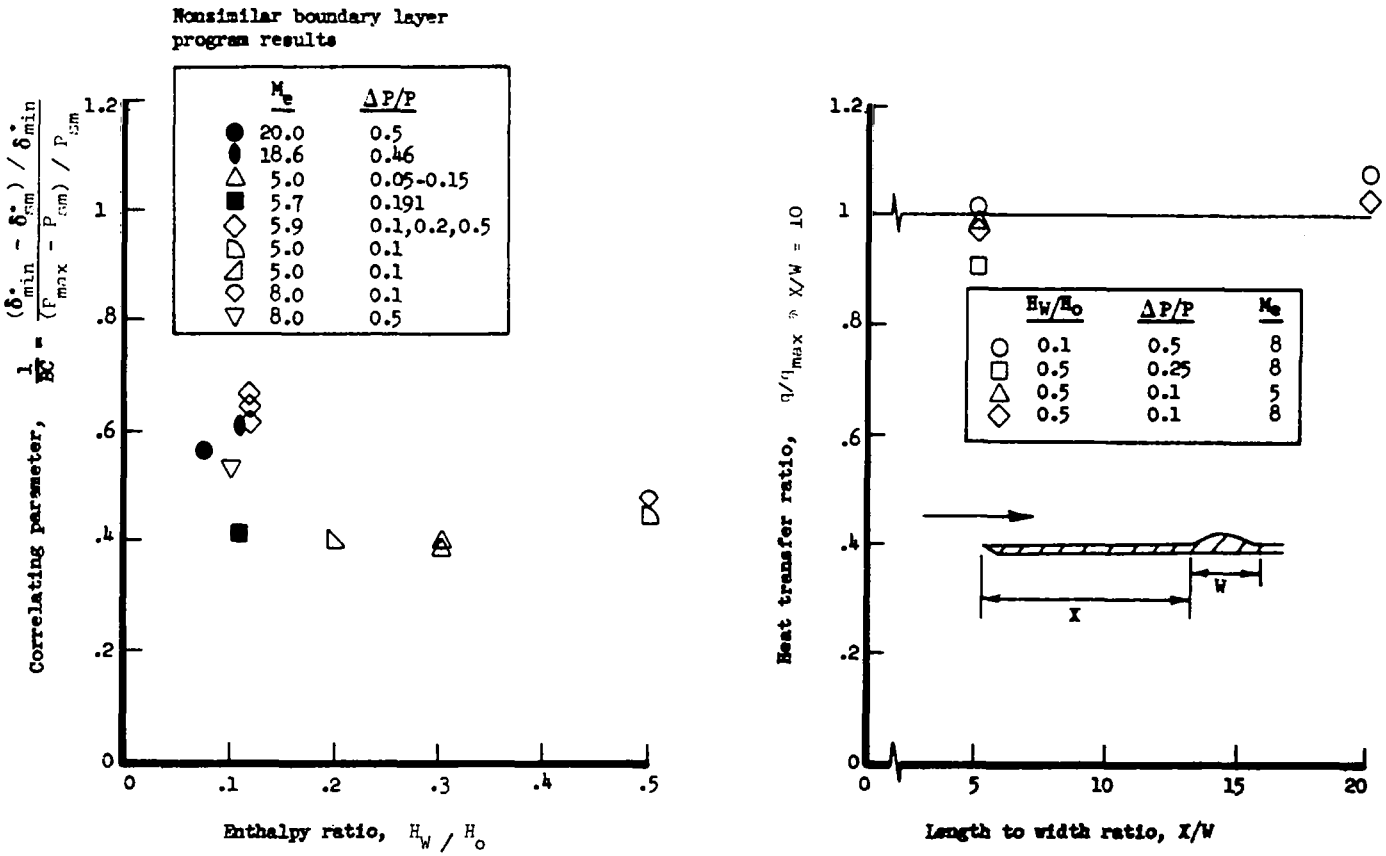

Figure 62.- Effect of wall cooling on the ratio of peak heating rate to maximum pressure rise.

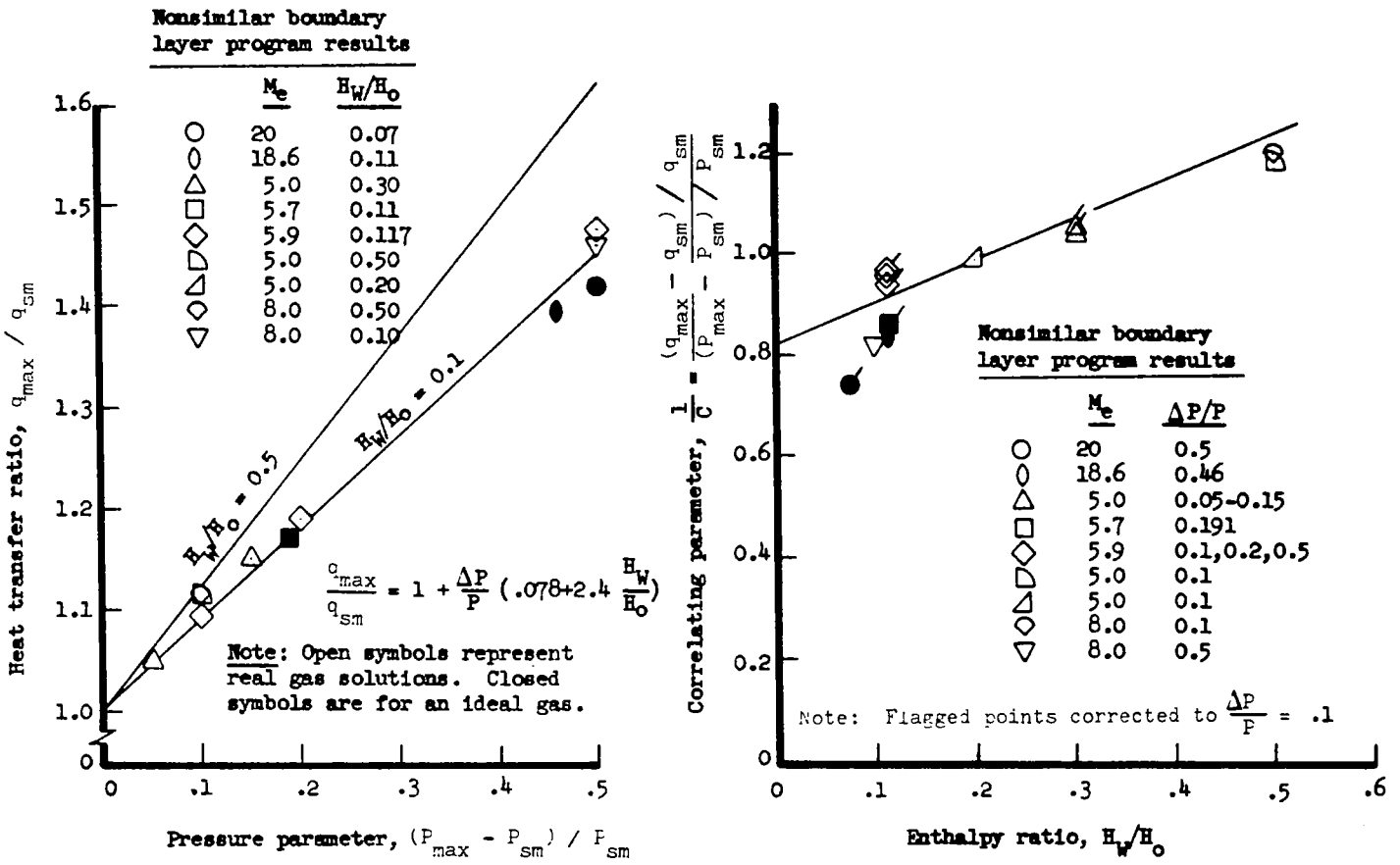

Figure 63.- Effect of wall cooling on displacement thickness with a sinusoidal pressure perturbation.

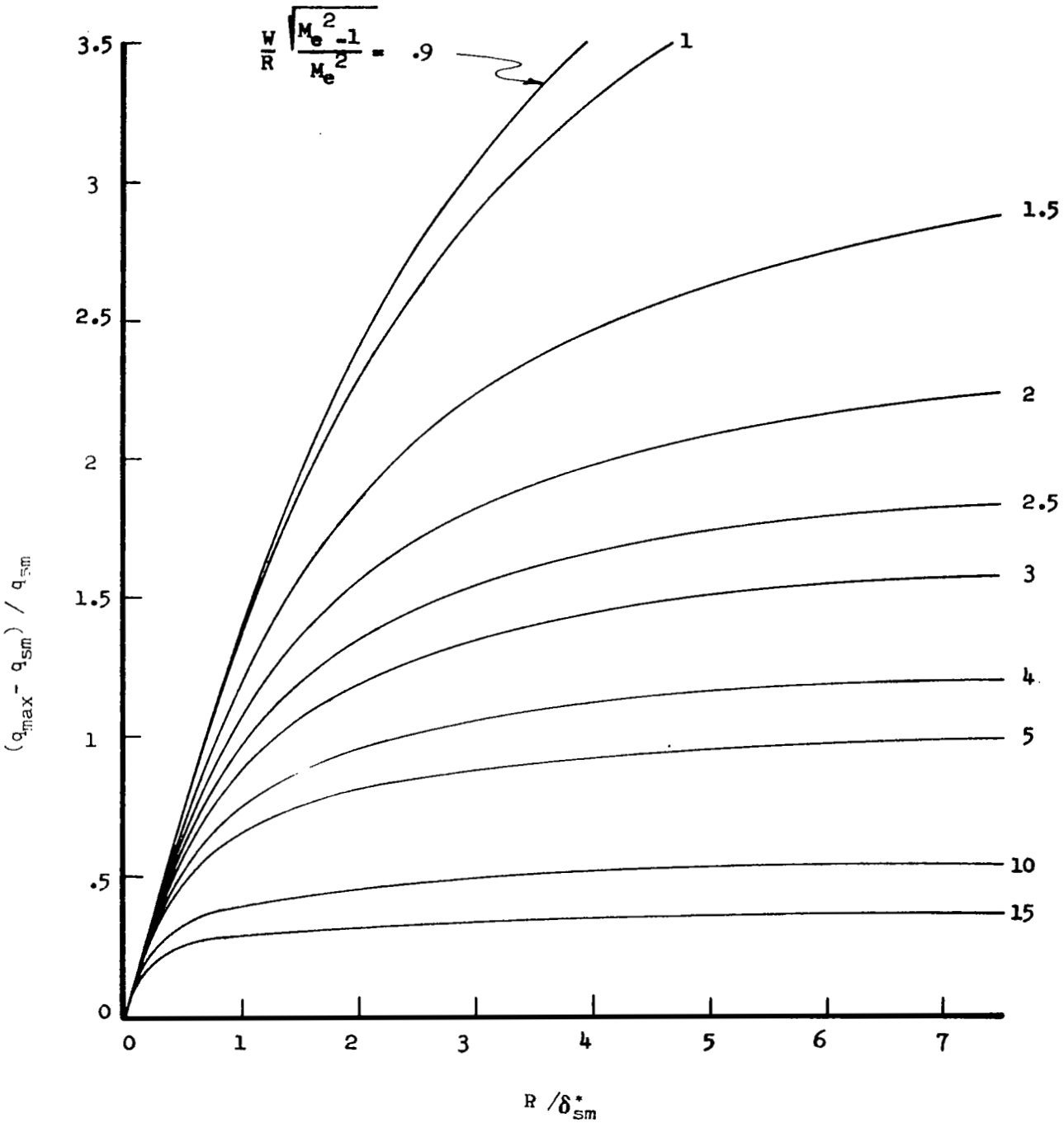

Figure 64.- Theoretical increase in laminar wave heating rate - H_w/H_o = 0.50, γ = 1.4.

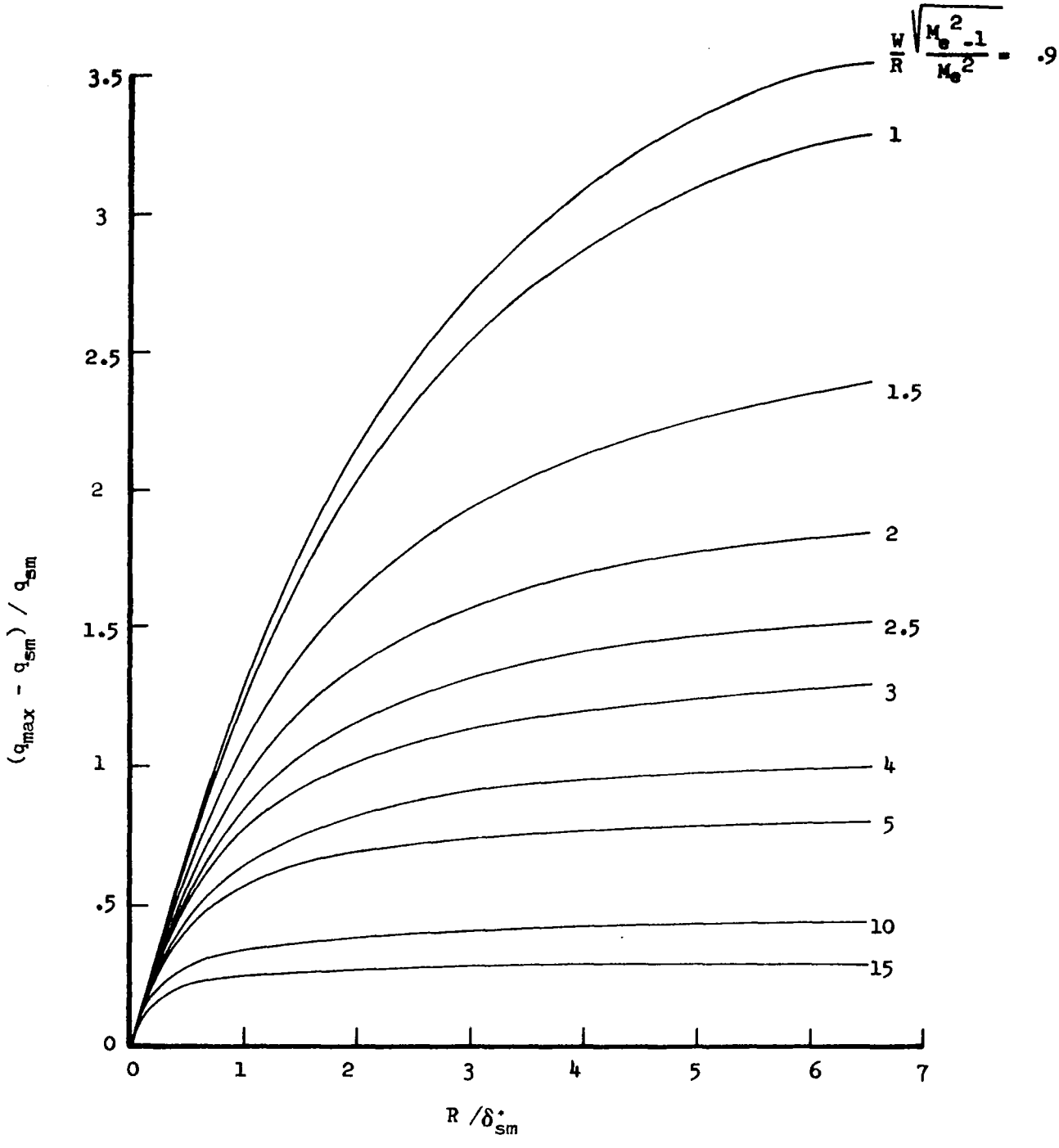

Figure 65.- Theoretical increase in laminar wave heating rate - $H_w/H_o = 0.262$, $\gamma = 1.4$.

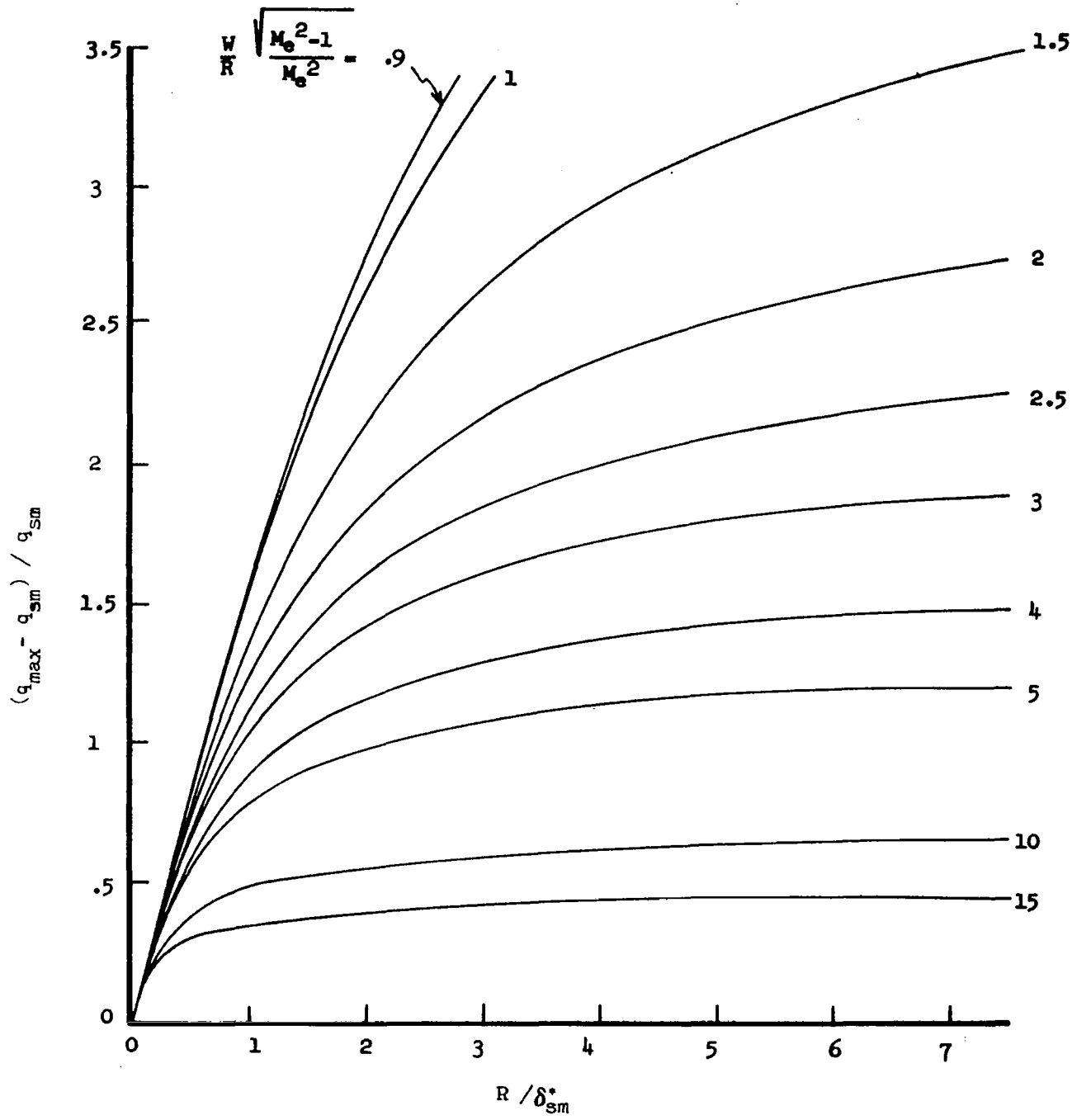

Figure 66.- Theoretical increase in laminar wave heating rate - $H_w/H_o = 0.85$, $\gamma = 1.4$.

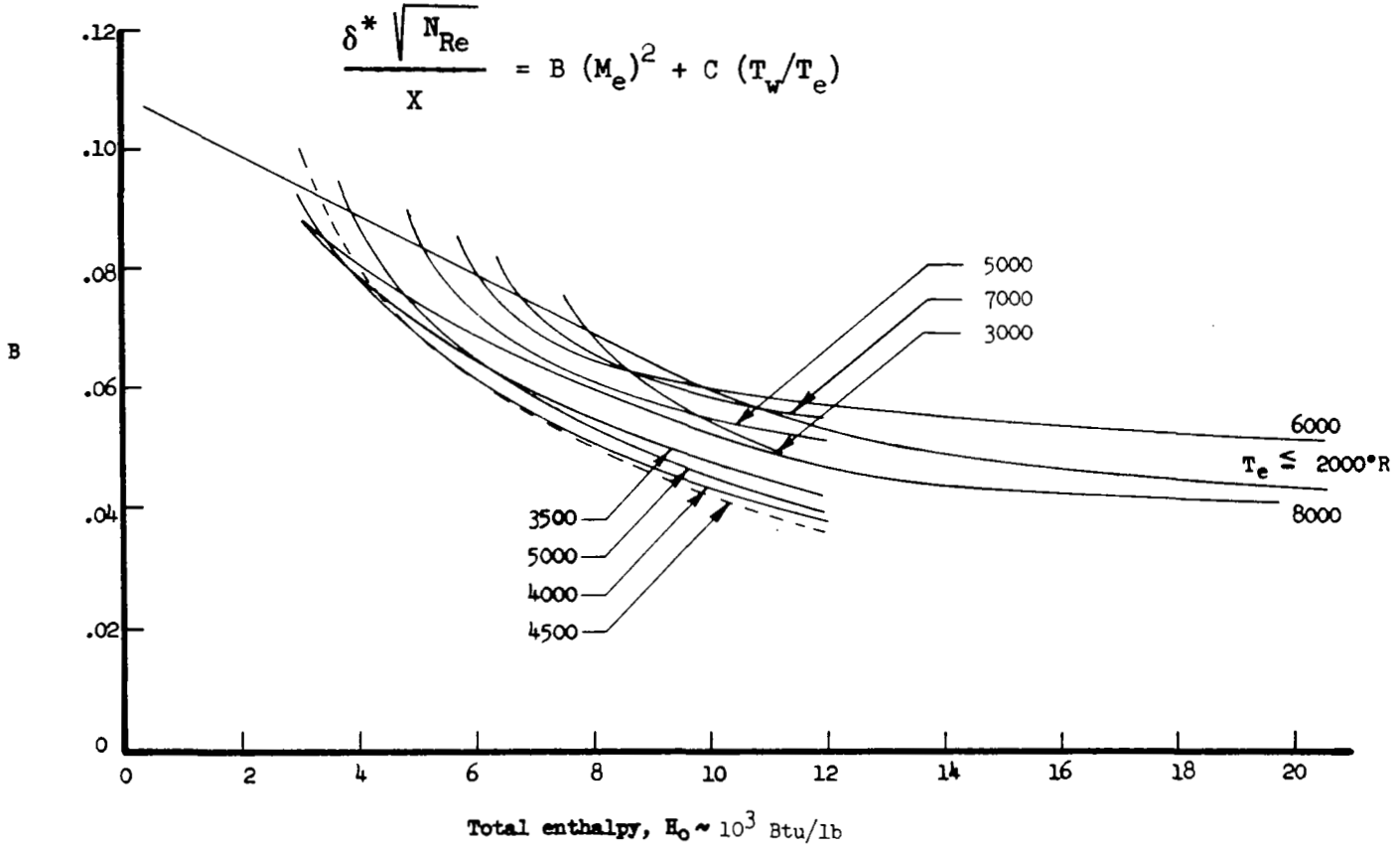

Figure 67.- Laminar boundary layer correlation coefficient.

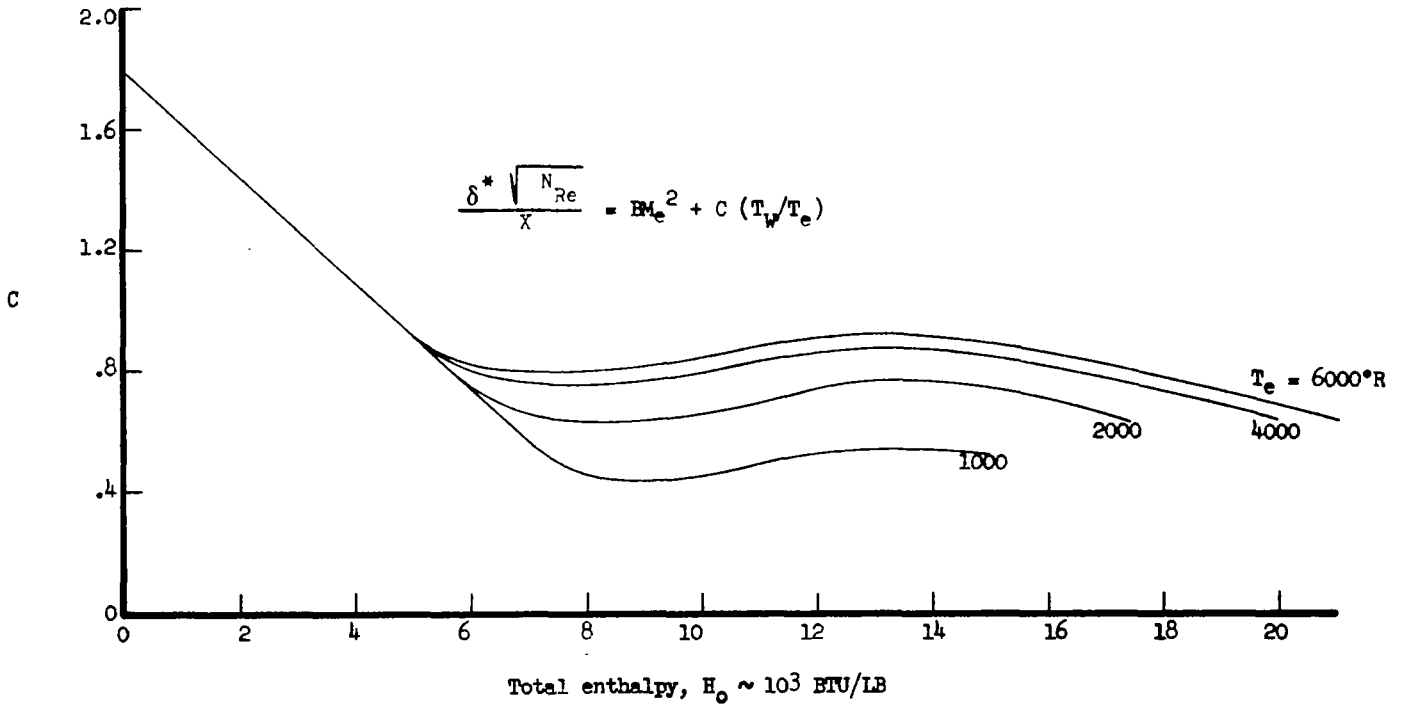

Figure 68.- Laminar boundary layer displacement thickness correlation coefficient.

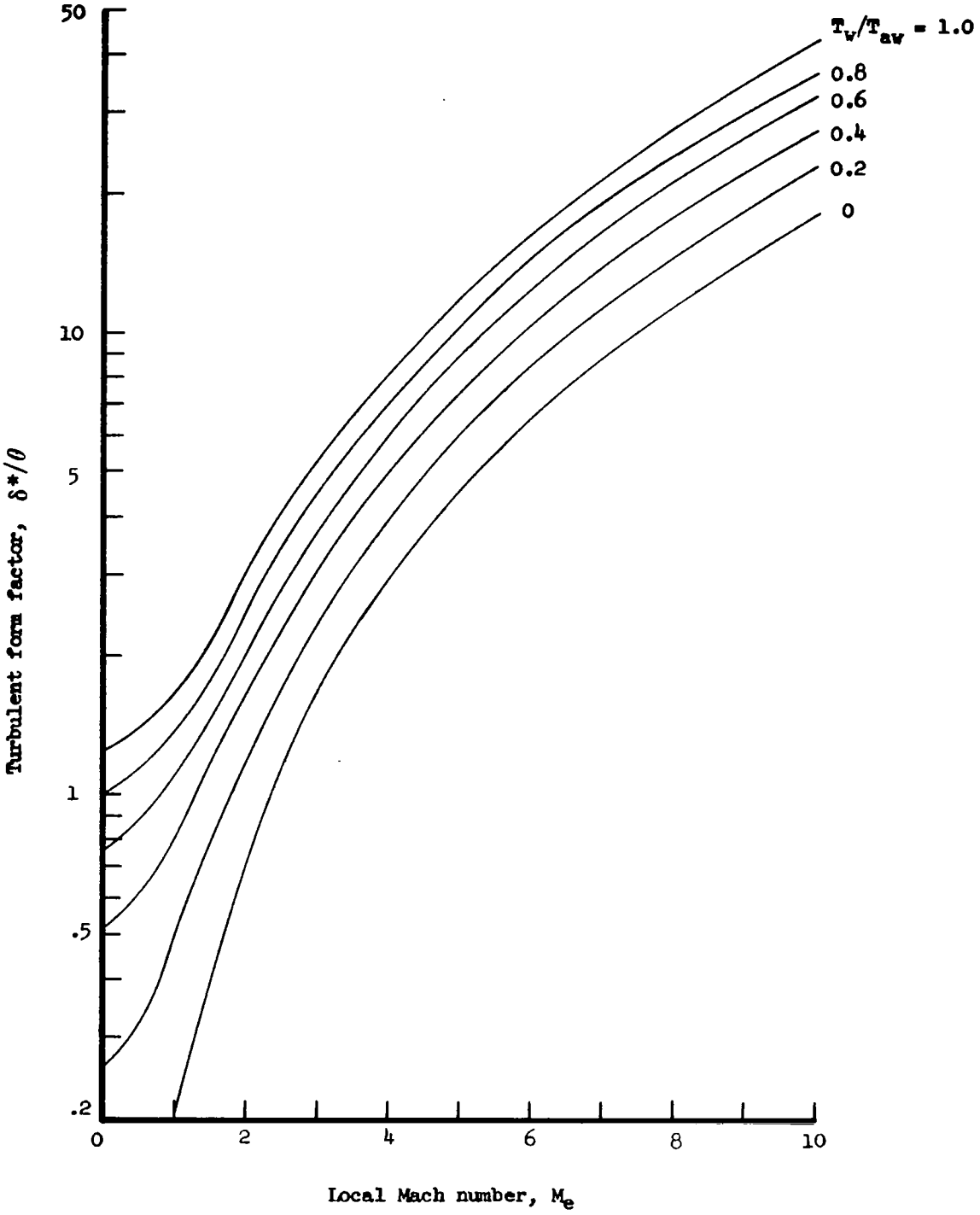

Figure 69.- Flat plate turbulent form factor, δ^*/θ.

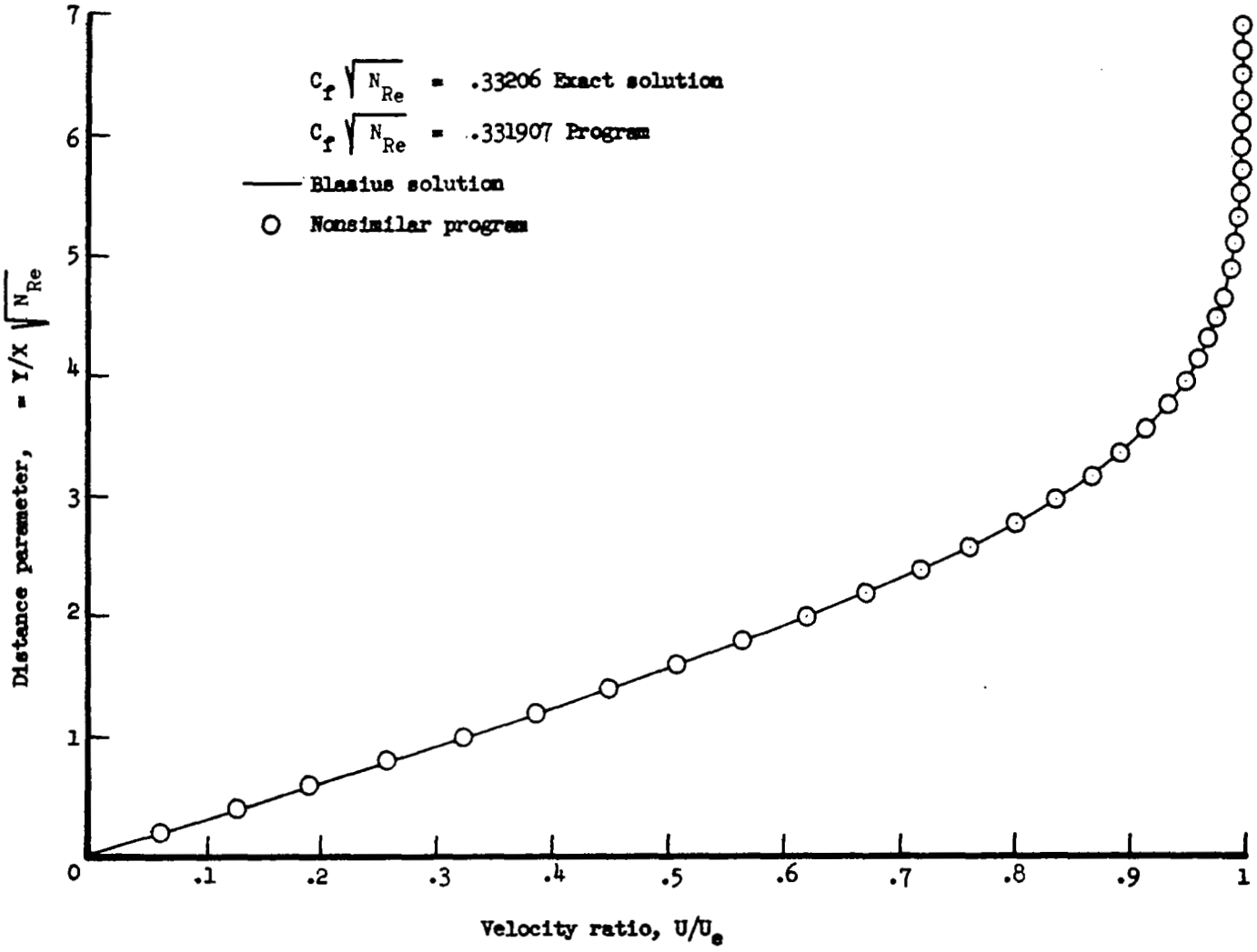

Figure 70.- Incompressible flow on a flat plate.

REFERENCES

1. Bertram, M. H.; and Wiggs, M. M.: Effect of Surface Distortions on Heat Transfer to a Wing at Hypersonic Speed. AIAA Journal, vol. 1, No. 6, June 1963, pp. 1313-1319.

2. Shore, C. P; Dixon, S. C.; and Griffith, G. E.: Experimental Turbulent Heat Transfer Coefficient Associated with Sinusoidal Protuberances on a Flat Plate. NASA TN D-1626, March 1963.

3. Baxter, D. C.; and Flugge-Lotz, I.: The Solution of Compressible Laminar Boundary Layer Problems by a Finite Difference Method, Part II; Further Discussion of Method and Computation of Examples. No. 118, Stanford University, October 1957.

4. Bogdonoff, S. M.; and Vas, I. E.: Some Experiments on Hypersonic Separated Flows. ARS Journal, vol. 32, No. 10, October 1962.

5. Charwat, A. F.; Roos, J. N.; Dewey, F. C.; and Hitz, J.A.: An Investigation of Separated Flows, Part I; The Pressure Field. Journal of Aerospace Sciences, vol. 28, June 1961.

6. Charwat, A. F.; Roos, J. N.; Dewey, C. F.; and Hitz, J. A.: An Investigation of Separated Flows, Part II; Flow in the Cavity and Heat Transfer. Journal of Aerospace Sciences, vol. 28, July 1961.

7. Rom, J.; and Seginer, A.: Laminar Heat Transfer to a Two-Dimensional Backward Facing Step from the High-Enthalpy Supersonic Flow in the Shock Tube. AIAA Journal, February 1964.

8. Roshko, A.; and Thomke, G. J.: Flow Separation and Reattachment Behind a Downstream Facing Step. Report SM-43056-1, Douglas, January 1964.

9. Korst, H. H.: A Theory for Base Pressures in Transonic and Supersonic Flow. J. Appl. Mech., vol. 23, 1956, pp. 593-600.

10. Thomke, G. L.: Separation and Reattachment of Supersonic Turbulent Boundary Layer Behind Downstream Facing Steps and over Cavities. Report SM-43062, Douglas, March 1964.

11. Chapman, D. R.; Kuehn, D. M.; and Larson, H. K.: Investigation of Separated Flows in Supersonic and Subsonic Streams with Emphasis on the Effect of Transition. NACA Rpt. 1356, 1958. (Supersedes NASA TN 3869)

12. Thomann, J.: Measurement of Heat Transfer and Recovery Temperature in Regions of Separated Flow at a Mach Number of 1.8. Report 82, The Aeronautical Research Institute of Sweden, Stockholm, 1959.

13. Beheim, M. A.: Flow in the Base Region of Axisymmetrical and Two-Dimensional Configurations. NASA TR R-77, 1961.

14. Giles, H. L.; and Thomas, J. W.: Analysis of Hypersonic Pressure and Heat Transfer Tests on a Flat Plate With a Flap and a Delta Wing With Body, Elevons, Fins, and Rudders. NASA CR-536, 1966.

15. Nagel, A. L.; Fitzsimmons, D. H.; and Doyle, L. B.: Analysis of Hypersonic Pressure and Heat Transfer Tests on Delta Wings with Laminar and Turbulent Boundary Layers. NASA CR-535, 1966.

16. Test Facilities Handbook. Arnold Engineering Development Center, 1963.

17. Description and Capabilities. Experimental Facilities Division Hypersonic Shock Tunnel. Cornell Aeronautical Laboratories 1964.

18. Skinner, G. T.: Analog Network to Convert Surface Temperatures to Heat Transfer. Report No. 100, Cornell Aeronautical Laboratory, Feb. 1960.

19. Vidal, R. J.: Transient Surface Temperature Measurement. Report No. 114, Cornell Aeronautical Laboratory, March 1962.

20. Bertram, M. H.: Hypersonic Laminar Viscous Interaction Effects on the Aerodynamics of Two-Dimensional Wedge and Triangular Planform Wings. Prospective NASA Langley Publication.

21. Bertram, M. H.; and Bardell, D.L.: A Note on the Sonic Wedge Leading Edge Approximation in Hypersonic Flow. J. Aeron. Sci., vol. 24, 1957, pp. 627-628.

22. Lees, L.: Laminar Heat Transfer over Blunt Nosed Bodies at Hypersonic Speeds. Jet Propulsion 26, 259-269-274 (1956)

23. Sivells, J. C.; and Payne, R. G.: A Method of Calculating Turbulent Boundary Layer Growth at Hypersonic Mach Numbers. AEDC-TR-59-3, Arnold Engineering Development Center, March 1959.

24. Hirschfelder, J. O.; Curtiss, C. F.; and Bird, R. B.: Molecular Theory of Gases and Liquids. John Wiley and Sons, 1954.